THE PREPARATION AND ANALYSIS OF SPUTTER DEPOSITED GLASS FILMS FOR THE PRESERVATION OF ANCIENT GLASS

by

D.M. USHER

Thesis submitted for the Degree
of Doctor of Philosophy

1981

CONTENTS

APPENDICES

ACKNOWLEDGEMENTS

The author takes this opportunity to express his gratitude to the many people who assisted him in the completion of this work. To Professor O.S. Heavens, and Dr. G.A. Cox thanks are due for their supervision over the three years. The enthusiasm shown by Dr. R. Hester in the field of Raman spectroscopy was of great benefit, and was surpassed only by that generated by Dr. J.A.D. Matthew. Dr. Matthew inspired the ELS spectroscopy and advised during the Auger work and the development of the electromigration theory in Chapter 8.

The experience and knowledge of Mr. J. Scott was invaluable during the design stages of the RF power oscillator. The sputtering chamber itself was admirably constructed by Mr. C. Wright, and the skill shown by Mr. L. Crosby in fabricating the electrodes is much appreciated. Thanks are due to Mr. J. Eastwood for his counsel on good vacuum design. Mr. P. Durkin offered considerable advice and assistance during the machining of many small components and the author would like to thank him for this and his seemingly unlimited tolerance.

Mr. S. Moehr, who has been involved in the project from its inception, was a constant fund of knowledge in all matters pertaining to the properties and machining of glass. His friendly and helpful support throughout the various stages has not only facilitated the work but also made it very much more enjoyable than otherwise it might have been.

During the final stages of the electron beam analysis, the CMA equipment was shared with Hilda Gray, who was investigating metallic glasses. For the assistance and support she selflessly gave, the author expresses his gratitude.

The help given by the staff of the Physics Department of the University of York has been enormous: thanks must be given to all.

DECLARATION

Except as specified in the acknowledgements, the work described is that of the author. Listed below are references to work previously published or pending publication, to which attention is drawn at appropriate points in the text.

PUBLICATIONS

"RF sputtering: design considerations for the disc and annulus system"

D M Usher and G A Cox Vacuum 31 p23 1981

"Sodium ion migration in glass on electron beam irradiation"

D M Usher J Phys C 14 1981 (pending)

"Problemes souleves par l'examen du verre par spectroscopie Auger"

O S Heavens and D M Usher Verres Refract 35 (1) p76 1981

ABSTRACT

This work is part of the project set up to study the composition of the ancient stained glass of York Minster with the aim of assisting in its conservation. A discussion of the structure of glass and its corrosion mechanisms, forms the basis of a treatise on sputtering glasses to form thin films. These films are designed to protect the stained glass from weathering. The necessary equipment is closely described, and details of the design and fabrication of various components are included. Recommendations are made concerning the problems attaching to RF power generation and transmission, and the performance of the coating plant is assessed.

In the second part of the volume is an account of the spectroscopic techniques that were used to determine quantitatively the composition of the glass films deposited by sputtering. Auger spectroscopy of glasses is discussed and a theory of electromigration of alkali ions is developed to account for the observed phenomena. Electron energy loss and Raman spectroscopies were used with limited predictive success, the reasons for which are set out.

Suggestions for future work on both the analysis and the deposition of films are included.

PRESENTATION

Throughout the following, the author has striven to adhere to the SI system of units and notation. Atavistic forms such as Å and cm (10^{-10}m and 10^{-2}m respectively) have been retained, however, because of their currency, convenient magnitudes and simple conversion factors. The relationships between the various units of pressure are indicated in the table below; pressures given in pascals in the text are often accompanied by their millibar equivalents.

Graphs were drawn using a software package developed by the author based on the GINO-F library routines supplied by DEC. The package includes a facility for smoothing the data by linear interpolation; shown in the top right of the plots is the number of times the data have been smoothed.

All computer programs were written in FORTRAN and run on the DEC 10 system.

The notation of units in equations is in accordance with the recent recommendations of the Royal Society. A physical quantity is represented in the form

quantity = numerical value x unit

and the ordinary rules of algebra are sustained. Thus, we may write

quantity/unit = value or expression

or quantity1/unit1 = value(quantity2/unit2)

and no confusion may occur between the symbols of the unit and those of the expression. The previous form

quantity(unit) -= numerical value

flouts the usual conventions and is not used herein.

Difficulties of spelling were reduced by reference to the Concise Oxford Dictionary.

TABLE OF CONSTANTS

SYMBOL	MEANING	VALUE	UNIT
e	elementary charge	1.6×10^{-19}	C
m_e	electron rest mass	9.1×10^{-31}	kg
m_p	proton rest mass	1.67×10^{-27}	kg
μ_o	permeability of free space	4×10^{-7}	Hm^{-1}
ϵ_o	permittivity of free space	8.85×10^{-12}	Fm^{-1}
a_o	Bohr radius	5.29×10^{-11}	m
e_M^2	$e^2/4\pi\epsilon_o$	2.3×10^{-28}	Jm

PRESSURE UNIT CONVERSION FACTORS

atm	Pa	mbar	Torr	kgm^{-2} (at $9.8ms^{-2}$)
1.0	101325.0	1013.25	760.0	10339.3
9.89×10^{-6}	1.0	0.01	7.5×10^{-3}	0.10204
9.89×10^{-4}	100.0	1.0	0.75	10.204
1.32×10^{-3}	133.32	1.3332	1.0	13.604
9.679×10^{-5}	9.776	9.776×10^{-2}	7.35×10^{-3}	1.0

INTRODUCTION

Ancient glass is irreplaceable. This statement may be disputed by no-one, of whatever discipline or disposition from fine artist to pure scientist, from historian to humanitarian, or from layman to specialist; it is self-evident. Less transparent are its interpretation and its implications. Here, opinions abound and controversy rages, following the dictates of fashion, constrained by the limits of technology. It is possible, however, to derive from the simple impossibility of replacing the glass a desire to conserve it, to prevent its loss or damage by whatever agency. This wish is not universally held, but the preservation of our cultural and artistic heritage by the best means available is, in the opinion of the author, not an unworthy aim.

It is in the nature of such disputes that the question of when and by whom sand was first fused with a flux to form a transparent glass has not been settled. The ancient peoples of China and Byzantium are among those mooted, and consequently it is probable that the art of glass making is as old as civilization itself.

Glass was manufactured during the Roman empire, and some of it has survived the millenia practically unharmed. The passing years have also left little impression on some of the glass made in Saxon times, recently excavated in the north of England. However, the craft of glass making was included in the huge and devastating loss of literature and learning as the Dark Ages fell. Not until the eleventh century, when the irresistible force of Mediaeval religious inspiration began to emerge, was glass again manufactured on a large scale. Even then, it remained mysterious; very little was written of the processes or of the materials; the knowledge was passed by example between generations of itinerant craftsmen. Their skill lay in applying years of experience to the problem of making glass from the

materials available locally, as they moved between the site of an abbey in France, a monastery in Germany or the burgeoning cathedral of St. Peter in York, known in modern times as York Minster. The east window of York Minster was constructed by John Thornton between 1405 and 1408 and may be regarded as the apotheosis of the craft. Subsequently, a greater range of techniques and influences dissolved the essential elegance, directness and naivete of the window maker's art to precipitate only a turgid sterility.

It was inevitable that mediaeval glass should have been of a very variable composition. Unfortunately the significance of that fact was not fully appreciated in York until the second world war, when the windows of the Minster were removed for their protection, and stored in oak shavings below ground. After the war, when the stupendous programme, conceived by the Dean and Chapter, to reinforce the foundations of the building, had begun, attention was turned to the task of restoring the windows to their original splendour. Then it was that the extent to which the condition of the glass had deteriorated over the years began to be recorded in detail. Not only were 'renovation' and other historical ravages seen to have taken their toll of the artistic integrity of the designs, but there was clear evidence of chemical attack to the glass sherds themselves.

Attempts were made to discover the reasons for the decay and the cause of an apparently sudden acceleration of the deterioration in recent times. To this end, the research programme at the University of York was initiated (1.15). In close collaboration with the 'York Glaziers' Trust', glass from the windows was analysed using X-ray fluorescence spectroscopy (1.19) to try to discover whether the different rates and mechanisms of decay could be attributed to compositional or to environmental factors. Photographs of decayed glass are reproduced in Fig. 1.8 and the results of the first three years of analysis are to be found in the work of Cox, Pollard et al (1.16, 1.17, 1.18). Chapter 1 of this thesis provides a brief

review of their findings, together with the necessary background for an explanation, not only of this work, but of that which is to follow. Blame is attributed squarely to water, particularly in droplet form. A bootstrapping process takes place; the products of the decay themselves tend to break the glass down further. A self-sustaining reaction occurs, which is the more virulent the smaller the volume of attacking solution.

The work described herein is a continuation of this research programme, being based on its results and conclusions. The conservation of glass windows is a subject fraught with differences of opinion. The debate between art historians and glass technologists concerning the various techniques and their effects has been passionate to an extent approached only by its proxility. Notwithstanding, we seek to make a contribution without becoming directly involved in the controversy.

Part A describes a technique known as RF sputtering (4.1, 4.2, 4.3) and how it may be used to provide samples of decaying mediaeval glass with a protective coating. The material of the coating must be durable; it must, indeed, have a longevity comparable with that of the sample. Hence, glass coatings suggest themselves. A film of durable glass only a few micrometers in thickness should, if bonded intimately to the substrate, provide sufficient protection. RF sputtering is shown to be capable of depositing very thin glass films on various substrates, and the design criteria for the equipment needed are discussed in detail in Chapters 4 and 5. Chapters 2 and 3 provide the mathematical bases of sputtering multicomponent materials. The performance of the sputtering plant is described in Chapter 6.

Part B forms a disquisition on attempts to quantify the composition of the films to assess their durability. Admittedly, success in this field has proved more elusive. Of the analytical techniques described, Auger spectroscopy, electron energy loss spectroscopy (Chapter 8) and Raman

spectroscopy (Chapter 9), none has yielded compositional data of sufficient accuracy to permit the reliable prediction of durability. Despite this, there are some illuminating results concerning the phenomenon of ion electro-migration under electron bombardment (8.13, 8.14, 8.15) and the effect of ion-etching the surface of analytes. The equipment used for the electron spectroscopy is described in theoretical and in practical terms in Chapter 8. The fact that the analytical techniques were discovered to be inappropriate may in itself be regarded as a pointer to the necessary future work, described in Chapter 10.

RF sputtering, in common with other methods for the preservation of stained glass windows, possesses both advantages and disadvantages. Principal amongst the disadvantages is that the specimens must be removed from the window and placed in the coating plant. However, since such windows must be releaded regularly (albeit infrequently), this problem is not prohibitive. The drawback of the undoubted expense of the process, particularly in terms of skilled operator involvement, must be viewed in the priceless light cast by the mediaeval glass itself. The samples are unique; what financial restraint may be placed upon their preservation? If an entire window cannot be treated, and important pieces such as representations of heads are endangered, then these may be preserved individually.

Criticism of the irreversibility of vacuum methods is cogent. Future conservationists might be frustrated if they wish to extirpate the feeble-minded attempts of the 20th century following the introduction of a superior technique or the long term failure of this one. The period of spectroscopic analysis has been protracted, and has provided a sound understanding of the mechanisms of the surface reactions with water, and the nature of the problem with which we are dealing. It is felt that damage to the specimens caused by the presence of a glass film is negligible (there would be no visible effect whatever) and that the requirement to

remove the coatings cannot conceivably arise.

The success of other conservation methods attempted in recent years has been variable. The controversial history is recounted in the newsletters of the Corpus Vitrearium Medii Aevi edited by Professor R.G. Newton. The organic coatings used at Chartres have been criticised for their failure specifically to exclude water from surface crevices and for their alleged long-term discoloration. Organic methods are quicker and cheaper than vacuum ones, but the latter cannot possibly fail to remove damaging residual water.

In many instances, ancient windows have been enclosed between modern ones, in the form of quarry panels. This provides protection from the elements (as well as from missiles) but unless the humidity is carefully controlled over the entire enclosed volume, the formation of condensation cannot be avoided. We have seen that condensation is potentially more damaging than rain. The additional necessity of preserving the appearance of the exterior of ancient buildings renders completely unacceptable the erection of modern float glass panels, with aluminium glazing bars, in an attempt to prevent the penetration of water.

Indeed, the only reliable method of conserving the glass would be to remove it to a museum with rigidly controlled atmospheric humidity and temperature. However, the windows themselves would not be conserved by such action; they would be destroyed. As representations of mediaeval culture, they cannot be divorced from their artistic context; as religious icons, they should not be removed from the spiritual centres for which they were conceived and constructed.

It should be observed that prior to any preservative treatment whatever, it will be necessary to clean the glass, possibly in an ultrasonic water bath, to remove the accumulated deposits. It is this process that 'damages' the glass most, because the quantity of light transmitted

by each piece may be substantially altered, profoundly changing the appearance of the windows. Despite the fact that a cleaned window more nearly approaches the original design, such changes have traumatized specialists. The aesthetic effects of protective coatings are overwhelmed by the changes caused by the preparations necessary for their application. In this context, the terms 'damage' and 'conservation' are open to a wide range of interpretation.

We may concede the necessity of temporarily removing the specimens from the windows and cleaning them, and turn to a consideration of methods of depositing films of glass. Thin films of most materials may generally be formed by condensation from the vapour phase. As a mixture of components, however, glass has no identifiable vapour (each oxide is fractionated separately) and thus the stoichiometry of the condensate might be expected to differ from that of the source material. Recently, several papers have recounted the success of 'ion plating' (10.1, 10.2, 10.3) in depositing thin films of substances ranging from titanium to ceramics. The University of Salford would appear to be the British centre of excellence in this field. The technique consists in connecting the substrate as the anode of a DC low pressure discharge, sputter-etching its surface until it is atomically clean, and evaporating on to it the material of the film, meanwhile maintaining the discharge. This does not appear to obviate the difficulties caused by the differential evaporation of glass components, and whether an irregularly shaped dielectric substrate may be coated is not clear. Indeed, no explicit reference to ion plating glasses is made, but the surprising success of Park and Weitzmann (10.4) in using electron beam evaporation to produce glass films of stoichiometry comparable with that of the source glass suggests that each component must vaporise at approximately the same rate. Hence, both ion plating and electron beam evaporation are techniques worthy of consideration, although the particular requirement of

bonding to irregular glass substrates puts them at a disadvantage.

In contrast, RF sputtering has been used extensively in the creation of glass films, whose composition has been shown by infra-red spectroscopy to be similar to their source material (9.12). The mathematical development in Chapter 3 indicates that the sputtered flux (the material which forms the film) would be expected to become stoichiometrically exact. Additionally, the slight but continuous ion bombardment of the substrate during deposition, which is a positive feature of ion plating, also occurs in RF sputtering. This leads to excellent bonding between film and substrate as the material of the film is introduced into the bulk of the substrate by collisional implantation (4.20, 2.15). The gradual transition is advantageous when considering the problem of differential thermal expansion; film and substrate need not be as exactly matched as other methods require. Very recently, some Austrian work (10.5) has shown RF sputter deposited 'organotin' coatings to be successful in reducing the corrosion of simulated mediaeval glasses. The coated specimens have withstood rigorous artificial weathering better than uncoated ones, and good film adhesion has been noted. It is suggested that the chemical reactivity of such films would be reduced by doping with hydrophobic groups, which work is continuing. The same problems with thermal expansivity mis-match are met with this material.

The above forms the background of the project. In the following chapters, RF sputtering of glasses is assessed as a weapon in the battle for an aspect of our cultural heritage against the constant attrition of the climate.

PART A

RF SPUTTERING OF GLASSES : THEORY AND PRACTICE

The following six chapters are devoted to a description of RF sputtering as a method of depositing thin glass films. The equipment was constructed in the laboratory, according to the machine drawings of the author.

The structure of glass is briefly discussed to permit its behaviour during ion-beam bombardment to be understood.

CHAPTER 1

GLASS STRUCTURE AND PROPERTIES

It is necessary, for an understanding of the work described in this volume, briefly to consider the general structural features of the type of material referred to as 'glass'. The complete absence of an evolution of 'latent heat' when certain mixtures of inorganic oxides are cooled from the melt is interpreted by postulating that the usual abrupt ordering of the atomic positions known as crystallization has not taken place. Such materials, being solid but having the disorder characteristic of liquids 'frozen in', are known as glasses. X-ray diffraction studies convincingly demonstrate the lack of order in glasses, since Bragg reflexions are replaced by broad rings (1.1).

As the temperature of a molten material is reduced, its specific volume will fall steadily (1.2) as seen in Fig. 1.1. On crystallization there will be a sharp drop in this quantity, after which its fall-off with temperature will be slower. Glass forming melts, however, exhibit no sudden transition; there is a gradual change of specific volume over a temperature range of a few hundred degrees around a temperature (the glass forming temperature) which depends on the rate of cooling of the batch. Thus, the properties of glass are not well defined; they may vary between batches and be altered by heat treatment in ways not easy to predict or to quantify.

Chemical bonding in glass is satisfactorily treated as wholly ionic while recognising that the Si-O bond does have an element of covalency. The discussion will be restricted to silicate glasses since this is the most useful and common type, and is of relevance to mediaeval glass studies. Organic glasses are not considered.

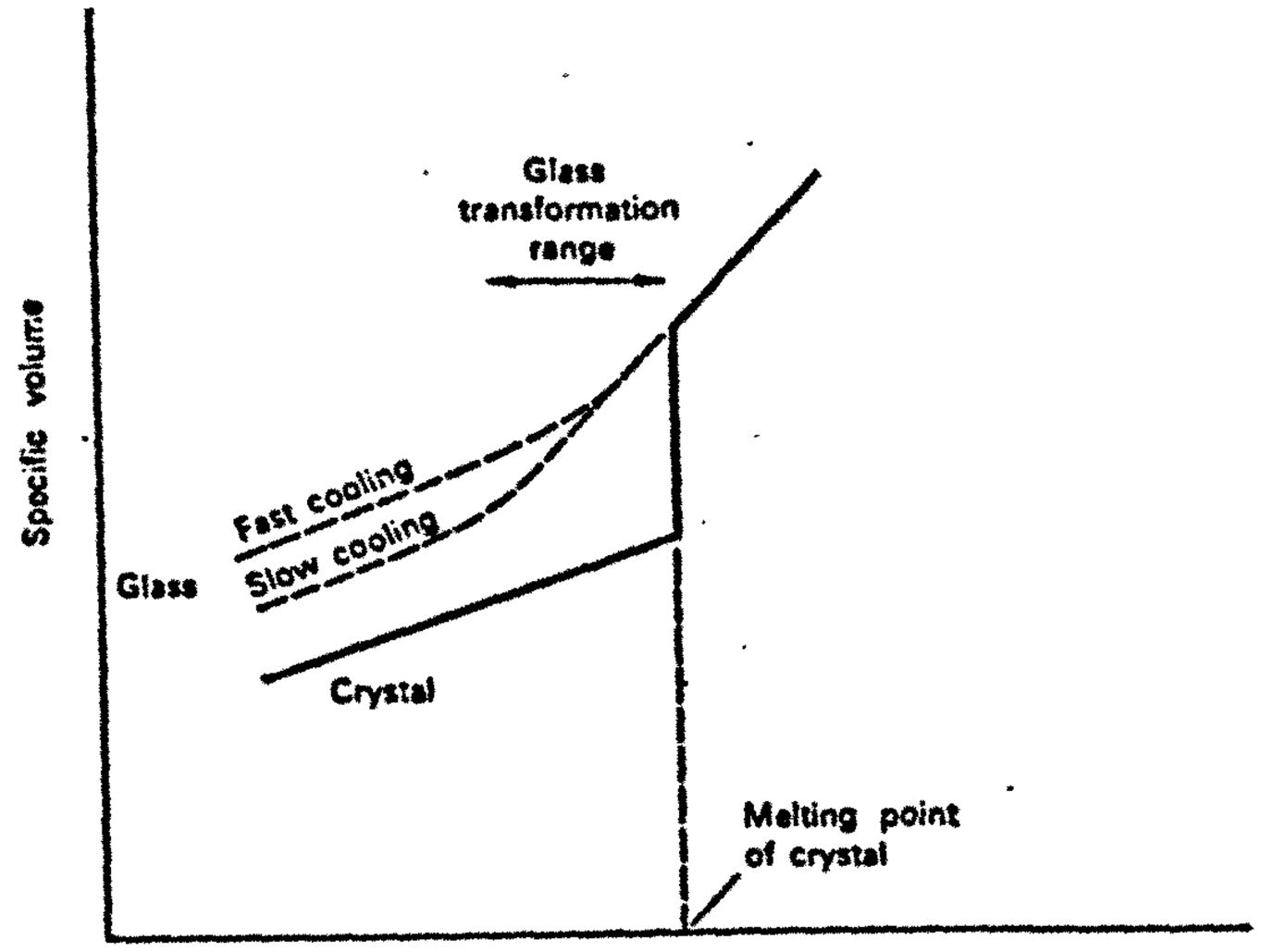

Fig.(1.1): Specific volume of melt against temp.

ref.(1.2)

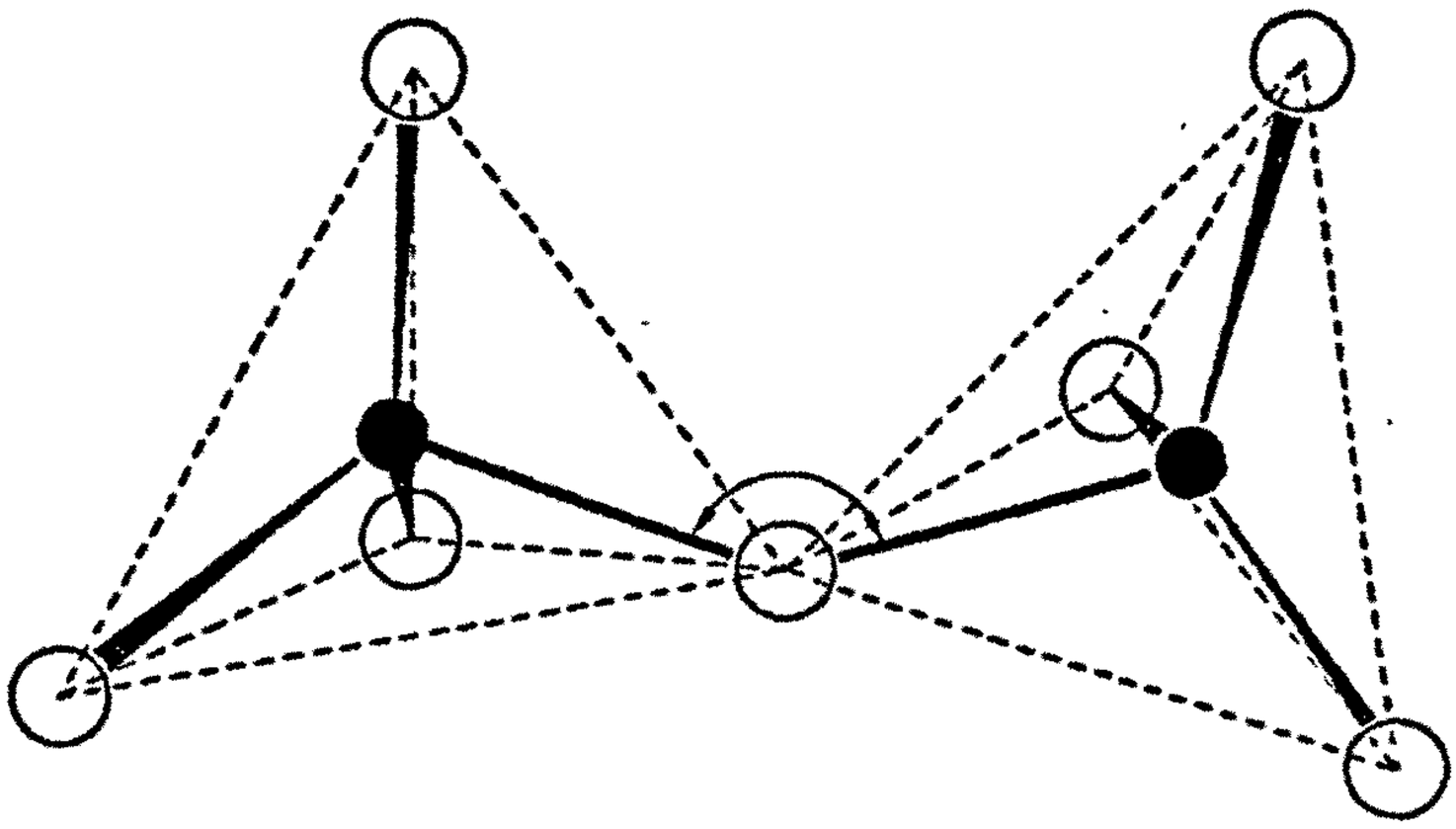

Fig.(1.2a): SiO_4 tetrahedra and bridging oxygen atoms.

ref.(1.2)

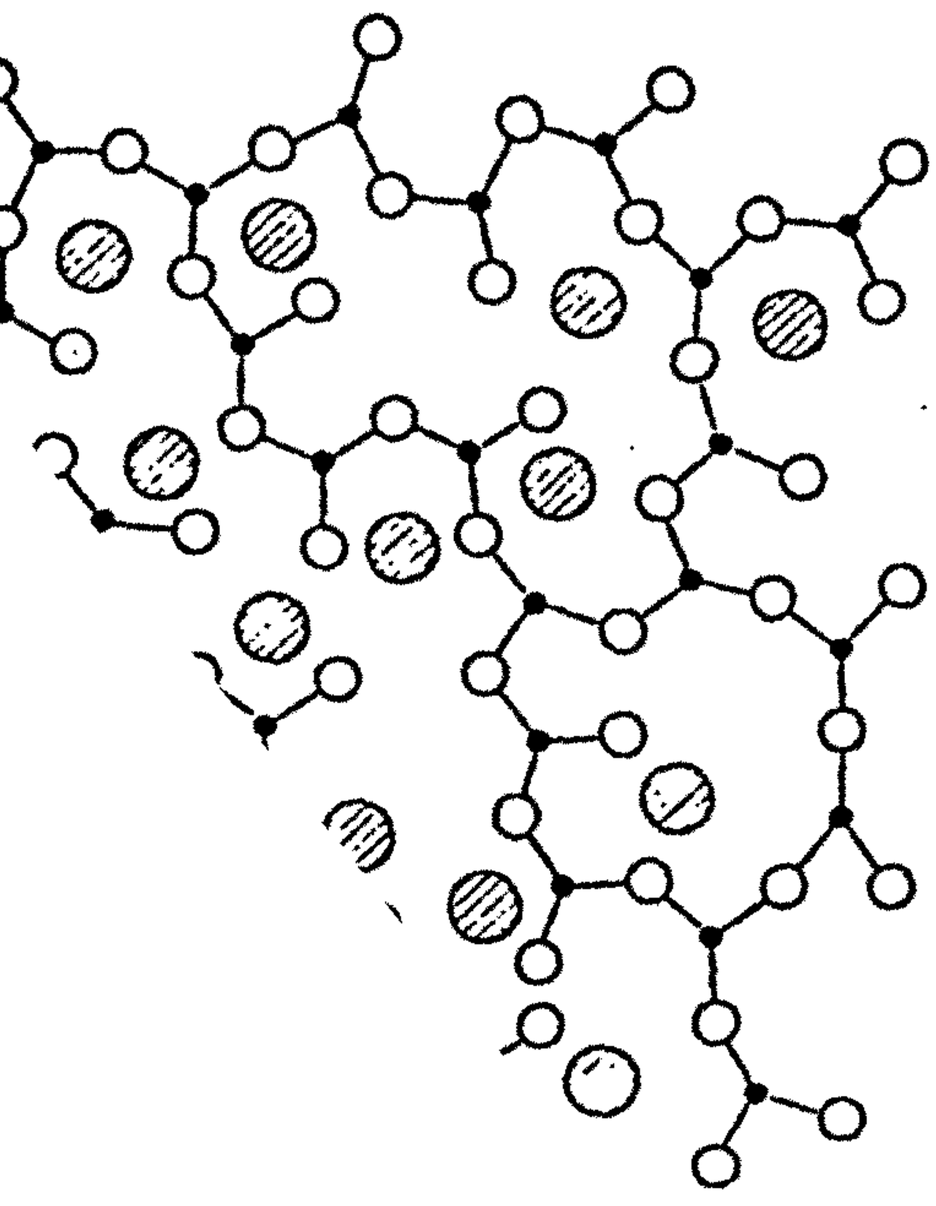

Fig.(1.2b): Two-dimensional random network (1.2)

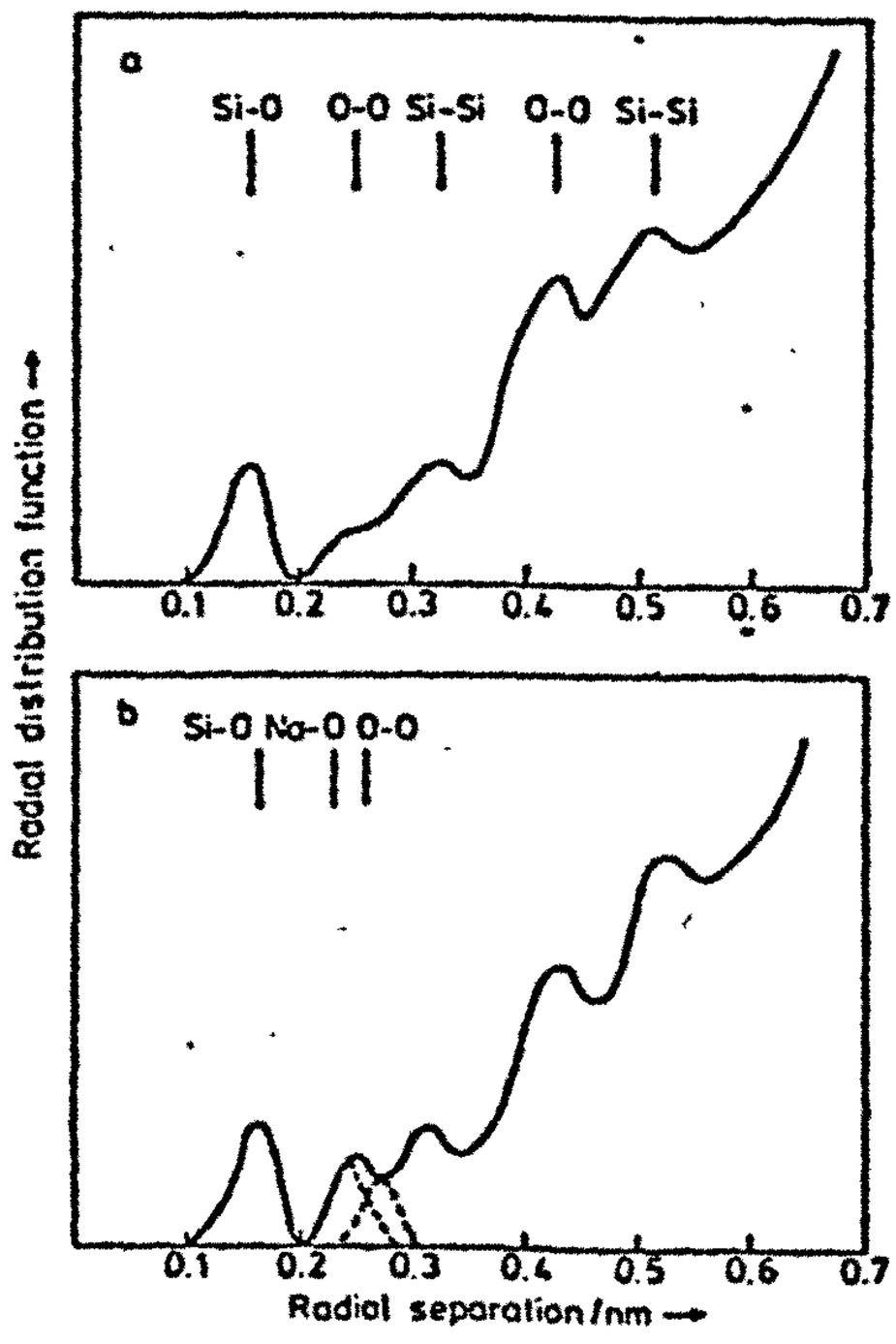

Fig1.3 Radial distribution curves for (a) SiO_2 (b) Na_2O-SiO_2 glass ref.(1.3)

Si-O length:0.162nm, Na-O

1.1 Random network theory

The atomic arrangement of glass is successfully described by Zachariasen's random network theory (1.3) in which each silicon ion is surrounded by oxygen ions at the four corners of a tetrahedron. Adjacent tetrahedra are linked by one common ('bridging') oxygen ion so any relative orientation is possible, as shown in Fig. 1.2a. Thus, there is short range order (~1 nm) in glasses, but long range disorder. The other ions of the melt are considered 'network modifiers' and are distributed throughout the glass in interstitial position as shown in two-dimensional analogue in Fig. 1.2b. Charge balance is maintained by 'non-bridging' oxygen ions.

Fig. 1.3 shows the results of Fourier analysis of X-ray diffraction patterns of a soda-silicate glass, (1.1, 1.4) yielding values for the bond lengths and coordination numbers which support Zachariasen's theory.

The network modifiers (Na, Ca, Mg etc.) are relatively loosely bound and can diffuse through the network under the influence of electric fields and temperature gradients. This is responsible for many properties of glass including chemical decay and the electrical conductivity, which will be considered in detail at a later stage.

Zachariasen's picture describes single component glasses well but when further components are added, small angle X-ray scattering experiments (1.5) have indicated the presence of localised differences in composition, a phenomenon which occurs in all glasses whose composition is intermediate between stable compounds, known as 'phase separation'. The durability of the glass and many of its other properties may be seriously affected by phase separation, and alumina is added to modern glass in an attempt to prevent its occurrence. This lack of homogeneity adds significantly to the problems of quantitative glass analysis.

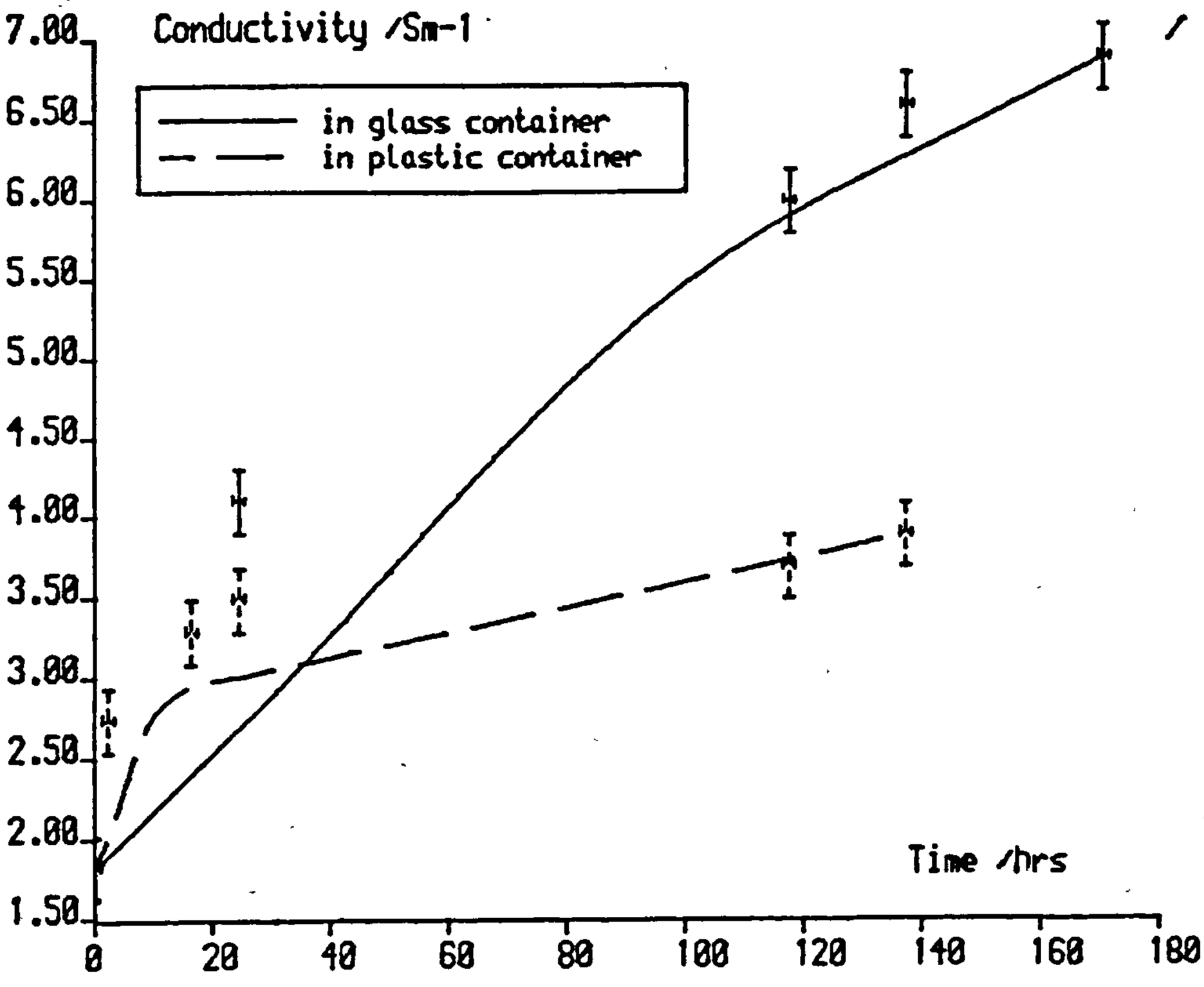

FIG(1.4): Water conductivity against storage time

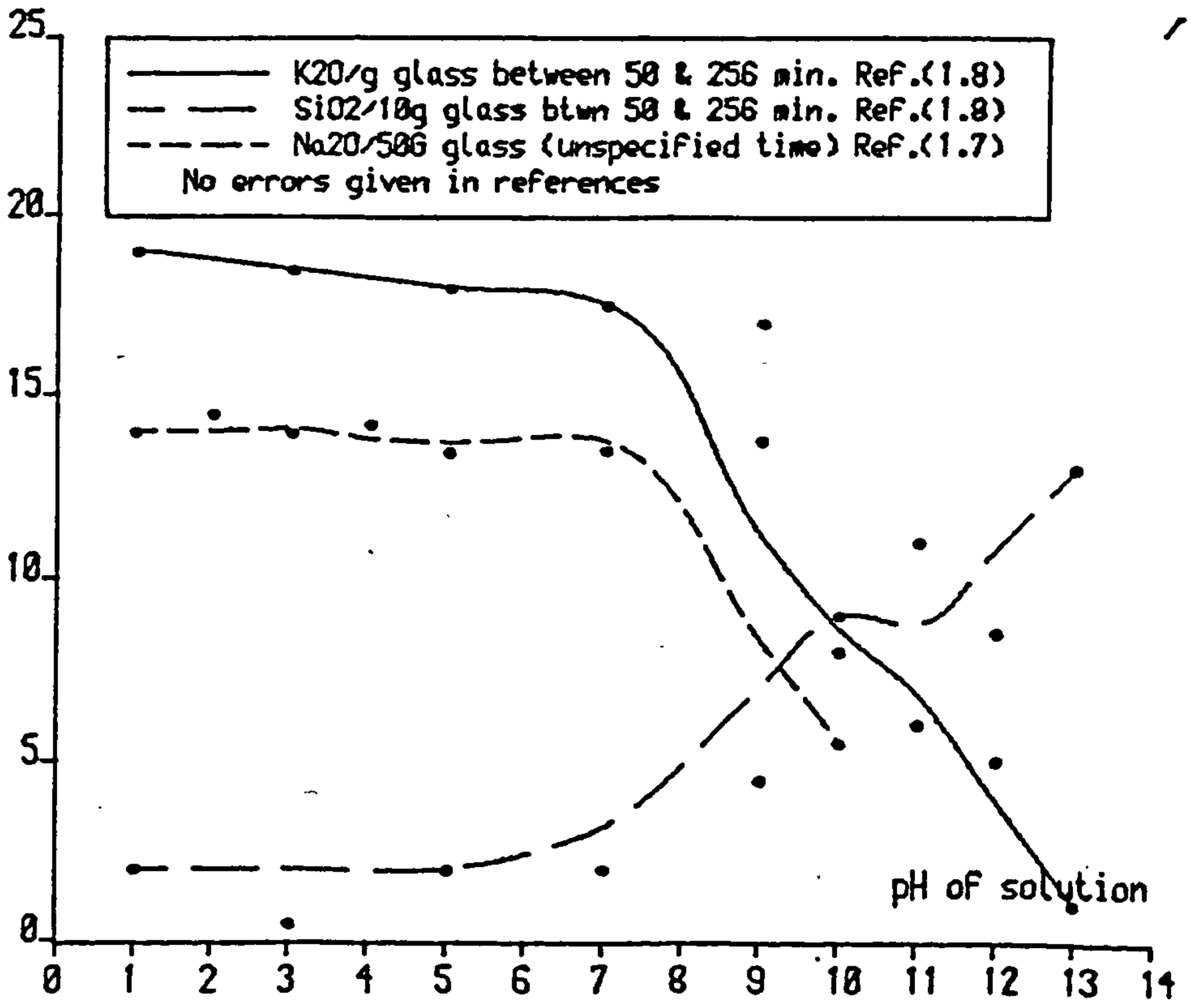

FIG(1.5):The dissolution of glass components by water

1.2 Decay processes

It is very easily shown that glass is attacked by water. Fig. 1.4 shows the increase in the conductivity of water stored in a glass and in a plastic container. This is interpreted as a diffusion of the cations through the silica network into solution. Douglas and Isard (1.6) postulated a counter-diffusion of protons into the glass, which is necessary for charge neutralisation and which creates an hydrated layer at the surface. A simple exchange process is denied by Ernsberger (1.7) bearing in mind the very high field intensity of the bare proton, and a diffusion of water molecules is suggested, with counter diffusion of alkali oxide. Comprehensive experiments performed by El-Shamy et al (1.8, 1.9) involving estimating chemically the quantity of alkali ions dissolved by water from ground glass granules, have established the dependence upon the pH of the solution shown in Fig. 1.5. Below a pH of 9, the alkali ions (M+) are extracted from the glass by a hydrolysis of the form (1.10):

$$\begin{array}{c} | \\ -Si-O-M \\ | \end{array} + H_2O \longrightarrow \begin{array}{c} | \\ -Si-OH \\ | \end{array} + M^+ + OH^- \qquad 1.1$$

which increases the pH of the attacking solution so as to break down the silica network according to the reaction:

$$\begin{array}{c} | \quad | \\ -Si-O-Si- \\ | \quad | \end{array} + OH^- + H_2O \longrightarrow \begin{array}{c} | \\ -Si-OH \\ | \end{array} + \begin{array}{c} | \\ -Si-O^- \\ | \end{array} + H_2O$$

$$\longrightarrow 2\left(\begin{array}{c} | \\ -Si-OH \\ | \end{array}\right) + OH^- \qquad 1.2$$

The surface of the glass is thereby eroded, causing cations to be leached from a greater depth, and the process becomes self-sustaining with the leached layer progressing further into the glass. Hlavac" (1.11) has derived the relation between the thickness of the leached layer and the reaction time, as in Appendix I. Shown in Fig. 1.6 is a graphical solution of the equation derived in this reference, assuming a linear concentration gradient of alkali ions in the leached layer. This assumption is not unreasonable (Scholtze et al (1.12) found a long S-shaped

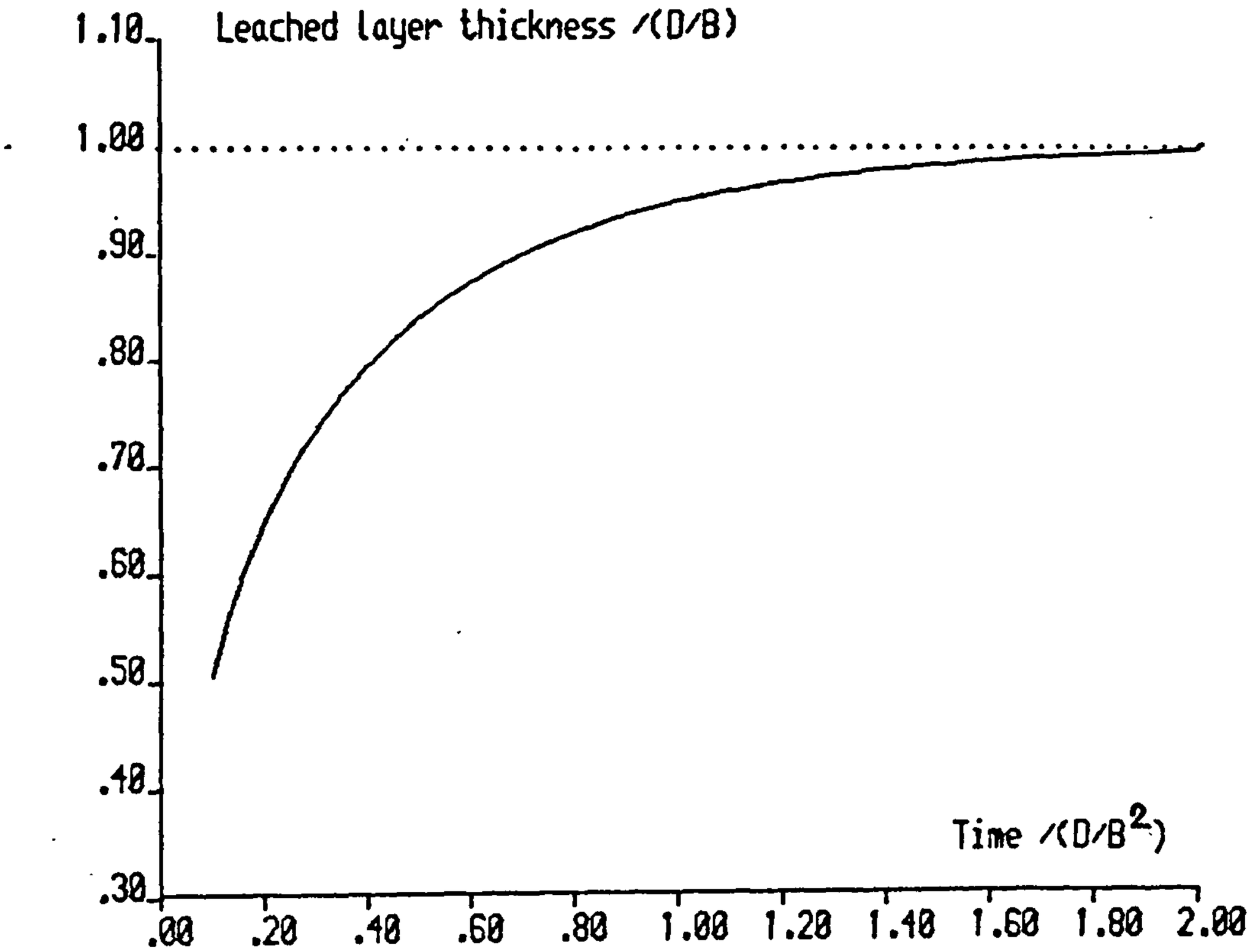

FIG(1.6):Leached layer growth in glass surface. Ref.(1.11)

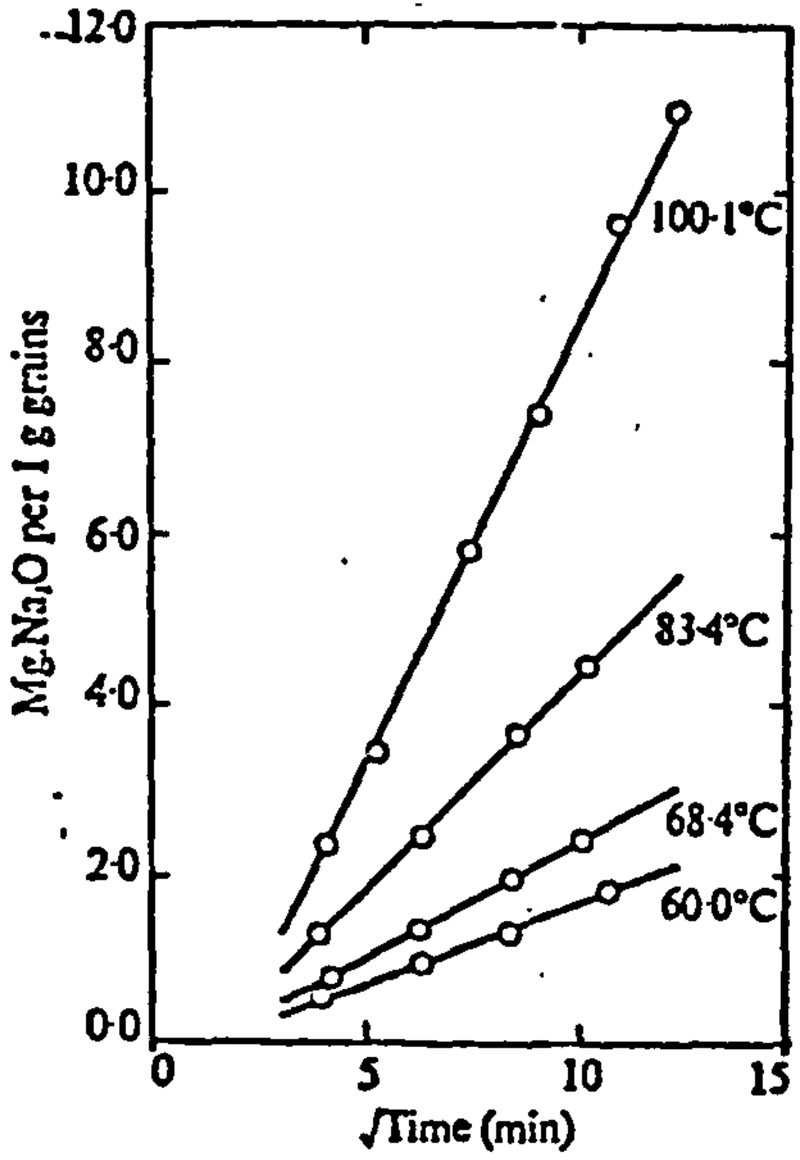

Fig.(1.7a):Short time leaching.
(Ref.1.13)

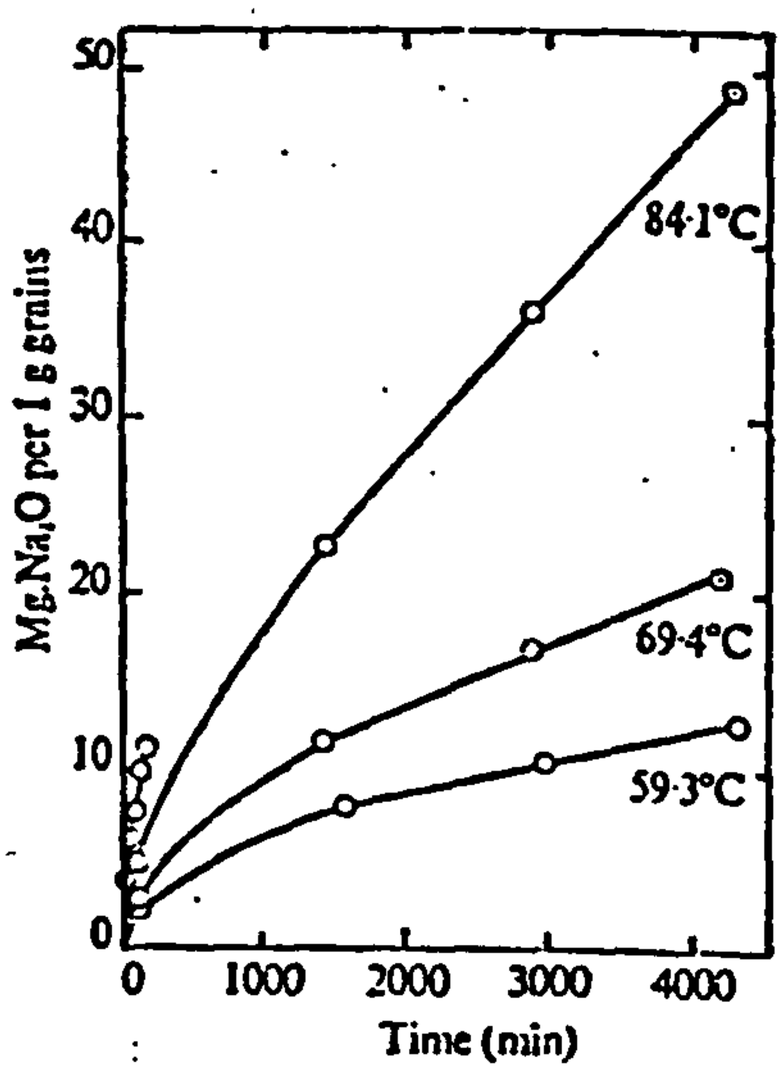

Fig.(1.7b):Long time leaching
(Ref.1.13)

profile) and Hlavac's treatment predicts the final establishment of a stable hydrated layer of thickness determined by the reaction rate (B) and the diffusivity (D) which is consistent with the experimental evidence.

Fig. 1.7, from the work of Rana and Douglas (1.13), shows that the quantity of alkali extracted from glass grains has two time dependencies, and we write empirically (1.8):

$$Q = a\sqrt{t} + bt \qquad 1.3$$

where the first term, significant for short times, represents diffusion through the leached layer (showing the $\sqrt{t}$ dependence characteristic of Fick's law (1.3)) and the second term represents the destruction of the network at a constant rate. The figure also shows the expected increased rate of dissolution at higher temperatures.

1.3 XRF analysis

The ancient glass of York Minster has been affected in various ways by the many centuries of weathering. The composition of the glass determines the rate constants of the chemical reactions (equation 1.1 and 1.2), which have not yet been specified (1.13). The research programme at York, discussed in the introduction, was initiated in an attempt to discover compositional differences between the badly corroded glass samples and those which were found to have decayed hardly at all (1.16, 1.17). It is remarkable that there are many pieces of blue glass of the twelfth and thirteenth centuries on which the intervening years have left little or no mark.

As samples of glass from York Minster (and many other sources throughout Europe) were studied, it became clear that they could be placed in categories according to the way they had weathered. The extreme classes were four in number: Unweathered, Pitted, Crusted, and Pitted and Crusted. Assigning a particular specimen to one of these classes was not

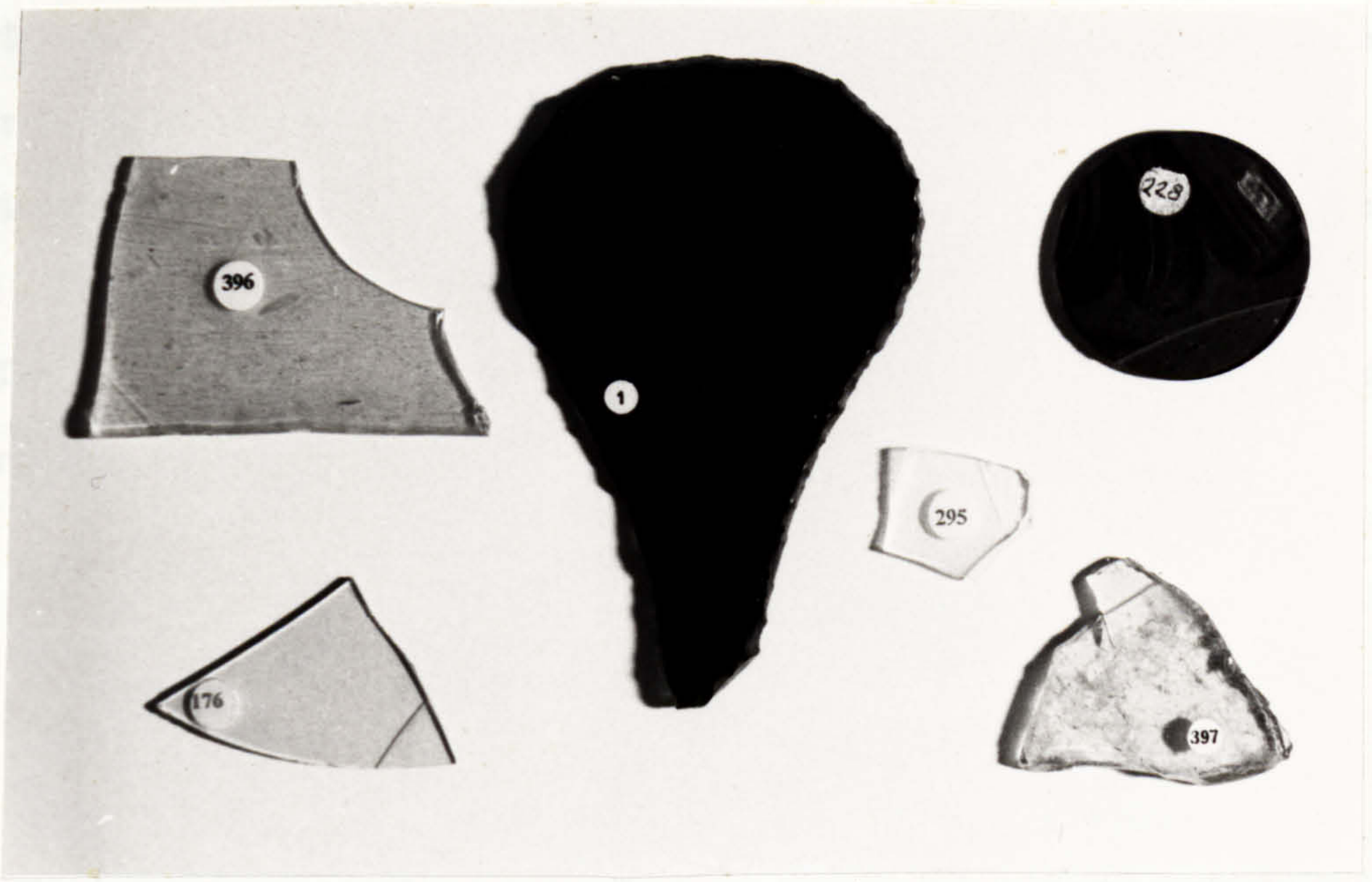

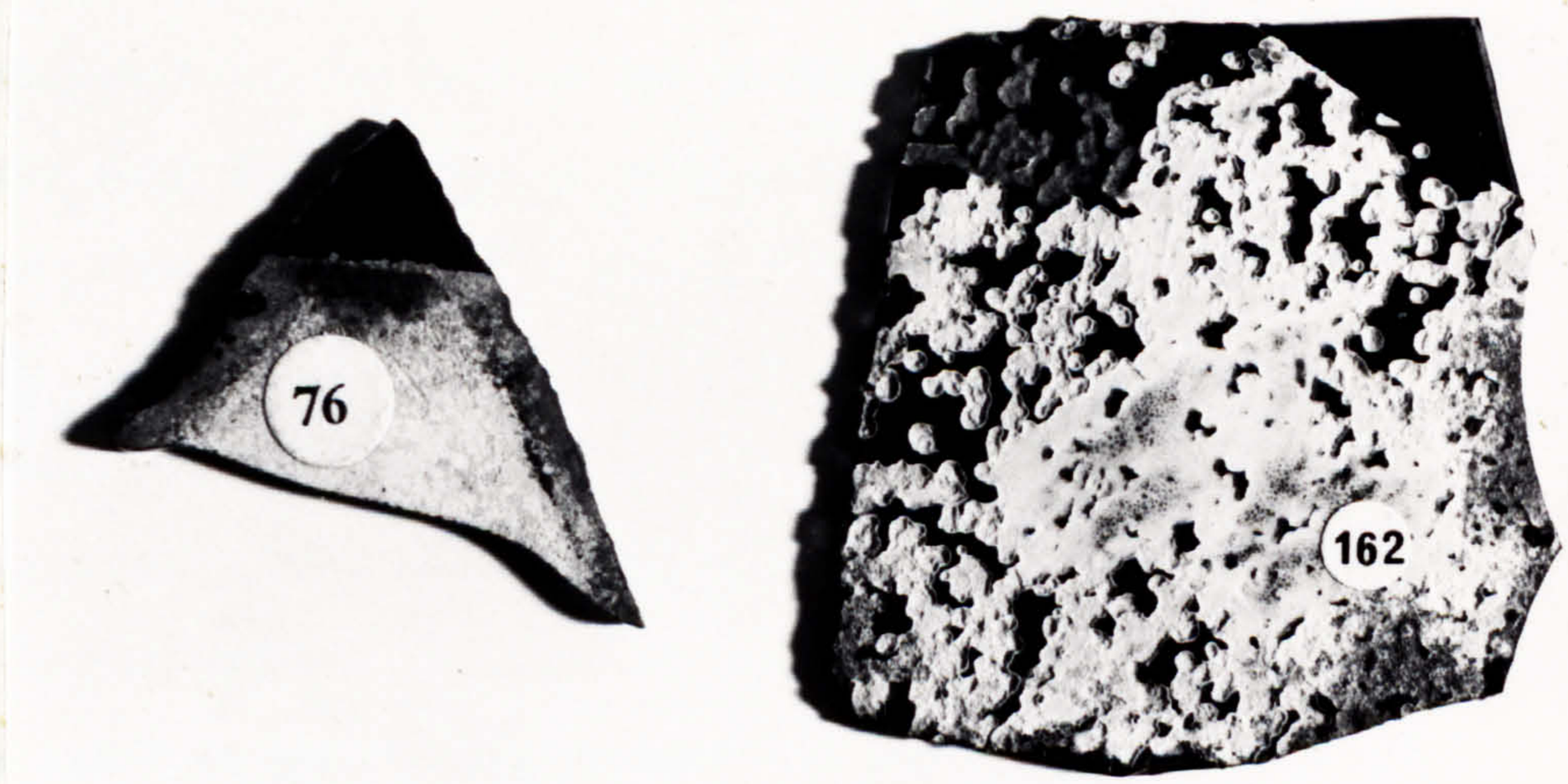

Fig.(1.8): Glass from York Minster showing various modes of decay. A complete description of each is given in ref 1.16

an easy task, as can be seen from the photographs of samples in Fig. 1.8.

The surfaces of the samples were ground and polished (1.18) before results representative of the bulk composition could be obtained from energy dispersive X-ray fluorescence analysis (1.19). The hard and soft ware are being developed at York.

The amounts present of twelve components were recorded in the study, and the composition of a typically pitted sample is given below:

Na_2O : 2.4	P_2O_5 : 2.4	Fe_2O_3 : 0.13
MgO : 9.7	K_2O : 10.1	CuO : 0.15
Al_2O_3 : 0.9	CaO : 15.3	ZnO : 0.04
SiO_2 : 57.9	MnO : 0.93	PbO : 0.01

where the figures are given in molar percentages, with a 95% confidence limit.

1.4 Triangular diagrams

Techniques such as cluster analysis for handling the data acquired in this way and relating them to the durability of the glass are at present being evaluated but the problem can be simplified by dividing the components into three groups of similar oxides according to the equations:

Network formers: $'SiO_2' = SiO_2 + P_2O_5 + 2(Al_2O_3) + 2(Fe_2O_3)$ 1.4a

Alkali oxides: $'R_2O' = Na_2O + K_2O - Al_2O_3 - Fe_2O_3$ 1.4b

Network modifiers: $'RO' = MgO + CaO + MnO + CuO + ZnO + PbO$ 1.4c

where the chemical symbols represent the molar percentages of the oxides present in the sample. In these equations, glass components of the type R_2O_3 are added to the network formers and subtracted from the alkali oxides because, being trivalent, they can form part of the network and their usual effect (that of loosening the network) is negated (1.17, 1.20).

A particular glass can then be located on a triangular diagram whose axes are the three quantities of equations 1.4, as in Fig. 1.9. It was discovered (1.16) that the coordinates of the analysed glasses from the

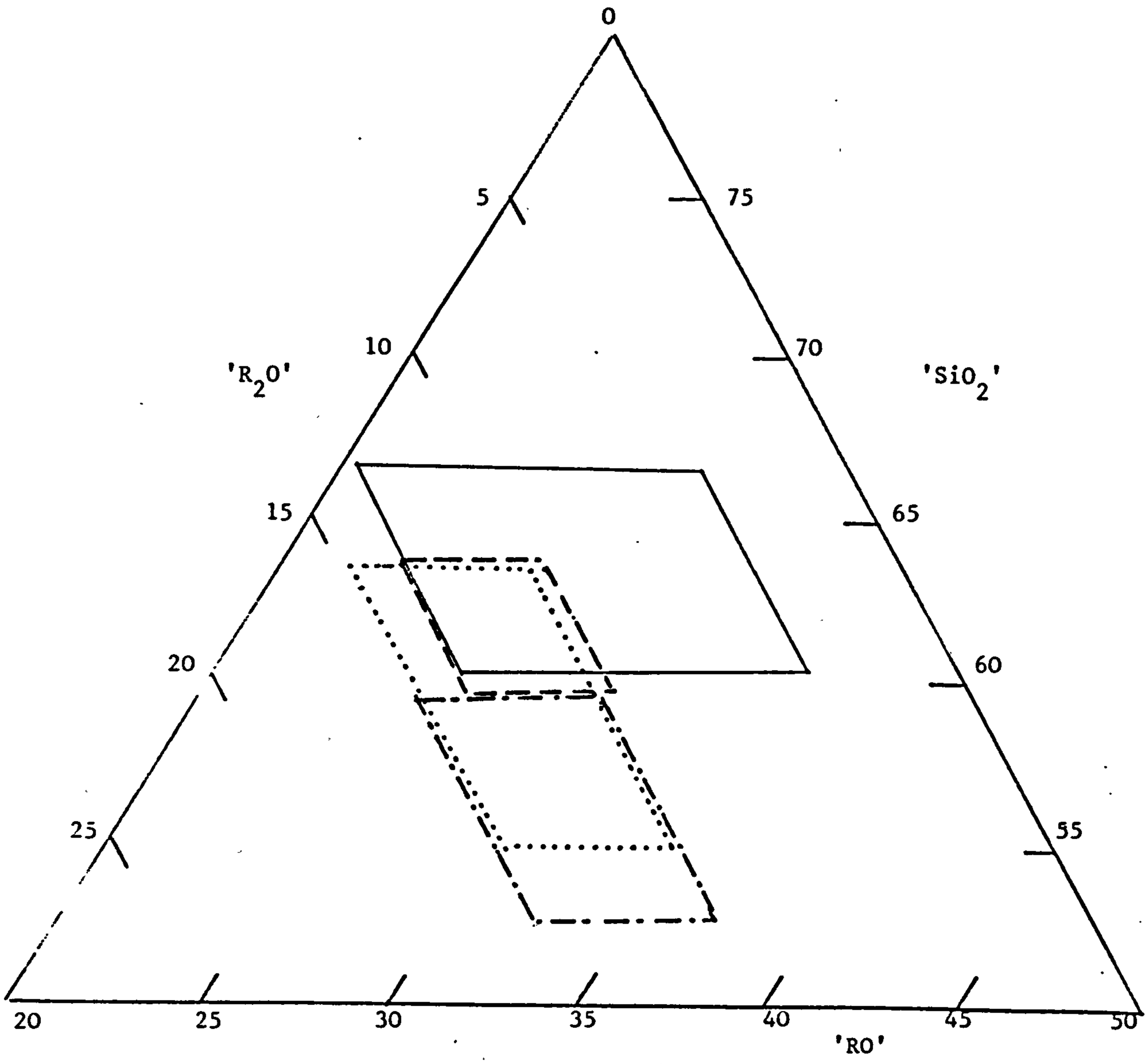

Fig.(1.9): Mediaeval glasses grouped on a triangular diagram according to their weathering behaviour. The sum of the three coordinates (network formers, network modifiers and alkali oxides) is 100%. The high proportion of 'SiO_2' in durable glasses can be seen, but the other groups are less distinct.

From ref.(1.16).

Minster fall into broadly defined areas on such diagrams, as Fig. 1.9 shows. Naturally much information of value to durability studies has been lost by combining the data according to equations 1.4, but the following conclusions can be drawn:

(1) that a durable glass has an 'SiO_2' content above 60 mol%,

(2) that a wide variation of composition (4 to 13 % 'R_2O' and 20 to 30 % 'RO') is possible in a durable glass,

(3) that the composition of the glass does not determine precisely the weathering behaviour of a sample, since there is considerable overlap of the regions.

El-Shamy (1.21) finds that the durability cf glass falls sharply when the SiO_2 (not 'SiO_2') content falls below 66% and makes the point that with this composition each silicon atom has a cation as a nearest neighbour, creating a pathway through the lattice, so that the ionic mobility will be increased and the durability reduced. This is in accordance with conclusion (1) mentioned above, which, it should be noted, is a necessary but not a sufficient condition.

1.5 Coefficient of thermal expansion

Since glass is conveniently regarded as a mixture of components rather than a chemical combination of them, we can describe accurately bulk properties (p) such as specific heat capacity, specific volume, refractive index and thermal conductivity by an additive relation of the form (1.2):

$$p = k_p + \sum a_{pi} w_i \qquad 1.5$$

where w_i is the weight percent of the oxide i, the set of coefficients a_p is determined by experiment, and the constant k_p is included in specific

cases to represent the thermal history of the sample.

There must be no great disparity between the thermal expansivity of the film of durable glass to be deposited and the Mediaeval glass substrate, or the stresses due to differential expansion might separate the two. By combining the data from Holloway (1.2), Babcock (1.22) and Morey (1.23), the coefficients $a_{\alpha i}$ shown in Table I were used to predict coefficients of thermal expansion (α) of glasses to within 5% of the published values. The constant k_α was set to zero throughout.

The ancient glasses analysed were found to have a mean thermal expansion coefficient of $9.65 \times 10^{-6}\ K^{-1}$ (with a standard deviation of 0.59), which is some three times that of modern glass. The coefficients $a_{\alpha Na}$ and $a_{\alpha K}$ can be seen to be much higher than the others making α very strongly dependent on the 'R_2O' content.

The problem, therefore, attaching to the determination of the glass composition to be used for coating the ancient samples is in reconciling two divergent requirements. For durability, as described in section 1.4, a high 'SiO_2' content is necessary; for an appropriate expansivity, the proportion of 'SiO_2' should be kept small.

It was found possible, using an iterative computer program, to reach convergence on glass compositions fulfilling both requirements, and some of these were melted commercially for us by Pilkington Brothers (St. Helens).

1.6 Glasses melted by Pilkington Brothers

Table I shows the compositions of the glasses which were melted for the project. They are all durable and of high expansivity; the multicomponent glass is very similar in composition to a piece of spectacularly unweathered blue glass from the 12th century YMG1 (1.16). They were produced as discs of 150 mm diameter for use as targets in the

sputtering chamber to be described in Chapter 4.

At the same time, two other glasses were melted for use as simulated Mediaeval substrates, in rectangular form (60 x 200 mm) and the composition of these is given in Table II. Trace compounds were added in each case to provide colouration for identification purposes.

During the process of glass manufacture, the different volatility of the components in the melt can alter the final composition of the glass, but with sufficient experience a glass may be produced to an accuracy of composition greater than that to which it can be analysed by energy dispersive XRF equipment.

1.7 Artificial weathering

The corrosion processes mentioned in section 1.2 are characteristically very slow, and consequently experiments designed to quantify the durability of glass must be artificially accelerated. The severity of the attacking solution might be increased, for example, as might the surface area (by using grains of glass) or the temperature, but it is likely that the result would be rendered unrepresentative of the true weathering behaviour.

Environmental chambers are frequently used for durability testing, for example in the paint industry, but a system was not found which could reproduce with any exactness the weathering effects encountered by glass in the windows of the Minster.

Nonetheless, when glass films had been deposited, using the equipment to be described, it was considered necessary to test their durability in some way, not necessarily representative of particular weathering conditions. An artifical weathering unit was constructed as described in AppendixII, designed in accordance with the decay processes mentioned in this chapter, which subjects the glass in a cyclic manner to

elevated temperature, water leaching and mechanical stress. No attempt is made to correlate lengths of test to years of York weather, for the reasons given above.

1.8 Summary

A simple outline of the atomic structure of glass has been presented, and some of its physical properties have been mentioned. The linear thermal expansion coefficient of Mediaeval glass has been shown to be a factor of three larger than that of more modern durable glass, but durable compositions have been found with large expansivities.

The primary results of the analytical part of the project, presented by Pollard (1.16) have been mentioned briefly where they relate to the durability of glass.

CHAPTER 2

SPUTTERING THEORY

The phenomenon of sputtering - the removal of discrete particles of material from a surface by energetic particle bombardment - is central to this thesis, and will be described in detail in this chapter.

2.1 Description of process

The impinging ion (primary particle) loses its energy to atoms of the target (secondary particles) both by elastic and inelastic scattering, and initiates a series of collisions among them. This collision sequence may be localised or extended in space and time according to the specific atoms, ions and energies involved. Fig. 2.1 shows the two regimes in schematic form.

2.1.1 Cascades

In the case of the linear cascade, the secondary atoms receive sufficient energy to be dislocated from their positions in the structure and to cause such dislocations themselves. The number density of recoil atoms is sufficiently low, however, for collisions between them to be rare. During the lifetime of the cascade, one or more secondary atoms might acquire a velocity directed towards the surface of sufficient magnitude to overcome the binding forces and leave the target. This is the sputtering yield. The small probability of interaction between two moving particles implies that superpositions of two cascades will double the yield of sputtered particles - hence the designation 'linear'.

2.1.2 Thermal spikes

Fig. 2.1b shows the spike or 'hot-spot' case; the probability of a moving particle interaction here is high, making a spike a non-linear sputtering event. It may be distinguished experimentally from a cascade

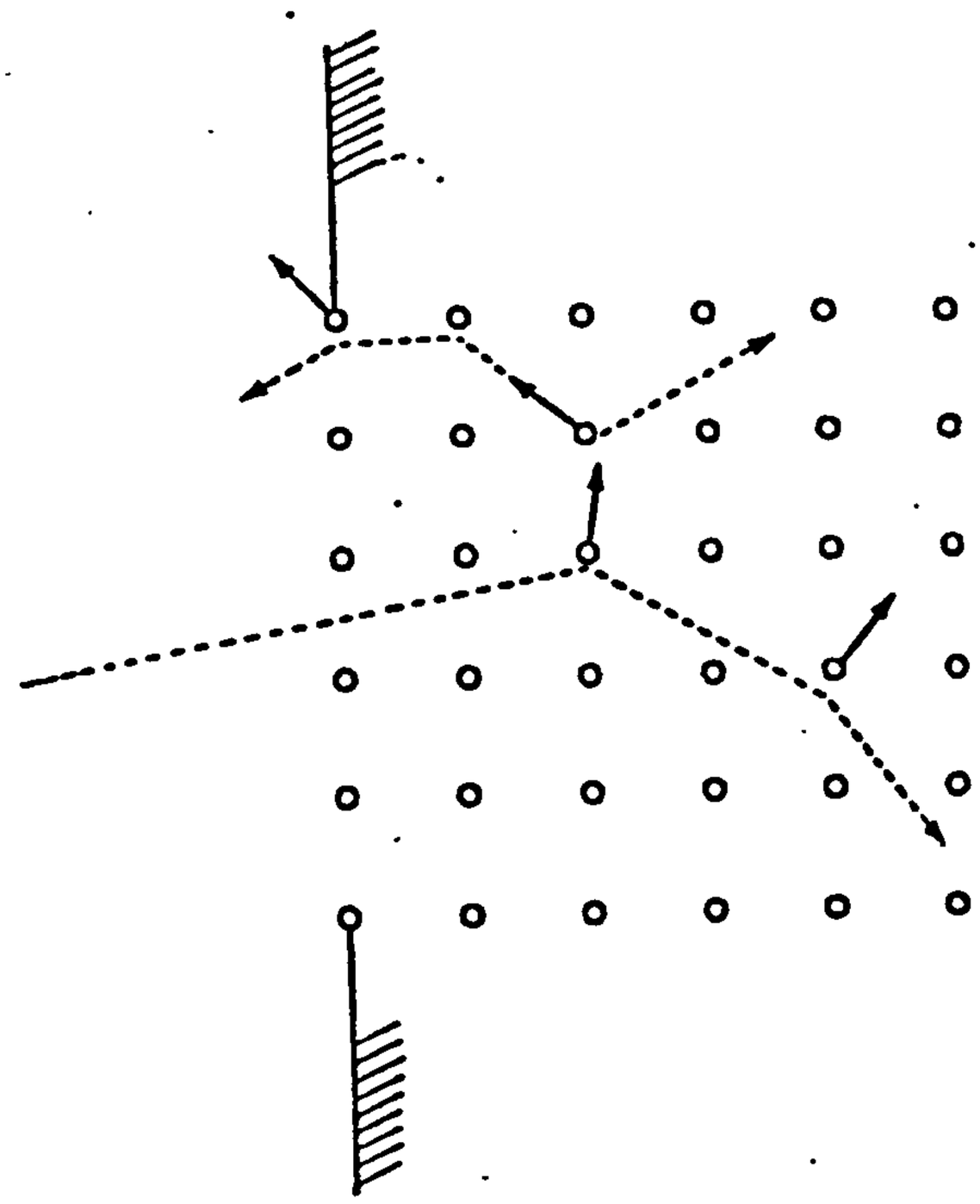

Fig.(2.1a): The linear cascade

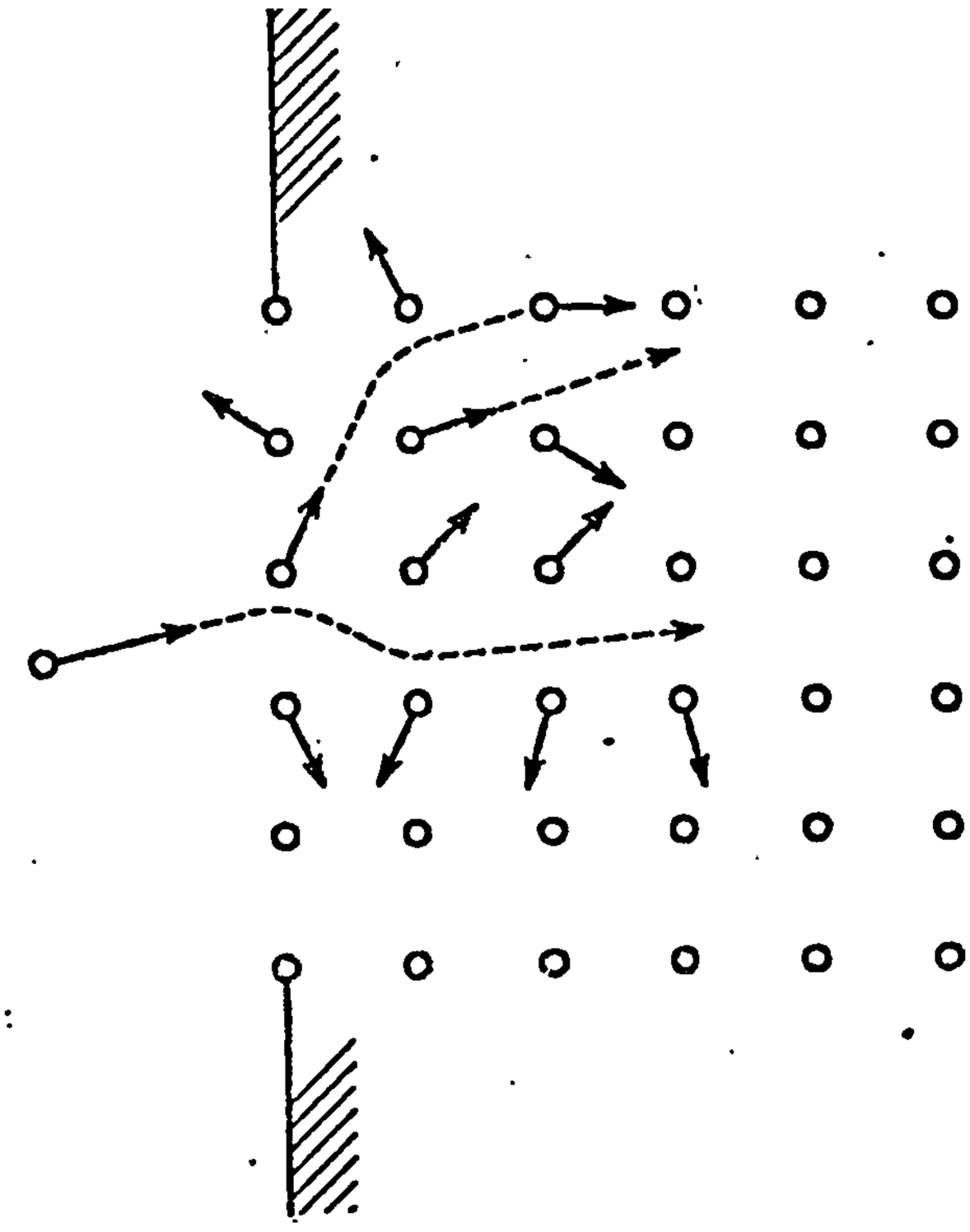

Fig.(2.1b): The thermal spike

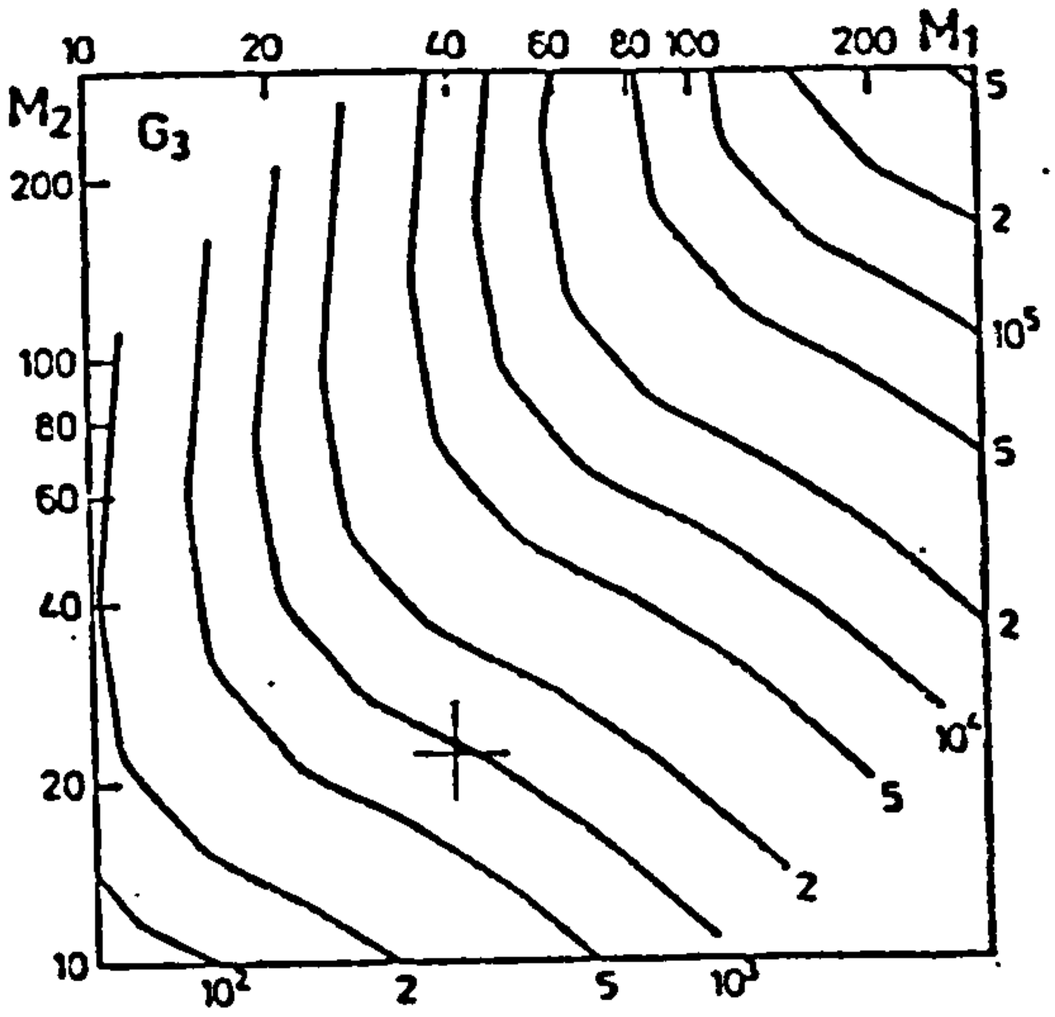

Fig.(2.2): The energy density function G_3 (ref.2.15)
Units: eV keV Å6

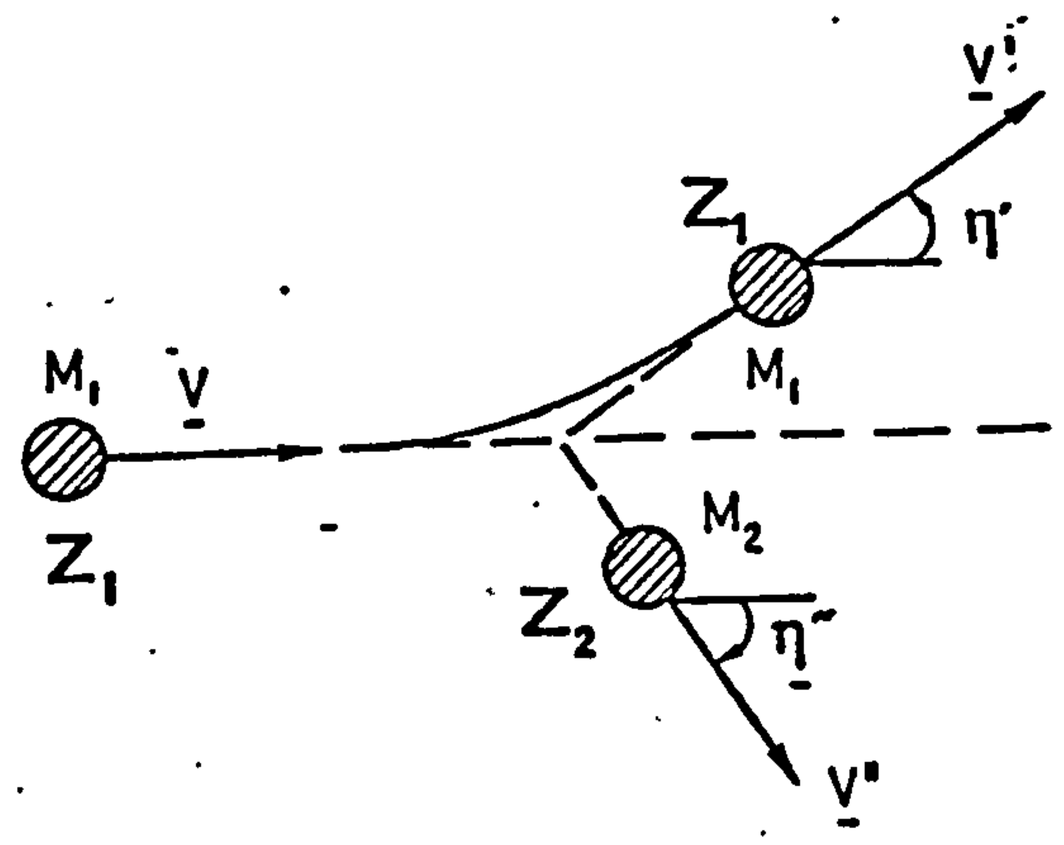

Fig.(2.3): Collision nomenclature

by measuring the sputtering yield obtained by bombarding the surface with ions and comparing it with the yield after molecular ion bombardment; the molecules having the same energy and being composed of the same atoms as the ions. The molecules dissociate immediately on impact and the atoms penetrate the target independently. The sputter yield will be found to have increased in proportion to the number of atoms in the molecule in the case of light to medium mass ions, and energies in the keV to low MeV region, (i.e. cascade theory applies here) but for very energetic and heavy ions, spikes will occur, and the yield will be greatly enhanced.

Consideration has been given (2.17) to the temperature reached inside thermal spikes, and Sigmund (2.15) calculated that an atom in the spike volume (approx. 10^6 $\mathring{A}^3$) will gain an energy given in eV by $G_3(M_1,M_2)N^2/E$, where the function G_3 is shown in Fig. 2.2, N is the number density of target atoms and E is the energy of the primary particles. The figure is valid for an energy range (2.4) inside which all the analysis of this chapter will fall: for $\varepsilon<0.2$, where the 'reduced energy' ε is defined by equation 2.25a. The temperatures predicted by such an approach show a surprising inverse behaviour with primary energy, but spike effects are not considered influential except in the energy region $60<E/keV<100$ (2.15). Bombarding copper, for example, with 80 keV Argon ions would induce a temperature of the order of 3500 K. Numerical estimates for glass bombardment based on Fig. 2.2 are provided in the following chapter.

Kelly (2.16) bases a theory of 'thermal sputtering' on a consideration of the deposition of energy in the spike volume and solving the diffusion equation for a Gaussian temperature profile. Sputtered particles are supposed to evaporate from the spike volume, and a small thermal sputtering term is added to the yield obtained from cascade theory. As mentioned above, this effect is not appreciable in the present context as the primary energies used are too low, but it probably

contributes to the problem of target overheating mentioned in Chapter 6.

2.1.3 Electronic excitation

Neither of the elastic collision theories can explain the periodicity with atomic number observed in sputtering yields (2.18). It is possible for target atoms to be excited into non-bonding states by the primary particles, and thus it becomes energetically favourable for them to leave the surface as is the case in electron-beam desorption, as described in sub-section 8.3.2. The mechanism is discussed by Pollitt et al (2.19) but no quantitative theory has so far been propounded. Clearly, if transitions between atomic levels are occurring, the emission of electron and light quanta is to be expected, (2.2) and the possibility that this is the source of the glow to be seen at the surface of the target is discussed in Chapter 4.

2.2 Linear cascade theory

The most satisfactory and detailed theory of sputtering is linear cascade theory and the treatment to be given here is based upon the fundamental work being done by Prof. P. Sigmund of Odense University, whose paper 'Theory of Sputtering' (2.1) is the basis of all modern theoretical treatments of collision cascades, and various later publicatio by him (2.2, 2.3). The theory allows the sputtering process to be describ mathematically from first principles, and can accurately predict the magnitude and energy dependence of sputtering yields, despite the questionable accuracy of some of the input quantities (2.2). The full derivation of yield formulae is included despite its length not only because of the insights provided into the processes involved, nor the relationships demonstrated on the way, but particularly because its result are usually published and quoted without proof, and a comprehensive

treatment might be of benefit to experimental workers in the field.

2.2.1 Elastic scattering

When a primary particle of mass M_1 and energy E collides with a secondary particle of mass M_2, the energy T transferred to the secondary has a maximum of

$$T_M = \frac{4M_1M_2}{(M_1 + M_2)^2} E \equiv \gamma E \qquad 2.1$$

when the collision is linear: Fig. 2.3 shows the geometry. The magnitude of T depends on the interaction assumed between ion and target atom. Using a Thomas-Fermi function of the form:

$$V(r) = \frac{Z_1 Z_2 e_M^2 U(r/a)}{r} \qquad 2.2$$

where the quantity e_M^2, as defined in the list prefacing this thesis, is used to simplify the notation in SI units. The function U(r/a) represents the screening of the nucleus and can be approximated by a power law:

$$U(r/a) = m\left(\frac{a}{r}\right)^{\frac{1}{m}-1} \qquad 2.3$$

where the screening radius is a and m is a variable. We can write the differential cross-section for scattering as:

$$d\sigma(E,T) = C_m E^{-m} T^{-1-m} dT \qquad 2.4$$

for $0<T<T_m$, where

$$C_m = \frac{\pi}{2} \lambda_m a^2 \left(\frac{M_1}{M_2}\right)^m \left(\frac{2Z_1Z_2e_M^2}{a}\right)^{2m} \qquad 2.4a$$

and λ_m is an experimentally determined parameter whose value varies with m between $\lambda_1 = \frac{1}{2}$ and $\lambda_o = 24$ (2.2). The magnitude of the screening radius is expressable in terms of the Bohr radius a_o (= 0.529 Å) thus:

$$a = 9\pi^2 \, 2^{-7/3} \, a_o \, Z^{-\frac{1}{2}} = 0.468 \, Z^{-\frac{1}{2}} \qquad 2.4b$$

where:

$$Z = Z_1^{\frac{2}{3}} + Z_2^{\frac{2}{3}} \qquad 2.4c$$

but the experimental data can be well fitted using a constant value (2.2) of 0.219 $\mathring{A}$ giving $Z = 5$ and $C_o = 1.808 \, \mathring{A}^2$.

It will be observed that at $m = 1$ the interaction $V(r)$ is coulombic implying that the electronic screening of the nucleus has been neglected. This is valid for high energies, and combining equations 2.3 and 2.4 for $m = 1$ yields:

$$d\sigma(E,T) = \pi \, \frac{M_1}{M_2} \, Z_1^2 \, Z_2 \, e_M^4 \, \frac{dT}{ET^2} \qquad 2.5$$

the Rutherford scattering formula. This shows that values of m less than unity represent low energy scattering, and it will be seen that m=0 is appropriate for sputtering cascades.

2.2.2 Stopping cross-section and range

The average loss of energy by the primary particle per unit distance of travel in a medium of N atoms per unit volume is given by the stopping power

$$\frac{dE}{dx} = -NS_n(E) \qquad 2.6$$

where $S_n(E)$ is the stopping cross-section:

$$S_n(E) = \int_o^{T_m} T d\sigma \qquad 2.6a$$

For elastic collisions only, using equation 2.4, this is evaluated as

$$S_n(E) = \frac{C_m}{1-m} \, \gamma^{1-m} \, E^{1-2m} \qquad 2.6a'$$

and from equation 2.6 we write for the range R of the ion in the material:

$$R = \int_o^E \frac{dE}{dE/dx} = (1-m)\gamma^{m-1} \, \frac{E^{2m}}{NC_m} \qquad 2.7$$

where the depth unit can be seen to be E^{2m}/NC_m.

2.2.3 Boltzmann transport equation

The target medium in which the collision cascade takes place is conveniently considered infinite in extent and homogeneous. Particles are counted as they pass a plane in the medium, representing the surface, at x=0. The self sputtering case will be considered, in which the target material is of the same species as the primary particle. The dependence on mass will be introduced at a later stage. Fig. 2.4 shows the geometry and nomenclature of the treatment.

We write the probability $G(x,v_o v,t)d^3v_o dx$ as the probability of an atom which started with a velocity v at x=0 having a velocity in the interval d^3v_o (at v_o) and a position in the interval dx (at x) a time t later. Now, obviously, $G(x,v_o v,t)$ must be equal to the sum of the probability densities of atoms in that velocity-position interval which have suffered a collision, and those which have not, in a time ∂t. If $d\sigma$ is the differential cross-section for collision, then the probability of collision is:

$$N v \delta t \int d\sigma$$

and that of not colliding is less than unity by the same amount. Thus, the probability of an atom having a velocity in $d^3\underline{v}_o$ at $\underline{v}_o$ and a position in dx at x after collision is:

$$N v\, \delta t \int d\sigma \left\{ G(x,\underline{v}_o,\underline{v}',t) + G(x,\underline{v}_o,\underline{v}'',t) \right\}$$

since the collision partners both add to G, and that of its velocity and position being in those intervals without collision is

$$(1 - N v \delta t) \int d\sigma \; G(x-\eta v \delta t, \underline{v}_o, \underline{v}, t-\delta t)$$

since the atoms in a plane $\eta v \delta t$ away will move to include themselves in G after a time δt. The important parameter η is the direction cosine of the velocity with respect to the x-axis.

By expanding the function G in this last expression as a

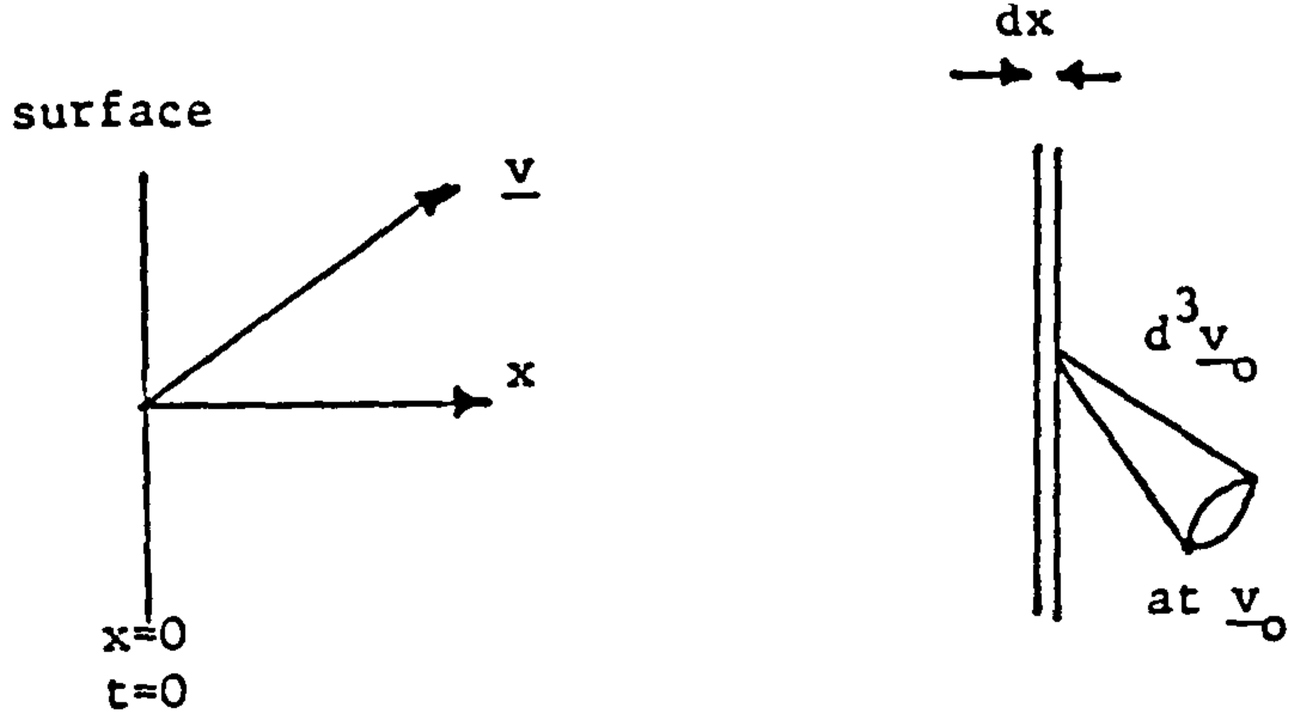

Fig.(2.4): Geometry of cascade theory

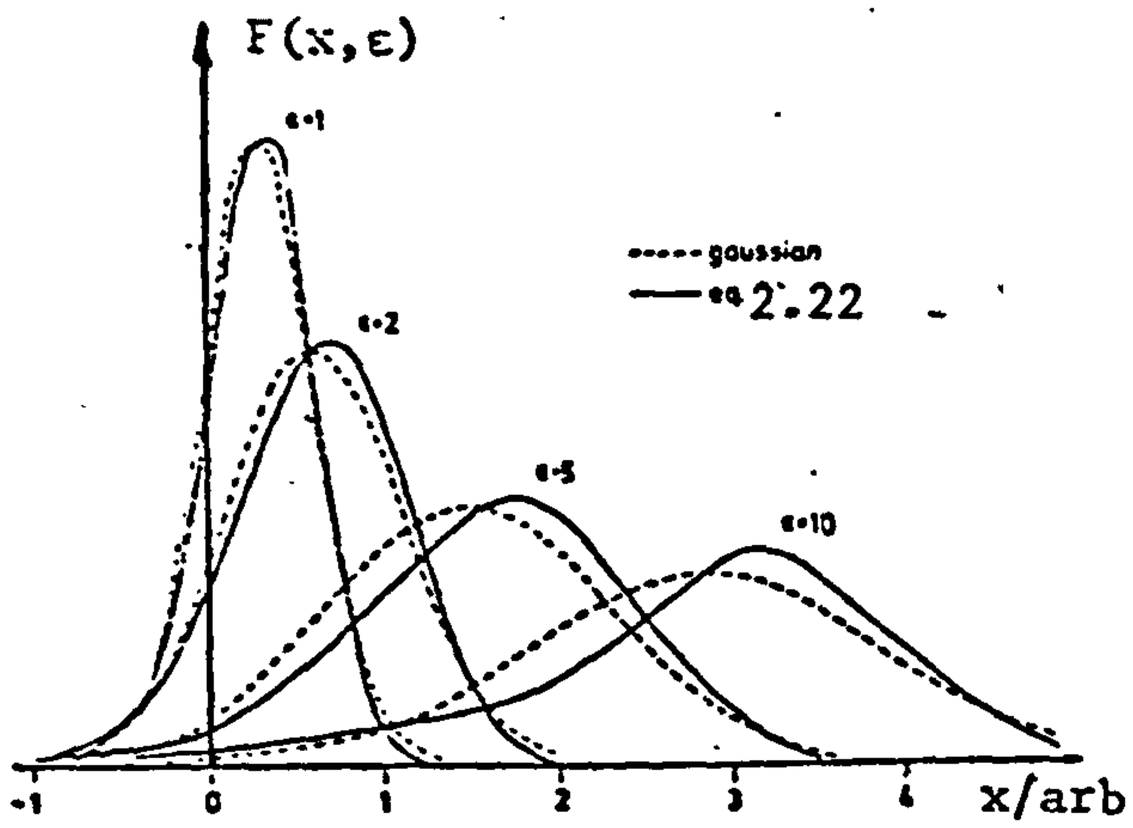

Fig.(2.5)Energy deposition function
(Ref.2. 13)

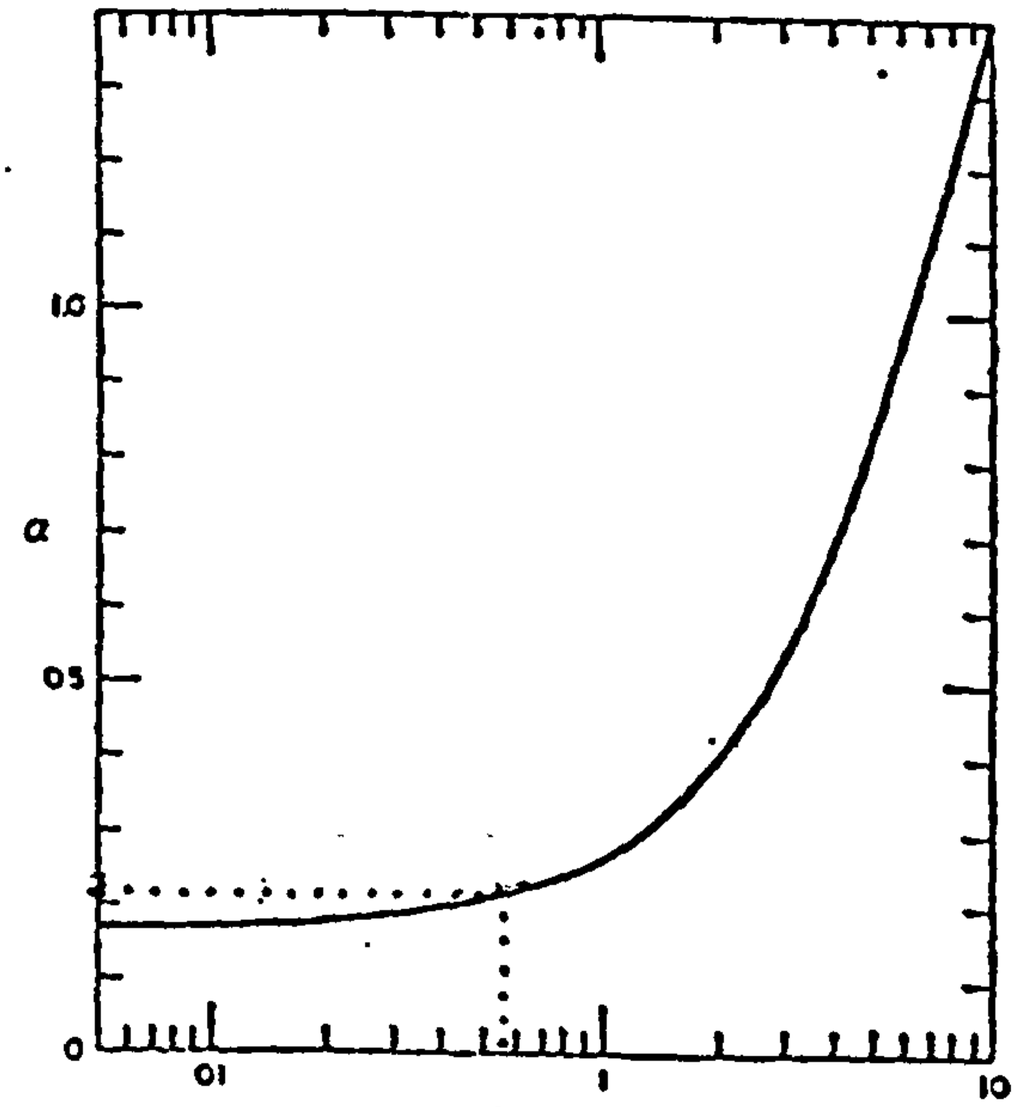

Fig.(2.6) Function $\alpha(M_2/M_1)$ averaged for small m.
(Ref.2. 1)

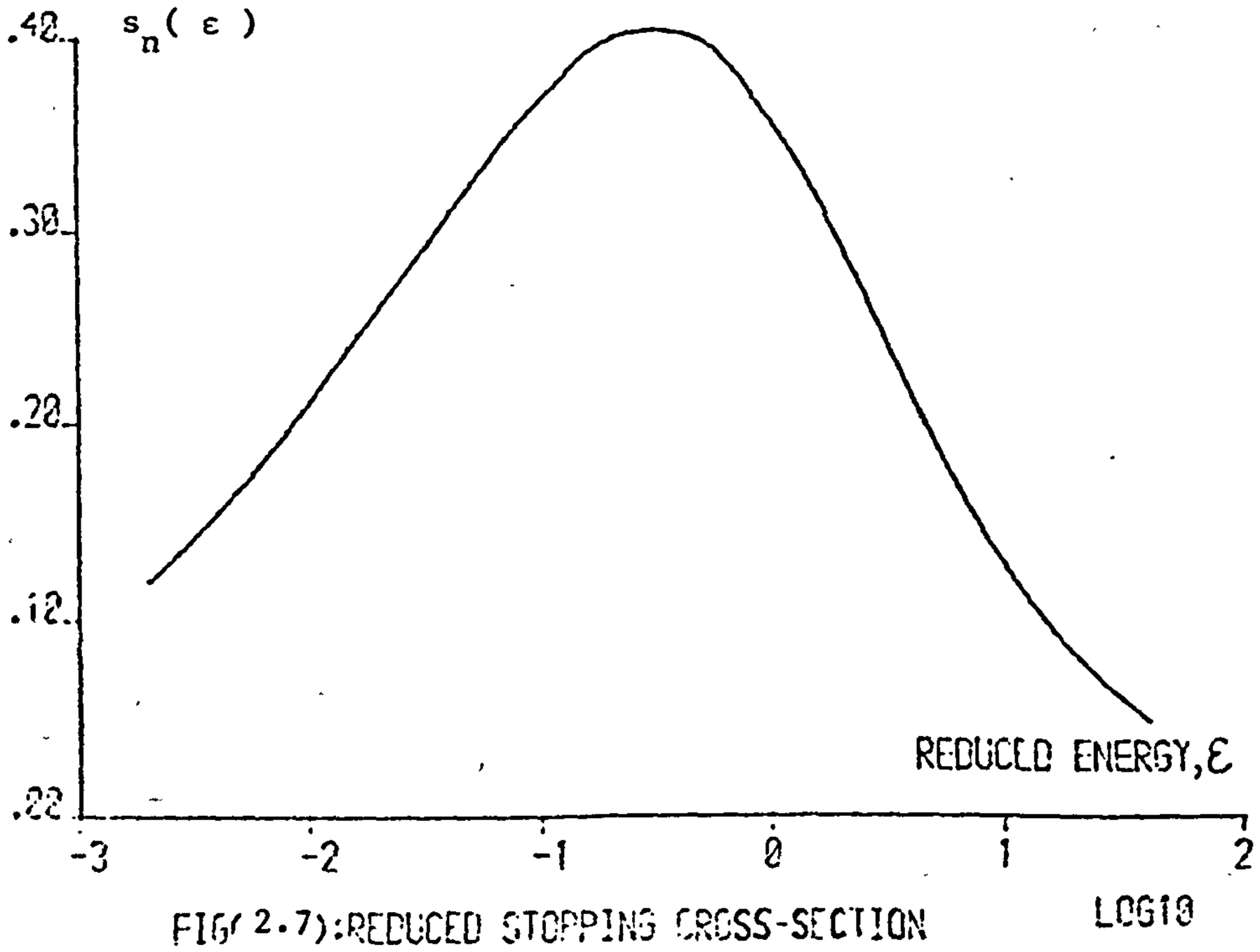

FIG(2.7):REDUCED STOPPING CROSS-SECTION
(Data from ref.2.20)

differential, and considering only terms of first order in δt, we have the full equation:

$$G(x,\underline{v}_o,\underline{v},t) = Nv\,\delta t \int d\sigma\left[G(x,\underline{v}_o,\underline{v}',t) + G(x,\underline{v}_o,\underline{v}'',t)\right] + (1 - Nv\delta t)\int d\sigma\left[G(x,v_o,v,t) + \frac{\partial G}{\partial x}\,n\,vdt + \frac{\partial G}{\partial t}\,dt\right] \quad 2.8$$

which yields immediately Boltzmann's transport equation:

$$-\frac{1}{v}\frac{\partial}{\partial t}G(x,\underline{v}_o,\underline{v},t) - n\frac{\partial}{\partial x}G(x,\underline{v}_o,\underline{v},t) = N\int d\sigma\left\{G(x,\underline{v}_o,\underline{v},t) - G(x,\underline{v}_o,\underline{v}',t) - G(x,\underline{v}_o,\underline{v}'',t)\right\} \quad 2.8'$$

This is the basic equation of radiation damage theory, and contains a formidable eight variables. The integral

$$\int_o^\infty G(x,\underline{v}_o,\underline{v},t)\,dt$$

is the number of atoms crossing a plane at x with a velocity $\underline{v}_o$ during a cascade, so that the function

$$H(x,\underline{v}) = \int n\underline{v}_o\; d^3\underline{v}_o \int_o^\infty G(x,\underline{v}_o,\underline{v},t)\,dt \quad 2.9$$

will represent the total number crossing a plane at x. If the velocity integration is done in such a manner as to include only those atoms travelling in a negative direction with sufficient energy to overcome a potential barrier at the surface, then we can write the sputtering yield per incident ion as:

$$S(\underline{v}) = H(0,\underline{v}) \quad 2.10a$$

or equivalently

$$S(E,n) = H(0,E,n) \quad 2.10b$$

2.2.4 Moments of the function H

Including the two integrations of equation 2.9, the basic sputtering equation becomes

$$-\delta(x)\,n\,\Theta(-n)\quad \Theta(E - Uo/n^2) - n\frac{\partial}{\partial x}H(x,E,n) = N\int d\sigma\left\{H(x,E,n) - H(x,E',n') - H(x,E'',n'')\right\} \quad 2.8a$$

where the first term on the left (the 'source term') provides a single starting particle at t = 0, x = 0 and the Helmholtz step function Θ expresses the restrictions, mentioned above, on the validity of equations 2.10. The term U_o/η^2 provides a planar potential barrier at the surface, having the nature of a sublimation energy.

This equation is transformed to reduce the number of variables in two steps, shown in Appendix III, proof 1. First it is noted that the angular dependence is not strong, and it may be eliminated by writing

$$H_l(x,E) = \tfrac{1}{2}\int_{-1}^{+1} H(x,E,\eta)\, P_l(\eta)\, d\eta \qquad 2.11$$

where $P_l(\eta)$ is a Legendre polynomial of order l. Then integrating over the whole range of η, we have

$$\delta(x)\, Q_l(E) - \frac{\partial}{\partial x}\left[lH_{l-1}(x,E) + (l+1)\, H_{l+1}(x,E)\right]$$

$$= (2l+1)N\int d\sigma\left[H_l(x,E) - H_l(x,E')P_l(\eta') - H_l(x,E'')P_l(\eta'')\right] \qquad 2.12$$

where

$$Q_l(E) = \frac{2l+1}{2}\int_{-1}^{+1}(-\eta)\ \Theta(-\eta)\ \Theta(E-U_o/\eta^2)\ P_l(\eta)d\eta \qquad 2.12a$$

$$= \frac{2l+1}{2}\int_{-1}^{\sqrt{U_o/E}} -\eta P_l(\eta)d\eta$$

Second, the position dependence is eliminated by taking moments defined by

$$H_l^n(E) = \int_{\infty}^{\infty} dx\ x^n\ H_l(x,E) \qquad 2.13$$

giving a recurrence relation:

$$\delta_{no}\, Q_l(E) + n\left[lH_{l-1}^{n-1}(E) + (l+1)\, H_{l+1}^{n-1}(E)\right] \qquad 2.14$$

$$= (2l+1)\, N\int d\sigma\left[H_l^n(E) - P_l(\eta')H_l^n(E') - P_l(\eta'')H_l^n(E'')\right]$$

where δ is the Kronecker δ-function. It turns out (2.1) that the solution at $n = 0$, $l = 0$ contains the essence of the physical behaviour of the full function $H(x,E,\eta)$.

Using equation 2.3 for $d\sigma$, we have, for $H_o^o(E)$:

$$\tfrac{1}{4}(1 - \frac{U}{E}o) = NC_m E^{-m} \int_o^E \frac{dT}{T^{1+m}} \left[H_o^o(E) - H_o^o(E-T) - H_o^o(T) \right] \qquad 2.15$$

which is soluble quickly according to a method communicated personally by Sigmund (2.10) and contained in Appendix III. Accordingly, we can write the approximate solution as

$$H_o^o \simeq \frac{m}{\psi(1)-\psi(1-m)} \cdot (1-2m)^{-1} \cdot \frac{E}{8NC_m U_o^{1-2m}} \qquad 2.16$$

where ψ is the digamma function (2.5),

$$\psi(x) = \frac{d}{dx}\left\{\ln(\Gamma(x))\right\} \qquad 2.16a$$

2.2.5 Low energy and inelastic collisions

In a collision cascade, the very great majority of collisions will be of low energy. Thompson (2.21) shows experimentally that copper atoms sputtered by 40 keV argon ions have an average energy of less than 10 eV. We can therefore further simplify equation 2.16 by taking the limit as $m \to o$, consistent with all the other approximations made, and appropriate to low energy as discussed in section 2.2.1. Thus, by proof 3 (Appendix III), we have:

$$H_o^o(E) \simeq \frac{1}{8NC_o\psi'(1)} \frac{E}{U_o} = \frac{3E}{4\pi^2 NC_o U_o} \qquad 2.17$$

where the trigamma function is defined (2.5) by

$$\psi'(x) = \frac{d}{dx}\psi(x) = \pi^2/6 \qquad 2.17a$$

The effect of inelastic collisions, energy lost to electronic excitation, is customarily included simply by writing in place of E in this equation the fraction of energy not lost to other processes.

2.2.6 Deposited energy function

Making the substitution:

$$H_1^n(E) = \frac{3}{4\pi^2 NC_o U_o} F_1^n(E) \qquad 2.18$$

we have directly (2.4)

$$F_1^o(E) = \delta_{1o} E \qquad 2.19a$$

leading to the equation for the normalisation of the distribution:

$$\int_{-\infty}^{+\infty} F(x,E,\eta)\, dx = E \qquad 2.19b$$

The amount of energy deposited in a layer dx thick by an ion of energy E starting at x=0 is $F(x,E,\eta)\, dx$. Consequent on equations 2.18 and 2.19 is the full function

$$H(x,E,\eta) = \Lambda\, F(x,E,\eta) \qquad 2.20$$

where Λ is a factor determined by the properties of the target material and the surface given by

$$\Lambda = \frac{3}{4\pi^2 C_o N U_o} \qquad 2.20a$$

$$\Lambda/\mathring{A}^{-2} = \frac{0.0420}{NU_o}$$

where C_o has been used from equation 2.4, with a = 0.219 $\mathring{A}$. Equations 2.10 and 2.20 give an expression for the sputtering yield:

$$S(E,\eta) = \Lambda\, F(0,E,\eta) \qquad 2.21$$

If the incident ions are of a different species, $M_1 \neq M_2$, the function F employed is that for the particular ion-target combination. The function F is similar to a Gaussian truncated by the surface, and in the elastic collision region, F can be approximated by an Edgeworth expansion (2.6, 2.14):

$$F(x) = \frac{E}{\sigma}\left[\phi_o(y) - \frac{\Gamma_1}{6}\phi_3(y) + \left\{\frac{\Gamma_2}{24}\phi_4(y) + \frac{\Gamma_1^2}{72}\phi_2(y)\right\}\right] \qquad 2.22$$

where, for a distribution centered at x_o, with a width σ we define:

$$\phi_n(y) = \frac{1}{\sqrt{2\pi}} \frac{d^n}{dy^n} \cdot e^{-y^2/2} \qquad 2.22a$$

$$y = (x-x_o)/\sigma \qquad 2.22b$$

$$\Gamma_1 = \langle(\sigma y)^3\rangle/\sigma^3 \qquad 2.22c$$

$$\Gamma_2 = \langle(\sigma y)^4\rangle/\sigma^4 - 3 \qquad 2.22d$$

The moments F_1^n yield the width σ (2.7) and the mean depth x_o, and these are given for a range of mass ratios and values of m in ref. (2.4). The analytical form of F(x,E) is shown in Fig. 2.5 where Lindhard's 'reduced' energy unit (equation 2.25a) is used for generality, and the approximation introduced by truncating equation 2.22 to the initial Gaussian can be seen to be small.

2.3 General yield formulae

The angular dependence is incorporated in the spread of the distribution:

$$\sigma(E,\eta) = \frac{E^{2m}}{NC_m} \; h(\eta) \qquad 2.23$$

and the experimental evidence (2.11) corroborates the analytical result (2.1) that:

$$h(\eta) = \eta^{5/3} \quad \text{for } \eta < \arccos 70^\circ \text{ and } M_2/M_1 \leqslant 3 \qquad 2.23a$$

so that by equations 2.22 and 2.23 we can write for normal incidence

$$F(0,E,1) = NC_m \; E^{1-2m}(1-m) \; (2\pi)^{-1/2} \exp\left(-x_o^2/2\sigma^2\right)$$

$$= (1-m)\gamma^{m-1} \; NS_n(E) \; (2\pi)^{-1/2} \exp(-x_o^2/2\sigma^2) \qquad 2.24$$

having used equation 2.6b for $S_n(E)$. We can evaluate this expression using Ref. (2.4) for x_o and σ, whereupon it is found that the dependence upon m is slight, and we can further simplify equation 2.21 to:

$$S(E) = \alpha \Lambda N S_n(E) = 0.042\alpha \; S_n(E)/U_o \qquad 2.21'$$

where α carries the dependence upon the mass ratio M_2/M_1, as shown in

Fig. 2.6, and where the units of $S_n(E)/U_o$ are $\overset{o}{A}^2$.

Having established that the sputtering yield is proportional to the stopping cross-section divided by the surface binding energy only, it is sensible to use the best available values for $S_n(E)$ and not necessarily those given by equation 2.6. Lindhard et al (2.8) publish an expression in 'reduced' form which, in SI units is:

$$S_n(E) = 4\pi Z_1 Z_2 e_M^2 a \left(\frac{M_1}{M_1+M_2}\right) s_n(\varepsilon) \qquad 2.25$$

where (SI units)

$$\varepsilon = \left(\frac{M_2}{M_1+M_2}\right) \frac{aE}{Z_1 Z_2 e_M^2} \qquad 2.25a$$

and a is from equation 2.4b, with the function $s_n(\varepsilon)$ as shown in Fig. 2.7 plotted from tables in Refs. (2.20) and (2.1). This function, and hence S(E), is seen to reach a maximum at $\varepsilon \simeq 0.25$

2.4 Depth of origin of sputtered particles

We have seen that during sputtering most of the particles set in motion have low energies, and that throughout the treatment it has been appropriate to set the interaction parameter m to zero. The distance moved by a particle inside the target is given approximately by equation 2.7, which becomes, with $M_1 = M_2$ and m = 0:

$$R = (NC_o)^{-1} \qquad 2.7'$$

For a b.c.c. structure of lattice constant r, and using $C_o = 1.808\ \overset{o}{A}^2$ as in section 2.21, this depth is $0.27r^3$ so that it is easily seen that in most solids a layer less than 10 $\overset{o}{A}$ thick provides the entire sputtered flux (2.12). This is of particular significance in the production of thin films by the sputtering process, and in the analysis of sputtered surfaces, as will be seen in the following chapter, where the sputtering of multi-component materials is considered.

2.5 Summary

This chapter has been concerned with the mathematical description of the physical processes involved in sputtering. The present understanding is not complete; the complex treatment contained herein fails conspicuously to explain many of the results obtained by experiment. However, a knowledge of cascade theory is indispensable as a guide to understanding the phenomena involved. The general formula (equation 2.21') which is often used to predict sputtering yields has been derived in a fairly rigorous way, and in the following chapter we shall see its use in the case of argon ions impinging on glass surfaces.

CHAPTER 3

SPUTTERING OF MULTICOMPONENT MATERIALS

Implicit in the theory of the linear cascade set out in the previous chapter is the homogeneity of the target. If alloys or glasses are used as targets, this condition is violated and efforts have been made recently to establish in what way multicomponent materials behave during sputtering. The experiments of Betz (3.1) on metallic alloys are central to the experimental side of the field, and Jimenez-Rodriguez et al (3.2) have attempted to apply linear cascade theory, with limited predictive success. Sigmund (3.3) has described the theoretical concepts involved.

In this chapter the effects of preferential sputtering are described, and the useful equations of chapter 2 are evaluated for glass.

3.1 The altered layer

If one component of the target is considered to sputter preferentially, there will form a layer at the surface, the 'altered layer', depleted in that component. Fewer atoms of that species will then be available to take part in the sputtering process, hence they will no longer be preferentially sputtered, and the surface must reach an equilibrium composition ('steady state') after which the sputtered flux will be stoichiometric.

The extreme superficiality of the process indicated in section 2.4 enables a simple two-dimensional argument to be put forward to show the time development of the altered layer composition.

Consider a binary target with initial surface concentration of $c(0)$ and $n(0)c(0)$ atoms per unit area of species 1 and 2 respectively. If their respective ejection probabilities during sputtering are $p(t)$ and $rp(t)$, we can write for the sputtered flux density of each species:

$$\phi_1(t) = c(t)\, p(t) \qquad 3.1a$$

and

$$\phi_2(t) = n(t)\, c(t)\, r\, p(t) \qquad 3.1b$$

For low doses, i.e. when the condition

$$\int_0^t \phi(t')\, dt' < c(0) \qquad 3.2$$

is satisfied, the surface concentrations of the species become respectively

$$c(t) \simeq c(0) - \phi_1(t)\, t \qquad 3.3a$$

and

$$n(t)c(t) \simeq n(0)c(0) - \phi_2(t)\, t \qquad 3.3b$$

After substituting equations 3.1 we have for the ratio of concentrations:

$$n(t) = \frac{n(0)\ (1 + p(t)t)}{(1 + rp(t)t)} \qquad 3.4$$

which at large t becomes

$$n(\infty) = n(0)/r \qquad 3.4'$$

and a steady state surface composition is achieved in inverse proportion to the ejection probability ratio of the species. The composition of the sputtered flux at large t is given by

$$\left[\frac{\phi_2(t)}{\phi_1(t)}\right]_{t\to\infty} = \left[n(t)\ r\right]_{t\to\infty} = n(0) \qquad 3.5$$

which shows that the flux should be stoichiometric after steady state has been reached.

Liau et al (3.4) used Rutherford backscattering (3.5) to establish the depth profiles of the relative concentration of Pt to Si in 1:1 PtSi alloy, after achieving steady state by sputtering. These profiles are shown in Fig. 3.1, where the linearity in composition ratio with depth and the strong dependence of the altered layer thickness on primary sputtering energy are to be noted.

The time development of the system was modelled mathematically by

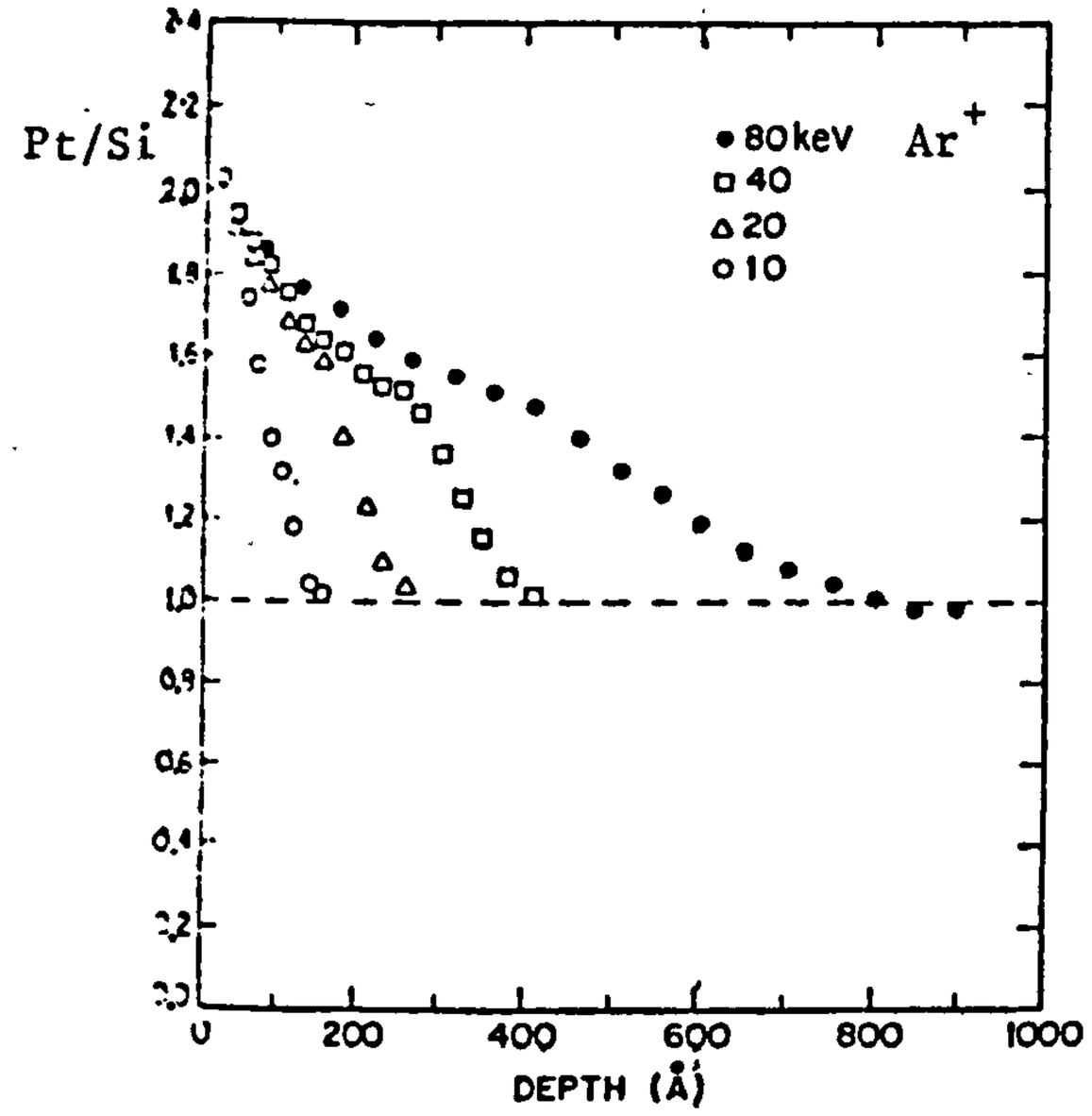

Fig.(3.1): Steady state Pt/Si concentration profiles of Ar^+ sputtered 1:1 Pt/Si (Ref.3.4)

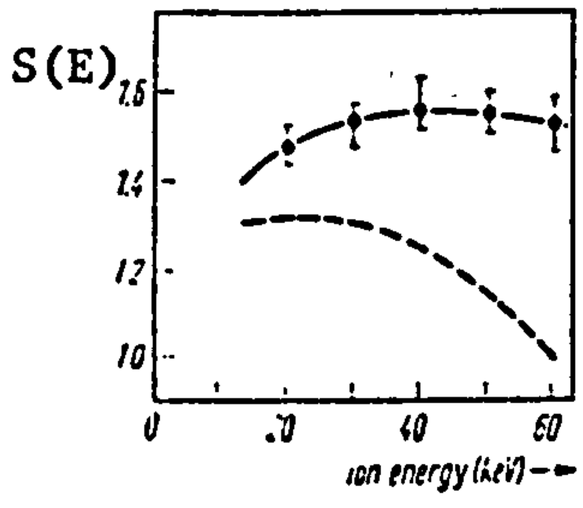

Fig.(3.3): Experimental glass sputtering yield as a function of Ar^+ energy and a theoretical yield calculation shown dashed (Ref.3.7)

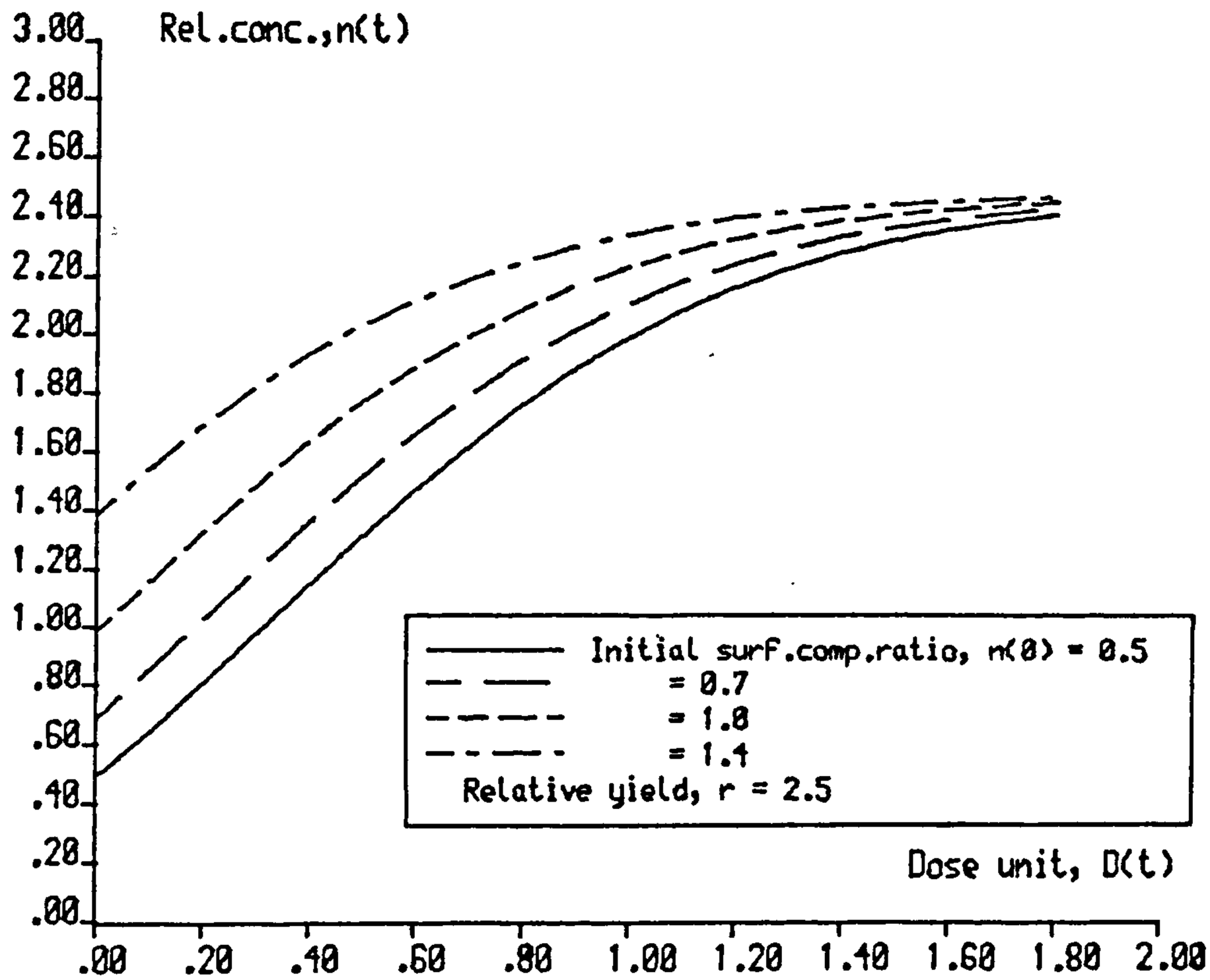

FIG(3.2a): Time development of sputtered surface composition

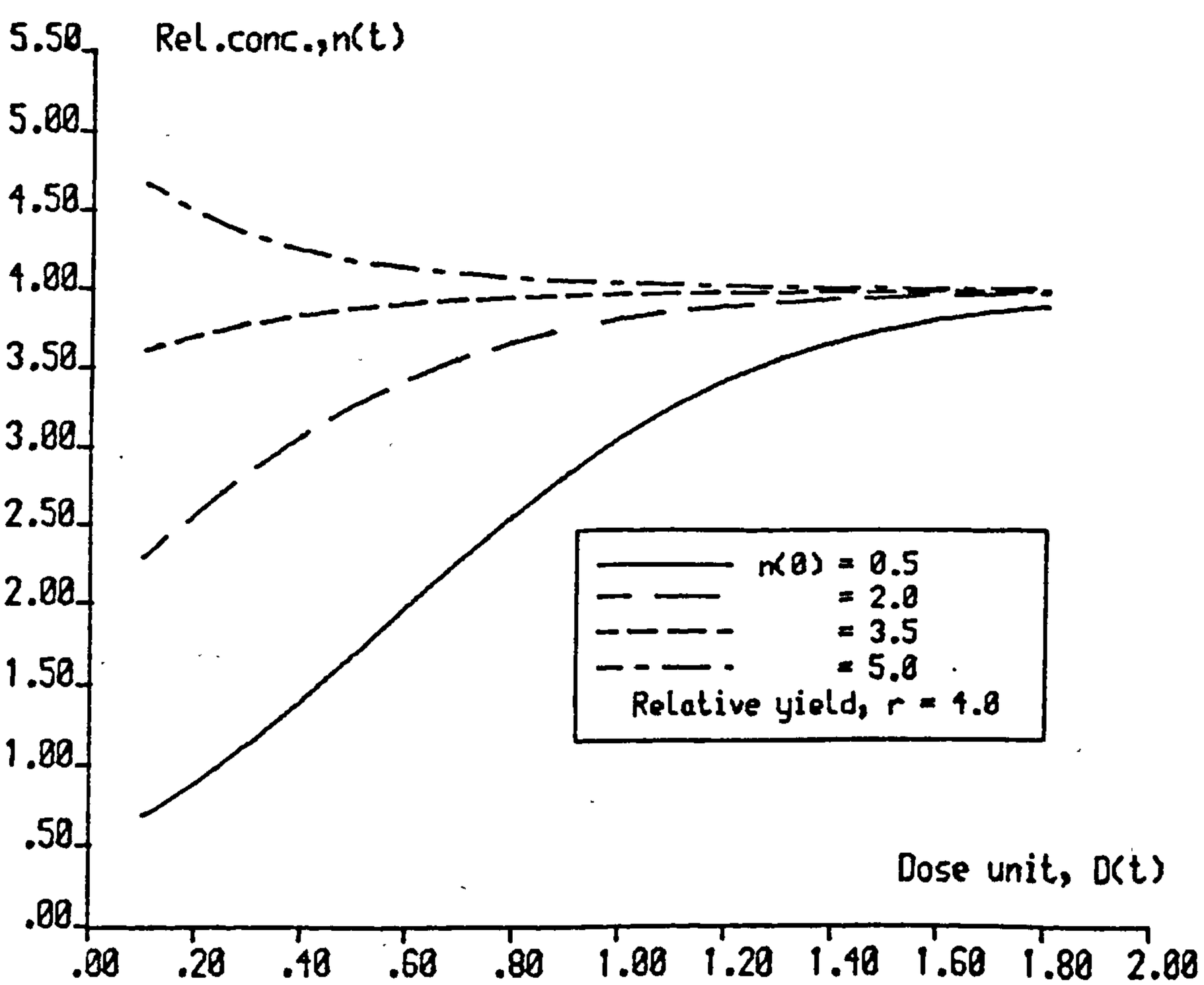

FIG(3.2b): Time development of sputtered surface composition

these workers (3.4) and the surface composition ratio n(t) was found to satisfy the equation

$$\int_{n(0)}^{n(t)} \frac{r+n'}{(r-n')(1+n')}\, dn' = \frac{\Phi St}{NW} = D \qquad 3.6$$

where Φ is the ion flux density, $S = S_1 + S_2$ the total sputtering yield, W is the altered layer thickness, and n(t) is defined consistently with the previous derivation by

$$n(t) = \frac{N_2(0,t)}{N_1(0,t)} \qquad 3.6a$$

where $N_i(x,t)$ is the number of target atoms of species i per unit volume, at a depth x and time t with $N_1 + N_2 = N$, the total number. A proof of this equation simplified from that of Liau et al is provided in Appendix IV.

Equation 3.6 was solved numerically for the different initial composition ratios shown in Figs. 3.2. The composition function n(t) approaches r in all cases, and after a dose of less than 2D the steady state composition has effectively been reached independent of n(0) and r. The rate of approach to $n(\infty) = r = 1.94$ of such a n(t) curve with n(0) = 1 was quantified by Liau et al by finding the intersection of the tangent to the curve at D = 0 with the line n = 1.94. This procedure gave them a value for the dose required to reach steady state in that case ($\frac{3}{4}$D), but it is easily seen from Figs. 3.2 that the method gives quite different results according to n(0).

The work of Ho (3.6), using similar concepts but including diffusion into the sputtered layer, shows that about 1.25 times the thickness of the altered layer must be sputtered off before steady state is reached.

Since the term NW in equation 3.6 is the number of atoms per unit

area of altered layer, and ΦSt is the number of atoms removed in a time t, it is seen that the approaches are consistent, and that an ion dose Φt of just over NW/S (i.e. D=1) is required to obtain a steady surface composition in most cases.

Values of the altered layer thickness W are contingent on the incident ion energy, as Fig. 3.1 shows, but are of the order of hundreds of Angstrom units, much larger than the depth from which sputtered particles come. Diffusion and collisional re-implantation effects can account for compositional changes at that depth as discussed qualitatively by Sigmund (3.2). The depth of the altered layer has the same order of magnitude as the peak of the energy deposition function $F(x,E,\eta)$ considered in Chapter 2.

The results obtained by sputter profiling glasses given in detail in chapter 8 of this thesis show a steady state surface composition to have been reached with a 2kV primary energy after about 300 Å had been sputtered away. This is consistent with the trend of Fig. 3.1.

3.2 Relative sputtering yield

There has been no prediction made so far as to which of the components of an alloy or glass might be expected to have the greater sputtering yield. Using the treatment of cascade theory in Chapter 2, the yield ratio of components 1 and 2 can be written from equation 2.21' as

$$\frac{S_2}{S_1} = r = \frac{\alpha_2 U_1 S_n^{(2)}(E)}{\alpha_1 U_2 S_n^{(1)}(E)} \qquad 3.7$$

where U_i and $S_n^{(i)}$ are the surface binding energy and the stopping cross-section of a component i, respectively.

Betz (3.1) considers that the functions $\alpha_i(M_i/M_1)$ and $S_n^{(i)}(E)$ vary only slowly with the species designation i, for moderate masses, and

makes the approximation

$$r \approx U_1/U_2 \qquad 3.7'$$

Hence, the final surface composition ratio is determined entirely by the relative surface binding energies of the components; the more tightly bound species being enriched.

However, Sigmund (3.2) and Jimenez-Rodriguez (3.7) both consider the ratio r to depend on the masses of the particles and the interaction parameter m, which it does, if Betz's approximation (equation 3.7') is not made and find it possible to predict surface enrichment in either species because the values of the many parameters to be used are so uncertain. Particularly uncertain is the crucial binding energy U_i. Indeed, sputtering is a method of determining surface binding energies by comparison of equation 2.21' with experimental yield values, which makes surface enrichment predictions using the equation somewhat circular.

Extending these considerations to three or more components becomes very complex mathematically, but clearly a steady state surface composition will result which is determined by the relative sputtering yields of a component i with respect to the others according to

$$n_{ik}(\infty) = r_{ij}\, n_{jk}(\infty) \qquad 3.8$$

where $n_{ik}(\infty)$ is the relative surface density at steady state of components i and k and r_{ij} is the ejection probability ratio of components i and j.

3.3 Application to the sputtering of glass

Irrespective of the compositional changes discussed above, it is interesting to calculate a sputter yield of the target by averaging the atomic masses M_i and Z_i of its components. The target is then treated as homogeneous and the equations of Chapter 3 can be used.

This method has been applied to the sputtering of glass in the

energy region from 20 to 60 keV by Rauschenbach and Hinz (3.7). They measured a higher yield than expected from calculation but such a discrepancy is not surprising in the light of the unknown scaling factor U_o, which they do not specify. Their experimental results (Fig. 3.3) show an energy dependence different from the theoretical one, especially at the higher end of the energy range. Extrapolation of the curves to lower energies (appropriate to the work described in this thesis) gives improved agreement, and at energies around 2 keV we have found the correspondence to be excellent.

3.3.1 Evaluation of linear cascade equations

It is convenient and illustrative to evaluate explicitly several of the more useful equations from sputtering theory for a glass target bombarded with argon ions.

A glass of molecular composition as follows: Na_2O (10%), CaO (20%), SiO_2 (70%) has an average atomic mass of $M_2 = 21.7$ and an average atomic number Z_2 of 10.57. For argon, these quantities are $M_1 = 40$ and $Z_1 = 18$ respectively, so that from equations 2.4b, 2.4c and 2.25a we obtain $Z = 11.68$ and $a = 0.137$ Å. This enables equation 2.25 to be written

$$S_n(E)/eV\text{Å}^2 = 3055.1\ \varepsilon_n(\varepsilon) \qquad 2.25'$$

where

$$\varepsilon = 1.1 \times 10^{14}\ E/J = 1.76 \times 10^{-5}\ E/eV \qquad 2.25a'$$

and at a primary energy of 2 keV, the reduced stopping cross-section $s_n(\varepsilon)$ may be estimated from Fig. 2.7 as

$$s_n(3.52 \times 10^{-2}) = 0.3 \qquad 3.9$$

The sputtering yield of a 2 keV argon ion impinging on glass at normal incidence is now calculable from equation 2.21' as

$$S(2\text{keV}) = 0.042\ \alpha\ (21.7/40)\ S_n(2\text{keV})/U_o \qquad 3.10$$

and using Fig. 2.6 for α (as shown) we have

$$S(2keV) = 0.042 \times 0.22 \times 3055.1 \times 0.3/U_o = \frac{8.5}{U_o} \qquad 3.11$$

Extrapolating the data of Fig. 3.3 to 2 keV, both experimental and theoretical yields converge at approximately 1.2, so that a surface binding energy close to 7 eV is predicted. Using the data for the glass composition used by Rauschenbach and Hinz (3.7) it can be calculated that these workers must have assumed U_o = 8 eV, but their basis for doing so cannot be established.

Estimates of the Madelung binding energy of sodium disilicate have been computed by Underhill (3.8). The results of such calculations depend upon exactly which particle is considered, and its position in the lattice. Sputtering yield calculations are less specific; a generalized 'glass particle' is caused to leave a generalized 'glass surface'. However, there is a surprising agreement between the two approaches, since a Madelung energy of about 16 eV is found by calculation, and half of this is a good approximation for the surface binding energy.

In the second half of this thesis, where DC sputtering of glass is described, it will be seen that a sputter yield of about 1.2 is measured. The surface binding energy U_o in an expression such as equation 3.10 can hence be taken as 7.5 $\pm$ 1.0 eV.

The peak of the reduced stopping cross-section curve of Fig. 2.7 occurs at approximately $\varepsilon = 0.25$. Thus, the primary argon ion energy which will sputter glass most efficiently is 14.3 keV (from equation 2.25a') when a maximum yield of about 1.5 is obtainable.

3.3.2 Thermal spike temperatures

In section 2.1.2, the temperatures of the 'thermal spikes' caused by ion bombardment were discussed. The magnitude of the number density N of glass may be obtained by dividing a typical glass density (2600 kgm^{-3})

by $M_2 m_p$ where m_p is the mass of the proton, to yield $N = 0.072$ $\mathring{A}^{-3}$. A typical interatomic distance is given by $N^{-\frac{1}{3}} = 2.4$ $\mathring{A}$. We may use this value of N in equation 2.1, for the energy in a thermal spike. The appropriate point on Fig. 2.2 is indicated, and we obtain

$$\frac{3}{2} KT_s = 1000 \frac{N^2 e}{E/keV} \qquad 2.1'$$

where T_s is the temperature of the spike. This treatment is valid only for E>60 keV, so that a spike may have a temperature not exceeding about 600 K.

3.4 Cluster formation

It has been implicit in the discussion of sputtering effects presented so far that particles are emitted as single, neutral atoms. For completeness, it should be noted that there is the possibility that the emitted flux might contain not only ions but also clusters of atoms, in the form of molecules or molecular ions. Staudenmaier (3.9) shows, by mass spectrometry, that the singly charged particles sputtered from tungsten may be clusters of up to four tungsten atoms, and Gerhard et al (3.10) estimate the rate of cluster emission as a few percent of the total sputtered flux.

The way in which clusters can be formed is imperfectly understood. An explanation has been given by Können et al (3.11) which may be described in a non-mathematical way as the combination of two or more atoms from the same collision cascade which were emitted simultaneously from the same place with the same velocity. The combination is considered to occur after the independent sputtering of the particles.

It is not to be assumed that cluster emission is any more likely in the case of multi-component materials or glass in particular. Können (3.11) discusses the effect of the surface binding energy and considers that atoms originally close together on the surface of the target may be sputtered in

the form of an aggregate, and it is clear that the possibility that $t\nu_s$ occurs in glass sputtering is not remote. The numbers of such aggregates must, of course, be very small.

3.5 Summary

A demonstration has been given of the way in which some of the equations from linear cascade theory may be applied to a target representative of glass. The procedure can be applied to any material, making the chapter of more general interest and applicability. It has been seen that sputtering experiments can yield the quantity U_o; which quantity can be used, conversely, to predict sputtering yields.

The time development of the surface composition of a sputtered target has been demonstrated theoretically, and it has been suggested that a thickness of material roughly equal to that of the altered layer must be removed before a steady composition is attained.

CHAPTER 4

RF SPUTTERING

The treatment of sputtering effects in Chapters 2 and 3 has concentrated on target processes. We have considered how particles are caused to leave the surface of the target, and discussed the development of the surface composition with time. We now turn to a consideration of equipment designed and built to enable the sputtered flux from glass targets to be used for the deposition of thin glass films.

In a DC discharge tube, where metal electrodes are in contact with an ionised gas, the negative electrode will be sputter-eroded by the energetic ions. If the electrodes are constructed of a dielectric material, the discharge will be short lived, as the impinging ions will neutralise the cathode and prevent any further passage of current. Hence, no sputtering of dielectrics is possible in a DC discharge.

Over the last two decades, a technique for the deposition of dielectric films has been developed, using a radio-frequency (RF) discharge to avoid the charging effect. This chapter deals with the principles of RF sputtering and indicates in detail the solutions found to some of the problems encountered in the design and construction of an RF sputtering system. Key papers are by Davidse and Maissel (4.1) and the reviews by Vossen and O'Neill (4.2) and Jackson (4.3). Holland et al (4.4) describe apparatus for sputtering of all kinds.

4.1 Theory of process

The target to be bombarded is mounted upon an electrode, opposite the substrate on to which the film is to be deposited. The whole assembly, shown schematically in Fig. 4.1, is contained in a vacuum vessel flooded with the sputtering gas.

By applying a high voltage RF signal to the backing electrode, the

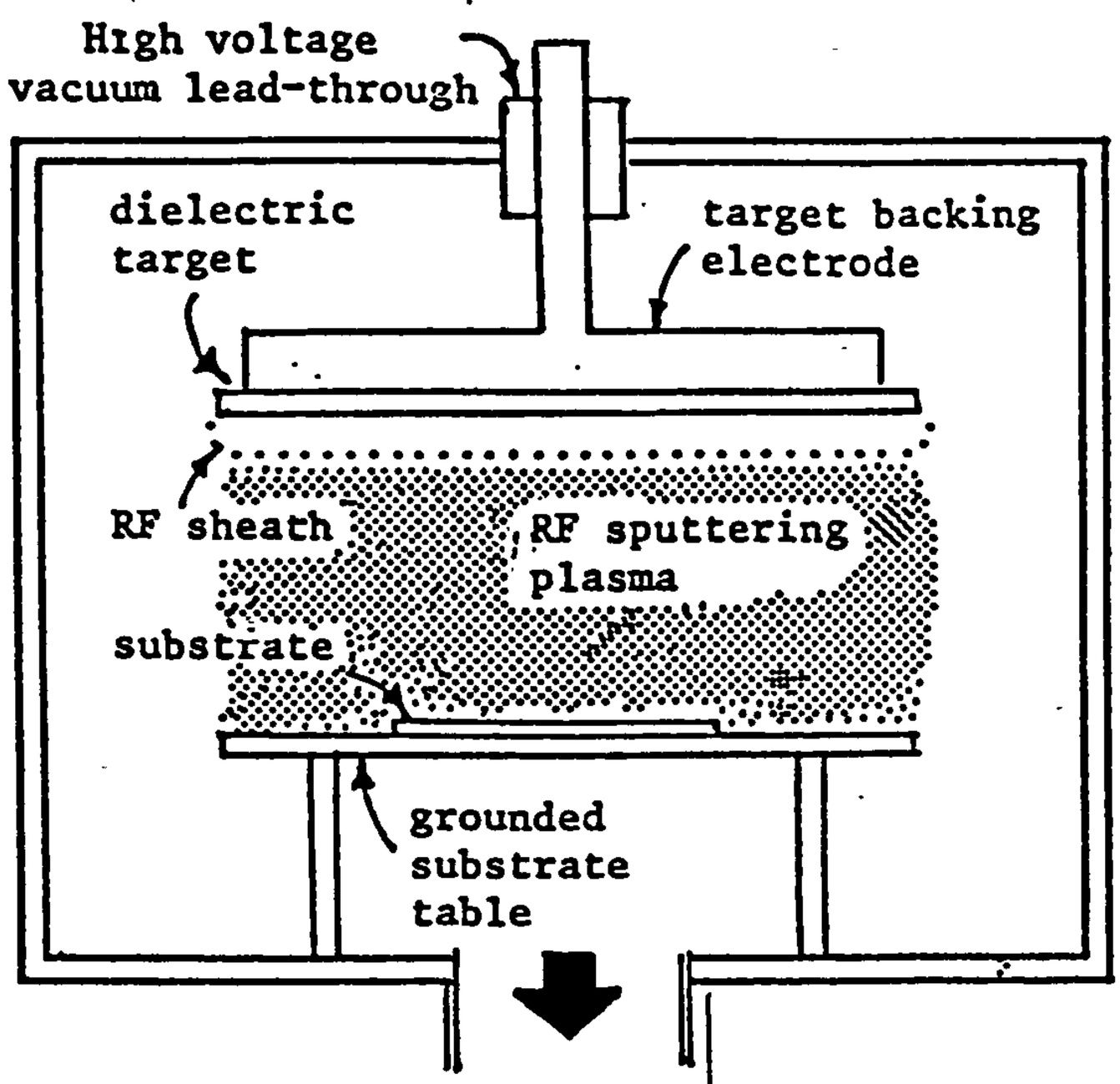

Fig.(4.1): Schematic diagram of a simple RF sputtering plant.

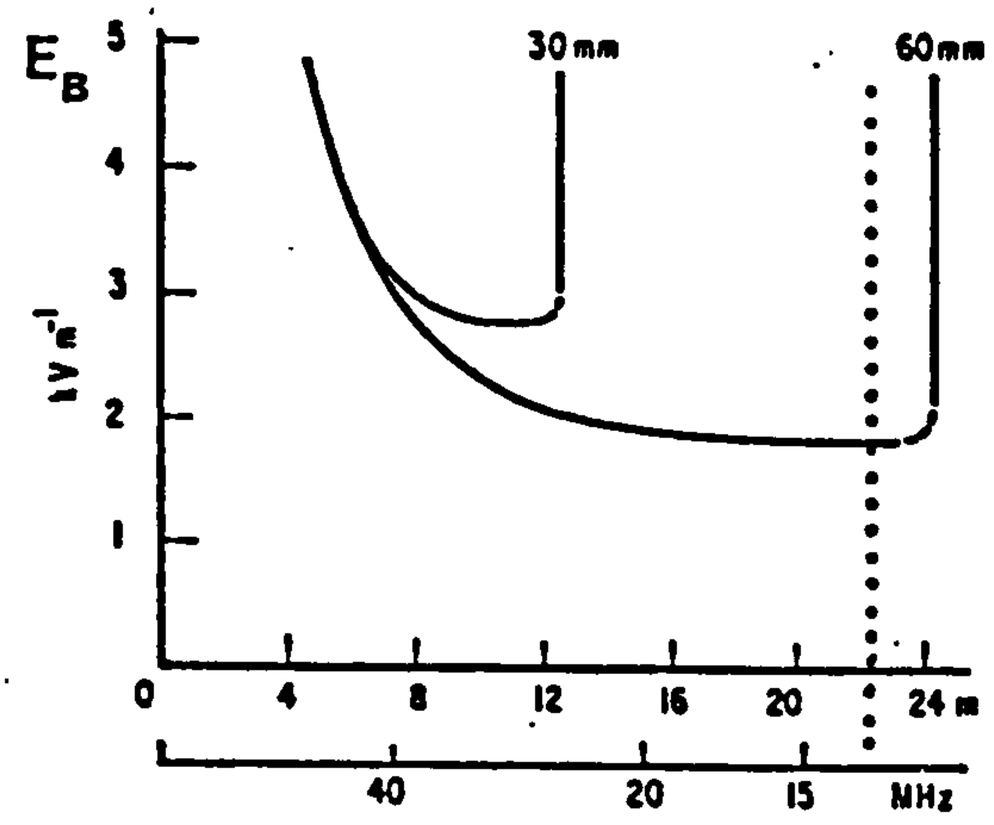

Fig.(4.2): Breakdown field E_B of a hydrogen discharge against wavelength for a flat ended cylindrical tube of length 30 and 60 mm, with axis parallel to the field. Pressure of gas: 0.133 Pa. (Ref.4.6). The working frequency is shown.

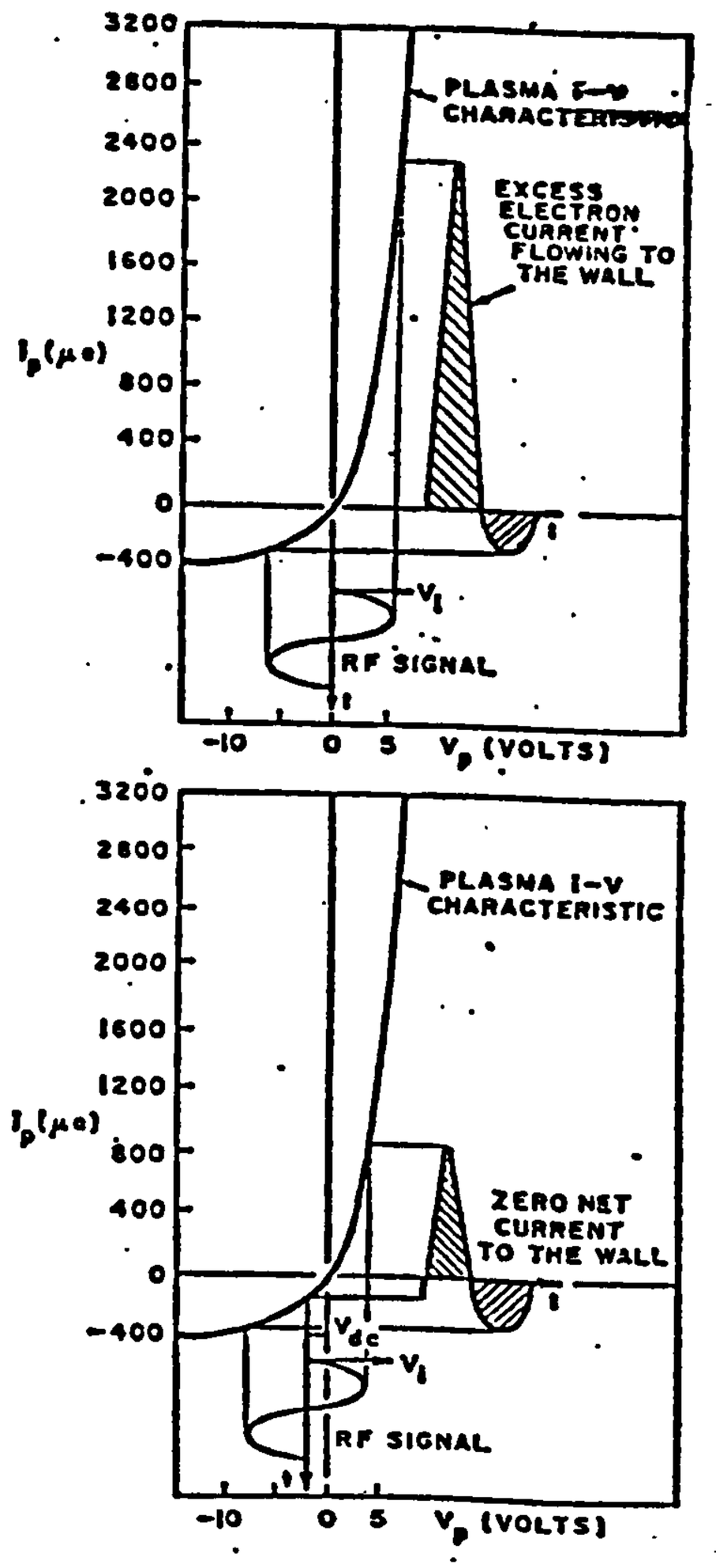

Fig.(4.3): RF signal superimposed on a typical I-V characteristic showing the development of the surface bias. (Ref.4.2)

gas is caused to ionise, and the target surface is sputtered according to the mechanisms outlined in the following subsections. Pertinent to the discussion are the pressures used for this work and the frequency. The pressures used are between 0.1 and 1 Pa, and international regulations concerning radio emission constrain the frequency to within 20 kHz of 13.56 MHz, which is referred to throughout as the 'working frequency'. At these pressures, the mean free path of argon ions is between 7 and 70 mm, making collisions between ions quite infrequent.

4.1.1 Secondary electron resonance

The field strength required to initiate a low pressure gaseous discharge can be very much lower at high frequencies than for a DC applied field (4.5). This phenomenon was investigated by Gill and von Engel (4.6) and Hatch and Williams (4.7), and can be explained by the theory of secondary electron resonance (4.8), sometimes called 'multipacting'. The breakdown of the gas in RF sputtering chambers is attributed to the same process, or a similar one, by Jackson (4.3).

The mean free path of electrons in a sputtering plasma is very much greater than the linear dimensions of the chamber, and the number of ions produced by collisions during the passage of one electron across the chamber can be estimated (4.14) at 0.055, for a typical target to substrate table spacing. Under the influence of an AC field, the electron trajectory will become oscillatory and the number of collisions per transit of the chamber will be increased. This is the cause of breakdown in low frequency discharges, but at radio frequencies, not only do calculations show that the paths are not increased sufficiently but also it is found experimentally (4.6) that the field required is independent of the ionisation potential of the gas, which would not be the case if merely the acceleration of free electrons were responsible

for the breakdown. Clearly, another process is active, and the secondary electrons produced by the impact with the target (and substrate) are found to be involved.

The few free electrons present in the gas will be accelerated by the applied field so as to impinge on the target, releasing a number of secondaries (δ per primary) from the surface. If the phase of the field is such that these secondaries are immediately accelerated away from the surface, and the frequency is such that before the field reverses they can just travel the full length of the chamber to impact with the substrate table, then the number of free electrons will be multiplied by δ^n, where n is the number of transits made. If the electrode is of glass, and the incident electrons have an energy greater than about 40 eV (4.7), δ rises above unity and the number of electrons in the oscillating cloud will increase geometrically. Since, at the working frequency, 2.7×10^7 transits are made each second, the number of electron-atom collisions will increase substantially in a very short time, causing the gas to ionise. To compensate for the loss of electrons from the discharge volume, δ must be as high as about 1.2, which is the case in sputtering systems, because typical electrode voltages used are in the kV region.

Hence, the starting field can be seen to be related to a length and a frequency; the frequency dependence giving the process a resonant nature. The resonance is not sharp, however, because of the variation in the time between a primary impact and the emission of a secondary electron. As Fig. 4.2 shows, discharges may be started with small fields ($5\,kVm^{-1}$) with frequencies between a lower limit determined by the spacing of the electrodes, and an upper limit of approximately 50 MHz in all cases. Fig. 4.2 can also be construed as indicating the minimum electrode separation d_o for which a discharge at a frequency f is possible, since the portion above the curve moves along the frequency axis as the separation increases.

Hatch and Williams (4.7) demonstrate experimentally and theoretically that the relationship between f and d_o is given by

$$d_o/\text{mm} = \frac{790}{f/\text{MHz}} \qquad 4.1$$

which is affected only slightly by pressure changes in the working region (4.3). At the working frequency, equation 4.1 implies that no discharge can be struck between electrodes less than 58 mm apart, which is approximately true for the sputtering chamber to be described in this thesis. It is of interest to note, with Brodie et al (4.27), that the maximum energy gained from the field by the ions is only 3 eV; they are almost unaffected by the RF field.

4.1.2 Surface biassing

Once the gas has ionised, the electrons and ions are accelerated in opposite directions by the field. The mobility of the electrons is much greater than that of the ions, causing the quantity of negative charge transferred to the surface of the target during one half cycle to be greater than the positive charge transferred during the next. This results in the target becoming biassed negatively, since the charge cannot leak away through the dielectric surface. The process is described pictorially by Fig. 4.3 from ref. 4.2, in which an RF sinusoid is impressed on the typical I-V characteristic of a solid surface in a plasma. A negative bias can be seen to be required if the surface is to prevent a net flow of current.

The magnitude of the biassing of the target surface is almost equal to the amplitude of the RF waveform, so quickly do the electrons arrive from the plasma to neutralise the target as it becomes positive, and it will be taken as half the peak to peak (p-p) RF voltage throughout the following (4.2).

It is due to this bias voltage, of course, that ions are

accelerated into the target and sputtering occurs.

4.1.3 Target sheath

Electrons will be repelled by the same voltage that accelerates the ions, and there will be a region of reduced electron density adjacent to the target, similar to a Crookes dark space, to be referred to as the target sheath.

The extent of the sheath can be easily observed, since the small electron density within it reduces the probability of the emission of visible photons by collisions with the plasma ions, making the region dark compared to the purplish glow of the discharge. The cross-section for excitation by ionic collisions is negligible (4.10).

Across this sheath, the target bias voltage is dropped, and ions are accelerated from the plasma. The thickness of the sheath (d) is determined by the ion current density j, the bias voltage V and the Langmuir-Childs law (4.11). We can write

$$d^2 = \frac{4\varepsilon_o}{9j}\left(\frac{2e}{M_1 m_p}\right)^{\frac{1}{2}} V^{3/2} \qquad 4.2$$

where M_1 is the atomic mass of the impinging ions, and m_p the mass of the proton. This relation is presented graphically for various ions by von Ardenne (4.12), and for argon it becomes

$$d^2 = 8.6 \times 10^{-9} \frac{V^{3/2}}{j} \qquad 4.2'$$

with d in meters, V in volts, and j in Am^{-2}. Westwood and Boynton (4.25) have fitted numerical values to the parameters of Aston's equation for the dark space distance in a DC discharge (4.26) to yield a relation which in SI units becomes

$$d_{DC} = \frac{0.11}{p/Pa} + \frac{0.00885}{\sqrt{j}} \qquad 4.3$$

This equation, if applied at a typical RF sputtering discharge pressure of 0.5 Pa predicts a dark space thickness very much greater than that of an

RF sheath, and we can conclude that the RF sheath is different in character from the DC dark space.

The unknown current density j was studied by Keller and Pennebaker (4.14), who derived an expression for it by equating the rate of production of ions by collisions and their rate of loss to the various surfaces and sheaths. The ions are first accelerated to the electron temperature kT_e before entering the RF sheath, as shown in Appendix V, (4.15) and if f is the frequency, p the pressure, D the target to substrate table spacing and A_t, A_s and A_w the areas of contact of the target, substrate table and walls respectively then we can write for argon, following these workers (4.14):

$$j/Am^{-2} = \frac{2.96 \times 10^{-16} f^2 A_t^2 V^{\frac{1}{2}} p (kT_e)^{\frac{1}{2}}}{D(A_t + A_s + A_w)} \qquad 4.4$$

with p in Pa, f in Hz, kT_e in eV and lengths in m. In this expression, the experimental relation for the electronic mobility μ in argon due to Brown (4.16) has been used:

$$\mu/m^2V^{-1}s^{-1} = \frac{4.3 \times 10^3}{p/Pa} \qquad 4.4a$$

and the fraction of dissipated energy lost to ionisation, to which j is proportional, has been set at 40% (4.14).

It must be recognised that the quantity kT_e, the electron temperature has a well defined meaning only if the electrons have a Maxwellian velocity distribution, which is the case when the electronic mean free path is smaller than the dimensions of the chamber (4.3). This is not the case in sputtering rigs, and accordingly, Fig. 4.4, from the work of Vacquie et al (4.17), shows an unusual peak in the high energy tail of the electronic energy distribution. This peak can be attributed to electrons accelerated across the target sheath (4.4). However, since there is a large peak in the spectrum at approximately 10 eV, it is legitimate to evaluate equation 4.3 with kT_e = 10 eV, whereupon we have

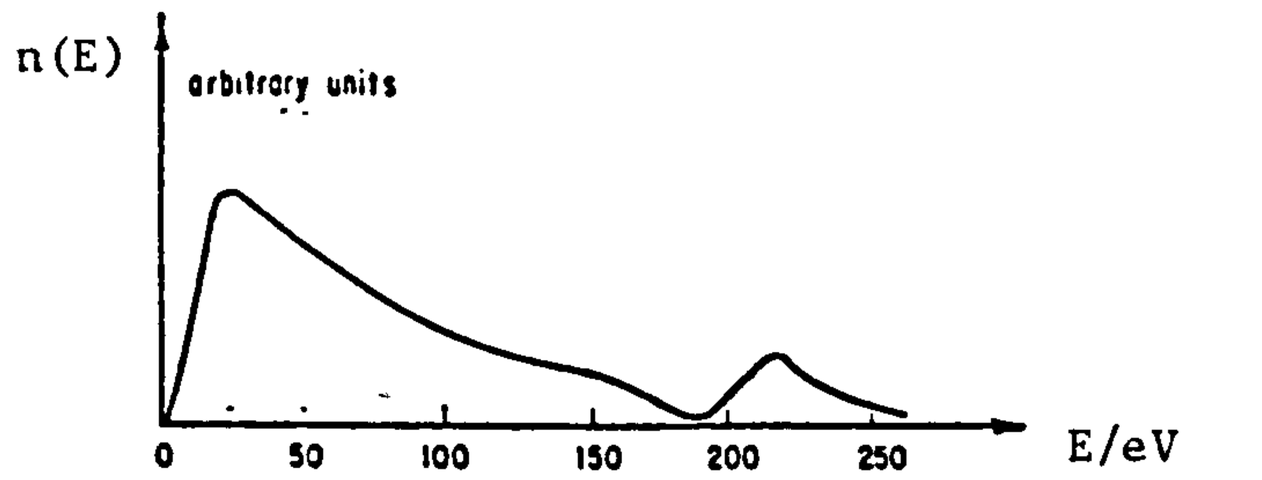

Fig.(4.4): Electronic energy distribution n(E) in a capacitive discharge (ref.4.17)

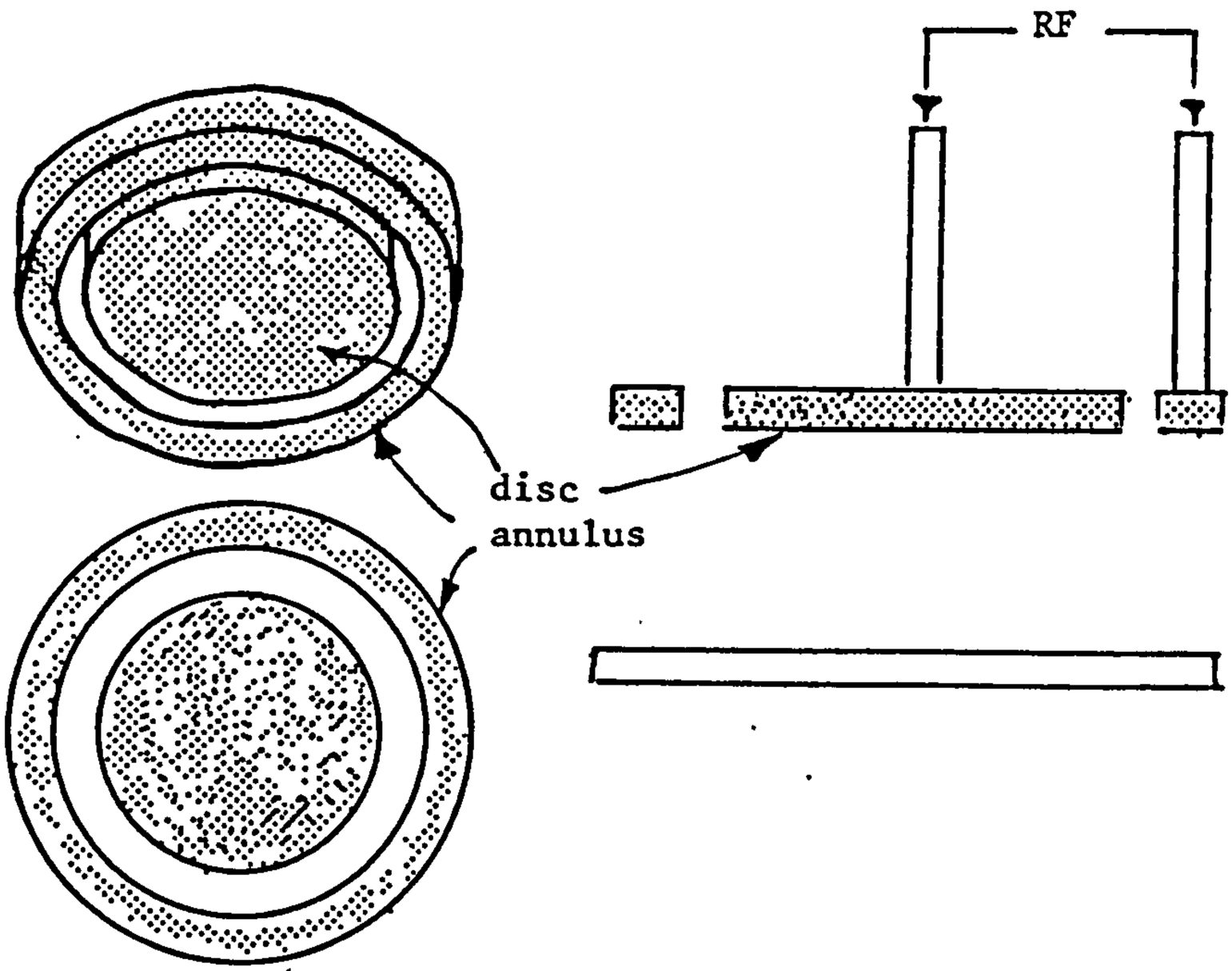

Fig.(4.5): Schematic diagram of the electrodes in the disc and annulus system.
The areas of the two electrodes are equal.

$$j/Am^{-2} = 0.024pV^{\frac{1}{2}} \qquad 4.4'$$

where $A_t = A_s = 0.014\ m^2$, $A_w = 0$, D = 0.05 m and f = 13.56 MHz have been used. We can combine this expression with equation 4.2' to yield a typical sheath thickness given by

$$d/mm = 0.6\left(\frac{V}{p}\right)^{\frac{1}{2}} \qquad 4.5$$

which for V=2 kV and p=0.8 Pa is about 30 mm. Observed sheath thicknesses are within 25% of this at an electrode p-p voltage of 4 kV. The validity of equation 4.3 is open to doubt, however, (4.14) and account has not been taken in its derivation of the practice of increasing the current density by superimposing a magnetic field on the plasma, as described in section 4.4. It is better, therefore, to use measured values of d as input parameters to equation 4.2' for calculation of ion current densities.

4.2 Bias sputtering

In the working pressure region there is a low probability of interaction between a sputtered particle crossing the chamber and a plasma ion, and the deposition is termed 'direct shot'. Diffusion processes begin to take over at about 1.3 Pa (4.34). However, the rate of film deposition is dependent not only on the emitted flux of sputtered particles from the target but also on the proportion of particles incident on the substrate which fail to bond to it, or the 're-emission coefficient'.

The work of Jones et al (4.18) shows that the re-emission coefficient of RF sputtered silicon can be reduced by biassing the substrate table positively, thereby increasing the deposition rate. The opposite would apply for negative biassing. This behaviour can be attributed to a reduction in the energy of the surface bombardment by plasma ions due to their repulsion by the potential on the substrate. It is uncertain whether this is the case for dielectric films. In fact, the structure of sputter-deposited films, that is their uniformity of density

and bonding to the substrate, is reported to be improved if they are sputtered to a small extent during deposition (4.20). A small negative bias is appropriate for this, which can be induced in the same way as described above, by diverting some of the RF power to the substrate table (4.35).

We have seen in Chapter 3 that the sputtering of multicomponent materials causes considerable compositional alterations to the surface, and therefore it is to be expected that a film deposited under bias sputtering conditions will have a composition different from that of the target. Although the design of the instrument to be described below includes a bias sputtering facility, our interest has been in the deposition of glass films, and consequently these considerations have militated against its extensive use.

4.3 Chamber design

The simple arrangement of components depicted in Fig. 4.1, a single target backed by a single electrode, and a substrate table connected directly to ground, is known as the 'grounded diode' system. This is a well studied and successful instrumental arrangement whose electrical characteristics are easily determined, as described in Chapter 5. Its name distinguishes it from the original experimental work, in which a separate pair of electrodes was used to initiate the discharge (4.20), which was known as the 'triode' system.

Fig. 4.5 shows a further arrangement in which the RF signal is applied to two electrodes in anti-phase, and sputtering takes place from both simultaneously (4.22). Known as the 'disc and annulus' system, it was developed by Holland, Putner and Jackson (4.21) and consists of two coplanar electrodes of equal area, each behaving as a separate sputtering discharge, the target material being attached to the surface of both.

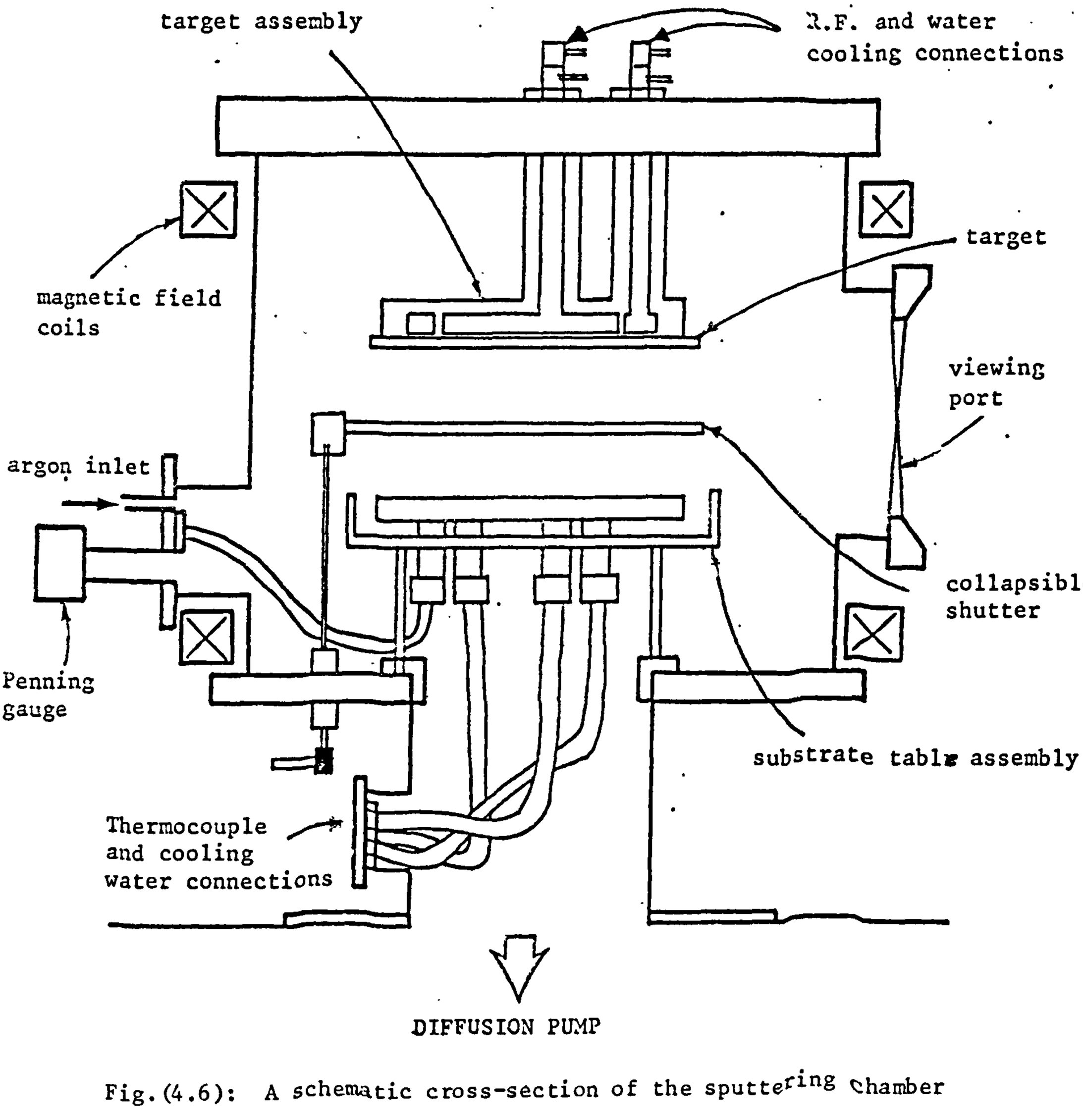

Fig.(4.6): A schematic cross-section of the sputtering chamber as photographed in the following figure.

In the case of dielectrics, a single piece of material can be used, but as will be seen, glass targets can cause difficulties. The disc and annulus arrangement has advantages over the grounded diode including its improved uniformity of deposition over a large area, and better ability to cover topographical discontinuities in the substrate, or 'throwing power'. Weathered mediaeval glass has a very uneven surface, and this led us to base our experimental equipment upon the disc and annulus system, but most of the design criteria discussed here will be relevant for all RF sputtering equipment. A scale drawing of the chamber is given in Fig. 4.6, and its features are described in the following sub-sections. The details of the construction of the electrodes are shown in Fig. 4.8 and Fig. 4.7 is a photograph of the apparatus in its operational state. The publication of a paper describing this work is pending (4.36).

4.3.1 Shielding

It will have been noted that no discharge can be sustained in a gap smaller than the sheath thickness d, and consequently, sputtering of the back of the electrodes can be eliminated if a grounded shield surrounds them, at a distance less than d. If the shield is too close, unnecessary power will be lost to ground through capacitive coupling; if is is too distant, the operating pressure and the magnetic field (increases in both of which reduce d) will be restricted in range, and the instrument will be less versatile.

A spacing of 6 mm was considered appropriate for reasons connected also with fabrication, and this is similar to the findings of other workers (4.9). The target assembly was designed so that all points at high RF potential are surrounded by a stainless steel shield with this spacing, as Fig. 4.8 shows.

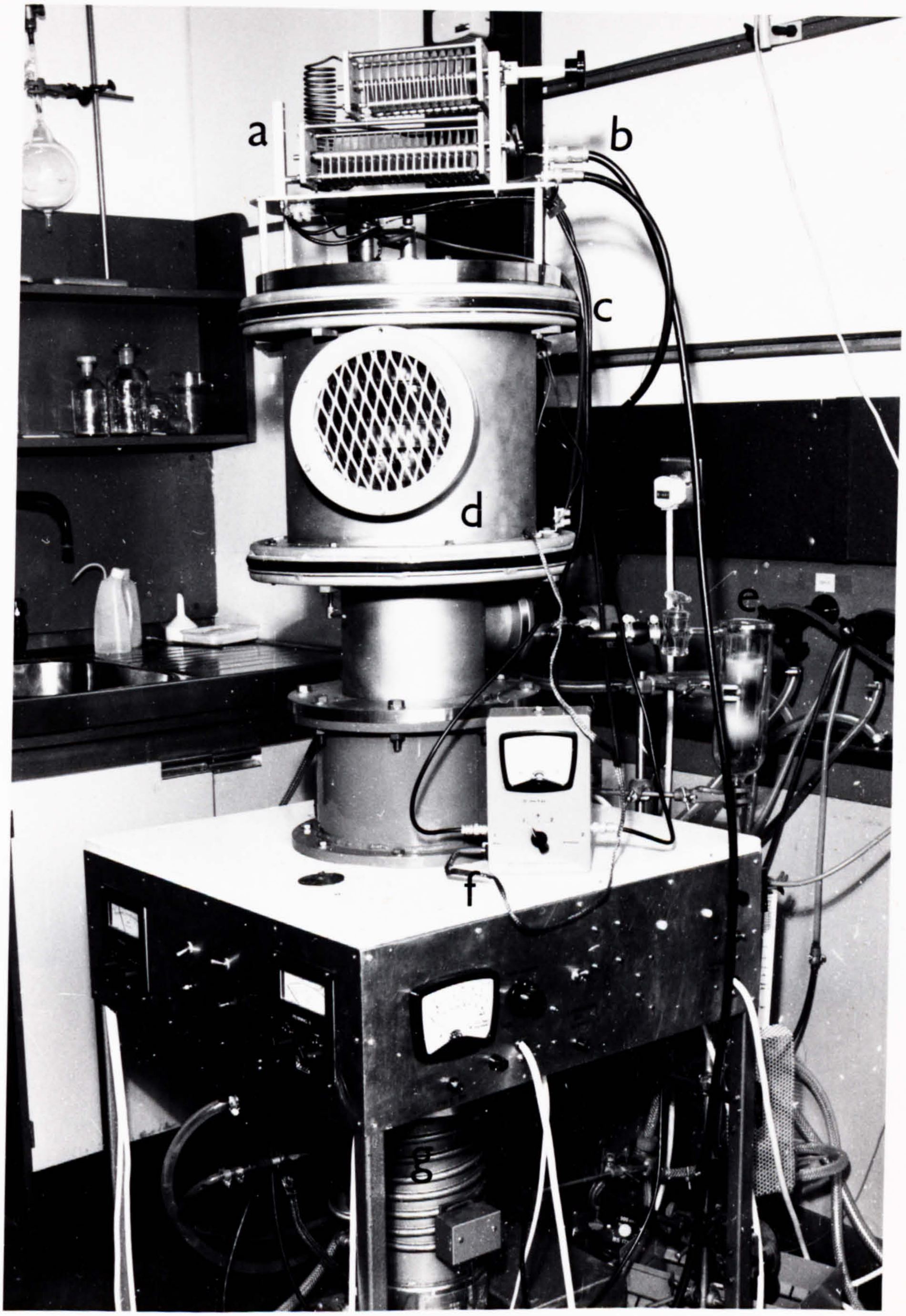
a
b
c
d
e
f
g

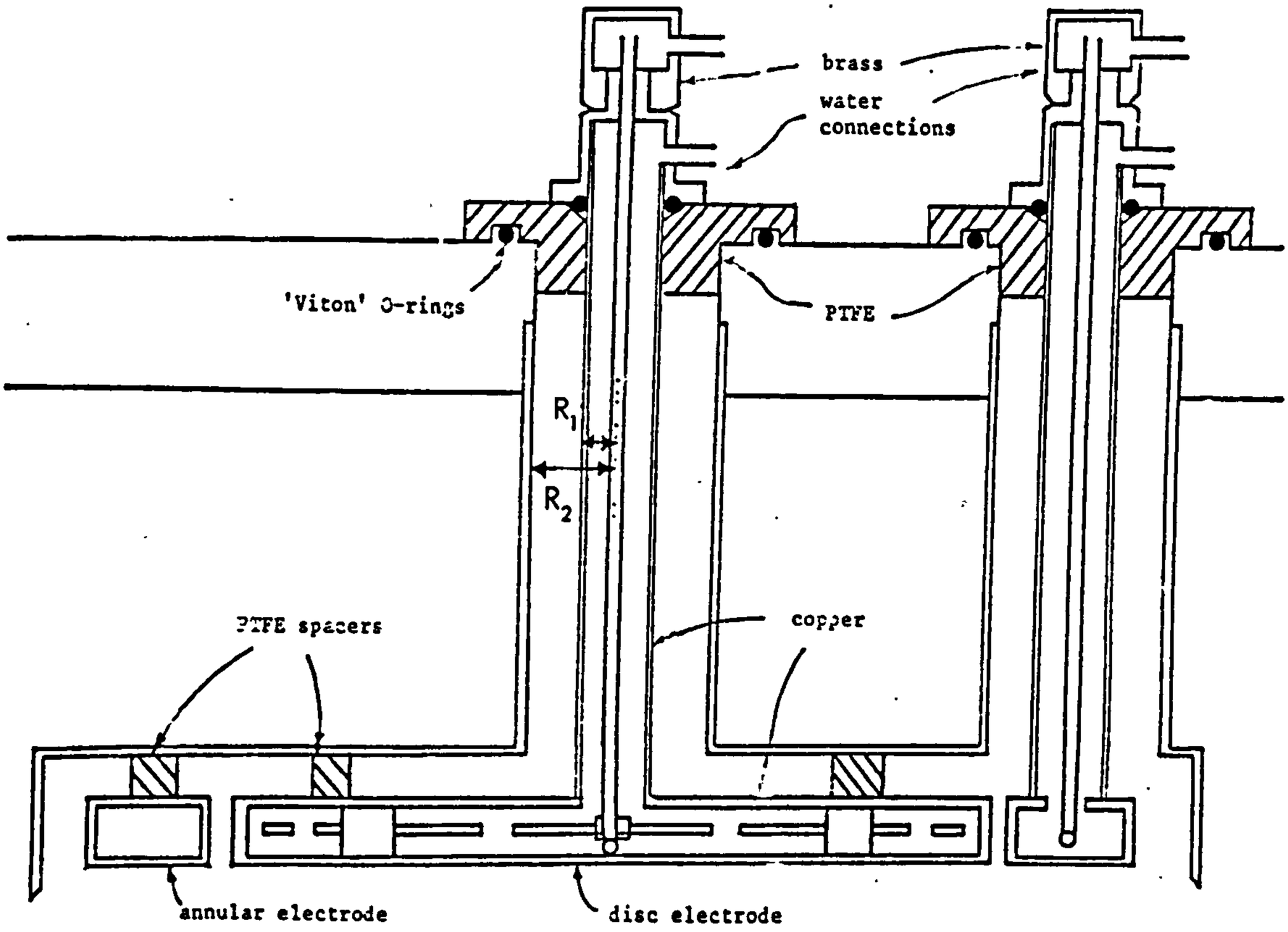

Fig.(4.8): Electrode assembly cross-section showing coaxial cooling water leads-through and electrode shielding. The RF connections are made to the brass electrode caps.

4.3.2 Electrodes

RF powers in the kW region are encountered in sputtering equipment, and the heat generated in various components is a continual source of difficulty. Water cooling of the electrodes is necessary in an attempt to prevent impedance changes caused by increases in temperature, to avoid deterioration of the vacuum leads through and to remove whatever heat is possible from the surface of the target.

As can be seen from Fig. 4.8, the whole of the interior of both electrodes can be flooded with water, with coaxial inlet and outlet. It was found adequate simply to use rubber hosing for the supply and drainage (not plastic), and baffles are fitted in the interior of the disc electrode to cause the water to circulate. A moderate flow rate of 15 mls^{-1} was used, at which no detectable increase in temperature occurred for input power levels around 1 kW. The assembly was fabricated from copper with brass fittings. Vacuum seals were made by the tightening of the water connection cap at the top of each electrode, the opposing force being provided by the PTFE spacers in the shield gap. It was not found difficult to ensure coplanarity of the flat surfaces of the electrodes.

4.3.3 Leads-through

The electric fields encountered in cylindrical high-voltage vacuum leads-through can be higher than the dielectric strengths of many materials. The field strength E(r) at a point in the dielectric, a distance r from the axis of the lead-through, is given from Maxwell's equations by (4.23):

$$E(r) = \frac{V}{r \ \ln(R_2/R_1)} \qquad 4.6$$

for $R_1 < r < R_2$, where V is the voltage at the central conductor of radius R_1, and R_2 is the outer radius of the lead-through. The maximum field occurs therefore at the surface of the conductor ($r = R_1$),

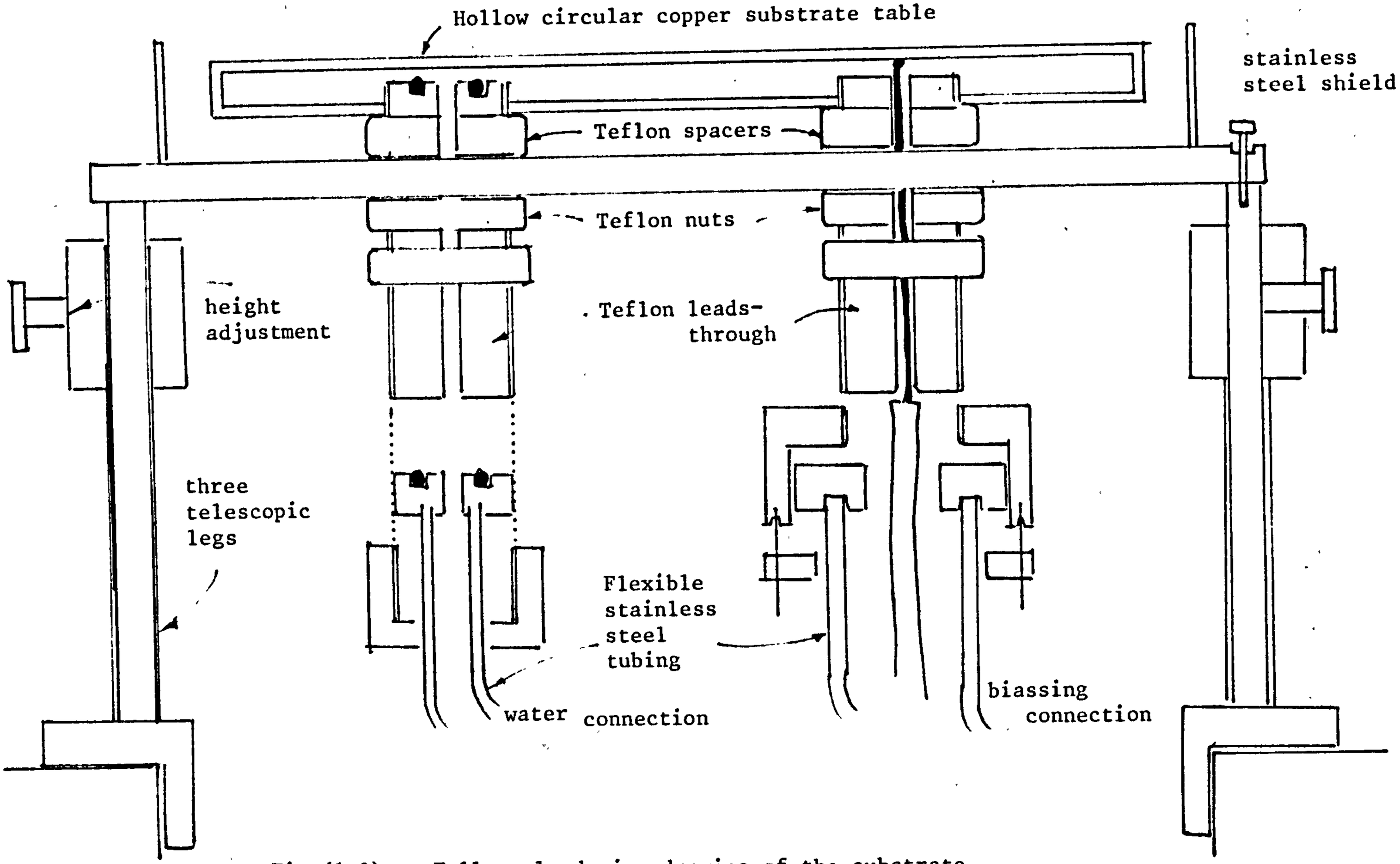

Fig.(4.9): Full scale design drawing of the substrate table assembly. One of the two water connections is shown, and the electrical biassing connection. The fourth teflon lead-through is used for the thermocouple.

and by differentiation with respect to R_1 it can be simply shown to be minimised if $R_2 = eR_1$, whereupon the dielectric strength required of the material becomes Ve/R_2. If two identical leads-through are to be mounted adjacent to one another, as required by the disc and annulus system, the outer radius R_2 is restricted to somewhat less than half their separation by the need to maintain the strength of the chamber wall; that is, R_2 can be no greater than about 20 mm. The material of a 20kV lead-through must therefore have a dielectric strength of greater than 2.7 $kVmm^{-1}$, despite the minimisation of the field occasioned by the ratio of radii, which renders unsuitable machinable glass ceramic and ordinary PTFE. A material strongly to be recommended is Polypenco PTFE, which not only has a 24 $kVmm^{-1}$ breakdown field, but also a low power factor (5×10^{-4}) and good machinability. It is quite inexpensive, and was satisfactory in this application.

Since the field reaches a minimum at $R_2/R_1 = e$, the effect upon it of small changes in R_1 and R_2 away from this relation is second order. The radii used were in the ratio $R_2/R_1 = 2.5$ (a 7% change), increasing the maximum field by only 0.24% from its smallest possible value.

4.3.4 Substrate table

We have noted that bias sputtering requires the substrate table to be insulated electrically from ground, and consequently it is also thermally isolated. During sputtering, energy is deposited in the table, mainly by secondary electron bombardment (4.27), causing its temperature to rise at a rate governed by the incident RF power. Deposition rates are reduced at elevated temperatures (4.3) and consequently cooling of the substrate table is advisable.

A cross-sectional view of a successful design is shown in Fig. 4.9; in plan view, the table is circular, in common with the chamber as

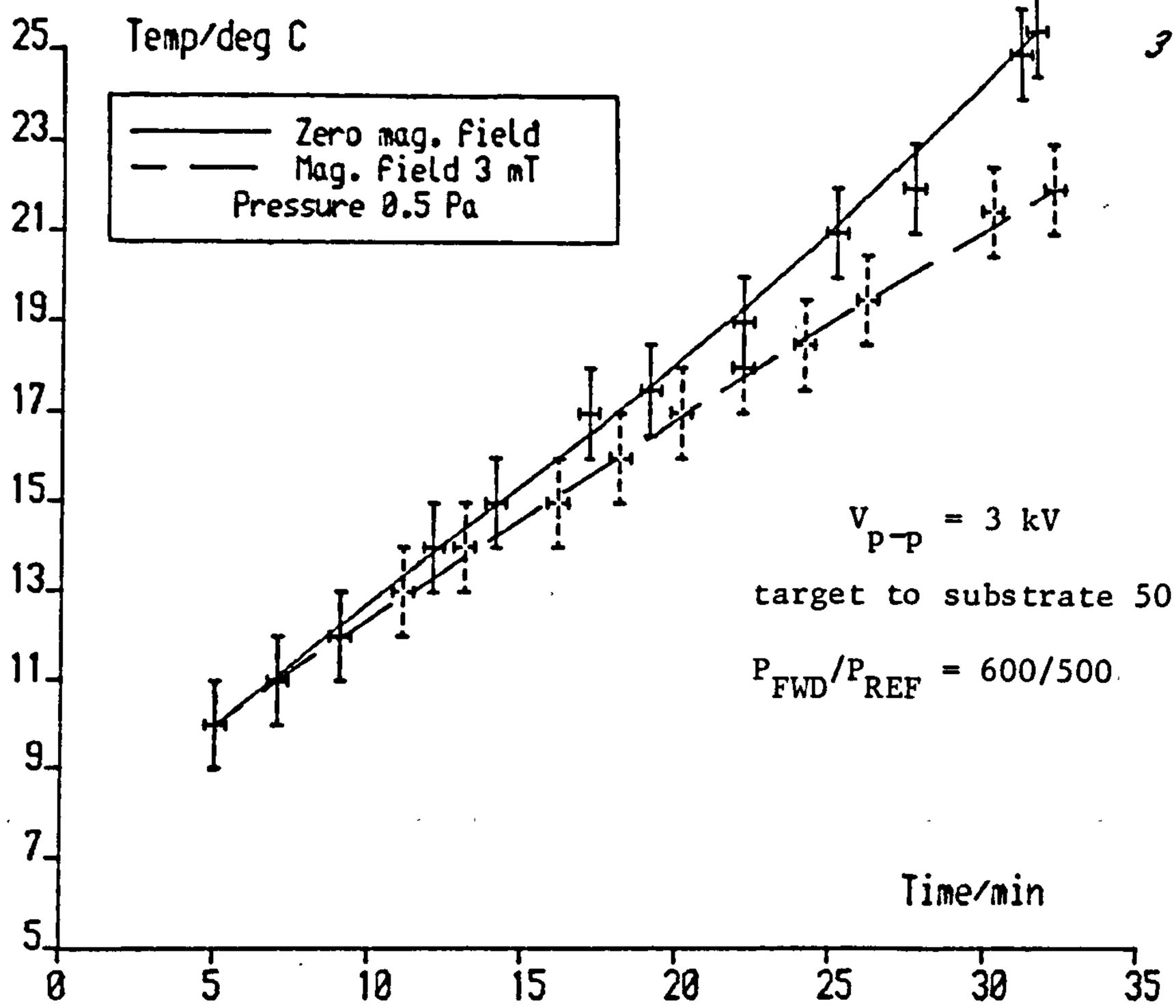

FIG(4.10): Effect of field on temp. of table

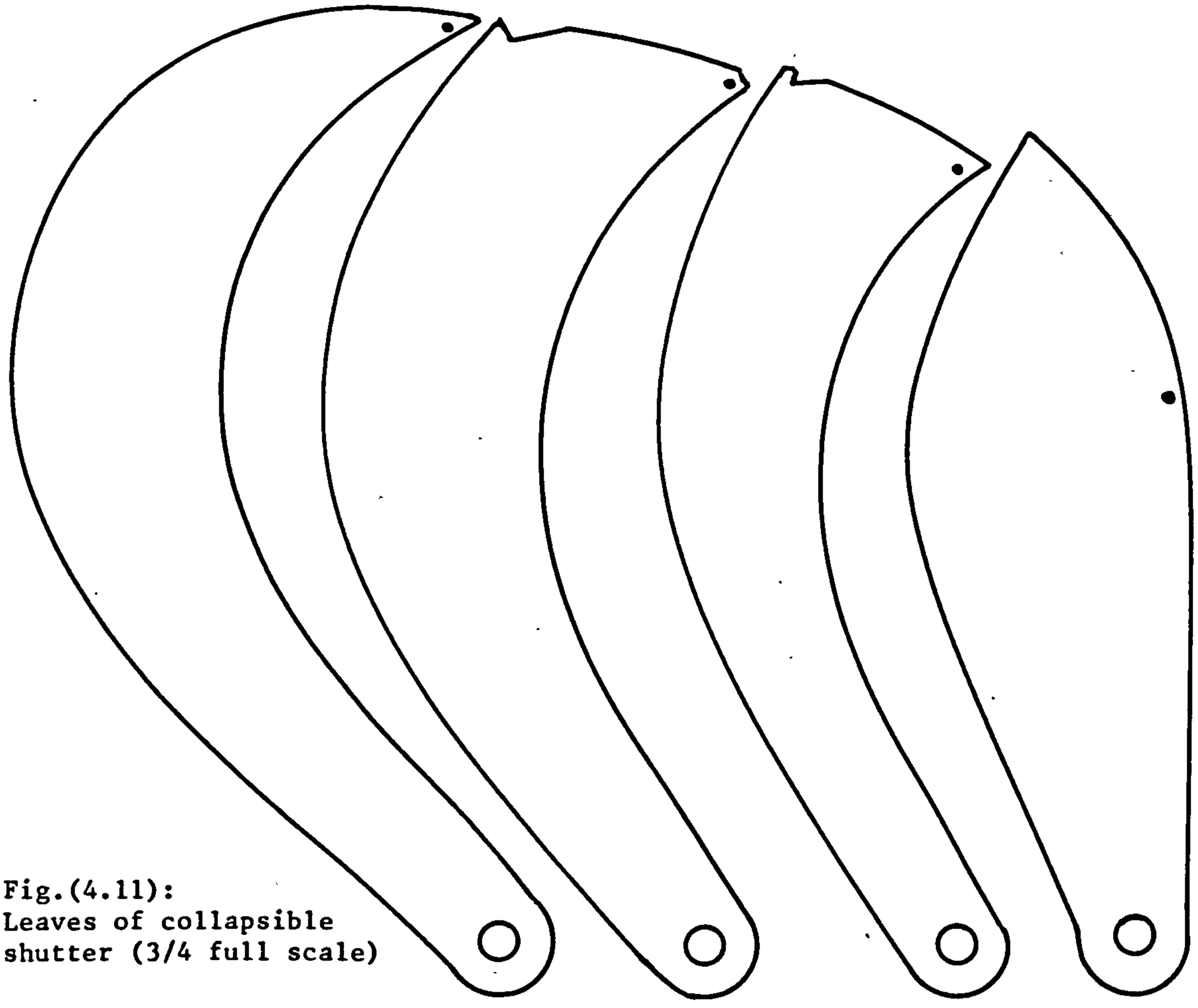

Fig.(4.11):
Leaves of collapsible
shutter (3/4 full scale)

a whole. Cooling water is admitted and discharged through two PTFE connectors which screw into brass sockets in the base, in which there is a hole for the passage of the water. The whole of the interior is flooded. Two other such fittings are available for the bias connections and a thermocouple. The vacuum seals are made by the compression of 'O' rings by the PTFE connectors. To permit bias sputtering, a shield is included around the perimeter, (required as described in section 4.3.1) and there is no gap large enough for a discharge beneath. Three telescopic legs support the entire assembly, which is mounted centrally in the chamber, and this enables the target-to-substrate distance (an important parameter in the electrical characterization of the discharge) to be varied continuously between zero and 100 mm. All connections to the table must hence be flexible, for which convoluted stainless steel tubing was used successfully.

With the flow of cooling water stopped, the graph of temperature of the substrate table against time of discharge shown in Fig. 4.10 was obtained, with the other conditions shown in the figure. The thermal capacity of the table (containing water) is approximately 5.2 kJK^{-1}, hence the power reaching the substrate table can be calculated to be close to 52 W. Substrate table heating is probably the major process of energy dissipation, and the results of this type of experiment are comparable with RF powers measured using commercial equipment, to be described in the next chapter.

Fig. 4.10 shows also that the effect of a magnetic field upon the discharge is to reduce energy loss from the plasma to the table. This is because the lengthening of the trajectories of the secondary electrons caused by the field, increases the probability of collision during their passage from the target, and hence attenuates the energy incident upon the substrate table per unit time.

Difficulty encountered in fabrication was circumvented by milling the lower half of the disc from solid brass, and welding a flat copper lid in place, with a central boss to prevent the lid from deformation due to the large pressure difference.

4.3.5 Shutter

To facilitate adjustment of the conditions of the particular sputtering run after the discharge has been struck, and to allow the sputtered flux sufficient time to achieve its stoichiometric composition, it is invaluable to include a shutter between target and substrate table to be opened to commence deposition when conditions are stable and correct.

Since both target and substrate assemblies have a diameter greater than one third of that of the vacuum chamber, and are mounted centrally in it, there is insufficient space for a solid shutter to be swung aside in its own plane. Fig. 4.11 illustrates a successful design, in which the area to be covered is divided into four segments which collapse fan-like into a configuration occupying a position between the chamber wall and the perimeter of the substrate table. The stainless steel segments are mounted on a telescopic shaft attached to a rotary vacuum lead-through in the base of the chamber, which was designed and manufactured according to customary vacuum practice. The shutter could be operated by a single movement.

This design was found adequate for its purpose, except that the electrical characteristics of the discharge are altered slightly on opening the shutter, and in consequence it is necessary to change the power matching conditions during the deposition of a film. Usually, this process is brief compared with the total time taken, so consistent conditions can be achieved, and the problem is not serious.

It is not clear whether, for example, a dielectric shutter would have a similar drawback, but since the volume, configuration and area of

contact of the plasma would still be affected, it is probable that the difficulty is insurmountable.

4.3.6 Viewing window

The design of a viewing window is complicated only to the extent that the thickness of the glass should be sufficient to withstand the pressure, and that it should not obstruct the field coils. The minimum thickness (T) required of a flat Pyrex disc of diameter D to enable it to withstand a pressure difference of p is given from reference 4.33 by the equation:

$$T = 2.086 \times 10^{-4} \sqrt{p/Pa}\ D \qquad 4.10$$

which becomes, at atmospheric pressure:

$$T = 0.0664\ D \qquad 4.10'$$

Ignorance of the above equation resulted in the chamber being damaged by the implosion of a 6.3 mm thick window spanning 170 mm. Subsequently, however, a 12.7 mm soda glass disc was employed successfully, and equation 4.10' can be regarded as approximately true for ordinary glass.

It is advisable to reduce the localised stress on the glass by using rubber O-rings, on both inside and outside surfaces. The window is contained by an aluminium ring secured by six bolts to the flange on the chamber.

4.4 Magnetic field coils

Mention has been made in preceding subsections of the magnetic field superimposed on the sputtering plasma. Its effect upon the ions is negligible, but the Lorentz force perpendicular to the direction of motion of the electrons causes them to spiral, increasing the probability of ionising collisions with gaseous atoms (4.2), and reducing the number lost from the plasma. The ion current density incident on the target thereby

rises, as do its concomitants, the sputtered flux density and deposition rate. The RF sheath is diminished in thickness according to equation 4.2.

In addition to the reduction of substrate surface heating described in subsection 4.3.4, the magnetic field can be shown to contain the plasma to the surface of the target, to stabilise the discharge, and to increase the uniformity of the deposited film. Paradis (4.24) reports that axial fields are more satisfactory in sputtering applications than transverse or quadrupole ones.

It is obvious that the coil cannot be mounted in the centre of the chamber because of the window, and a uniform field cannot therefore be produced by a single coil. Two field coils separated by their common radius R (in Helmholtz configuration) each of N turns, carrying a current I produce an induction B given by:

$$B = \left(\frac{4}{5}\right)^{3/2} \mu_o \frac{NI}{R} \qquad 4.7$$

$$B/mT = 9 \times 10^{-4} \ \frac{NI}{R} \qquad 4.7'$$

where I is in A, and R in m. The field required is moderate ($B \approx 10$ mT) but equation 4.7' shows that two coils of radius 0.2 m and of 200 turns each must draw over 11 A, and that the total heat generated W (kW) in their windings is given by:

$$W = IV = 1.1 \ \times \ \frac{BRV}{N} \qquad 4.8$$

where V is the driving voltage across the coil pair.

Most available power supplies capable of producing sufficient current will be of fixed output voltage, but if, for example, the coils specified above were operated at 250 V, each would be required to dissipate energy at a rate of 1.375 kW, which would be quite impossible except in the very short term.

Clearly, the generation of heat in the windings is reduced by increasing N, and it is at this point that the economics of coil design are best considered. Unless it is very finely drawn, copper wire is of a price proportional to its cross-sectional area a, and hence the cost of each field coil is determined principally by the total cross-sectional area of the wire, Na. (The cross-sectional area of the whole winding must, by simple geometry, be greater than $2\sqrt{3}\ Na/\pi$).

4.4.1 Coil winding

If the product Na is to be minimised (to bring down the expense) and N maximised (to reduce the heat generation) it is clear that the diameter of the wire should be as small as possible, with the limitation that the tensile strength should be sufficient to avoid breaking of the wire during winding. Polyurethane insulated copper wire of 0.71 mm diameter was found reasonably satisfactory in the water-cooled design described below, and probably a narrower gauge wire still would have been an improvement.

The 340 turn coils were wound on aluminium alloy channel using a slowly turning glass-blowers lathe. Aluminium cooling pipes were previously welded to two sides of the channel, as can be seen in the photograph of the entire chamber, Fig. 4.7.

4.4.2 Temperature distribution

The distribution of temperature inside rectangular windings has been studied analytically by Cockcroft (4.28) for the case of known uniform surface thermal resistance, and by Higgins (4.29) for coils operating at constant current, with their entire surface at a single temperature. Neither of these treatments is applicable to coils of large diameter but small cross-section and in our case three faces of the coil are cooled, and the fourth allowed to rise in temperature.

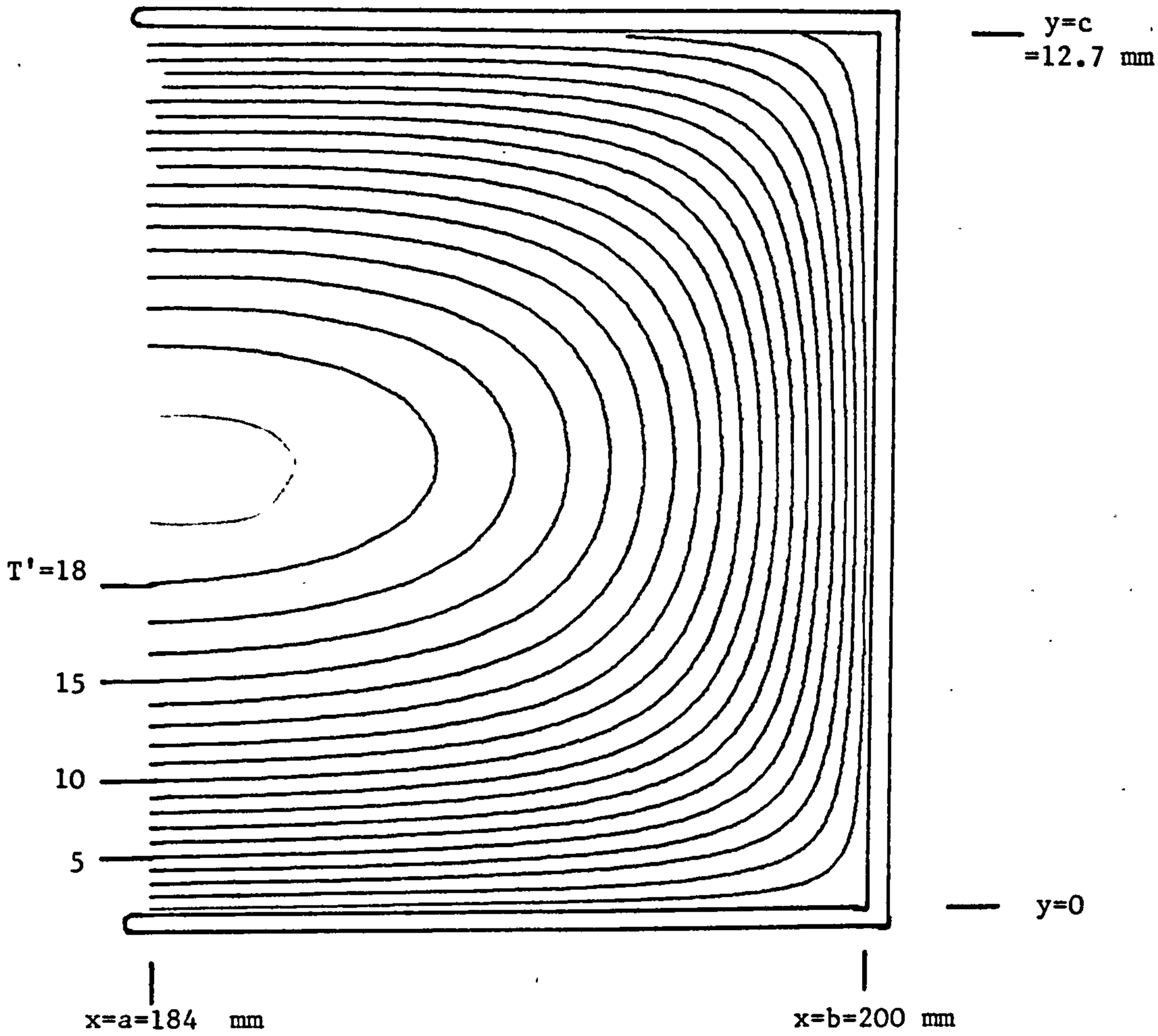

Fig.(4.12): Isothermal contours inside field coils

The temperature parameter is $T' = (\kappa/H)\ T$ in units of $10^{-6}\ m^2$

Using $\kappa = 0.63\ Wm^{-1}K^{-1}$ as discussed in the text, the temperature can be read from the diagram as $T = (H/\kappa)\ T' = 1.59 \times 10^{-6}\ HT'$ where H is in Wm^{-3}. If, for example, Joule heating occurs at a rate of 3 MWm^{-3}, the temperature in the winding, above that of the frame will be given by:

$$T(x,y)/^{o}C = 4.77\ T'(x,y)$$

The temperature T(x,y) in a body of thermal conductivity κ, in which heat is generated at a rate H per unit volume, is given by (4.30):

$$T(x,y) = \frac{Hy(c-y)}{2\kappa} - \frac{4c^2H}{\kappa\pi^3}\sum_{n=0}^{\infty}\frac{F\left\{(2n+1)\frac{\pi a}{c}\ ,\ (2n+1)\frac{\pi x}{c}\right\}\sin\left\{(2n+1)\frac{\pi y}{c}\right\}}{F\left\{(2n+1)\frac{\pi a}{c}\ ,\ (2n+1)\frac{\pi b}{c}\right\}\qquad(2n+1)^3} \qquad 4.9$$

with:

$$F(p,q) = I_1(p)K_o(q) + K_1(p)I_o(q) \qquad 4.9a$$

where the body is bounded in the radial direction by $a < x < b$, and in the vertical direction by $0<y<c$, and where the boundary at x=a allows no heat flow, and the other three faces are maintained at T=0. See Fig. 4.12. These boundary conditions are appropriate if cooling of the surface at x=a by radiation and convection is neglected, and if good thermal contact between the winding and the metal frame is assumed. The functions I and K are modified Bessel functions, in the usual notation, of order indicated by subscripts. The isothermal contours shown in Fig. 4.12 were computed using polynomial approximations (4.31) with the parameter H/κ as a scaling factor. The maximum temperature is seen to occur at the centre of the outer face, as would be expected, since the sum of the distances from the walls is greatest at that point.

The value of κ is unknown a priori, but an iterative procedure by which it can be found is as follows:

(i) calculate the resistance of the coil from standard tables (4.32).

(ii) calculate the Joule heating per unit volume per unit time (H) assuming a constant supply voltage and dividing by the volume of the winding (which is approximately $4\sqrt{3}$ NaR).

(iii) Use H and an ansatz value of κ to compute a temperature distribution from equation 4.9.

(iv) For annuli of small cross-section (compared with that of the coil) compute an average temperature and hence a new resistance using tables of temperature coefficients (4.32). An annulus cross-section of 1 mm^2 is satisfactory.

(v) Sum the resistances of the annuli to find a new total coil resistance taking into account the average number of wires per annulus.

(vi) Use the new resistance to find a new H, and the current flowing.

(vii) Iterate until convergence is reached.

The difference between the value of the current on which this routine converges and an experimental steady-state value will yield an estimate of the accuracy of the initial choice of κ. If the current at convergence is lower than the experimental one, then the theoretical temperatures are too high, and the value of κ should be increased. The re-scaling can easily be incorporated in a further iteration loop, and the value of the thermal conductivity required to equalise the predicted current after the convergence of the first part of the program, and the experimental final steady-state current, can be found.

Our first experimental coils, wound from 1 mm diameter (SWG 21) wire, passed a steady current of 9.0 A and the program converged on this current when the thermal conductivity was 0.63 $Wm^{-1}K^{-1}$. Using this value of κ, the maximum predicted temperature was 150°C, which was confirmed by the quick burning out of the coils, because this is 30°C above the limiting temperature of the insulation. It is shown in Appendix VI, also, that the diameter of the wire has no first order effect upon the diffusion of heat in the windings of the coil, and hence

the result for the thermal conductivity is general for all coils wound from polyurethane coated copper wire. The distribution of temperature of Fig. 4.12 is particular to a coil of the dimensions shown, however.

4.4.3 Control circuit

The magnetic field applied to the discharge may be varied by controlling the current through the coils. We have seen that currents can be as high as 10 A, which makes simple resistive current limiters inappropriate.

A triac-controlled chopping circuit developed for the purpose is shown in Fig. 4.13. Current from the mains supply is passed through a power triac whose triggering level is adjusted by means of a potentiometer. The waveform is chopped, as shown in the figure, and the average current is hence controlled. All the components of this circuit are inexpensive and easily obtainable, and it satisfactorily regulates currents up to 12 A. The self-inductance of the load, which sometimes disables similar circuits, is only a few μH, and is not a source of difficulty.

It will be noted that the coils are connected across a high power silicon bridge rectifier. The enormous disparity in frequency between the oscillations of the electrons and that of the mains is such that an AC field could be used for sputtering purposes, but the rectifier was included to permit calibration of the field by a DC magnetometer. The effect of using smoothed DC was not established because of the difficulty attaching to the smoothing of a 10 A supply at 200 V. It is unlikely that the behaviour of the discharge would be any different using smoothed DC than in the case of an AC field increased by a factor of $\sqrt{2}$.

Magnetic fields induced were within 5% of those predicted by equation 4.7 despite the chamber design not quite allowing a Helmholtz spacing. The effect upon the field of the stainless steel of the chamber was negligible.

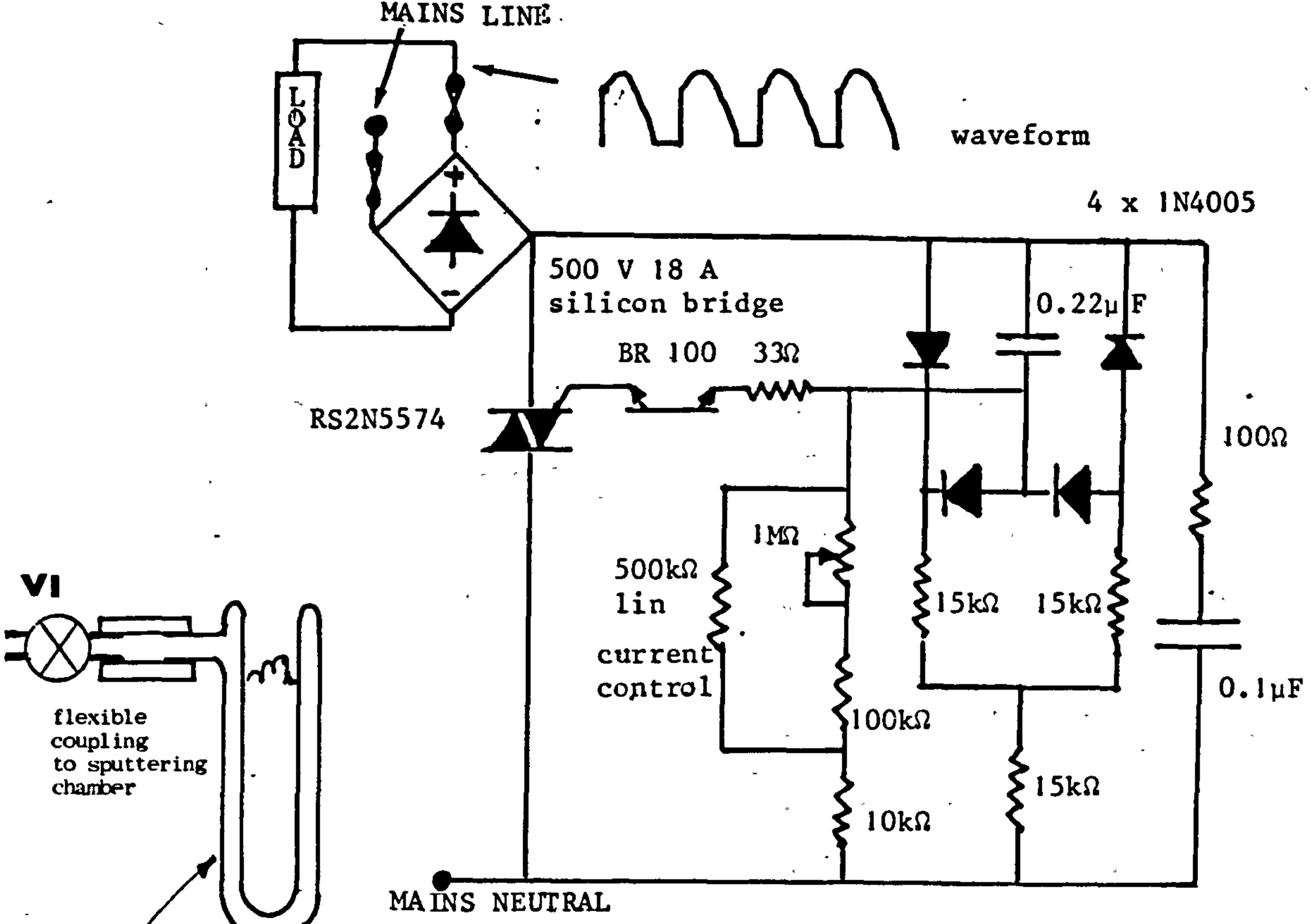

Fig.(4.13): Circuit for limiting current in field coils. RS component codes used.

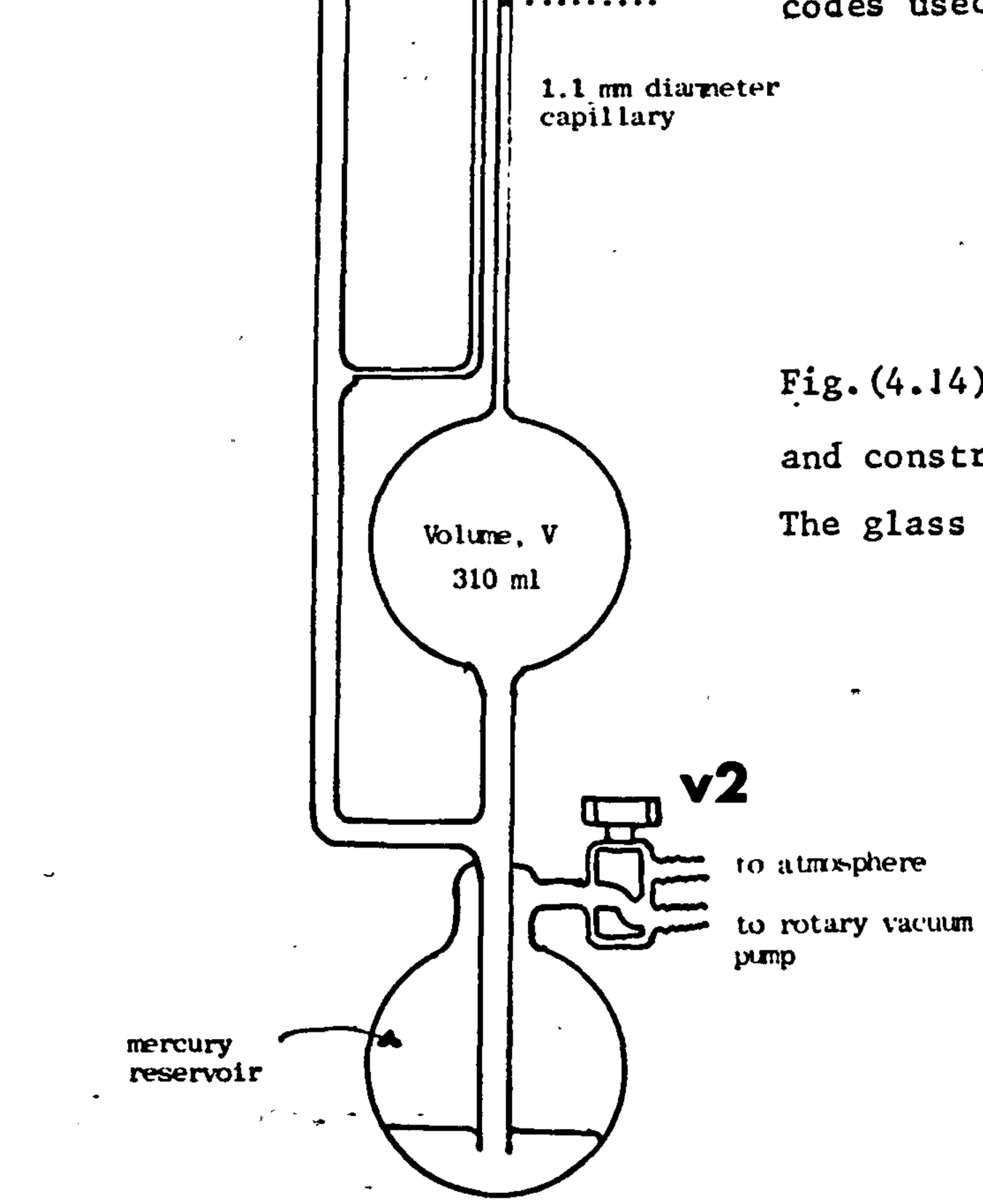

Fig.(4.14): The McLeod gauge designed and constructed for the project. The glass was blown by S. Moehr

4.5 Vacuum pumps

A rotary pump is used for roughing out the chamber and for backing the diffusion pump, in the usual manner. The Edwards High Vacuum 850W mercury vapour pump employed has a 150 mm inlet, contains a charge of 200 ml of mercury, and could achieve pressures of 10^{-4} Pa in about 6 hours. It was not always considered necessary to evacuate the chamber to a pressure as low as this; 10^{-3} Pa (obtainable after ~1 hour) was sufficient for most purposes.

The chamber must be evacuated to a pressure very much lower than that of operation to ensure the purity of the discharge gas. Residual oxygen can be occluded in films, or combine chemically with freshly exposed surfaces, affecting the stoichiometry of the film.

4.6 Pressure measurement

The measurement of pressure is a somewhat imprecise exercise. No single gauge is capable of measuring from atmospheric pressure ($\sim 10^{5}$ Pa) to ultrahigh vacuum ($\sim 10^{-8}$ Pa) because a different mode of operation is appropriate according to the pressure regime. A logarithmic scale is universally used because of the enormous range.

4.6.1 Commercial gauges

Equipment is commercially available for measuring pressure, and no great sophistication is required for sputtering purposes. In the pressure range from atmospheric to 10 Pa, an Edwards Vacuum Pirani 14 gauge was used, and and Edwards Vacuum Penning 8 (with a CP25 head) was used for the range from 1 to 10^{-6} Pa (10^{-2} to 10^{-8} mbar). The scale of this instrument was multiplied by 0.7 for use with argon, since it is calibrated for air.

The Penning gauge operates by measuring the conductivity of a small discharge struck in a strong magnetic field: conditions unfortunately very similar to those obtaining in the sputtering plasma.

The RF fields interact with the gauge head, rendering it unusable during sputtering. Stray RF signals superimposed on the mains supply (or earthing leads) may be an additional source of interference.

4.6.2 McLeod gauge

It is of paramount importance to maintain a steady pressure in the chamber during deposition since the impedance of the discharge, the ion current density, the atomic re-emission coefficient and the RF sheath thickness are all connected more or less directly to the pressure. For this reason, and because of the unreliability of the electronic gauges during discharges discussed above, a McLeod gauge was constructed (whose operation is entirely mechanical) for use in the pressure region 0.1 to 10 Pa. Fig. 4.14 shows the arrangement and the nomenclature. The bulb of volume V contains gas admitted through valve V1 at the pressure of the chamber. Air is admitted through V2 causing the mercury in the reservoir to rise, compressing the gas in the bulb into a length h of the capillary until the mercury in the reference side-arm (of the same diameter to avoid a difference in capillary action) has risen to the top, as shown in the figure. The pressure above the mercury in the capillary is h Torr (by the definition of Torr), and the pressure p of the chamber is written:

$$p(V + ah) = h.ah \qquad 4.11$$

where a is the cross-sectional area of the capillary, of diameter D. Directly for $ah \ll V$,

$$h = \frac{2}{D}\sqrt{\frac{Vp}{\pi}} \qquad 4.12$$

and it is seen that the height is proportional to $\sqrt{p}$. A pressure of 0.5 Pa is expressable as $p = 3.2 \times 10^{-3}$ mmHg, and for a capillary diameter of 1 mm, we have from equation 4.12,

$$h/mm = 0.06\sqrt{V} \qquad 4.12'$$

and it can be seen that a bulb capacity of about 400 ml is required if h is

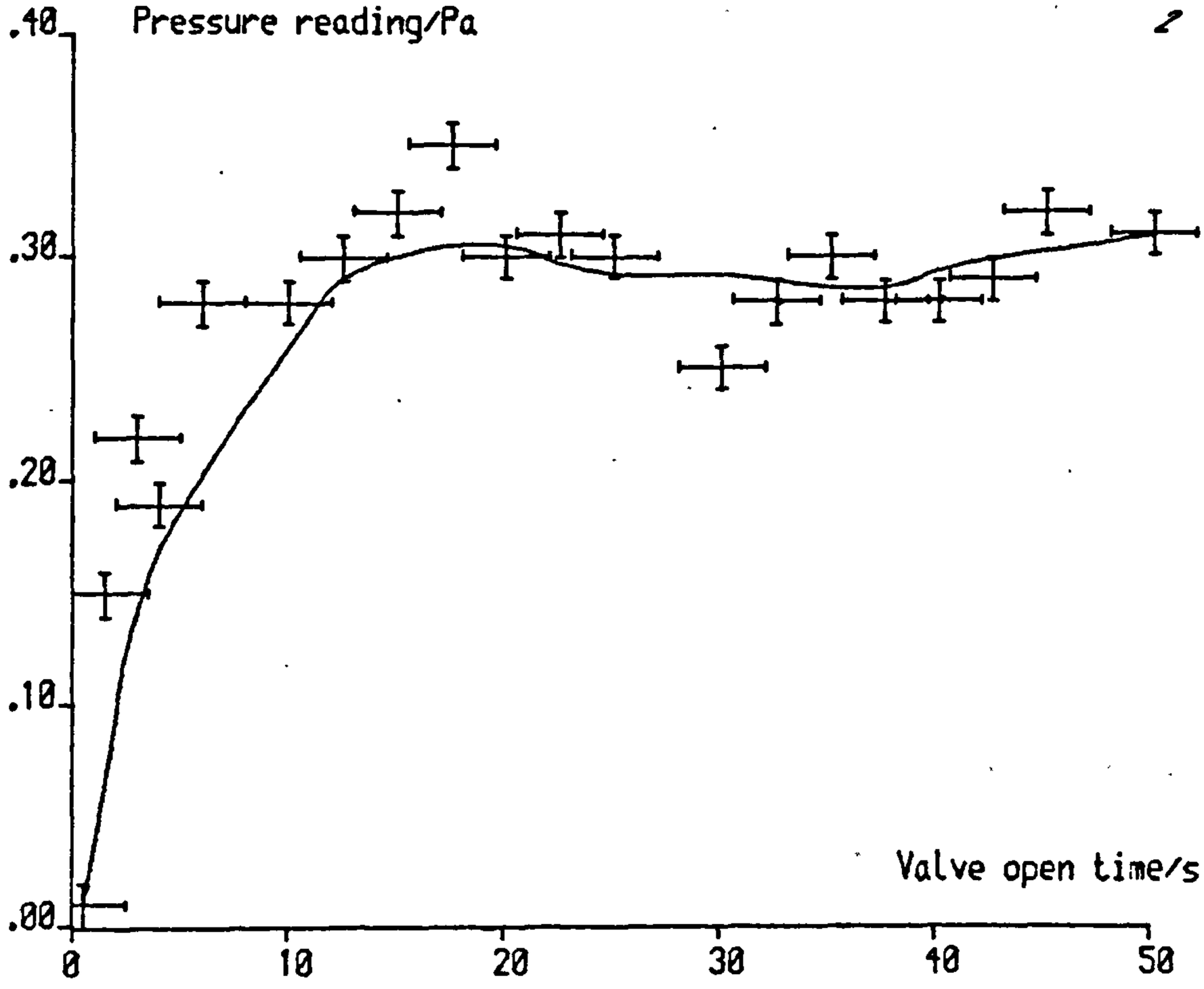

FIG(4.15):McLEOD GAUGE READING AGAINST TIME

to be large enough to read (~40 mm) at working pressures.

The sensitivity, s is given by

$$s = \frac{dh}{dp} = \frac{1}{D}\sqrt{\frac{V}{\pi p}} \qquad 4.13$$

which, using the bulb and capillary sizes instantiated above, is about 6 mm per mTorr (or 48 $mmPa^{-1}$), at a pressure in the centre of the working range, 0.5 Pa. Thus, it is seen that the scale must be about 50 mm long for RF sputtering purposes.

A McLeod gauge was constructed in the laboratory according to these design equations, with V = 310 ml, and D = 1.1 mm, and was found to be successful. A graph of pressure reading against time after opening the inlet valve (V1) is shown in Fig. 4.15. The bulb was evacuated prior to taking these readings. The pressure reading obtains its steady value only after about a minute, but a reading within 10% of the final value can be obtained after only 10 s. In normal circumstances, of course, the flow of gas will not be as great since the bulb will be already full of gas at approximately the same pressure as the chamber, but this experiment establishes the instrument's characteristic time constant.

The gauge must be very well supported, as the 300 ml of mercury required weighs over 4 kg, and is caused to accelerate abruptly from the reservoir to the bulb. A liquid air vapour trap is indispensable.

With practice, a pressure reading may be obtained in about 10 s, if the valve V1 is left open throughout. The accuracy of pressure readings made in this way may be estimated at $\pm$ 0.05 Pa, and the readings are very consistent with the Penning gauge, when there is no RF discharge.

4.7 Summary

The principles of RF sputtering have been presented and a number of equations given pertinent to the design and construction of an RF sputtering chamber. Some of the features of the York rig have been described.

The following chapter will deal with the problems attaching to the generation of RF power and its transmission to the sputtering plasma, and the performance of the entire apparatus will be discussed in Chapter 6.

CHAPTER 5

RF POWER GENERATION AND TRANSMISSION DESIGN

The main features of an RF sputtering vacuum chamber have been described, and attention must be turned to a discussion of the generation of RF power and its transmission to the chamber. The rate of sputtering varies approximately linearly with the power reaching the discharge (4.2) and hence it is this parameter, the power at the working frequency entering the plasma, which is of central concern.

The first two sections will discuss the design of RF generators, the problems involved in matching the power to the load will be considered in the second two, and finally the experience gained in connection with the measurement of RF power and voltage will be described.

Excellent references for all problems encountered in the design of circuits operating in the radio frequency region are the venerable text by Terman (5.1) which, unfortunately, is no longer in print, and can be difficult to obtain, and that by Johnson (5.2) who treats comprehensively power transmission problems at all frequencies.

5.1 RF power oscillators

Most generator units for use in sputtering systems operate at an output power level of around 2 kW, which necessitates heavy duty components. Simple circuits are preferable, and a triode valve is usually employed in place of the tetrode or pentode found in the more sophisticated designs appropriate at lower power levels.

One method of generating RF power is simply to amplify the output from a crystal oscillator to a level appropriate for sputtering. This would convey the advantages aver the self-excited oscillator of greater stability of frequency against alteration in load conditions, increased simplicity of analysis, and greater efficiency. However, the self-excited

power oscillator is more common, having a capital cost per kW of less than half that of the crystal controlled type (4.22), at the lower end of the power scale, and is entirely satisfactory in sputtering applications. The discussion will be limited to this type.

5.1.1 Theory of self-excited oscillators

It is necessary briefly to discuss the operation of simple amplifiers, such as that shown in Fig. 5.1, before the oscillator can be satisfactorily explained. The amplification factor μ and the impedance ρ of a valve are defined by the equation for the anode current:

$$I_a = \frac{1}{\rho} (V_a + \mu v_g) \qquad 5.1$$

where V_a and v_g are the anode and grid voltages respectively. The alternating part of the anode voltage is clearly given by $-I_a Z_L$ (subtracting the DC supply voltage V_b) and hence for AC signals, from equation 5.1:

$$\rho I_a = -Z_L I_a + \mu v_g$$

$$I_a = \frac{\mu v_g}{Z_L + \rho} \qquad 5.2$$

In consequence, the AC equivalent circuit can be drawn as shown in Fig. 5.2, treating the valve as a voltage source of magnitude $-\mu$ times the input grid voltage, the 180° phase shift being included to account for the direction of I_a. The open circuit gain of the amplifier, defined as the ratio of output to input voltages, can therefore be written:

$$A = \frac{V_o}{v_g} = \frac{I_a Z_L}{v_g} = \frac{-\mu Z_L}{Z_L + \rho} \qquad 5.3$$

and if a fraction β of the output voltage is added to the input signal v_g through a feed-back network, the gain becomes (5.4):

$$A_f = \frac{V_o}{v_g + \beta V_o} = \frac{A}{1 + \beta A} \qquad 5.4$$

which goes to infinity when the 'loop-gain' is given by:

$$A\beta = -1 \qquad 5.5$$

An infinite circuit gain implies that there will be an output signal for zero input signal, which is the primary requirement of an oscillator. Indeed, equation 5.5 is the 'Barkhausen criterion' for sustained oscillations which every oscillator must satisfy.

The feed-back network can be a simple voltage divider as shown in Fig. 5.3 with component reactances X_1 and X_3, in which case the feed-back ratio is written:

$$\beta = \frac{X_1}{X_1 + X_3} \qquad 5.6$$

and the total load on the plate, Z_L, is given by:

$$\frac{1}{Z_L} = \frac{1}{i(X_3 + X_1)} + \frac{1}{iX_2}$$

$$Z_L = \frac{-X_2(X_1 + X_3)}{i(X_1 + X_2 + X_3)} \qquad 5.7$$

The Barkhausen criterion (equation 5.5) can then be written from equations 5.3, 5.6 and 5.7, in the form:

$$\frac{\mu X_1}{X_1 + X_3} = 1 - \frac{i(X_1 + X_2 + X_3)\rho}{X_2(X_1 + X_3)} \qquad 5.8$$

whence it is seen that the single imaginary term must vanish. The reactances required for self-excited oscillators are hence determined by the simple equation:

$$X_1 + X_2 + X_3 = 0 \qquad 5.9$$

and the components must either be two capacitors and an inductor, in which case the circuit is of 'Colpitt's' type, or two inductors and a capacitor, when it is a 'Hartley' oscillator.

Considering, for illustration, the Hartley arrangement of Fig. 5.4, equation 5.9 becomes

$$\omega(L_1 + L_2) - \frac{1}{\omega C} = 0 \qquad 5.9'$$

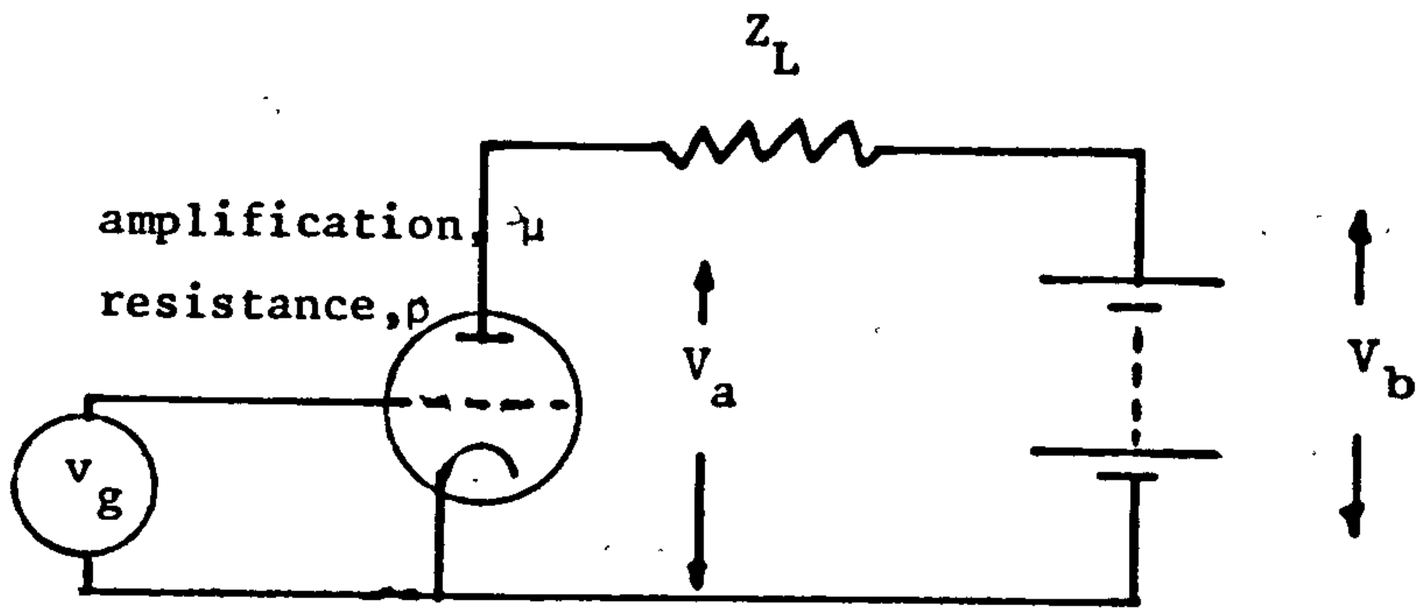

Fig.(5.1): Simple amplifier circuit

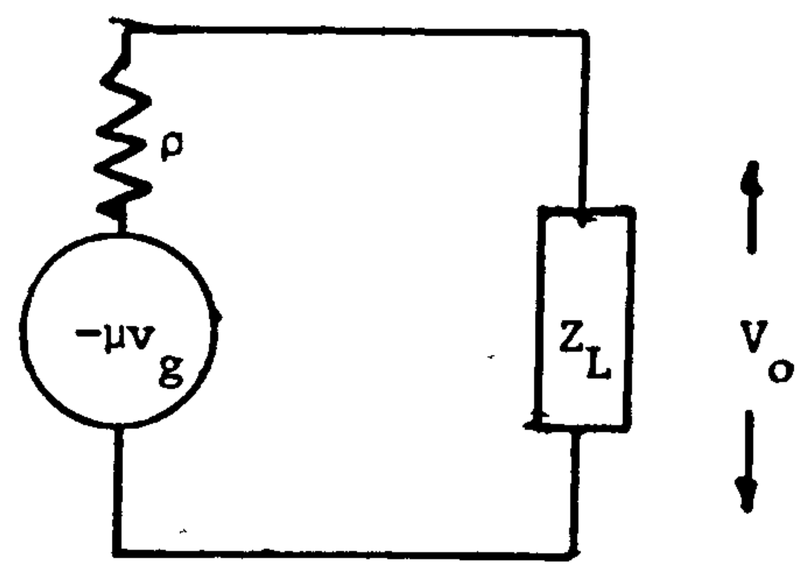

Fig.(5.2): A.C. equivalent circuit of Fig.5.1

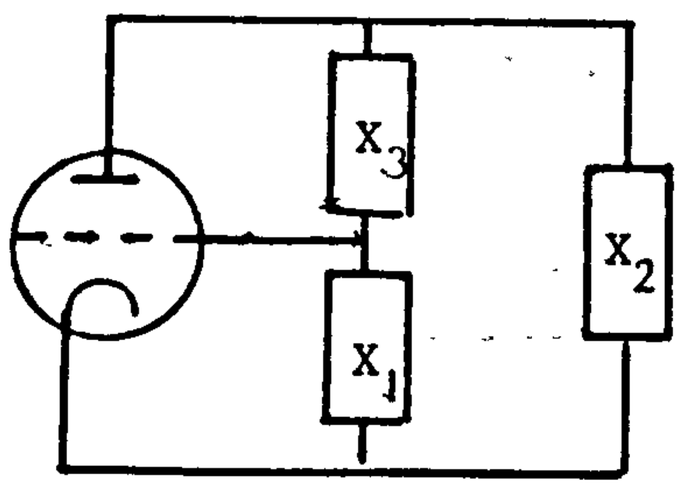

Fig.(5.3): Equivalent circuit of a self-excited oscillator

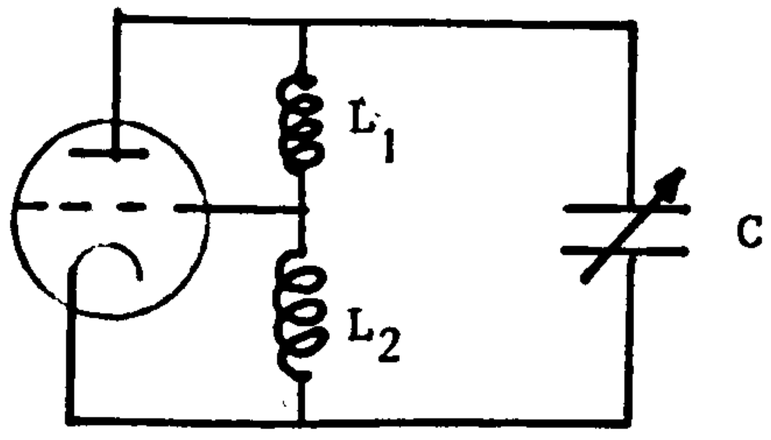

Fig.(5.4): Equivalent circuit of a Hartley oscillator

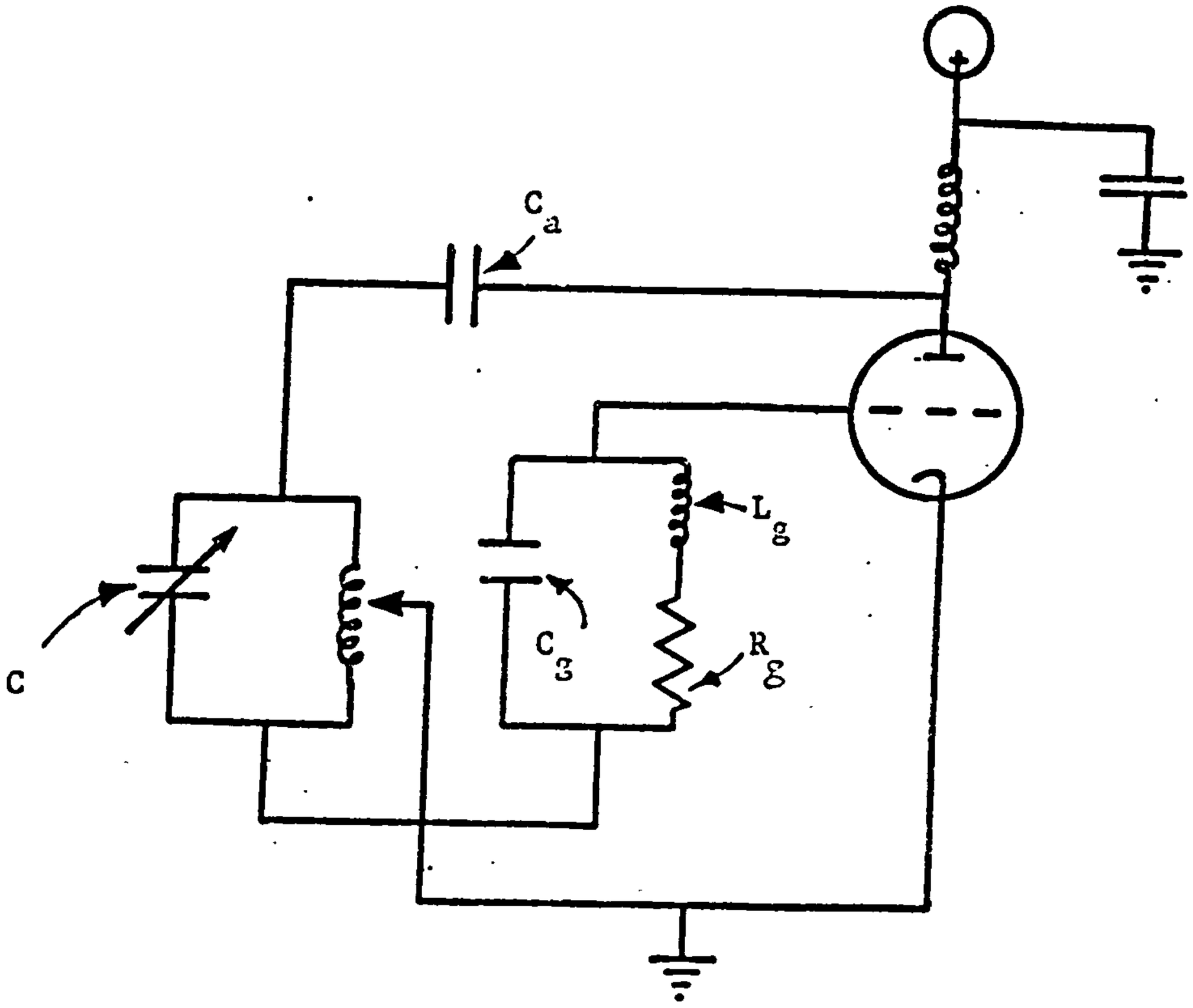

Fig.(5.5): A basic Hartley oscillator circuit.

and the frequency of operation ω_o is found as:

$$\omega_o = \frac{1}{\sqrt{LC}} \qquad 5.10$$

where the combined inductance $L = L_1 + L_2$.

The resonant LC circuit is known as the 'tank', because the quantity of charge stored in it is very much greater than that flowing out of it per cycle; the components of value L and C will be referred to as the tank coil and tank capacitor respectively.

5.1.2 Practical circuit operation

The voltages induced across the tank are very high (of the order of 10 kV), which can make the choice of tank capacitor a difficult one, because of the limitation of working voltage. The Colpitt's oscillator has two capacitors in the feedback circuit and since their values (and ratio) are known only approximately at the design stage, it is necessary to use variable split-stator capacitors, which are not easily obtainable at high working voltages. The Hartley oscillator requires a single variable capacitor and a coil, which can be wound easily and tapped at any point, and thus it is the Hartley which forms the basis of most sputtering RF generators.

A simple shunt-fed Hartley oscillator is shown in full in Fig. 5.5, where a valve with an indirectly heated cathode is used, for simplicity. The steady state operation of such a circuit, and the many variations upon it, may be analysed in the following way, making reference to the nomenclature of Figs. 5.4 and 5.5.

A positive grid voltage causes an increasing plate current and a reducing plate voltage. This plate voltage signal is coupled to the tank circuit (by C_a) and the frequency component which causes the tank circuit to resonate is displayed in antiphase at the grid (through C_g) with a larger amplitude than the other components. This drives the plate current still higher, reducing the anode voltage still further, until the valve saturates

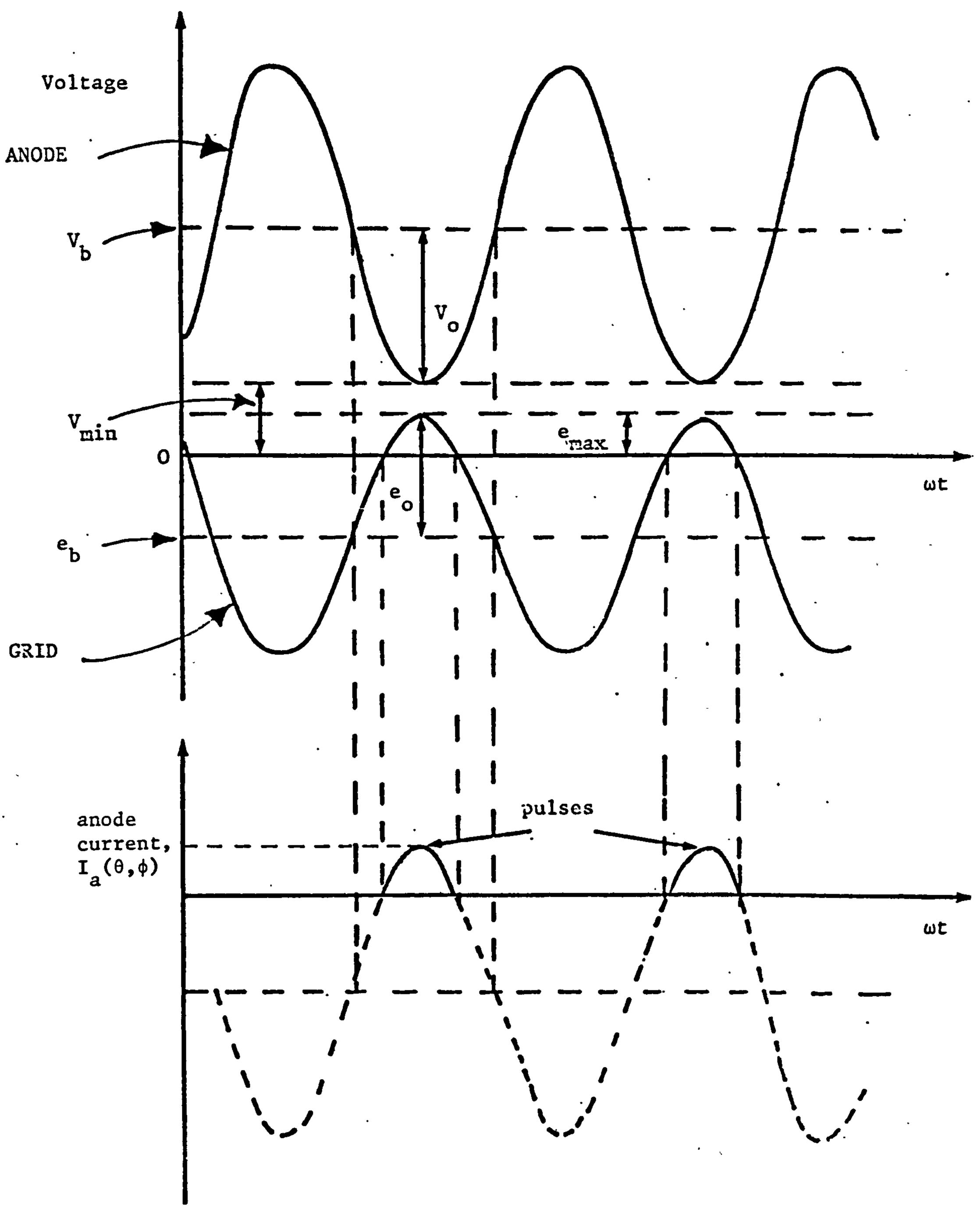

Fig.(5.6):

The steady state operation of class 'C' oscillator showing the phase relations between the anode current pulses and the grid voltage.

and the process reverses itself, with the grid voltage falling so as to cut off the plate current entirely.

The sequence described above produces an undesirable square waveform, but if the grid is biassed to constrain the operation to the linear region of the v_g-V_a characteristics shown in Fig. 5.8, then a sinusoidal waveform can be produced. The grid bias e_b can be applied by an external voltage supply, but it is simpler to utilise the current from the cathode to the grid as in the slightly different version of the circuit shown in Fig. 5.7, where the voltage dropped across the grid-leak resistor sets the bias level. This, the final circuit employed in the system constructed for the project, is a 'series-fed' Hartley oscillator (5.5), so called because the DC component of the plate current flows through the tank coil.

That fraction of the period during which the valve conducts is known as the conduction angle or 'angle of flow'. The power dissipated at the anode, the product $I_a V_a$ (Fig. 5.1), is clearly reduced when this angle is small, but the power input (and hence the power output) would be reduced in this case so a balance must be struck such that the output power is sufficiently high, and the heating of the anode is not too great. Conduction angles between 120° and 150° are commonly employed (defining the operation as class 'C') giving maximum theoretical efficiencies of 80% to 60%.

We can calculate an approximate grid bias level in terms of the conduction angle 2θ, by considering the voltages when the current pulse starts to flow. From Fig. 5.6,

$$e_b + e_o\cos\theta = -\frac{1}{\mu}(V_b - V_o\cos\theta) \qquad 5.11$$

by the definition of μ and of the other quantities given in the figure. Also, using:

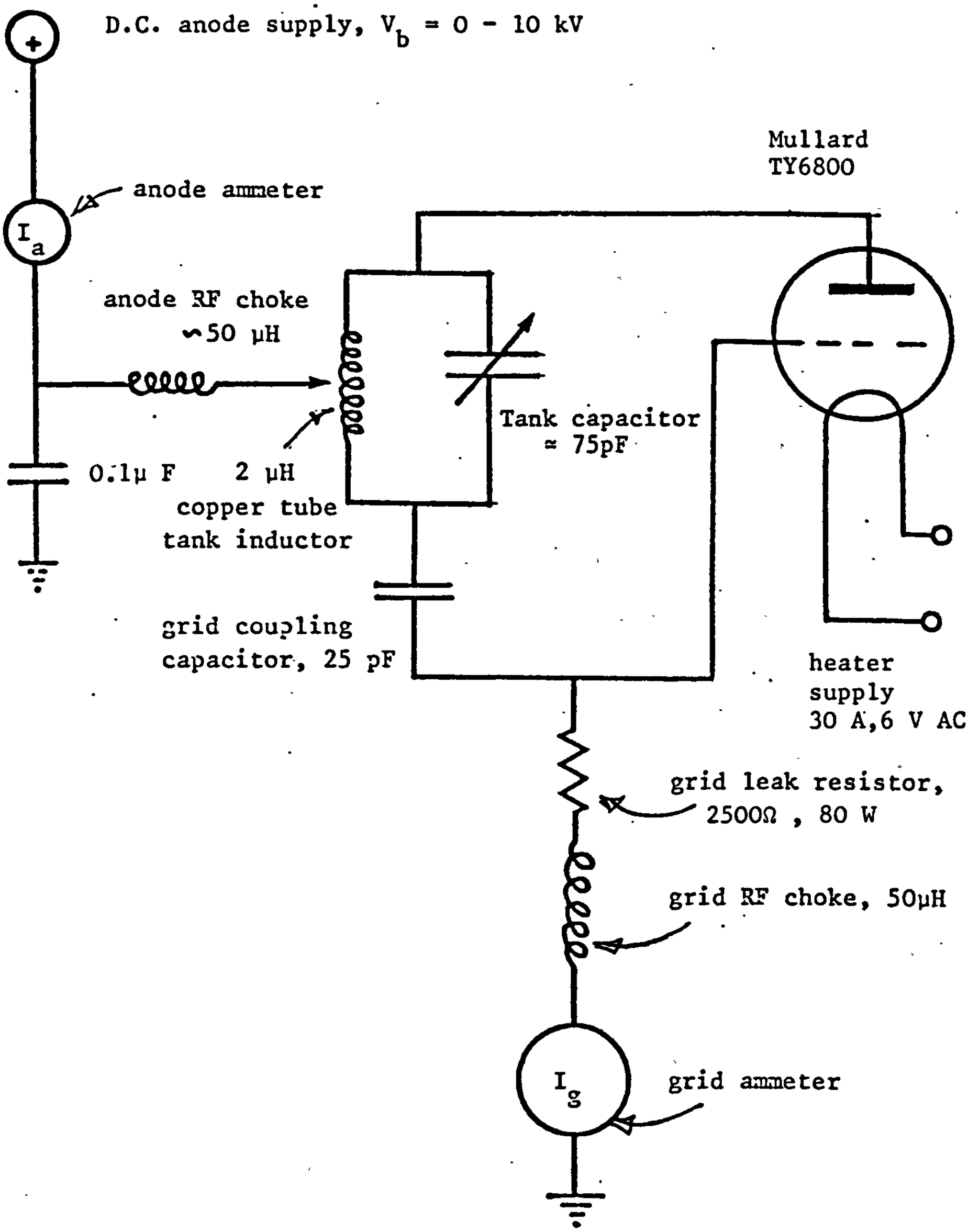

Fig.(5.7): A series fed Hartley oscillator showing component values and types. This is the most satisfactory circuit constructed and was used for most of the film deposition.

$$e_o = e_{max} - e_b, \ (e_b \text{ is a negative quantity}) \qquad 5.12a$$

and $$V_o = V_b - V_{min} \qquad 5.12b$$

the bias can be written as:

$$e_b = - \frac{V_b}{\mu} - \left[\frac{V_{min}}{\mu} + e_{max}\right]\left[\frac{\cos\theta}{1-\cos\theta}\right] \qquad 5.11'$$

From this equation, the correct bias level can be found if 2θ is known; if e_b is measured, the conduction angle can be determined.

The anode current pulse admits of the treatment by Fourier analysis given in Appendix VII, proof 1, which shows that the amplitude of the current entering the tank at the fundamental frequency is given by

$$a_1(\theta) = \left[\frac{\theta - \sin\theta\cos\theta}{\sin\theta - \cos\theta}\right] I_{av} \qquad 5.13$$

where the angle of flow is 2θ, and I_{av} is the average current. Hence, for example, if the current pulse persists for one third of the period, then

$$a_1(\pi/3) = 1.79\ I_{av} \qquad 5.13'$$

and the amplitude of the fundamental component of current is 1.79 times the reading of the anode ammeter. The function $a_1(\theta)$ is shown in Fig. 5.9, where the advantage of using a small conduction angle can be seen.

The valve employed in the apparatus constructed for the project was a Mullard TY6800, and from the constant current characteristics shown in Fig. 5.8 the operation of the circuit can be seen more clearly. The centre and end of the 'load line' have coordinates (V_b, e_b) and (V_{min}, e_{max}) respectively, and the intersection of this line with the smallest non-zero current curve defines the cut-off angle $\pi/2 - \theta$.

The heater requires a 30 A supply at 6 V AC and the valve was cooled from beneath with a fan. It has proved completely satisfactory for a low power experimental application. The other components shown in Fig. 5.7 will be discussed in the following sections.

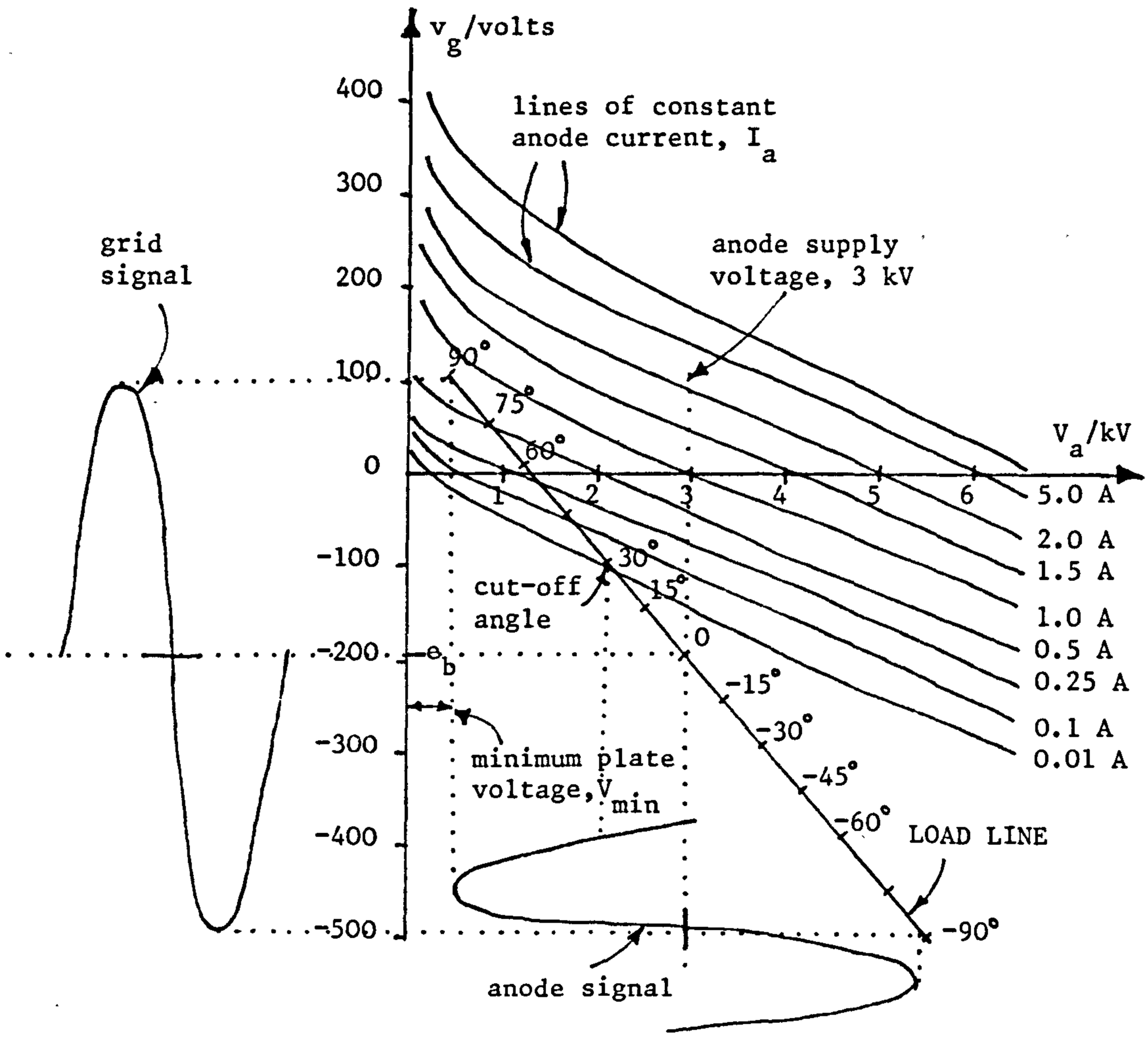

Fig.(5.8): Mullard TY6800 triode constant current characteristics showing the load line for operation at 3 kV. The valve can be seen to cut off at a phase angle of 30^o; the conduction angle is hence 120^o.

5.2 Components

The requirement for components to be robust, and to operate satisfactorily in conditions of elevated temperature, is manifest. It will be seen that the problems arising from this necessity can be solved adequately using very simple component design. Photographs of the front and rear of the finished oscillator unit are given in Figs. 5.10 and 5.11.

5.2.1 HT supply

The high voltage DC anode supply is an expensive item, requiring a heavy duty high voltage transformer and mercury arc rectifiers. The unit employed for this work was adapted in a straightforward manner from an arc welding generator, and hence the experience gained in the design of such equipment was limited. The output voltage of the supply can be altered by a Variac control in the range 0 to 10 kV, and this formed the usual method of altering the power of the sputtering run. The output current was displayed by meters in the HT supply itself and in the oscillator casing. The smoothing of the supply need be only rudimentary; a 3 kV full wave rectified output can be smoothed with a 20 μF capacitor to supply 300 mA with a 5% ripple factor.

5.2.2 Capacitors

It was found, in the case of the first few oscillator circuits constructed, that the difficulty mentioned in section 5.1.2 of obtaining a tank capacitor with a high enough operating voltage was insurmountable without resorting to a vacuum capacitor. These are extremely expensive and difficult to obtain, since the main suppliers are in the USA.

Consequently, a cylindrical vacuum jacket was designed and constructed from stainless steel, to house a variable capacitor for use in the tank circuit. A small ceramic lead-through was used for one of the electrical connections to the capacitor, the other being grounded to the

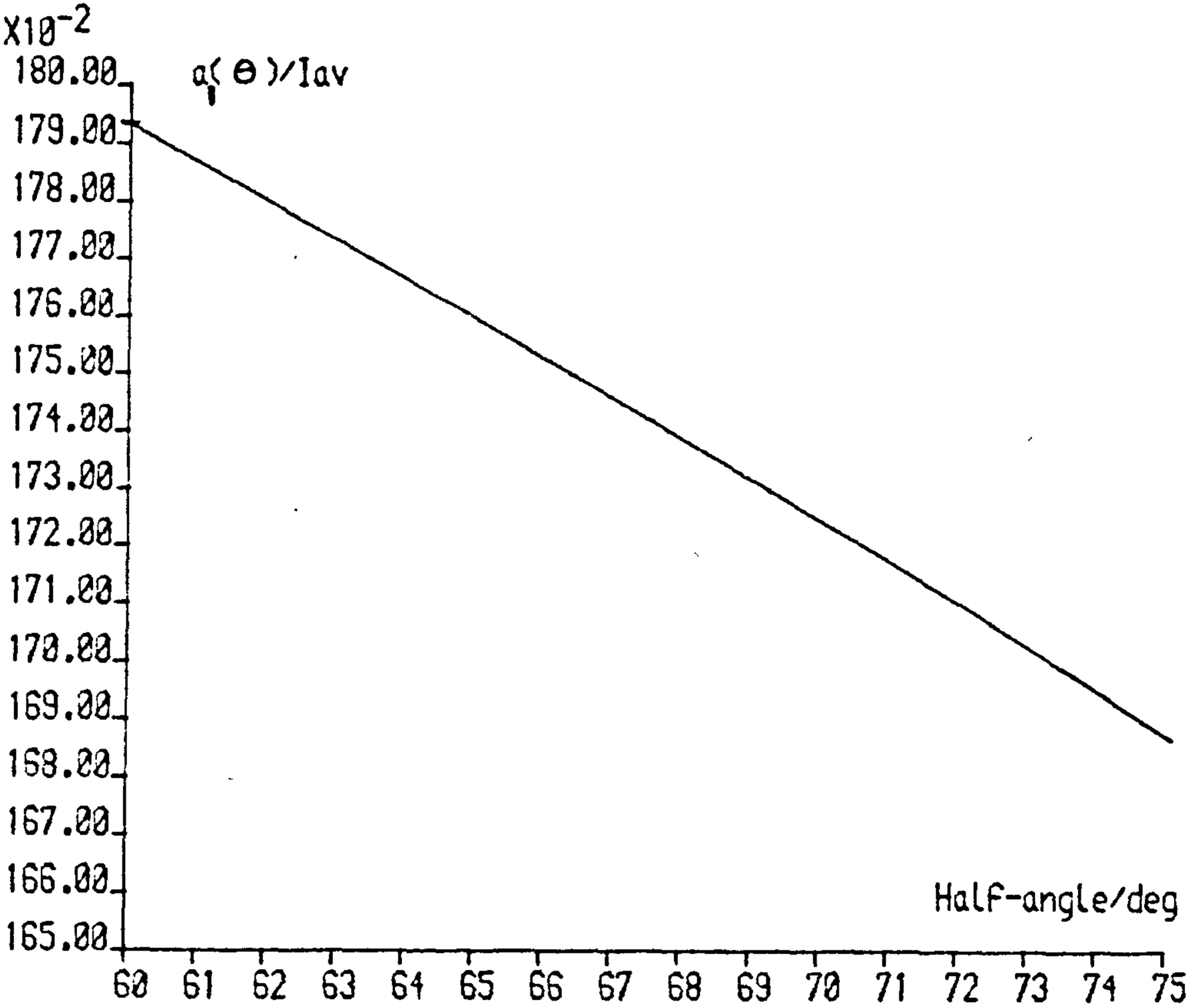

FIG(5.9): Fundamental tank current component

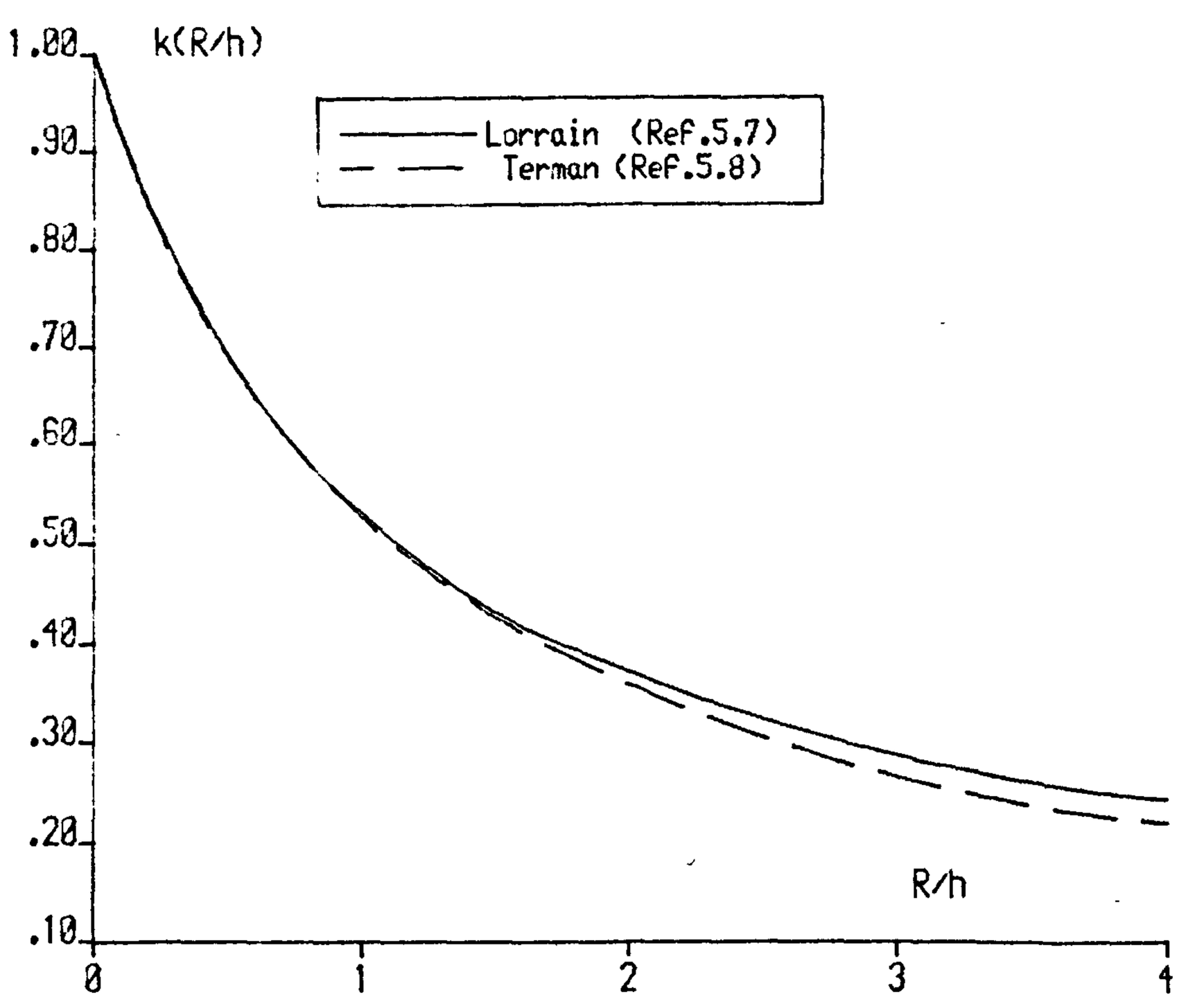

FIG(5.12):Derating Factor For short coils

The coil is of length h and radius R

chassis, and a rotary vacuum lead-through, consisting of two Viton 'O' rings around a steel shaft, enabled the capacitance to be adjusted, but the inevitable leakage associated with this prevented the pressure in the interior from remaining sufficiently low to avoid arcing between the plates. Such a construction would have to be continuously pumped, rendering it most inconvenient. An improvement would be to construct the vacuum vessel from glass (to make visible the position of the rotor and any arcing that may occur) and to use magnetic coupling for adjustment.

In the circuit of Fig. 5.7, both terminals of the tank capacitor are at high potential, which rules out completely the use of the vacuum capacitor designed above. However, the problem was solved by increasing the air gap of a commercial variable capacitor (5.6) from 3.25 to 4.18 mm, mounting it on an insulating stand-off, and controlling its setting with a worm-driven paxolin lever. It is of general interest to note that such capacitors as these will break down if the RF field strength exceeds about 2 $kVmm^{-1}$ in the air gap.

The tank capacitance is variable from about 15 to 65 pF by means of the control shown in Fig. 5.10. Commercial high voltage capacitors were used successfully for all other purposes.

5.2.3 Coils : self-inductance

The fundamental resonance equation 5.10 is evaluated at the working frequency as:

$$LC = 137.8 \qquad 5.10'$$

where L is in μH and C is in pF, from which it is seen that the tank inductance must be around 2μ H, if capacitors of the size considered above are used.

If a coil has N turns, is of radius R, cross sectional area A and length h, its self inductance L can be written in the case of $h/R \gg 1$ as (5.7):

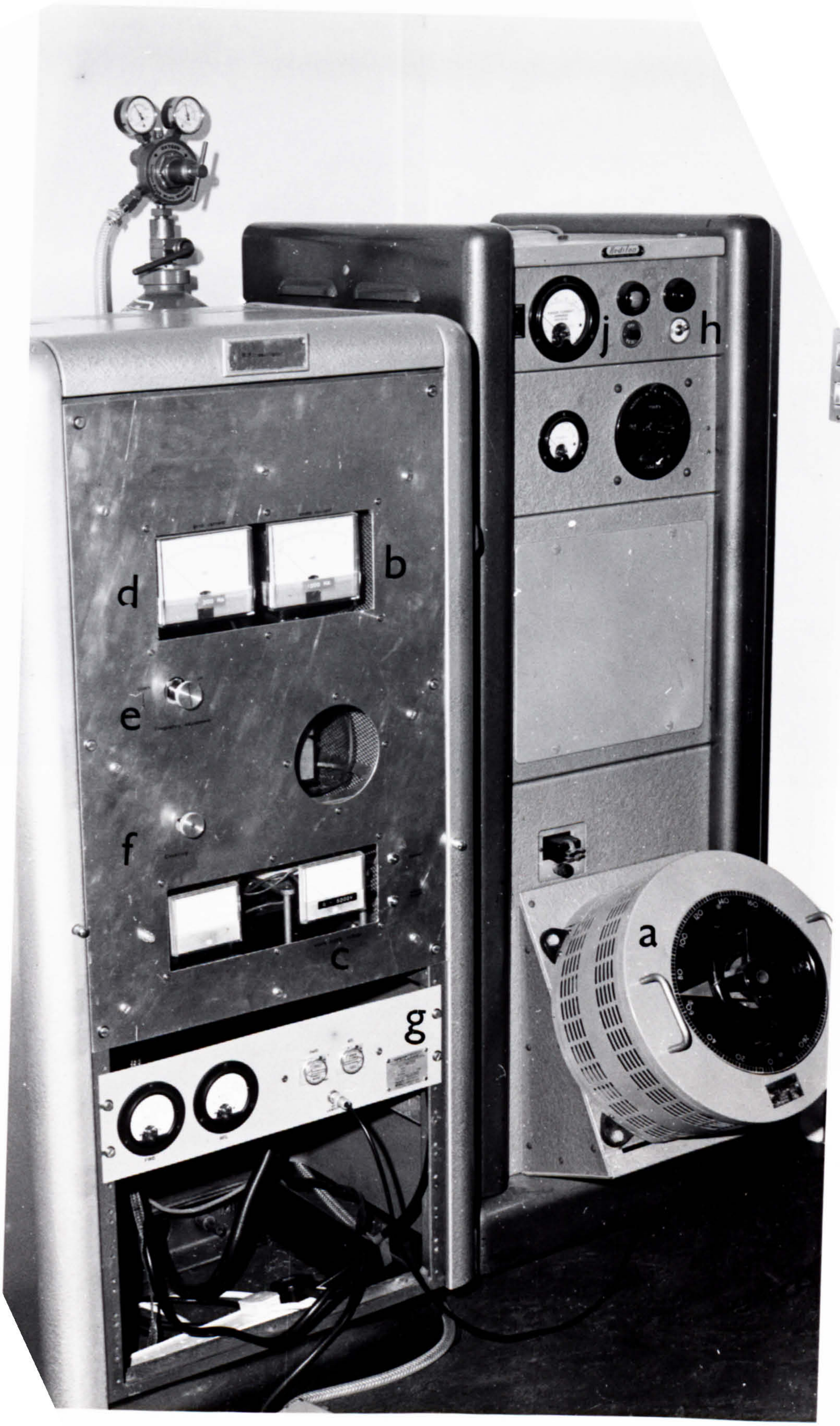
Endress
j
h
d
b
e
f
c
g
a

Fig.(5.11): Rear view of RF oscillator

(an early version is shown; many modifications followed)

a: triode

b: tank coil

c: tank capacitor

d: pick-up coil

e: rotating gantry

f: matching capacitor

g: anode supply kilovoltmeter

$$L = \frac{\mu_o N^2 A}{h}$$

$$L/\mu H = 0.00395 \ \frac{N^2 R^2}{h} \quad \text{(lengths in mm)} \qquad 5.14$$

Considerable heat is dissipated due to ohmic losses at high frequencies, and the use of copper tubing for the tank coil is customary. The number of turns that can be wound is hence restricted, and coil dimensions are commonly used for which the ratio h/R is not large.

Modifications of equation 5.14 for the case of short coils have been published by Terman (5.8) in the form:

$$L/\mu H = 0.00395 \ \frac{N^2 R^2}{h} \ x\left(\frac{1}{0.9R/h + 1}\right) \qquad 5.14'a$$

and in tabular form by Lorrain and Corson (5.7); as Fig. 5.12 shows, the derating factors k(R/h) are very similar. Norström (5.9) has used an expression:

$$L/\mu H = 0.00444 \ N^2 R \ x\left(\frac{1}{4.5R/h + 1}\right) \qquad 5.14'b$$

in place of equation 5.14 but this appears to give quite different numerical results, besides not tending to equation 5.14 in the limit as R/h tends to zero.

The derating factor from the work of Lorrain and Corson, shown in Fig. 5.12, was used for estimating self inductances in the present work, with an accuracy of approximately 10% (with respect to the reading of a commercial instrument) which was quite sufficient for winding general purpose coils.

Five turns of copper tubing of 10 mm diameter were used for the tank coil; 3 mm gauge was appropriate for most of the other inductances constructed.

5.2.4 Coils : mutual inductance

The mutual inductance between two circuits is defined by the Neumann double integral:

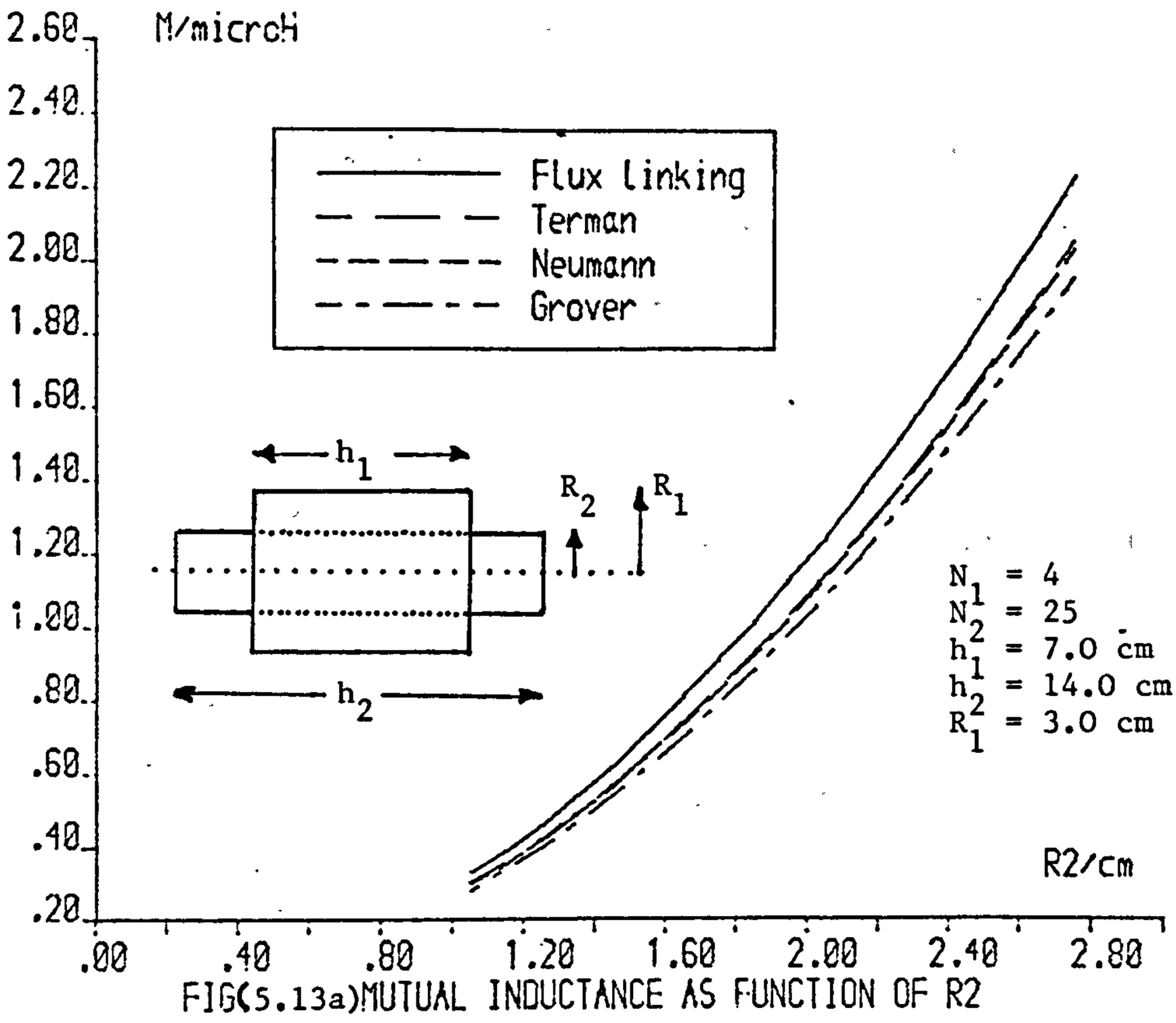

FIG(5.13a)MUTUAL INDUCTANCE AS FUNCTION OF R2

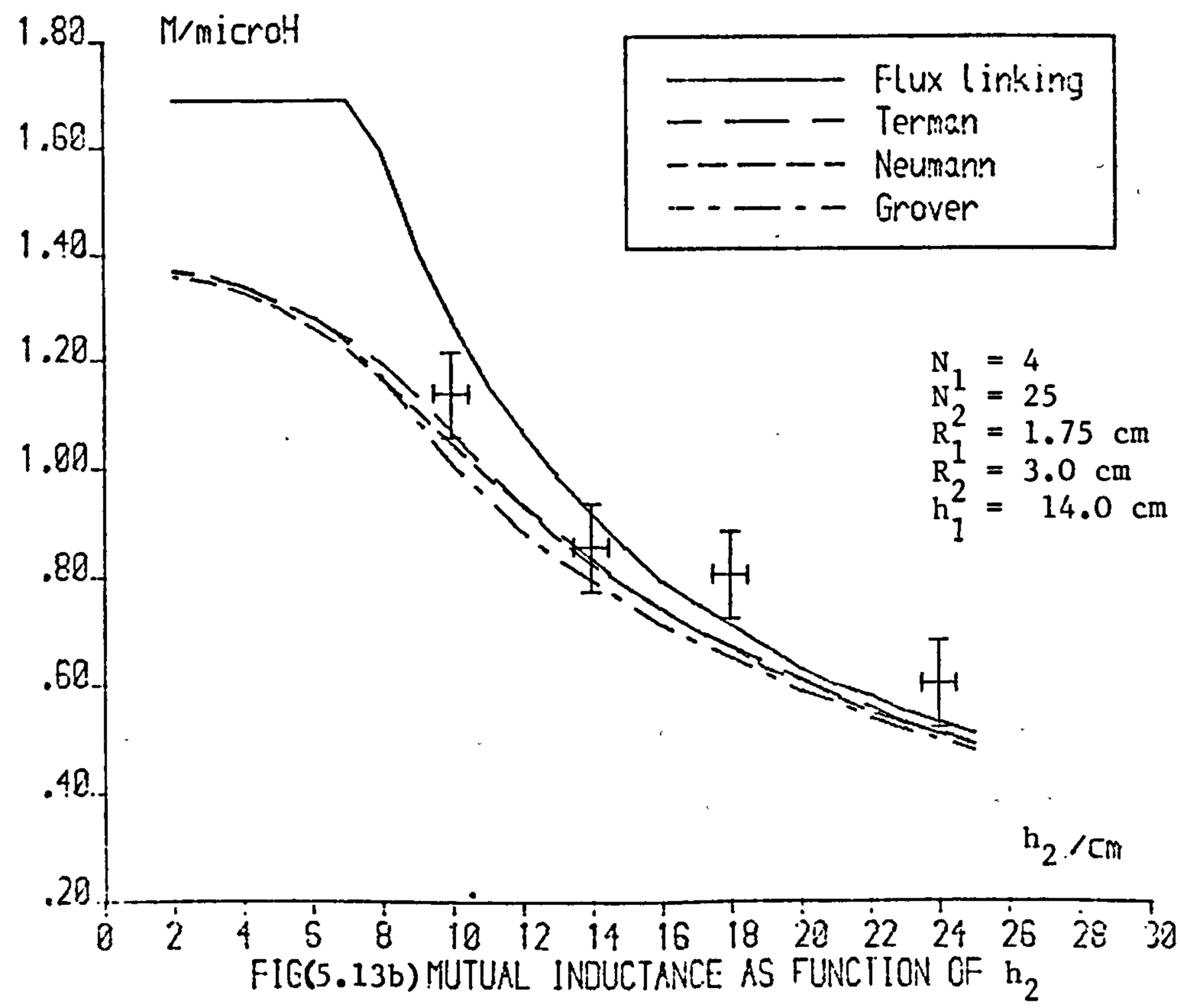

FIG(5.13b) MUTUAL INDUCTANCE AS FUNCTION OF h_2

$$M = \frac{\mu_o}{4\pi} \oint\oint_{12} \frac{\underline{dl}_1 \, \underline{dl}_2}{r_{12}} \qquad 5.15$$

where r_{12} is the separation of the incremental vectors $\underline{dl}_1$ and $\underline{dl}_2$ which are in the position (and direction) of the current in circuits one and two respectively. Terman (5.11) approximates this integral for two coils of lengths h_1 and h_2 and radii R_1 and R_2, as in Fig. 5.13a, to yield the formula:

$$M/nH = 1.97 \; \frac{R_2^2 \, N_1 N_2}{g} \left\{ 1 + \frac{(R_1 R_2)^2}{8g^4} \left[3 - \left(\frac{h_1}{R_2} \right) \right]^2 \right\} \qquad 5.15'$$

where $g^2 = R_1^2 + (h_2^2/2)^2$ 5.15'a

and where, if the inner coil is the shorter, the subscripts on the lengths h in equations 5.15' are exchanged. All coil dimensions are in millimetres. Earlier, Grover and Dwight (5.12) published the expression:

$$M/nH = \frac{1.97 \; R_2^2 \, N_1 N_2}{g} \left\{ 1 + \frac{X_1}{8} R^2 + \frac{X_2 Y_1}{32} R^4 + \frac{X_3 Y_2}{32} R^6 + \ldots \right\} \qquad 5.15''$$

where

$$R = \frac{R_1 R_2}{g^2} \qquad 5.15''a$$

$$X_1 = 3 - (h_1/R_2)^2 \qquad 5.15''b$$

$$Y_1 = 3 - (h_2/R_1)^2 \qquad 5.15''c$$

$$X_2 = \frac{5}{2}\left[1 - (h_1/R_2)^2 + \frac{1}{10}(h_1/R_2)^4 \right] \qquad 5.15''d$$

$$Y_2 = \frac{5}{2}\left[1 - (h_2/R_1)^2 + \frac{1}{10}(h_2/R_1)^4 \right] \qquad 5.15''e$$

$$X_3 = \frac{1}{16}\left[35 - 70(h_1/R_2)^2 + 21(h_1/R_2)^4 - (h_1/R_2)^6 \right] \qquad 5.15''f$$

As is shown in Figs. 5.13, where these approximations are compared with the double integration of equation 5.15 performed numerically, the truncated form due to Terman is remarkably accurate.

If there were no loss of magnetic flux, as in the case of long coils, the mutual inductance would be given by:

$$M = \frac{\mu_o N_1 N_2 A_2}{h_2} \qquad 5.16$$

$$M/nH = \frac{1.97\ N_1 N_2 R_2^2}{h_2/2} \qquad 5.16'$$

which expression is included in Figs. 5.13 for purposes of comparison, and is seen to overestimate M by more than 10%.

Equation 5.15, although somewhat complex, is to be recommended for accurate computation of mutual inductance, but can only be used when the coils are mounted symmetrically on a common axis.

The total self-inductance L_t of a circuit containing two coils between which there is flux linkage is given by:

$$L_t = L_1 + L_2 \pm 2M \qquad 5.17$$

with the usual notation, where the choice of sign occurs because the emf induced by one coil can add to, or subtract from, the voltage across the other, according to the polarity of the connections. This is used to determine M by subtracting the two total self inductances (one with each polarity) and dividing by four. The experimental results in Fig. 5.13b were obtained in this way and the agreement can be seen to be reasonable, despite the difficulty of allowing for the inductance of the leads to the meter, a Hewlett Packard LCR meter, Model 4261A.

5.3 General features

There are a number of features to which attention might usefully be drawn, of both an electrical and a mechanical nature.

5.3.1 Q-factor

If the tank circuit resonates at a frequency ω_o and contains an energy E, the 'quality factor' Q is shown in Appendix VII, proof 2, to be given by:

$$Q = \frac{\omega_o E}{dE/dt} = \frac{\omega_o L}{R} \qquad 5.18$$

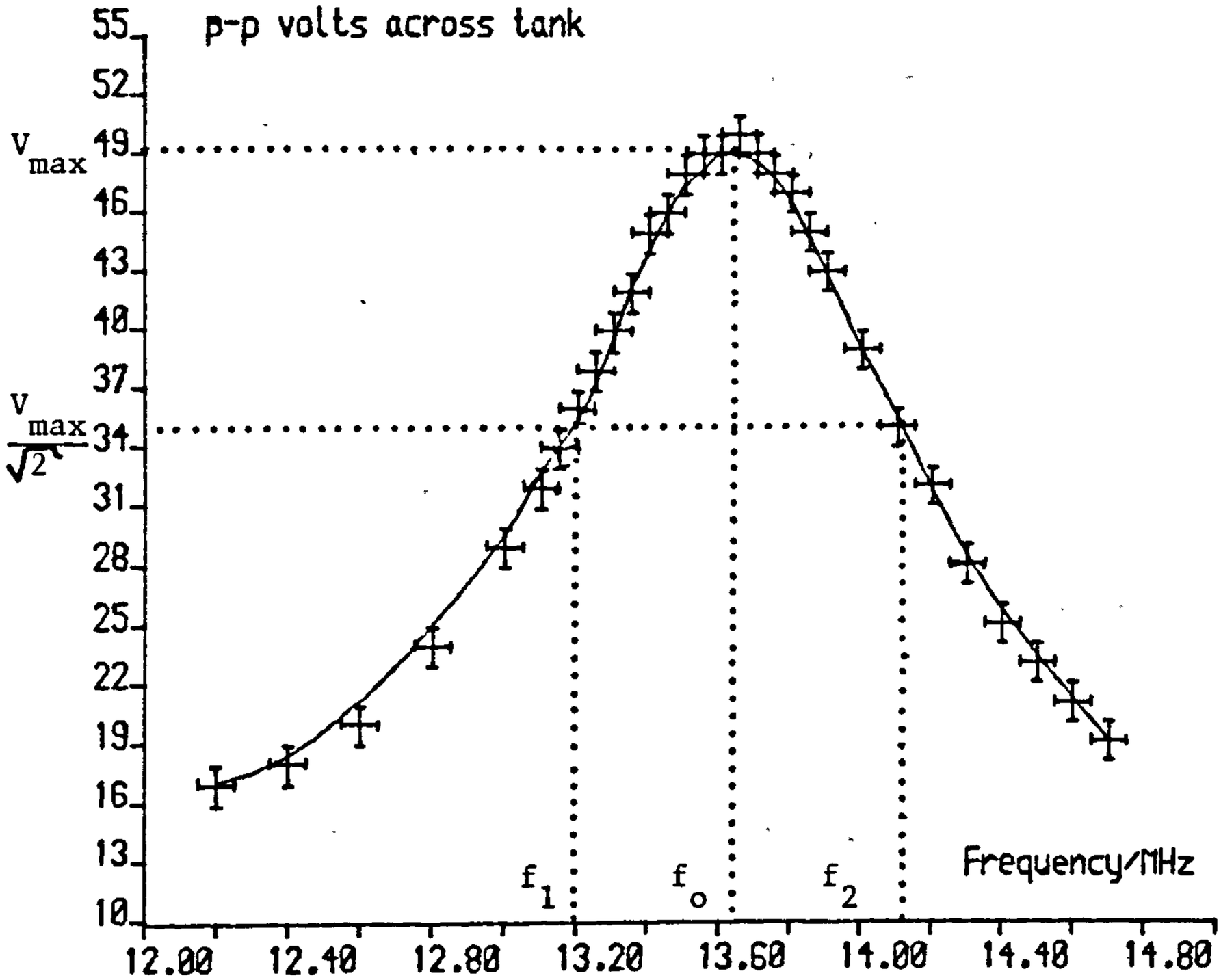

FIG(5.14): Determination of tank Q

that is, by the ratio of reactive to resistive impedances.

As shown in many standard texts (5.13), at the '3db' points f_1 and f_2, (at which the reactance of the tank becomes equal in magnitude to its resistance), the total impedance of the circuit is reduced by a factor of $\sqrt{2}$. These two frequencies also define Q, by:

$$Q = \frac{f_o}{f_2 - f_1} \qquad 5.19$$

enabling it easily to be measured, as shown in Fig. 5.14. The quality factor of the tank circuit is seen to be 14.8 when operating without load. In this circumstance the chief contribution to the value of R is made by the losses in the grid circuit. Otherwise, R becomes the value of the load impedance as coupled into the tank. The RF resistance of the coil is small compared with these impedances. The importance of the Q-factor is in its determination of the breadth of resonant curves such as that of Fig. 5.14. A large Q will reduce the magnitude of the unwanted frequency components at $f \neq f_o$, but the oscillating tank current I_t is given by Q times the supply current, i.e:

$$I_t = Q\, a_1(\theta)\, I_{av} \qquad 5.20$$

and the heating losses will increase at high Q. A Q-factor of about 12 is found appropriate by McDowell (5.14), which corresponds to a coupled resistance of some $.7\Omega$, using equation 5.18 with a tank inductance of $1\mu H$.

5.3.2 Output impedance

In order that the maximum power should be delivered, the load impedance must be equal to the output impedance of the oscillator (5.15). Measurement of this quantity is most satisfactorily performed by calculating the power dissipated in a dummy load (of high power resistors) as a function of its resistance. The results of such measurements are

shown in Fig. 5.15 where a load of 1350 Ω can be seen to dissipate maximum power; this value was taken as the internal impedance of the generator.

5.3.3 Pick-up coil

The RF power is extracted from the tank circuit by inductive coupling to a 'work' or 'pick-up' coil suspended so as to link the flux of the tank coil. In our instrument, the 120 mm diameter pick-up coil was constructed of 3.2 turns of 3 mm copper tubing mounted upon a gantry, parallel to the axis of the tank coil, which enabled it to be moved into and out of the magnetic field lines of the tank, altering the mutual inductance. This feature, which was not used extensively in our case, would be invaluable if the anode voltage were not variable, since it controls the power output of the generator.

Mutual inductances in the region of 1μH were calculated, using equation 5.15, between the pick-up coil and the tank coil.

5.3.4 Viewing port

Under conditions of high reflected power, the anode of the valve will glow red and damage will ensue. An invaluable feature is a window to permit viewing of the state of the valve at all times. A perspex sheet sufficed in our case.

5.3.5 Safety cut-out

To avoid the temptation to 'tweak' the oscillator whilst it is operating, which is extremely hazardous because of the high RF and DC voltages present, it is recommended that the HT supply be automatically disconnected as the cover of the unit is lifted. It is a worthy, and not too troublesome feature.

5.4 Power transmission

Unless the oscillator is mounted directly adjacent to the

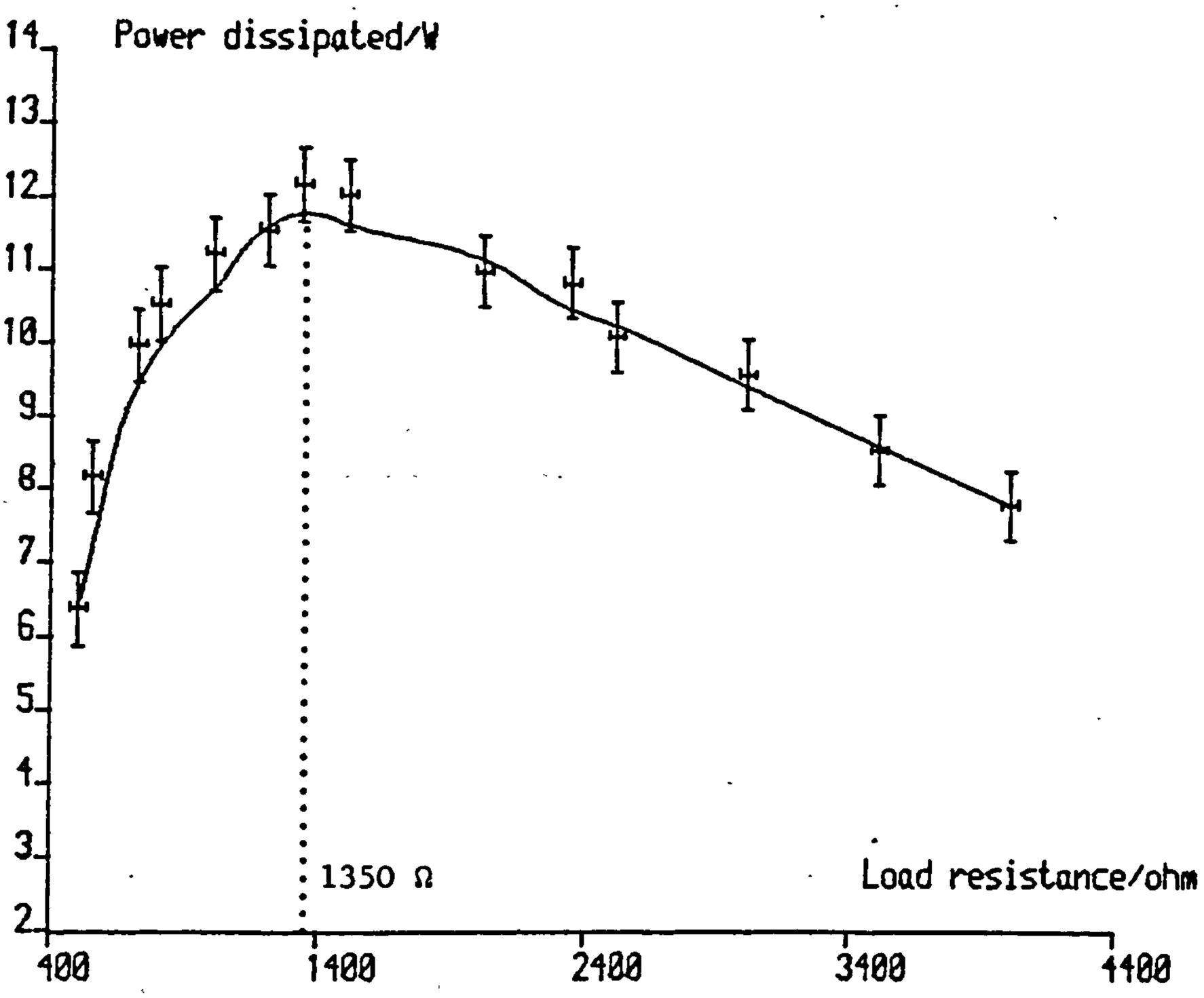

FIG(5.15)Determination of internal impedance

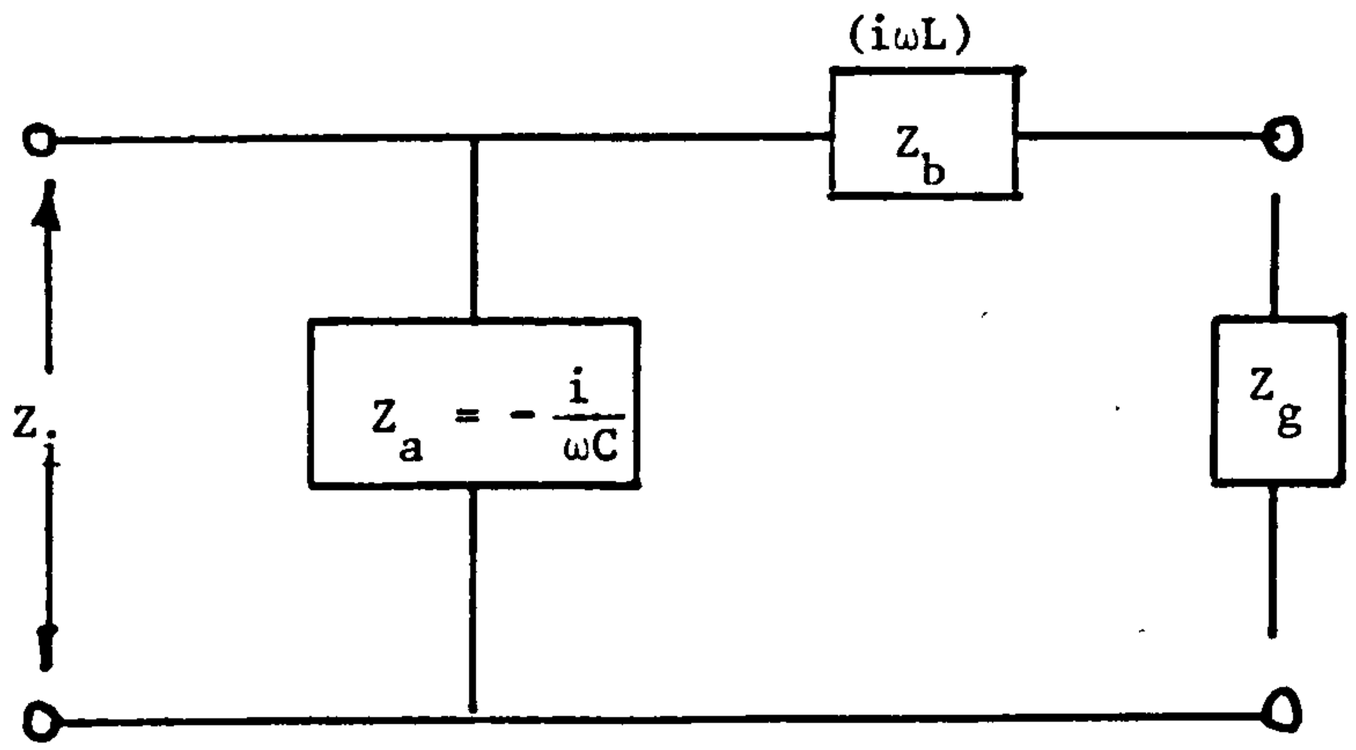

Fig.(5.16): 'L-section network'

sputtering chamber, the RF power must be supplied to the electrodes through a transmission line. If the line, of length l, has characteristic impedance Z_o, the input impedance Z_i seen at the 'sending end' of the line is given by (5.2):

$$Z_i = \frac{Z_o \{ Z_L + Z_o \tanh \gamma l \}}{\{ Z_o + Z_L \tanh \gamma l \}} \qquad 5.21$$

where the load impedance at the other end is Z_L, and the propagation constant γ is given by

$$\gamma = \alpha + i2\pi/\lambda \qquad 5.21a$$

α being the attenuation constant (nepers m^{-1}) and λ the wavelength.

For short RF lines, the attenuation can be neglected to a good approximation, so that equation 5.21 becomes:

$$Z_i = \frac{Z_o \left\{ Z_L + iZ_o \tan(2\pi l/\lambda) \right\}}{Z_o + iZ_L \tan(2\pi l/\lambda)} \qquad 5.21'$$

and the impedance presented by any line can be found. The full behaviour of equation 5.21 is expressed in a 'Smith chart', the use of which has been explained by Southworth (5.16).

Points of interest occur at a line length of $\lambda/4$ (the quarter wave line), when the relative input impedance Z_i/Z_o becomes equal to the inverse of the relative load impedance Z_L/Z_o, and at $l = \lambda/2$ when no transformation of the load is effected. In our apparatus, a half-wave line was employed, of U69 50 Ω cable, which with its velocity factor of 0.66 was of the convenient length, 7.38 m. An increase in the temperature of the cable was noticeable at current maxima, indicating an unnecessary loss of power. This type of cable is satisfactory for low power units, but for powers much above a kilowatt, a more robust system should be used, possibly rigid coaxial tubes, despite the increased inconvenience.

5.5 Impedance matching

The impedance of the glow discharge, Z_g must be matched to the

generator in order that power should not be reflected and that the valve should not overheat. It is shown in Appendix VII, proof 3, that the parallel and series reactances required for the simple matching network shown in Fig. 5.16 are respectively (5.2):

$$Z_a = -iZ_i \left[\frac{Z_i}{Z_g} - 1 \right]^{-\frac{1}{2}} \qquad 5.22a$$

$$Z_b = iZ_g \left[\frac{Z_i}{Z_g} - 1 \right]^{\frac{1}{2}} \qquad 5.22b$$

where Z_i is the transformed load impedance.

If the shunt arm be capacitive, then the series impedance must be inductive, and directly from these equations the necessary component values can be written respectively as:

$$C = \frac{1}{\omega Z_i} \left[\frac{Z_i}{Z_g} - 1 \right]^{\frac{1}{2}} \qquad 5.23a$$

$$L = \frac{Z_g}{\omega} \left[\frac{Z_i}{Z_g} - 1 \right]^{\frac{1}{2}} \qquad 5.23b$$

Norström (5.9) has followed Logan et al (5.17) in using equations 5.23 to determine the glow discharge impedance. The component settings of an 'L-section' network, Fig. 5.16, are adjusted until the reflected power reaches a minimum, when the equations are assumed to be satisfied. Using the values of L and C at which this occurs, the glow impedance Z_g can be found. The conductance and capacitance per unit area of electrode are shown in Figs. 5.17 and there is good agreement between the workers, but the assumption that the parameters are constant across the surface of the electrode has been questioned by Jackson (5.18).

Using a quite different method of measurement, that of noting the frequency shift on striking the discharge, Jackson (5.18) found impedance values somewhat dissimilar to those of Figs. 5.17 and recorded conductance

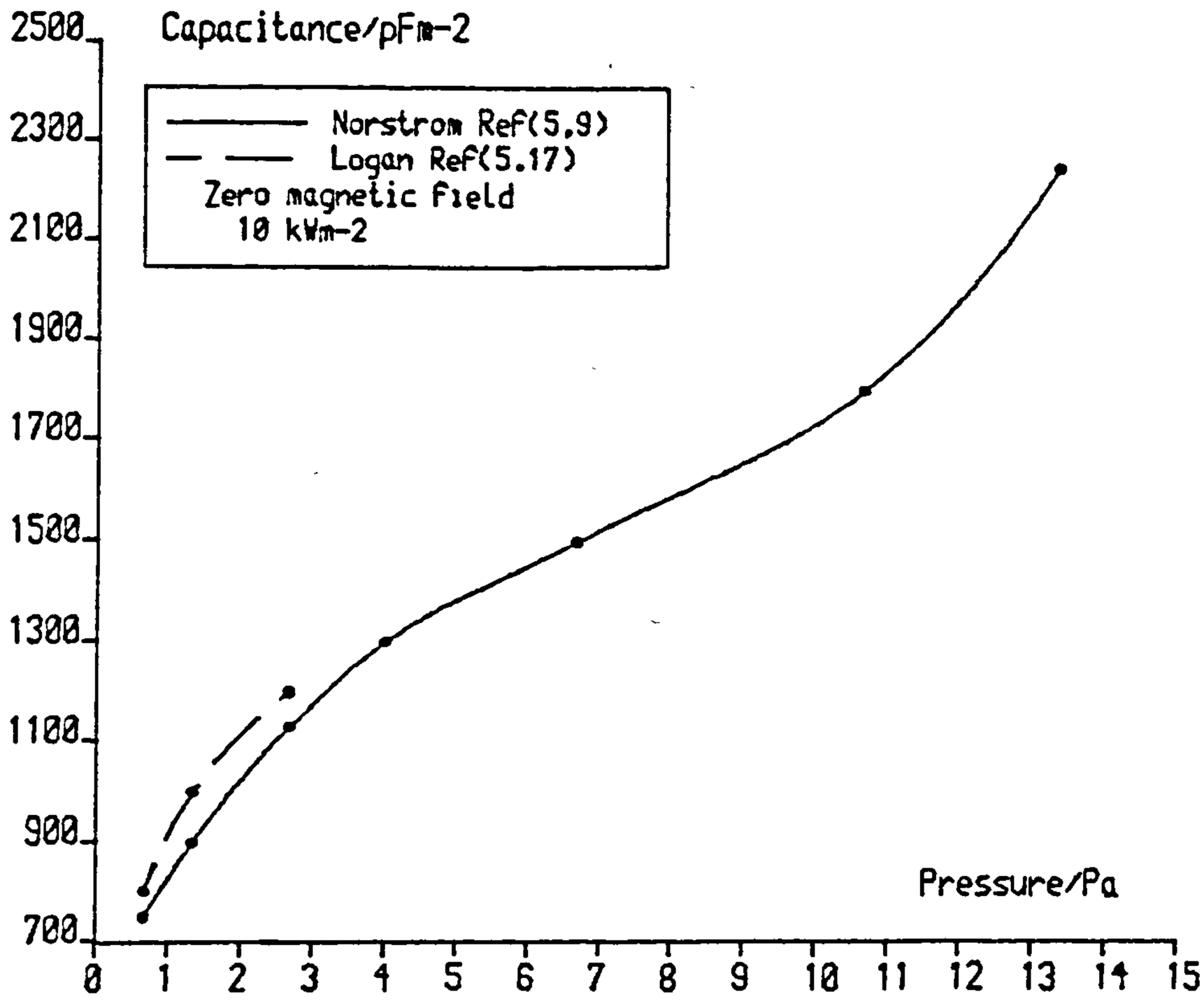

FIG(5.17a):Capacitance of glow discharge

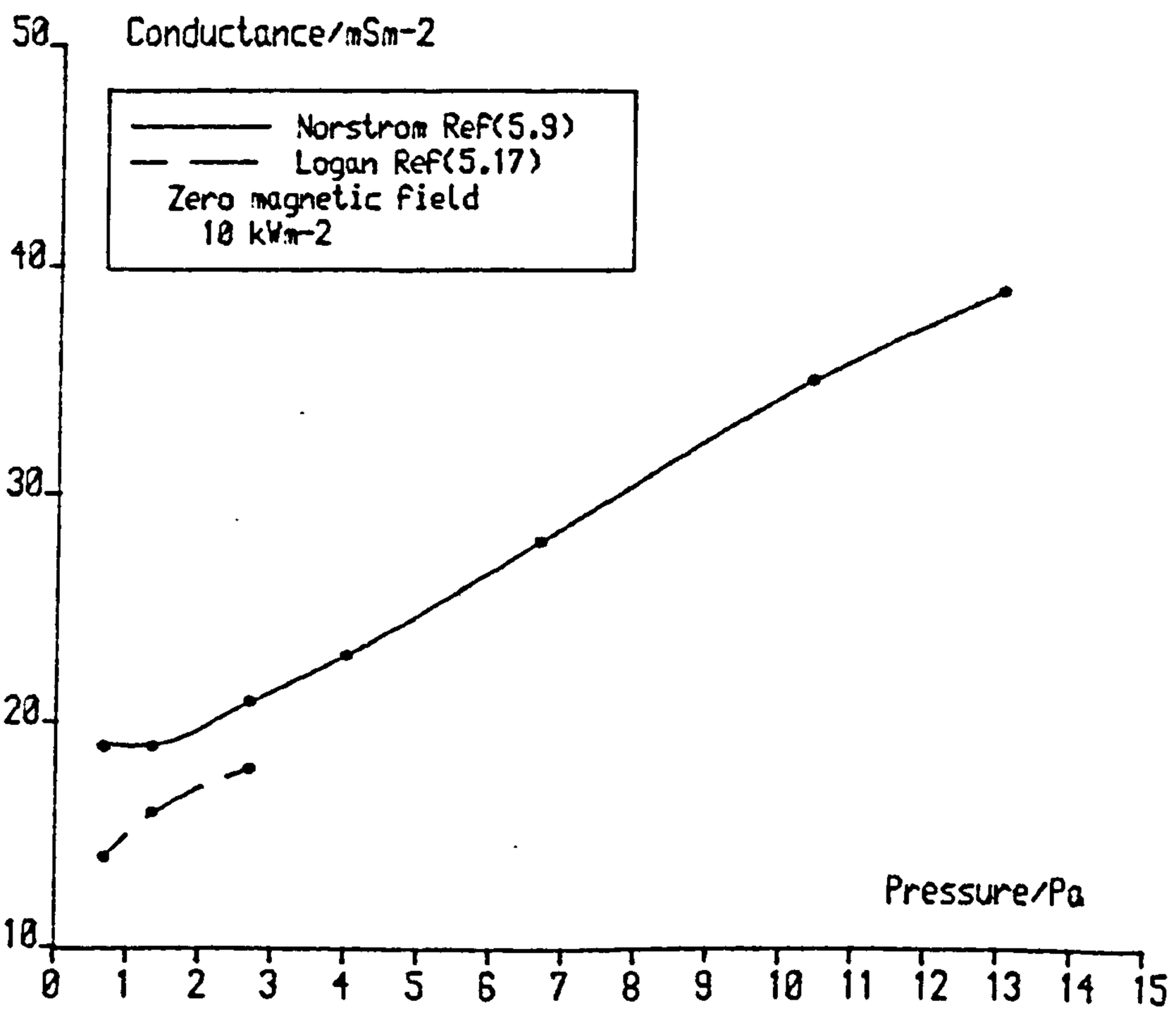

FIG(5.17b):Conductance of glow discharge

variation with input power density, which Logan neglects. To obviate the particularly large discrepancy in capacitance at 0.66 Pa (5 mTorr) and 5 mT (Logan: $\sim$ 1400 pFm^{-2}; Jackson: $\sim$ 340 pFm^{-2}), Jackson suggests that the phase time between the applied voltage and the current flowing in the plasma should be used as the descriptive parameter rather than capacitance, since it is very similar in the two cases above, being 16.3 ns and 17 ns respectively. Considerable variation in Z_g with target to substrate spacing is also found in this reference, as shown in Figs. 5.18, and the point is made that the very large number of variables (the target capacitance and target material should be added to the list) makes difficult the comparison of results between researchers. As will be seen in the following chapter, the data of Logan et al (5.17) have been used preferentially, particularly when operating in the single ended mode, and those of Jackson (5.18) were considered more appropriate to the double electrode mode, although the discrepancies are not all as significant as in the example above. The considerable error involved in the use of such data is described in the following subsection.

Matching was achieved with success using the 'L-section' network of Fig. 5.16 in the single ended mode, but it has the disadvantage of causing imbalance in the disc and annulus system.

5.5.1 Uncertainty in load impedance calculation

The glow impedances are discussed in the preceding subsection in terms of parallel components, but the more tractable series values are calculated according to:

$$\frac{1}{Z_g} = G_g + iX_p$$

$$\frac{1}{R_g + iX_g} = G_g + i\omega\left(C_g + C_s\right) \qquad 5.24$$

where G_g and C_g are the glow conductance and capacitance, C_s is the stray

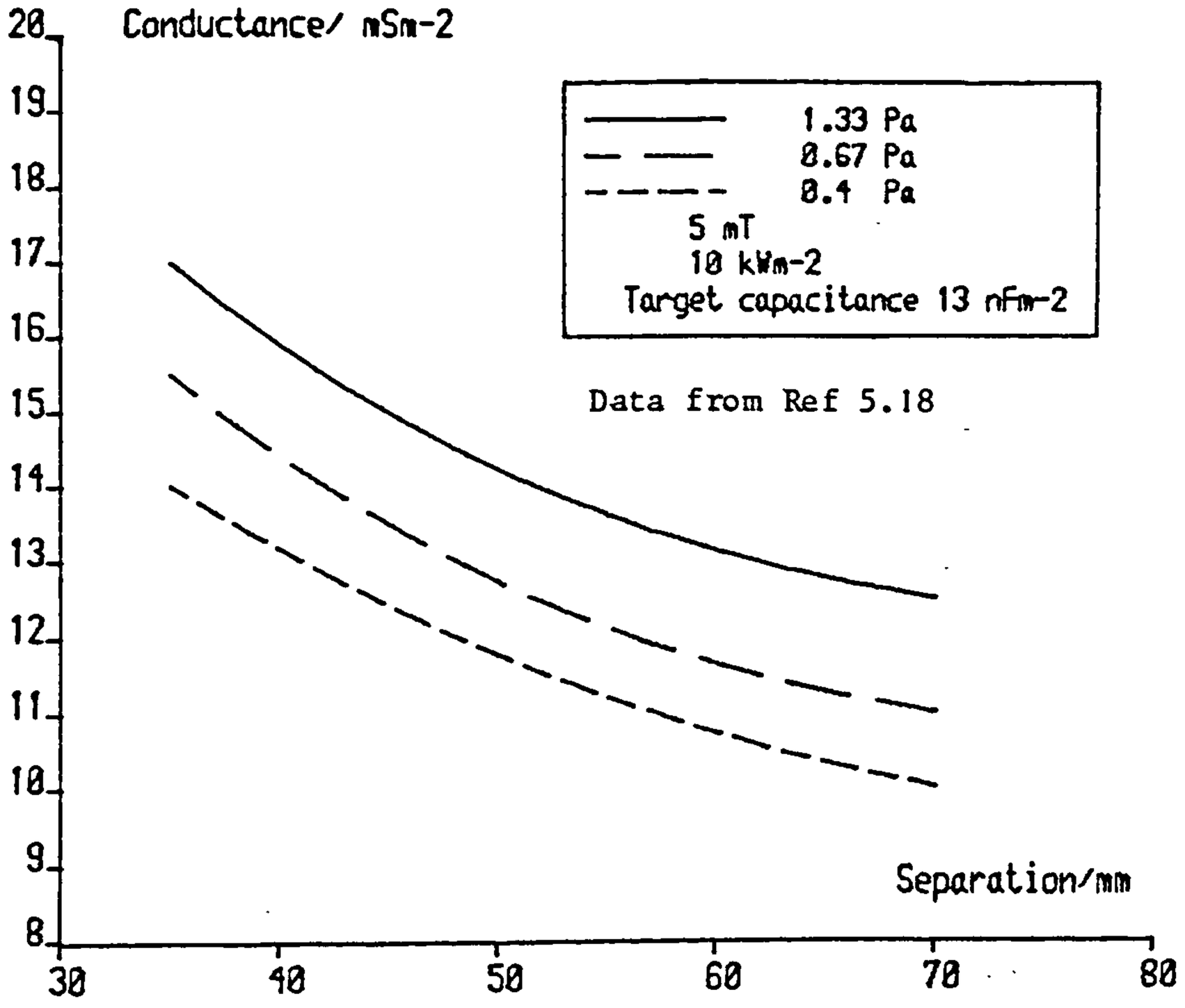

FIG(5.18a):Conductance /substrate-target spacing

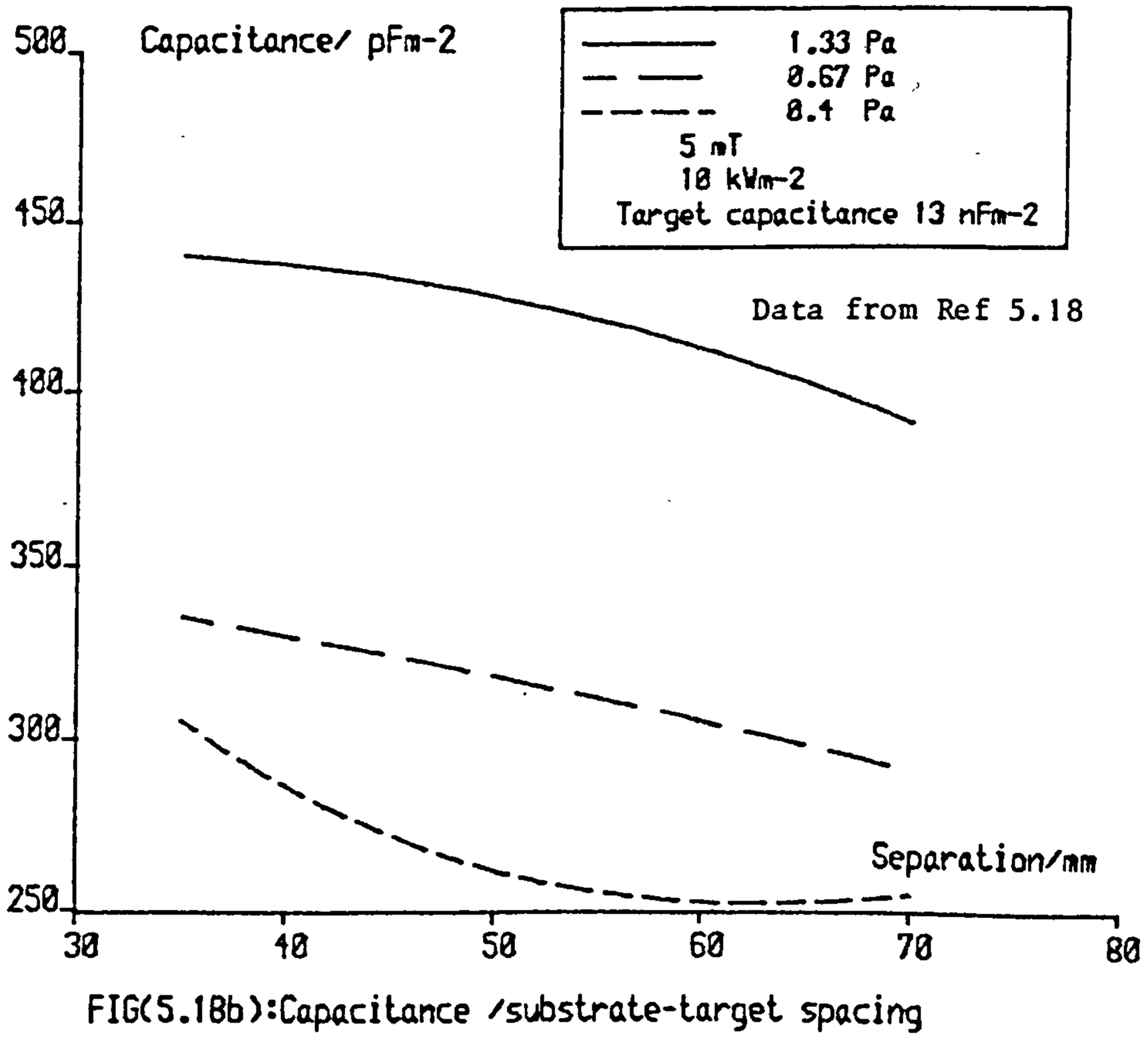

FIG(5.18b):Capacitance /substrate-target spacing

capacitance of the electrode assembly, which is usually much larger than C_g, and X_p is the total parallel reactive component.

It is shown in Appendix VII, proof 4, that in solving this equation for $Z_g = R_g + iX_g$, the uncertainty in the quantities is given (in the case of sputtering chambers) by

$$\Delta R_g \sim \frac{1}{X_p^2}\left[\Delta G + \frac{2G\Delta X_p}{X_p}\right] \qquad 5.25a$$

$$\Delta X_g \sim \frac{\Delta X_p}{X_p^2} \qquad 5.25b$$

if ΔG_g and ΔX_p are the uncertainties in the input quantities G_g and X_p respectively.

Typically, if $G = 2.2 \times 10^{-4}$ S, $X_p = 71.3 \times 10^{-4}$ S, $\Delta G_g = 5.8 \times 10^{-6}$ S $(= 0.026\ G)$ and $\Delta X_p \sim 8.5 \times 10^{-4}$ S $(= 0.12\ X_p)$ the series load Z_g is expressed from equations 5.24 and 5.25 as

$$Z_g/\Omega = 4.32 \pm 1.04 - i(140 \pm 16.8) \qquad 5.26$$

and it is seen that an error of 25% in R_g (and 12% in X_g) can be inherent in this kind of manipulation.

Data such as those shown in Figs. 5.17 and 5.18 should be viewed in this light. If they are used to match a load to a generator errors may easily accrue, and components must be fully adjustable.

5.5.2 Loosely coupled resonant circuits

If the load Z_g forms part of a coupled resonant circuit as in Fig. 5.19, the input impedance Z_i may be written from standard network theory (5.19) as:

$$Z_i = \frac{\omega^2 M^2}{R_g} \qquad 5.27$$

if the other resistances in the circuit are smaller than the series resistance of the discharge, R_g. The resonance has the effect of

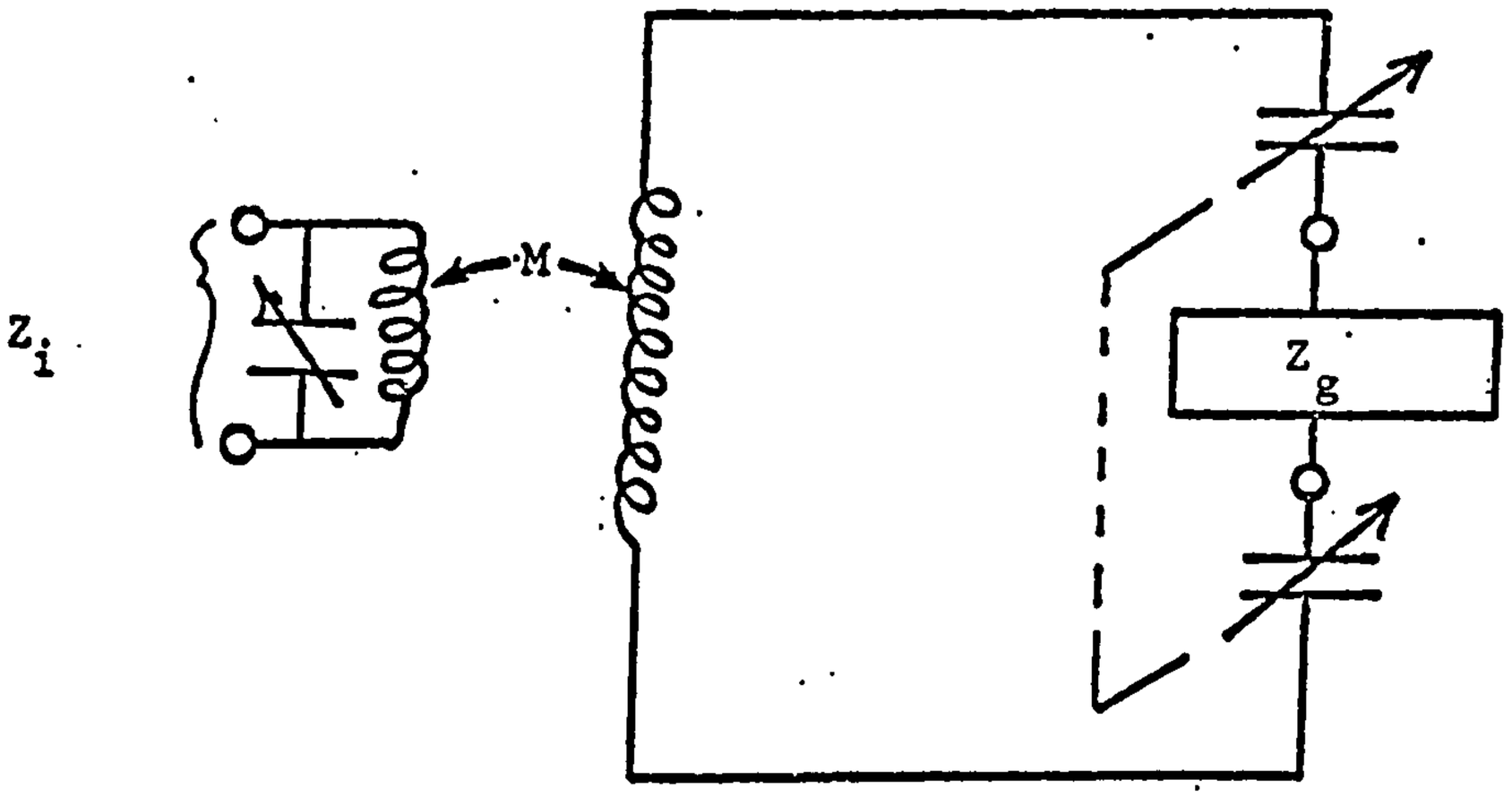

Fig.(5.19): Circuit for matching balanced load

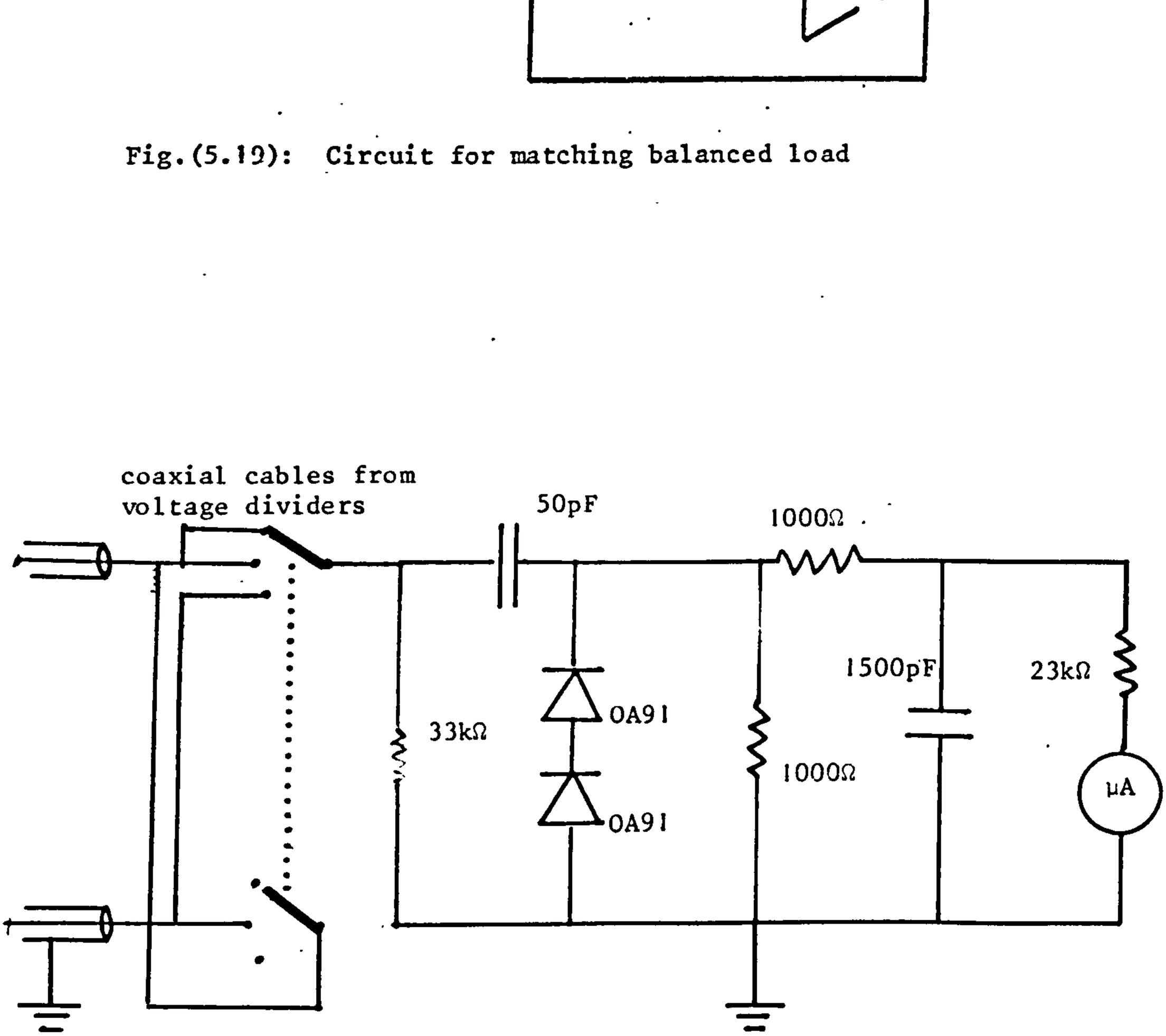

Fig.(5.20): RF kilovoltmeter

nullifying the reactive component.

At the working frequency, using the illustrative Z_g of equation 5.26, this relation becomes:

$$Z_i = 1680(M/\mu H)^2 \qquad 5.27'$$

and the load on the generator (at the end of the $\frac{1}{2}$-wave line) can be altered by varying the mutual inductance. This can be done in a continuous way if one of the coils is smaller than the other, by mounting the smaller inside the other and rotating it about a diagonal to reduce its flux linkage. Alternatively, the inner coil may be stretched or compressed to change M according to equations 5.15' and Fig. 5.13, which was the technique employed for this work. The input impedance should be 1350Ω, the output impedance of the generator, and thus the mutual inductance must be of the order of 1μH.

In the case of the double electrode system, the fact that two discharges are in anti-phase suggests that their impedances should be combined as though they were in series (i.e. simple addition of their series impedances) but component values appropriate to this, according to equation 5.27', did not yield a well-matched line. The uncertainty in the stray capacitances, particularly that of the electrodes (with the unknown effect of the cooling water), was probably the cause of error, as mentioned in the previous subsection.

The arrangement of Fig. 5.19, known as loose coupling, was used for depositing films using the double electrode system, but the ratio of the reflected power to the incident power was always greater using this technique than when the L-section network was used.

5.6 RF electrical measurements

5.6.1 Power

A 'Bird' 'Thruline' directional coupler (5.20) was used for power

measurement, being inserted in the line without difficulty. Both forward and reflected powers are displayed continuously, which is of extreme usefulness in matching impedances. The instrument can be adapted for RF powers between 5 W and 5 kW, and the range from 50 to 2500 W was available in our case. Directional couplers are discussed by Monteath (5.21) and Early (5.22), and operate by measuring the voltage induced across a load inductively coupled to a line, which is proportional to the power travelling therein. The measurement of RF output powers is reviewed by Conhaim (5.23) and Rumfelt et al (5.24), and the behaviour of this instrument is described in section 6.7.2. An RF standing wave ratio and power meter was constructed according to the outline given in the 'Radio Amateur's Handbook' (5.25) but it was not found successful in this application.

5.6.2 Voltage

Shown in Fig. 5.20 is a circuit which was developed for the measurement of RF voltages in the region 0 to 10 kV. The voltage on the electrode terminals is dropped by capacitive division, and then rectified (using special low capacitance diodes) to pass a current through a moving coil meter: a mode of action based upon that of the 'diode clamp' (5.26). Calibration was performed with a n oscilloscope using a high voltage probe, and the accuracy of measurement of voltages in the keV region is estimated at $\pm$ 100 V. The operation was found to be satisfactory, albeit with a small drift over long periods of time.

5.7 Summary

The theory of RF power oscillators has been developed almost from first principles, and some of the practical techniques for their construction have been introduced. The methods by which power may be delivered to the sputtering discharges have been discussed, in the light of a knowledge

of the series and parallel impedances. Measuring power and voltage at radio frequencies has been seen to be relatively easily accomplished.

CHAPTER 6

RF SPUTTERING UNIT: OPERATION AND PERFORMANCE

The description of the operation and behaviour of RF sputtering units in Chapters 5 and 6 has been quite general, and results obtained from the laboratory system have been merely instantiated. This chapter consists of a brief presentation of the procedures used for depositing glass films and for measuring their thickness.

6.1 Electrode voltages

In the case of the grounded diode arrangement, the electrode voltages are in phase; in the disc and annulus system, they are in anti-phase. The kilovoltmeter shown in Fig. 5.20 possesses a switch setting for adding the electrode voltage signals, to ascertain their phase relationship, which can be in doubt during experimentation with matching techniques in the double electrode system.

Changes in sputtering conditions can most easily be observed through monitoring the electrode voltage, which, in cases of poor power matching, can be seen to fluctuate according to the proximity of objects (and personnel) in the laboratory. For the majority of deposition runs, the peak-to-peak voltage on the electrodes was measured at 3 ± 0.1 kV, but a range from 1 to 5 kV was available.

The setting of the oscillator anode supply Variac was used throughout for the adjustment of the electrode voltages and thus the power entering the chamber. Its effect was found to be almost linear for settings below ~ 5 kV.

6.2 Magnetic fields

It was found convenient to use a moderate magnetic field of 3 mT for almost all film deposition, at which setting the current in the field coils was 2.5 A. Since, in this case, a power of about 300 W is

dissipated in each winding (of volume 2.4 x 10^{-4} m^3), the maximum temperature attained can be calculated from Fig. 4.12 to be about 40°C. This was confirmed approximately by experiment, although good thermal contact between the winding wire and the thermocouple was difficult to achieve.

The immediately observable effects of applying the field to the plasma were a reduction in the RF sheath thickness and the constraint of the plasma further to the centre of the chamber. Changes could be measured in electrode voltages and power readings as the magnetic field altered the glow impedance and caused mis-match.

6.3 Film deposition procedure

The surface of the substrate table and that of the target were cleaned with alcohol and the substrates were placed in position with a portion masked to provide a film edge, as shown in Fig. 6.1a, a photograph of the sputtering discharge. The charging port was then closed, and the chamber was evacuated (usually overnight) to a base pressure of about 5 x 10^{-5} Pa with the mercury vapour pump described in section 4.5. Before commencing a sputtering run, the McLeod gauge mercury vapour trap was filled with liquid air and the gauge was pumped for a period of over ten minutes.

Prior to the admittance of argon, the aperture of the diffusion pump inlet was reduced to a constant setting (half a turn of the control wheel). A needle valve on the gas inlet was found to be necessary to provide an adequately controlled gas flow rate, and its settings were sufficiently reproducable to allow the approximate calibration of its scale against pressure. A gas cylinder head pressure of 0.1 Pa (1 kgm^{-2}) was used. It was not found practicable to monitor the argon flow rate, as an alternative to continual pressure measurement, without employing

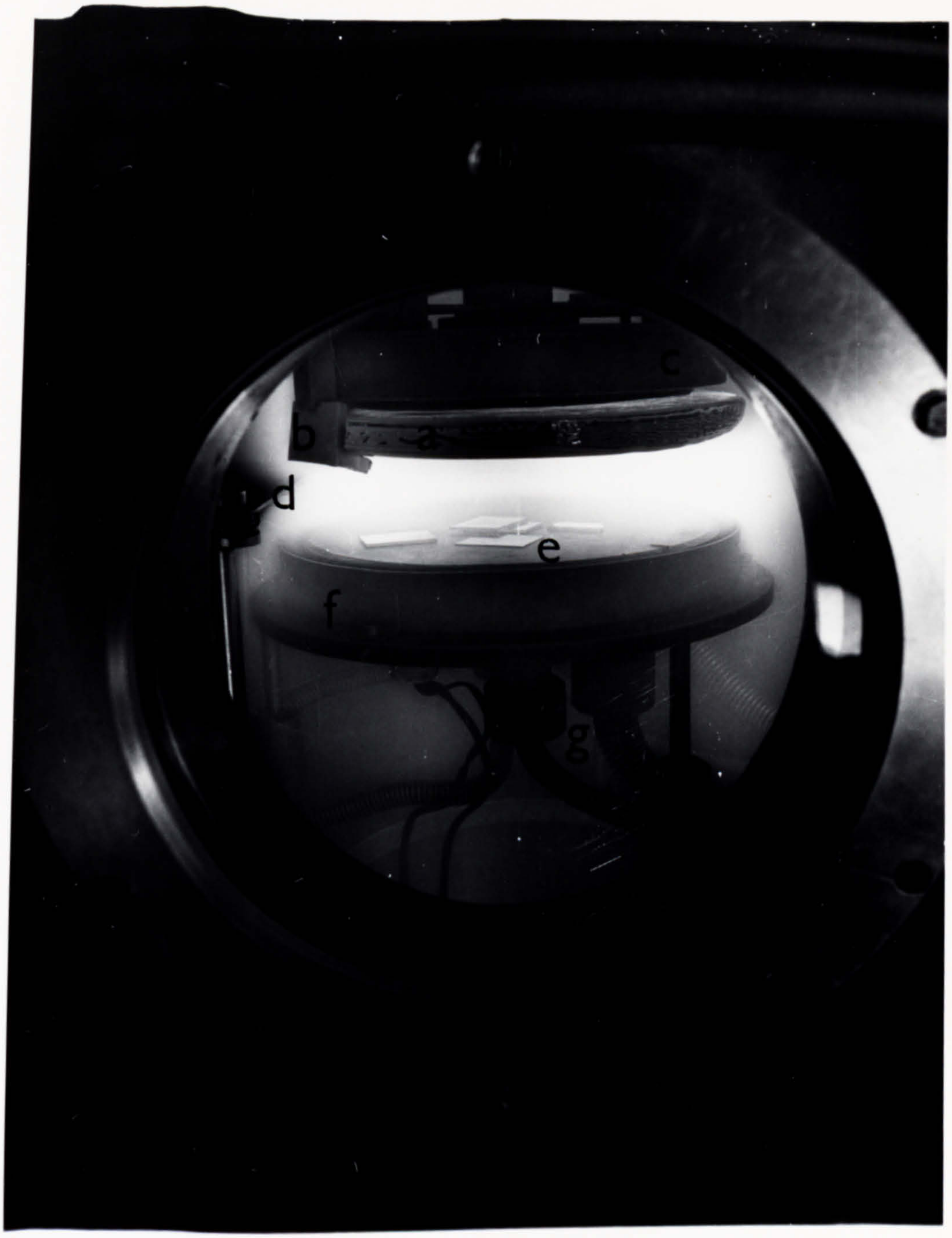
c
b
d
e
f

Fig.(6.1b): View of target surface during sputtering. The RF sheath may easily be seen, the light from the target surface less so.

specialist equipment, because commercial instruments capable of measuring flow rates below 417 mm^3s^{-1} (25 cm^3min^{-1}) were not available.

When the pressure in the chamber was stable and correct, the shutter was closed and argon was flushed briefly through the chamber while the magnetic field coils attained their steady temperature distribution.

Once the discharge had been struck, and the matching capacitors adjusted for maximum electrode voltage, approximately one minute was allowed to elapse (for the sputtered flux to attain its stoichiometric composition) before the shutter was opened and the timing of the deposition run started. A few seconds were sufficient for the necessary small changes in matching settings contingent on the movement of the shutter, as mentioned in section 4.3.5.

All the instrument readings were recorded on sheets similar to that shown in Fig. 6.2, where typical conditions are indicated.

At the end of the run, the H.T. was disconnected, the gas leak valve closed, the McLeod gauge and the diffusion pump sealed off, and air admitted to the chamber through the backing line. The samples were removed with tweezers and stored in polythene pouches.

6.4 Target heating

After less than a minute from the start of the run, a red glow could be observed, localised to the sputtered surface of the target opposite the area of contact of each of the electrodes. In Fig. 6.1b the light from the target surface can with difficulty be seen.

If an object is placed in the RF sheath, but not in the discharge region, a well defined shadow is cast in this light which moves without observable delay with the object. It is probable that direct ionic impact is involved in the production of visible photons as mentioned in section 2.13, rather than the light being considered as black-body

SPUTTER DEPOSITED FILMS

sheet no: 19

DATE 22/7/80

Electrodes: Single Ended ✓ Balanced

Matching: LC filter

Run code: C2

RF
- Forward power: 575 W
- Reflected power: 450 W
- Delivered power: 575 − 450 = 125 W
- Electrode voltages:
  - Disc: 3 kV
  - Annulus: 3 kV

DC
- Anode voltage: 1220 kV
- Anode current: 225 mA
- Power: 275 W

Efficiency: 125/275 = 45.5 %

Magnetic Field: 3 mT

Pressure: [Valve setting 220] 8 μbar

Sheath thickness 10 mm

Cooling
- Disc ✓
- Table ✓
- Annulus ✓

TIME: 245 min.

THICKNESS; 4125 Å

COMMENTS: 11-55 h 13-00 , 14-25 h 17-25

Fig.(6.2): A typical sputter run log sheet

radiation from thermal spikes. However, the contribution of the elevated temperature of the target cannot be ruled out because no light is emitted during the initial 30 to 40 seconds of the run.

An investigation of the temperature of the target surface was attempted, but was frustrated by many considerations, particularly the difficulty of ensuring good thermal contact between a thermocouple and the glass without affecting the RF sheath (epoxy resin adhesives proved reactive in this environment), and because of the very low thermal conductivity of the glass. Glass targets of 20 mm thickness reached a temperature typically in the region of 100°C (estimated from thermocouple measurements at the side of the target) with an input power of about 50 W, an electrode voltage of 3 kV p-p, and with cooling water flowing, but this is not a measure of the surface temperature. No meaningful data were recorded from studying the light emitted from the surface with an optical pyrometer (6.1) or a spot photometer (6.2).

6.5 Target shattering.

In the preliminary stages of the study, the glass targets were found to shatter after a few minutes of sputtering. This problem has been encountered by Holland et al (4.21) with glass targets at high deposition rates, but these workers find that pure silica targets do not shatter under the same conditions.

Many different glass target thicknesses were used, but no clear trend could be identified. A thin target might be expected to be more effectively cooled by the electrodes,but a thick one has a reduced thermal gradient. Thicker targets, with their increased robustness, were found generally to be more successful.

Targets were found to shatter very much more readily in the disc and annulus system than in the single ended mode, with electrode voltages of the same amplitude. Notably, the only reference in the literature to

the phenomenon (4.21) also concerns the disc and annulus system, and we can perhaps infer that the electric field in the glass is involved, since it is very much greater when the electrode voltages are in antiphase. The shattering must be due to a combination of high thermal and potential gradients.

It is to be regretted that due to the high cost of thick glass targets, the long turn-round time, and the characteristically large fluctuations in glass properties, no exhaustive investigation of the problem of target shattering could be made. The preservation of the specially prepared targets described in section 1.6 was of paramount importance and consequently the sputtering conditions employed were constrained to low power settings, and comcomitant low deposition rates. In developing the sputter deposition of thin glass films, with the disc and annulus system, this problem must first be solved.

6.6 Film thickness measurements

Many methods of measuring film thicknesses are in common use. One of the most well-established is ellipsometry, in which plane polarised light is reflected from a coated surface and the parameters of the elliptically polarised reflected wave provide information on the thickness of the coating. Rothen (6.3) claims an accuracy of 0.1 Å in measuring transparent films on metal surfaces for a range of film thicknesses from many thousand angstroms down to 1 Å. Heavens, in his review article on the properties of thin films (6.4), suggests that the constants of the material can affect the results of optical methods in unsuspected ways.

For our purposes, the step produced by the partial masking of the substrate during deposition was used in all cases to estimate the thickness of the films. In the early runs, interference fringes were set up between the substrate and an optically flat disc, using the monochromatic light from a sodium vapour lamp, and the fringe shift at the film edge was

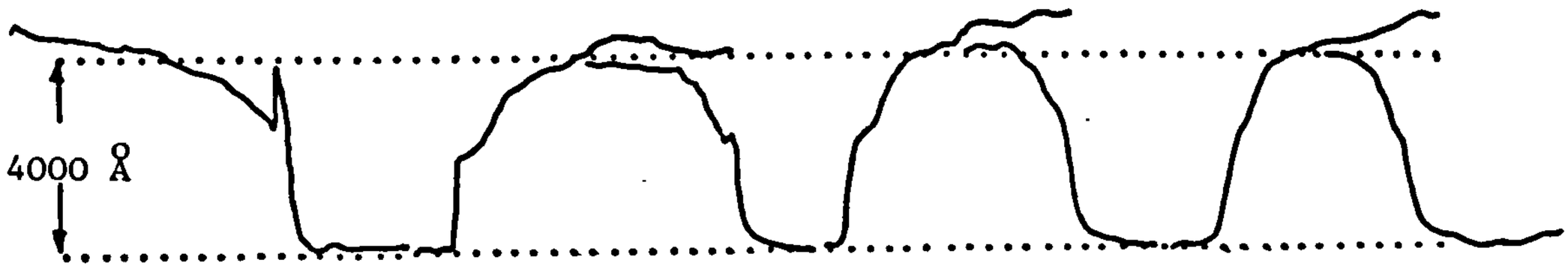

Fig.(6.3): Talystep traces at seven positions along the edge of film C2. (Scale 4, 400 Å div^{-1}). The traces have been redrawn for the purpose of the diagram.

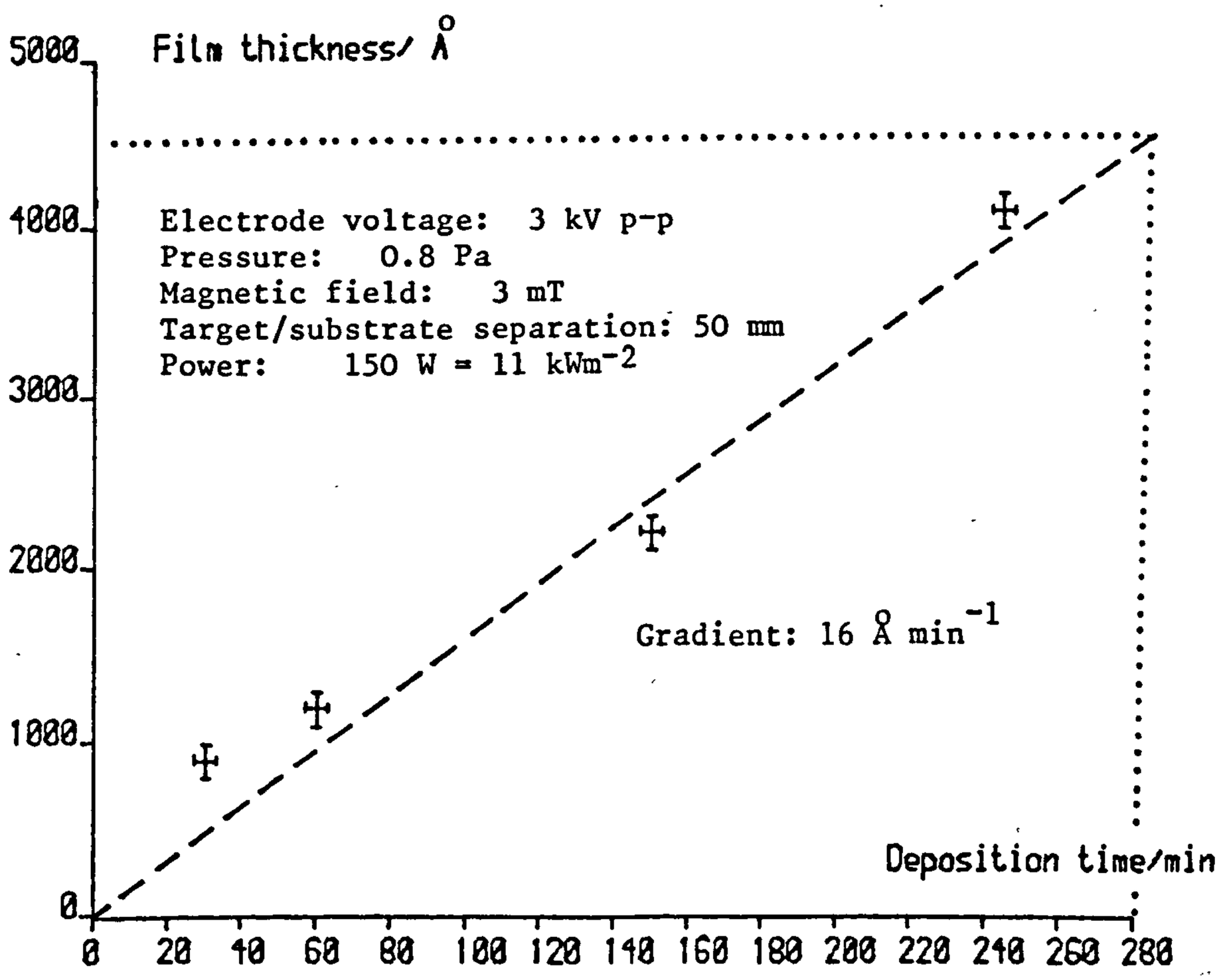

FIG(6.4):Film deposition with grounded diode system

observed. This method was not found satisfactory because of the great difficulty in accurately estimating the shift, and its general inconvenience. Jones et al (4.18) have used a similar method for SiO_2 films and claim a precision of 0.1 fringes, or 200 Å.

In preference, a Talystep instrument was used, whose mode of action is to amplify the vertical motion of a stylus traversed over the step (6.5). Fig. 6.3 shows typical traces obtained in this way, measured at several points along the edge of a film. The surface of the film may be seen to be rougher than the substrate glass, which was in this case a microscope slide. When films were deposited upon surfaces too uneven for measurement by the Talystep instrument (for example on copper and beryllium copper foils), a half masked slide was placed adjacent to the substrates in the chamber and the step produced on it was measured. A constant deposition rate was assumed over the table surface, as no variation could be measured. The accuracy of thickness measurements is estimated at 100 Å. Talysurf measurements of the depth of a scratch through the film were used by Davidse and Maissel (4.1), but this is obviously impossible in the case of glass films on glass substrates. Interference colours could be seen in white light in the films deposited on metal sheets, which lent support to the thickness determinations.

The graph of film thickness against deposition time, Fig. 6.4, was obtained in four separate sputtering runs using the grounded diode system, and shows a scatter of points indicative of the reproducibility of conditions in the sputtering chamber. The rate of glass film deposition is calculated at 16 Å min^{-1}, with the conditions shown in the figure, which is low compared with rates achieved by most other workers (4.1, 4.21) but is consistent with an extrapolation to lower powers of the deposition against power curves of Putner (6.7). A rate of 70 Å min^{-1} was attained in a 7 minute run before the shattering of the target. It is modern practice to use quartz crystal rate monitors (6.8) in deposition plants of all kinds.

Their mode of operation is to measure the change in the natural frequency of oscillation of a crystal as the film is deposited upon it. To calibrate such a monitor, a knowledge of the physical constants of the film material is required, so that the interaction of the film with the crystal can be parameterised. The necessary quantity, called 'Z-match' is given by:

$$Z = 2.97 \times 10^{7} (\rho s)^{-\frac{1}{2}} \qquad 6.1$$

where ρ/kgm^{-3} and s are the density and shear modulus of the film respectively. This calculation is performed automatically by modern deposition controllers, but such sophistication was not considered necessary in our case.

6.7 General

The following additional points are of general interest.

6.7.1 Oxygen content of gas

Small bright sparks could be seen on the grounded parts of the electrode and substrate assemblies when the power matching to the discharge was imperfect. Davidse and Maissel (4.1) observed a similar phenomenon during experiments to determine the deposition rate as a function of the oxygen content of the sputtering gas, but provided no explanation.

Since a high oxygen content reduces the deposition rate sharply (4.1, 4.19), and the observations above imply that oxygen might be present, an experiment was performed in which 99.999% pure argon was supplied to the chamber from a small glass bottle mounted close to the gas leak valve. The sparks were again observed but unfortunately it was impossible to determine whether they appeared more or less readily, because of the uncertainty of power input to a badly matched load.

The diffusion pump, being unusually large, might be expected to overwhelm tiny air leaks in the chamber, and hence oxygen (and nitrogen) contamination of the gas is possible. The argon was not dried prior to

its entry into the chamber, the effects of which are further unknown factors.

The production of these sparks remains unexplained.

6.7.2 Power meter performance

The commercial RF power meter used (5.20), indicated in section 5.6.1, was found to operate adequately. The forward power altered as the matching conditions were changed, as is to be expected if the power drawn from the generator changes. The difference between the forward and reflected powers was used as an estimate of the power entering the plasma. Power readings were considered accurate only to about 20%, which limits the comparability of the measured deposition rates with those of other workers.

6.7.3 Low deposition rates

The reasons for the low deposition rates can be collated as follows: (a) low DC input powers were used to avoid shattering the targets; (b) power matching to the double electrode system was poor, in general; (c) the substrates were not bonded to the substrate table, and their surfaces were consequently at an elevated temperature (indium foil has been used to improve thermal contact in this situation); (d) according to Ref (4.1), thicker targets (above 5 mm) will be expected to have a reduced yield, although no explanation is provided for this statement; and (e) the surfaces of all the glass targets used were fire polished. As shown in section 2.3 the sputtering yield is increased sharply at oblique angles of incidence (2.1) and possibly some of the work reported was performed using roughened glass surfaces. Also, slight oxygen contamination of the discharge gas is possible, with deleterious effect on the deposition rate.

6.7.4 Sputter-up

If it is impossible to avoid glass targets shattering, it might not be necessary to halt the deposition run if the chamber were to be redesigned upside down, and the target held in position by gravity. After shattering, the sherds would remain as they were, and sputtering could continue. The energy loss by sputtered particles travelling upward against gravity to the substrate is completely negligible. The substrate specimens would each have to be bonded effectively to the substrate table, which could be advantageous as mentioned in section 6.7.3, but would not be as convenient as the existing system.

6.7.5 Target thermal contact

In an attempt to improve the rate of removal of heat from the target, silicone grease was smeared over the two electrodes. No real difference could be observed, and if small amounts of grease were present in the region between the electrodes (on the back surface of the glass target), which is difficult to avoid, the RF currents flowing through them caused immediate glass shattering.

6.8 Summary

The method of operation of the experimental RF sputtering unit has been indicated, using which glass films have been successfully deposited. General points of interest have been noted, particularly the reasons for the generally low rates of deposition, and the problem of the breaking of the targets.

PART B

SPECTROSCOPY OF GLASSES

Chapters 2 to 6 have been concerned with the sputtering phenomenon and its use in the deposition of thin glass films. The remainder of this thesis describes the various spectroscopic techniques that were employed, with greater or lesser efficacy, in the analysis of the films. It will be seen in Chapter 8 that a familiarity with sputtering theory is necessary since the apparatus to be described in Chapters 7 and 8 (with which the electron beam surface analysis was performed) possesses the facility for ion bombarding the analyte, and it is by this means that what are commonly referred to as 'depth profiles' of the sample can be obtained.

CHAPTER 7

ELECTRON SPECTROSCOPY OF SURFACES : THEORETICAL

Electron spectroscopy is the analysis of the energy of the electrons scattered from a bombarded surface. Any form of primary irradiation may be used, for instance X-rays, ultra-violet light, or energetic ions. The study to be described was performed using excitation by electron beams of moderate energy ($\sim$ 3kV) which is a popular technique because of its convenience and controlability.

If a surface is to be bombarded with electrons, the ambient gas pressure must be extremely low. Ultra-high vacuum (UHV) technology (7.1) is required, not only to facilitate this but also to maintain the atomic cleanliness of the surface. The rate of contamination of a surface may easily be calculated from the kinetic theory of gases. From the equations given by Prutton (7.2) the time taken for the equivalent of a monolayer of gas to strike a surface may be calculated for a given temperature and pressure. For an initially gas-free surface (produced, for example, by cleavage of a crystal in a vacuum), the time taken for the formation of a monolayer of nitrogen at a pressure of 10^{-4} Pa ($\sim 10^{-6}$ Torr) is 2.3 s, if a sticking coefficient of unity is assumed. This is obviously far shorter than the time required for an experiment, and it was not until the advent of UHV techniques that surface spectroscopy became possible. At 10^{-8} Pa ($\sim 10^{-10}$ Torr), a monolayer of nitrogen would take 6 hours to form under the same, somewhat artificial conditions, and it is therefore in this pressure regime that surface spectroscopy must be carried out.

The very high degree of sample cleanliness required in all such work contrasts with that appropriate to RF sputtering, where only technical vacuum ($\sim 10^{-3}$ Pa) is required.

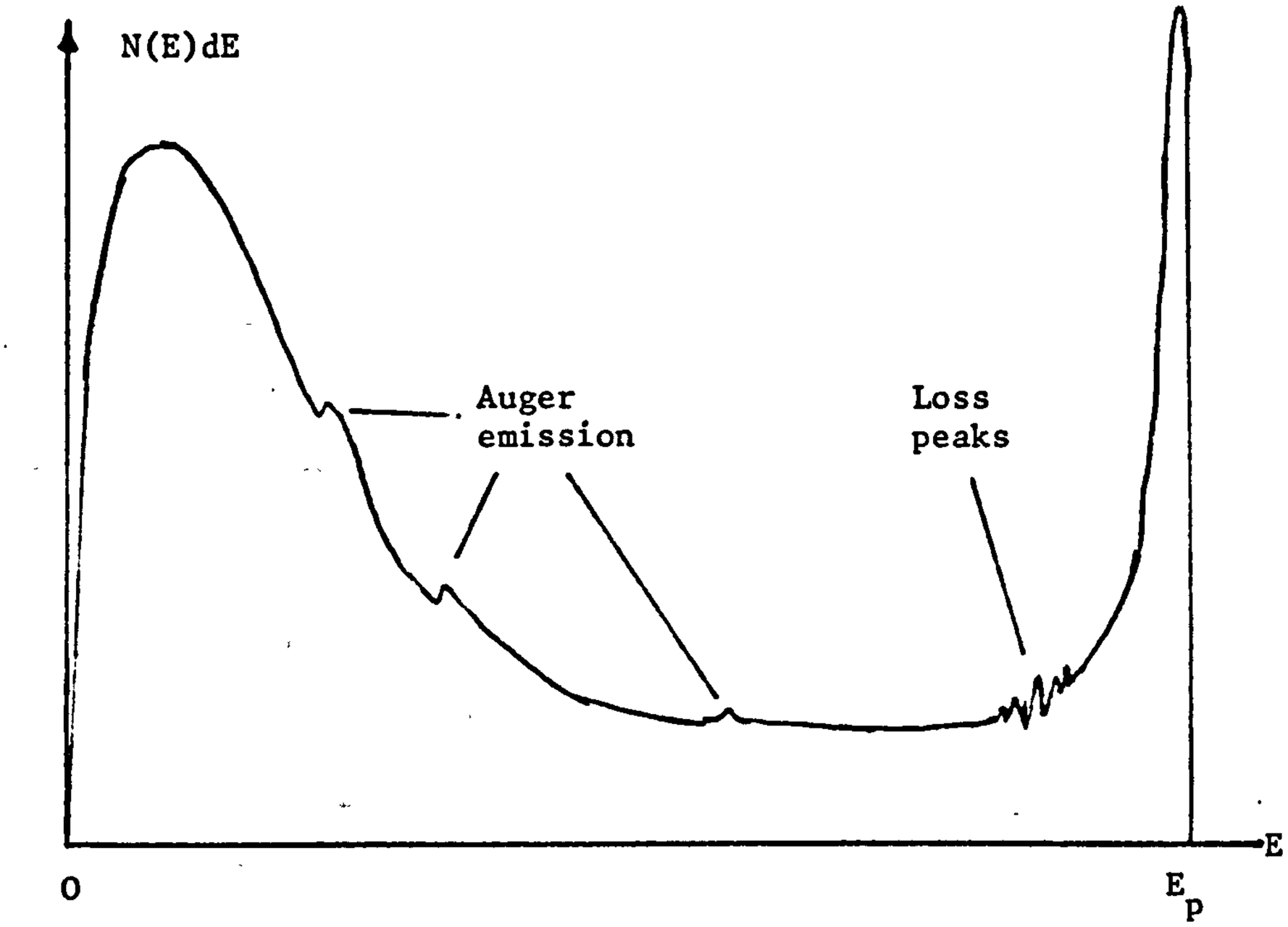

Fig.(7.1): Secondary electron spectrum

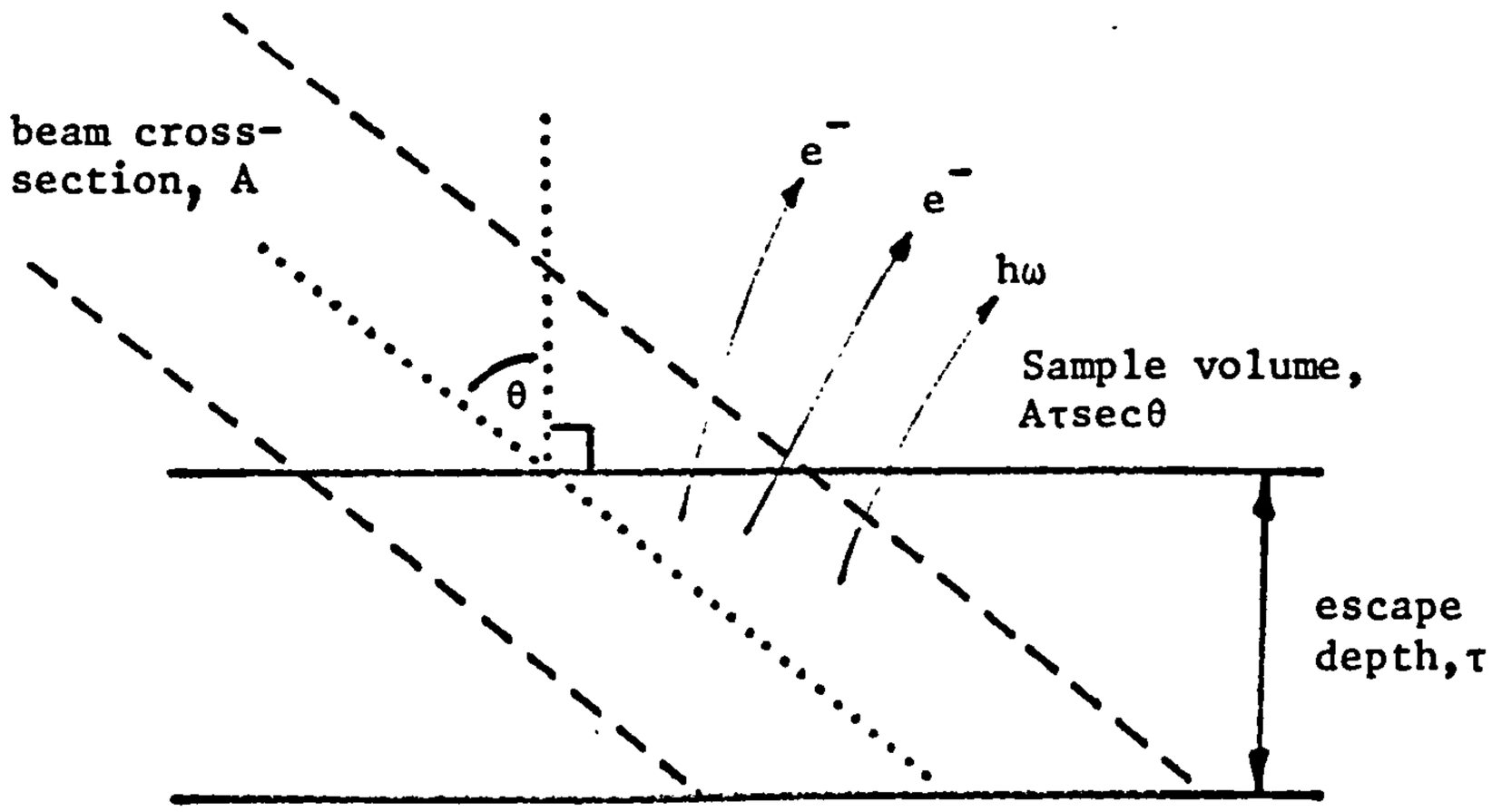

Fig.(7.3): Electron beam bombardment nomenclature

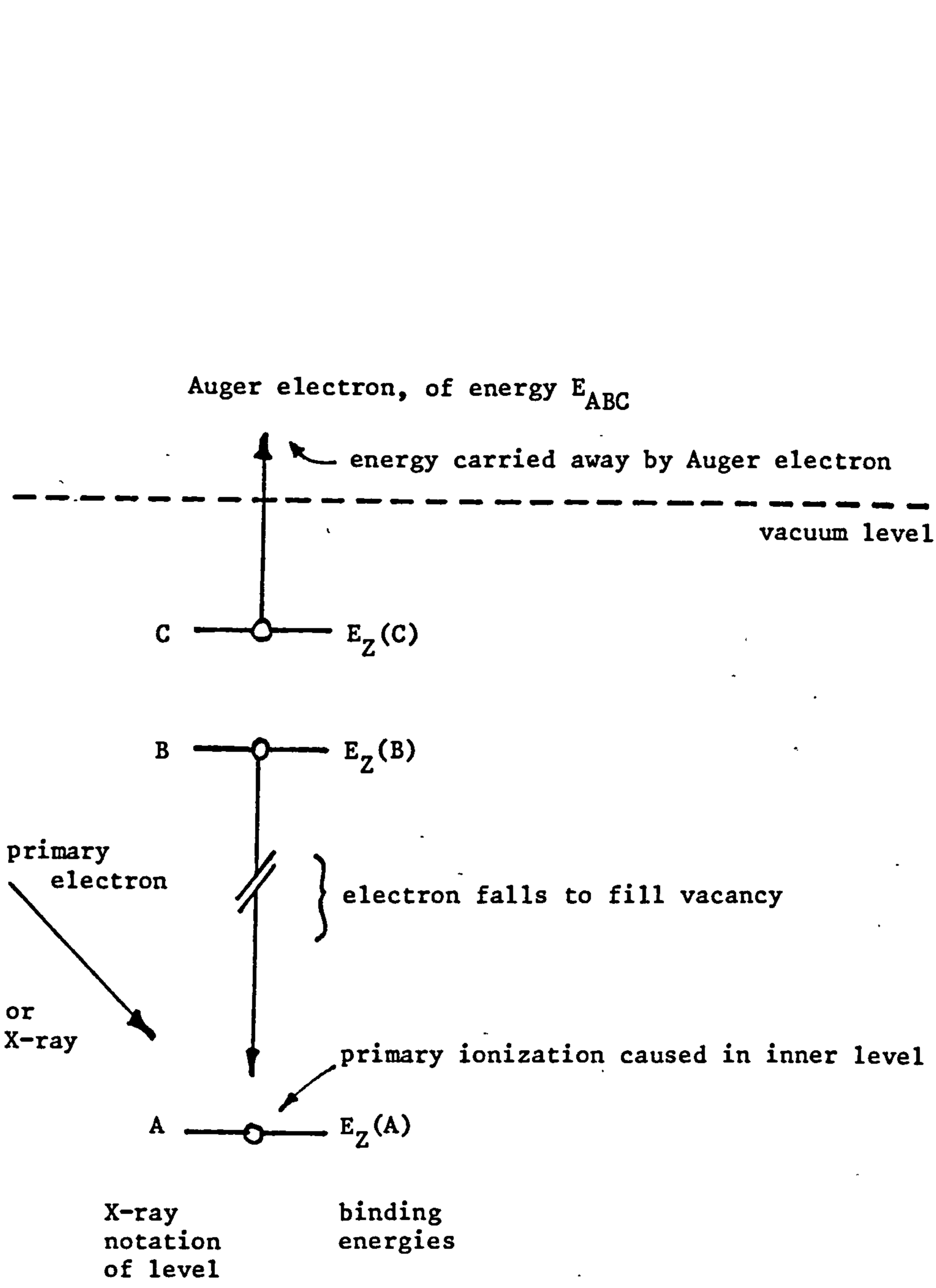

Fig.(7.2): The atomic Auger process. The transition is labelled according to the holes in the order of their creation; in this case, ABC.
Z is the atomic number of the atom.

When an electron beam is incident upon a surface, the scattered electrons are found to have an energy distribution as shown in Fig. 7.1. There is a sharp peak at the primary energy E_p due to elastic scattering, and a steeply sloping background at low energies, peaking at around 10eV, comprising the 'true secondaries' from the collision cascade.

Superimposed on this curve are features due to the emission of Auger electrons (whose energy is fixed) and structure in the tail of the elastic peak due to primary electrons whose interaction with the surface has caused them to lose fixed amounts of energy. These two effects can be used to characterise the surface, and the techniques of Auger electron spectroscopy (AES) and electron energy loss spectroscopy (ELS) have been developed since the 1960s as improved electron spectrometers have become available. The Auger effect was first discovered using X-rays in 1925 (7.3).

Electron stimulated AES and ELS were used for the major part of the study of glass films and the glasses from which they were made ('source glasses'), and the suitability of these techniques for the task is best described after a brief theoretical exposition.

7.1 The Auger effect

If an atom has been ionized in an inner shell, it is energetically favourable for an electron from a higher level to take the place of the lost electron. The energy difference may be manifested as a quantum of EM radiation, or may be given, through a radiationless transition, to a third electron, which is ejected from the atom. The former process is fluorescence and the latter Auger emission, as illustrated in Fig. 7.2. The relative rates of these two processes are discussed below.

The initial vacancy may be created by X-radiation (7.4) or by ion bombardment, but because of the very great simplicity and availability of

electron guns, most Auger work has used electron beams of energy in the low keV range, as is the case in this study. The reviews by Gallon and Matthew (7.5), Gallon (7.6) and Chang (7.7) are indispensable references for all aspects of Auger spectroscopy.

7.2 Labelling of Auger lines

An Auger transition is conventionally labelled according to its initial and final vacancies, in the X-ray notation as shown in Fig. 7.2 and Table III. Chang (7.7) points out that implicit in this notation is j-j coupling (7.9) in which the total angular momentum j of each electron (the combination of its spin and orbital angular momenta) is coupled to the j vectors of the others; this scheme is valid only at the high energies found in the core levels of elements with $Z>80$. Since Auger spectroscopy is done entirely at energies below about 2.5 keV, where the interaction of the total spin (S) and the total orbital angular momentum (L) vectors dominates (L-S coupling), the precise assignment of Auger lines according to the X-ray notation is made difficult.

However, turning from the case of the isolated atom to Auger emission from glasses, we find that the atomic notation remains useful even after the atoms have been combined in a solid, since the inner levels remain atomic in character. The situation in amorphous solids is distinguished from that in crystals by the formation of localised 'trapping states' (7.10, 7.11) in the gap below the conduction band, between which electrons may move by various 'hopping' processes (7.12), and from which electrons may be excited (across the 'mobility edge') into states of longer mean free path.

Mott (7.10, 7.11) has pointed out that though the creation of band gaps in crystals is usually considered a consequence of the periodicity of the structure, such gaps must also exist in glasses, where there is no periodicity, since most glasses are transparent.

In the light of the approximate nature of our understanding of the electronic states in glasses, the use of the broad X-ray notation is justified. A line caused by an initial vacancy in the K shell of an atom being filled by an electron from the L shell and ejecting an electron from the M shell is written KLM.

7.3 Auger energies

7.3.1 Free atom

A first order approximation to the energy E_A of the Auger emission in the process depicted in Fig. 7.2 can be written (7.5):

$$E_A = E_Z(A) - E_Z(B) - E_Z(C) \qquad 7.1a$$

where the substantial alteration to the energy levels caused by the initial ionization has been neglected. Many improvements to equation 7.1a have been proposed (7.6, 7.8), and one of the commonest is the heuristic

$$E_A = E_Z(A) - \tfrac{1}{2}\left\{E_Z(B) + E_{Z+1}(B)\right\} - \tfrac{1}{2}\left\{E_Z(C) + E_{Z+1}(C)\right\} \qquad 7.1b$$

where the atom ionised in an inner core level is treated as having an atomic number between Z and Z+1. Using X-ray emission data for the energy levels (7.13), equation 7.1b can predict the position of Auger lines to within 5 eV. Matthew (7.14) has used the energy levels of the free ion of the next element in the periodic table:

$$E_A = E_Z(A) - E_Z(B) - E_{(Z+1)+}(C) \qquad 7.1c$$

with improved accuracy. The bases of the various solutions to this problem and their successes have been reviewed by Nicolaides and Beck (7.15) and Barlow (7.16).

Semi-empirical methods, in which experimental data from optical emissions are manipulated to account for the interactions mentioned above, are generally most successful (7.16).

7.3.2 Chemical shifts

Auger electrons emitted from solids are shifted in energy with respect to their emission from a free atom. The screening of the final doubly charged ion by the polarisation of the medium reduces the final state energy and increases the energy of the Auger line. This is known as 'relaxation'. The interaction between the two final state holes must also be considered; both intra and extra-atomic relaxation effects are involved.

In metals, the shift is larger because the conduction electrons can very effectively screen the nucleus, and the energy of the LMM line from metallic arsenic, for example, is 6.4 eV above that from the oxide (7.16).

As will be seen, the absolute energies of the emitted electrons from glasses depends upon the surface charging effect, encountered in all dielectrics, of magnitude contingent upon the geometry of the electron bombardment. In consequence, the relative energies between Auger lines are more easily found.

Particular Auger emissions were identified, in this study, from the standard compilation of Palmberg (7.17), whose spectra were taken from elemental samples and not glasses.

7.4. Auger currents

The efficiency of production of Auger electrons of energy E_A in an homogeneous solid is given by the ratio of the total Auger current $I_A(E_p,E_A)$ emitted into 4π steradians and the primary beam current I_p:

$$\frac{I_A(E_p,E_A)}{I_p} = N(1-\omega)\, r\tau \sec\theta\, \Phi(E_p,E_A) \qquad 7.2$$

where N is the number density of atoms, ω is the fluorescence yield, r (≥ 1) is the backscatter factor introduced to account for the ionizations caused by scattered electrons, τ is the escape depth of electrons of energy E_A,

θ is the angle of incidence of the primary beam and $\Phi(E_p, E_A)$ is the ionization cross-section of the inner levels of the atoms. The geometry is shown in Fig. 7.3.

7.4.1 Fluorescence yield, ω

The competition with the Auger process provided by fluorescence has been mentioned in section 7.1. The probability of photon production after the ionization of the K-shell of the atom has been established from theoretical considerations by Burhop (7.18) in the approximate form:

$$\omega_K(Z) = (1 + aZ^{-4})^{-1} \qquad 7.3$$

and fitting to experimentally determined photon yields sets $a = 1.17 \times 10^6$. For $Z>14$, K-shell electrons are bound too strongly to be removed by a primary beam energy of a few keV, and we can therefore calculate the maximum probability of photon production by transitions involving the K-shell as

$$\omega_{Kmax} = \omega_K(14) = 0.033 \qquad 7.3'$$

For transitions involving the L-shell, the corresponding quantities are

$$\omega_L = (1 + 6.4 \times 10^7 Z^{-4})^{-1} \qquad 7.4$$

and

$$\omega_{Lmax} = \omega_L(38) = 0.032 \qquad 7.4'$$

It is seen that both of these quantities are very small and that the production of Auger electrons dominates (7.19). The form of equations 7.3 and 7.4 has been altered better to fit the experimental data by the inclusion of relativistic and screening effects (7.20), but for low atomic number ($5<Z<18$) their predictions are accurate (7.21). In estimating Auger currents photon production can be neglected.

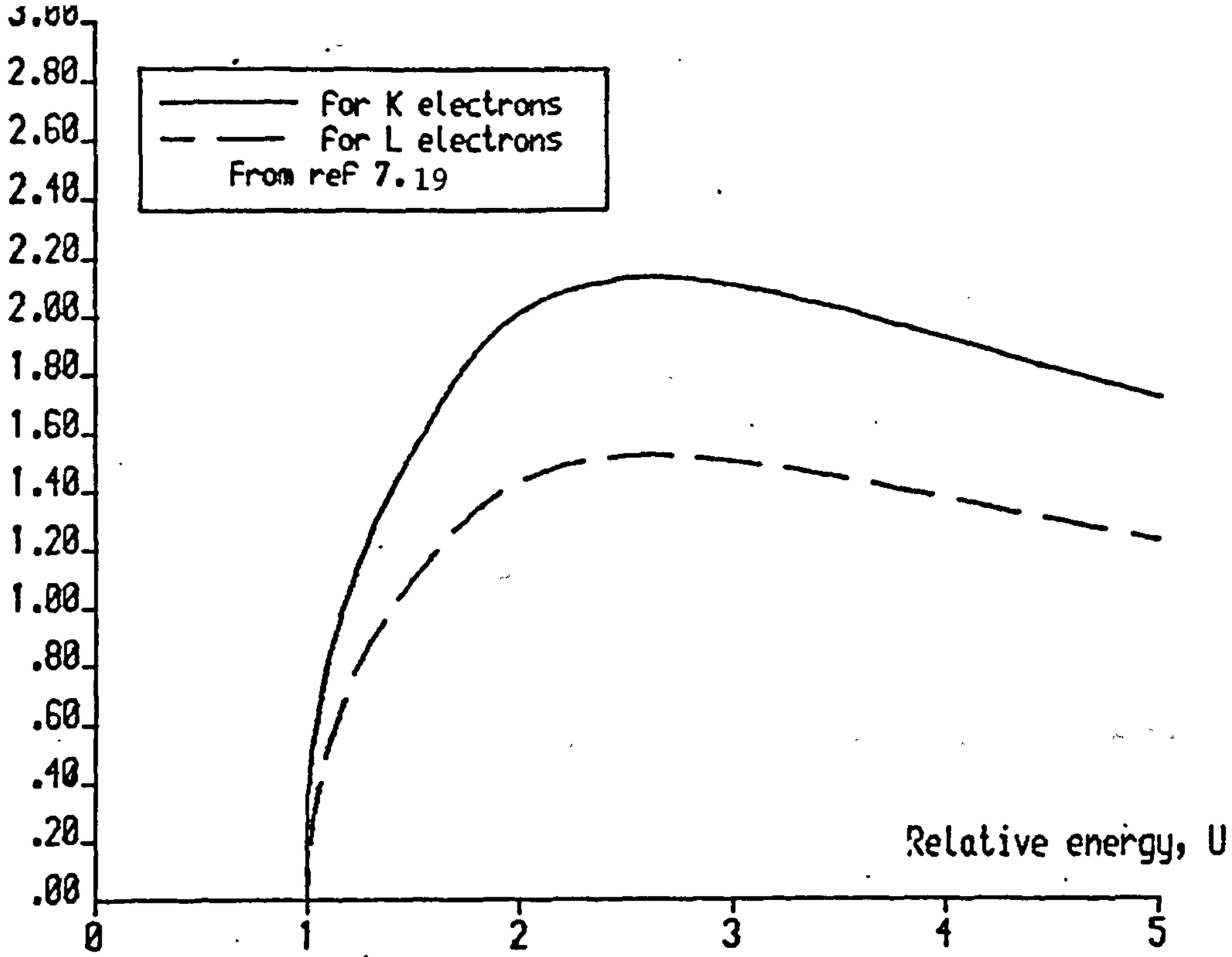

FIG(7.4a)The ionisation cross-section function

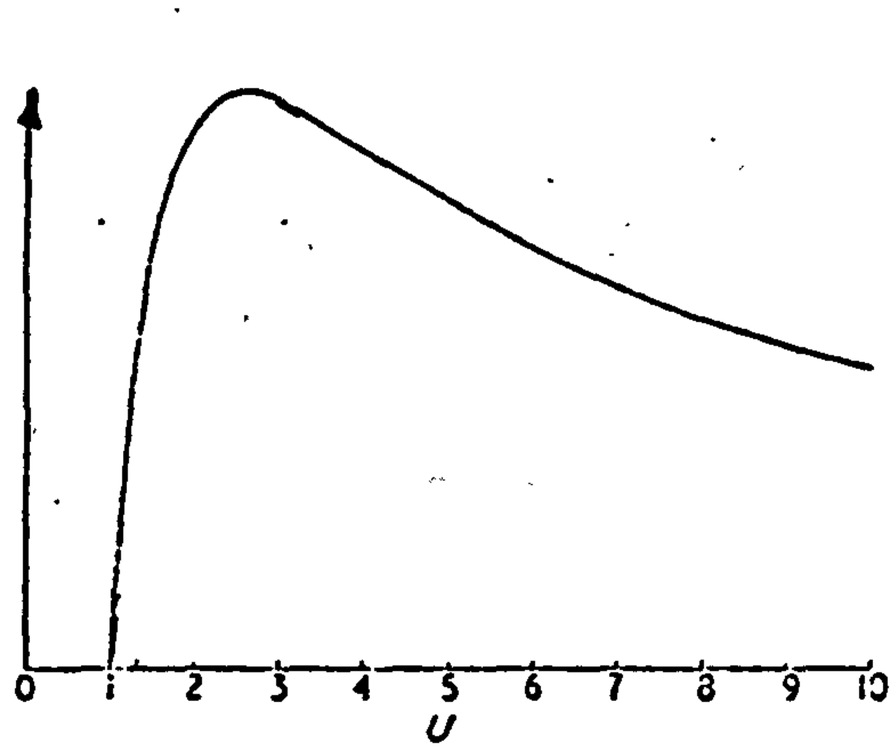

Fig.(7.4b):
Ionization cross-section
Ref.(7.23)

Fig.(7.4c):
Auger current versus
primary energy
Ref.(7.24)

7.4.2 Ionization cross-section, Φ

Worthington and Tomlin (7.22) long ago showed from quantum mechanical considerations that the ionization cross-section of an atom by X-rays may be expressed by the proportionality

$$\Phi \sim \frac{\ln\left[\frac{4E_p}{B}\right]}{E_p E_A} \qquad 7.5$$

This function may be tailored to fit the experimental results by setting

$$B = E_A \left\{1.54 + 2.35 \exp\,(1-U)\right\} \qquad 7.5a$$

with $U = E_p/E_A$, whence Φ goes correctly to zero at both high and low energies, and has a maximum when the primary energy E_p is approximately 2.6 times the Auger energy, E_A. The treatment is considered appropriate for primary ionization by electron bombardment (7.14). The function Φ of equation 7.5 is plotted in Fig. 7.4a in units of 130 E_A^{-2} $\mathring{A}^2$. Gryzinski (7.23) bases an approximation for Φ on a classical treatment and, as Fig. 7.4b shows, a broadly similar function is found. The extent to which these functional forms are valid may be judged by measuring the Auger current from a bombarded solid at different primary energies, for which the results are given in Fig. 7.4c , from the work of Weber (7.24). The 152 eV peak of sulphur was used for this plot, and a shape very similar to the theoretical predictions is observed, but with the peak occurring at $E_p \sim 7E_A$, rather higher than predicted. A typical cross-sectional area for Auger electron production is 10^{-3} $\mathring{A}^2$.

7.4.3 Backscatter factor, r

Electrons which pass through the first few atomic layers of the substrate may yet return to cause ionization if they are scattered through a large angle by the deeper layers. In an analysis of a silicon surface,

using $E_p/E_A \sim 10$, Gallon et al (7.25) have measured a backscatter coefficient of about 1.24; the calculated value, according to the scheme of Bishop and Riviere (7.19) would be closer to 1.3.

The coefficient r increases with E_p, which may partially explain the shift in the position of the peak of the experimental curve, Fig. 7.4c from that of the theoretical one, Fig. 7.4a.

7.4.4 Escape depth, τ

The escape depth is probably the least well known factor in equation 7.2. Broadly, as an energetic electron travels within a medium, it loses energy through inelastic scattering (ionization or excitation of the host atoms) and is deflected from its path by momentum transfer in nuclear collisions. Kanaya and Okayama (7.26) used the quasi-elastic scattering theory of Lindhard et al (2.8, 2.20, 7.27) given in Chapter 2 to define the range of an electron exactly as in equation 2.7, by integrating the inverse of the rate of loss of energy function up to the initial energy, E_o. In Chapter 8, some of the ramifications of this approach are applied to the problem of the charge distribution to be expected in an electron-bombarded glass, but for the present, we quote the range from the theory of these workers (7.26) in the form:

$$R/m = 2.76 \times 10^{-7} \frac{M}{\rho} E_o^{5/3} Z^{-8/9} \qquad 7.6$$

where M/kg, ρ/kgm^{-3} and Z are the atomic mass, density and atomic number of the medium respectively, and E_o/eV the initial energy of the electron. Inserting values in equation 7.6 for copper, for example, yields:

$$R/\mathring{A} = 9.8 \times 10^{-4} (E_o/eV)^{5/3} \qquad 7.6'$$

or $R \sim 30$ $\mathring{A}$ at an initial electron energy of 500 eV.

The Thomson-Whiddington law describing the penetration of electrons into solids is

$$E_o^2 - E^2(x) = b\rho x \qquad 7.7$$

where E(x) is the energy at a depth x, ρ is the density of the material, and b is a constant. Experiments by Spear (7.28) have determined b for various materials, and Lineweaver (7.29) has used this equation to define the range of an energetic particle by setting E(R) = 0. For borosilicate glass he obtained

$$R/\mathring{A} = 0.16 \frac{E_o^2}{\rho} \qquad 7.8$$

where the units of the quantities are unchanged from equation 7.6. Thus, a 500 eV electron might travel some 10 $\mathring{A}$ in glass before coming to rest.

Experimental measurements of the mean free paths of electrons in solids have been collated by Brundle (7.30), as shown in Fig. 7.5, and attempts have been made to fit a universal curve to these data (7.31). Recently, Seah and Dench (7.32) have proposed the relation

$$\lambda/a = \frac{538}{E_o^2} + 0.41 \ (aE_o)^{\frac{1}{2}} \quad \text{for } 1 < E_o/eV < 10^4 \qquad 7.9a$$

for solids, and

$$\lambda/a = \frac{2170}{E_o^2} + 0.72 \ (aE_o)^{\frac{1}{2}} \quad \text{for } E_o > 150 \text{ eV} \qquad 7.9b$$

for inorganic compounds, where a is the lattice spacing, and these equations are found to fit the experimental data closely over most of the energy range. For example, the prediction from equation 7.9b of 34$\mathring{A}$ for 1382 eV electrons in silica compares well with the 37 $\pm$ 4 $\mathring{A}$ mean free path measured by Hill et al (7.43).

The escape depth τ is clearly much less than the range R, since electrons travelling a distance R will have lost most of their energy, but is perhaps more than the mean free path λ, since a collision will not necessarily prevent the eventual emission of the electron. Hence, escape depths of electrons of energy below 1000 eV are of the order of 10 $\mathring{A}$ and electron emission spectroscopy can sample only a few atomic layers at the

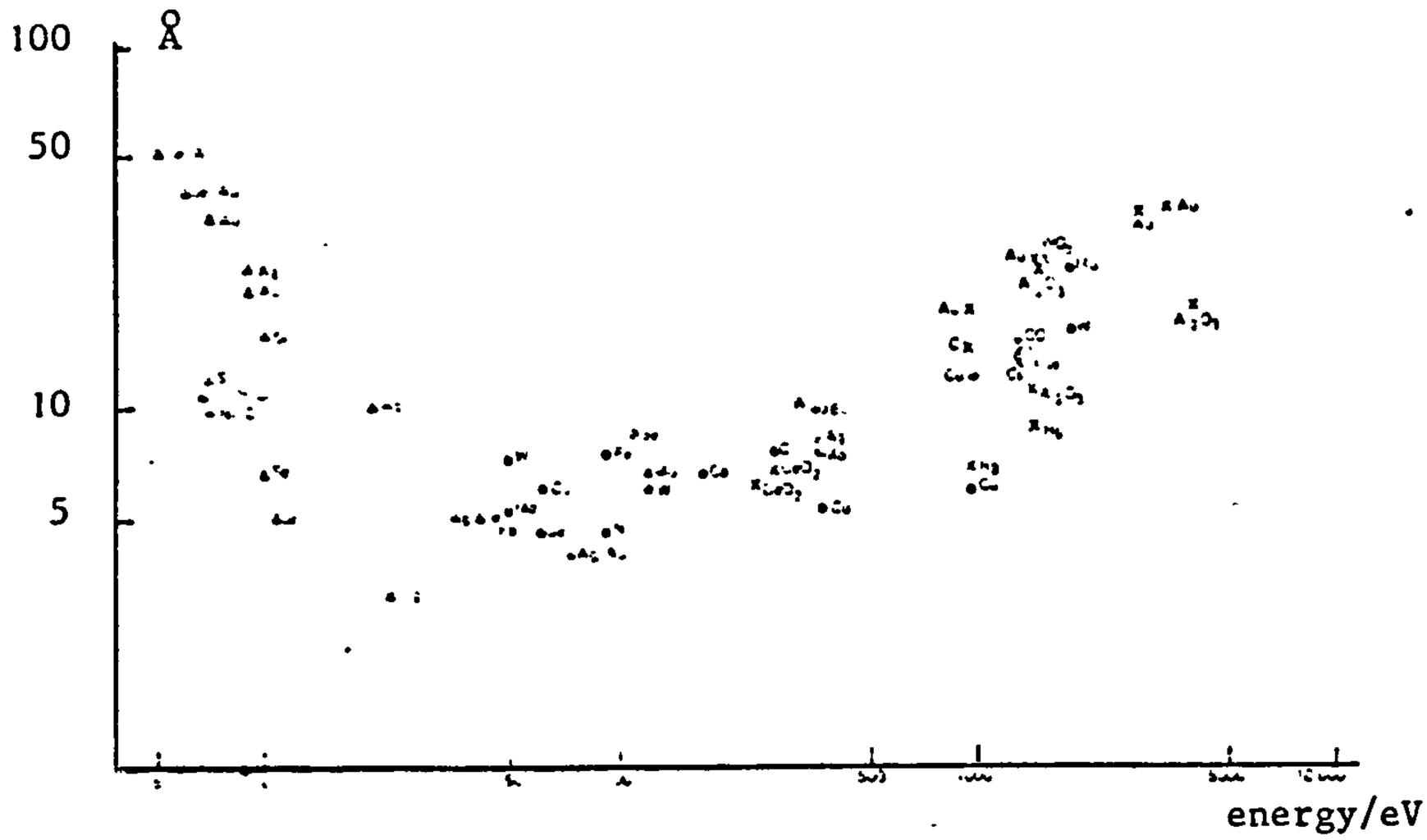

Fig.(7.5): Mean free paths of electrons in solids
Ref.(7.30)

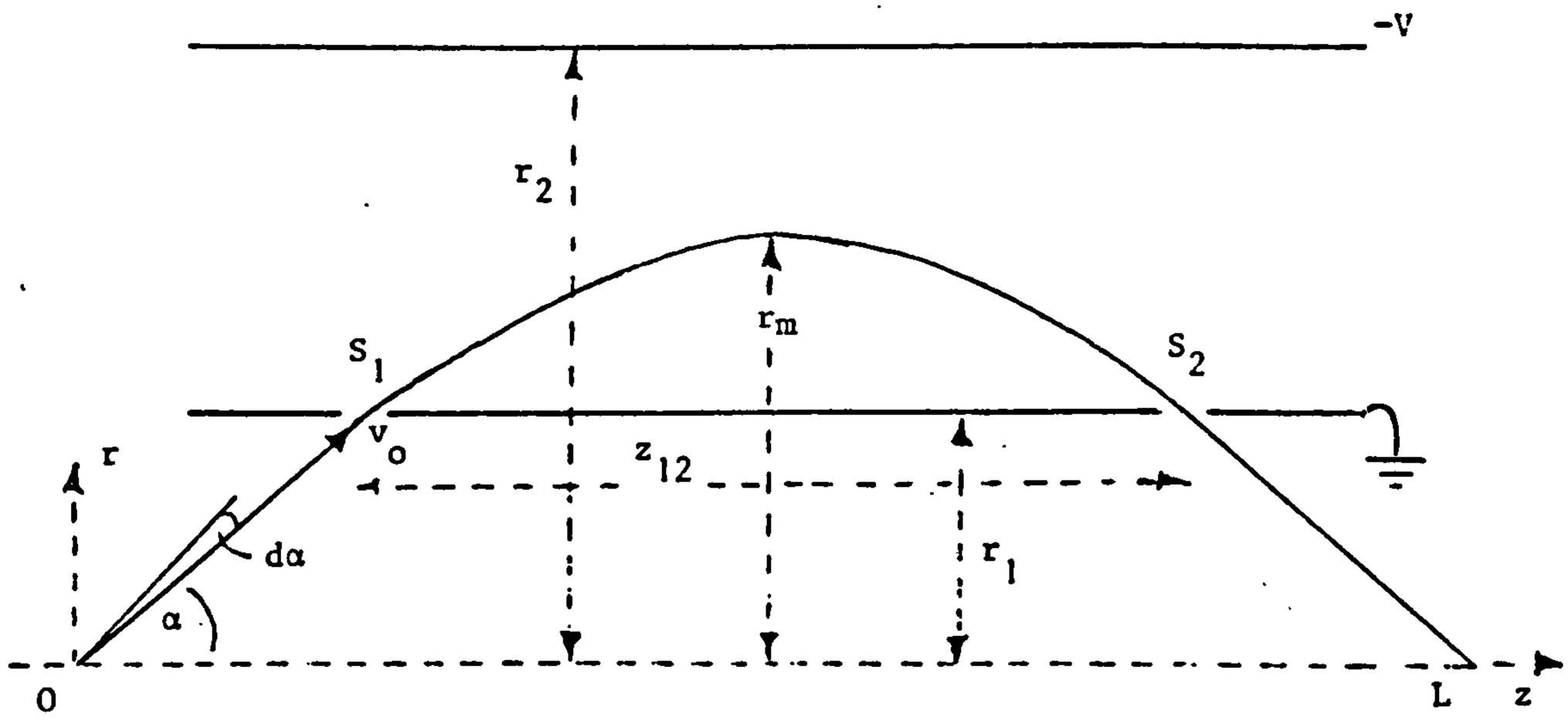

Fig.(7.7): Schematic of CMA showing nomenclature

extreme surface of the analyte.

7.5 Quantitative AES

Making use of the data given in the preceding section, the Auger efficiency may be shown to be typically 5×10^{-3}, from equation 7.2 with $N = 0.25\ \mathring{A}^{-3}$.

If the concentration of an element i in a sample be c_i, the Auger current is reduced by that fraction. However, as we have seen, most of the factors of the equation are known only approximately, and others must be introduced for particular conditions such as a rough surface for example (7.33). Also, the factors r and τ depend both upon the atomic species i and on the host material, or matrix, in which it is contained (7.6). It is consequently very difficult directly to relate Auger peak heights to sample compositions and recourse is necessary to the use of standards. If the magnitude of an Auger line from a pure sample of element i is S_i, from the analyte it is I_i, the concentration of element i is given by

$$c_i = \frac{I_i}{S_i}\left[\sum_j \frac{I_j}{S_j}\right]^{-1} \qquad 7.10$$

where the summation is over all the elements of the analyte.

This, the most successful quantitative method available, has an accuracy only of the order of 30%, however (7.31). The quantitative difficulties are exacerbated by the use of differentiated spectra (which is usually the case, as explained in subsequent sections) since small changes in the shape of an emission peak between two samples (or between two analyses of the same sample) can have a dramatic effect upon the differentiated peak size. Peak shape effects are considered in detail in the following chapter.

7.6 Experimental apparatus

The electron beam spectroscopy was carried out in a commercial

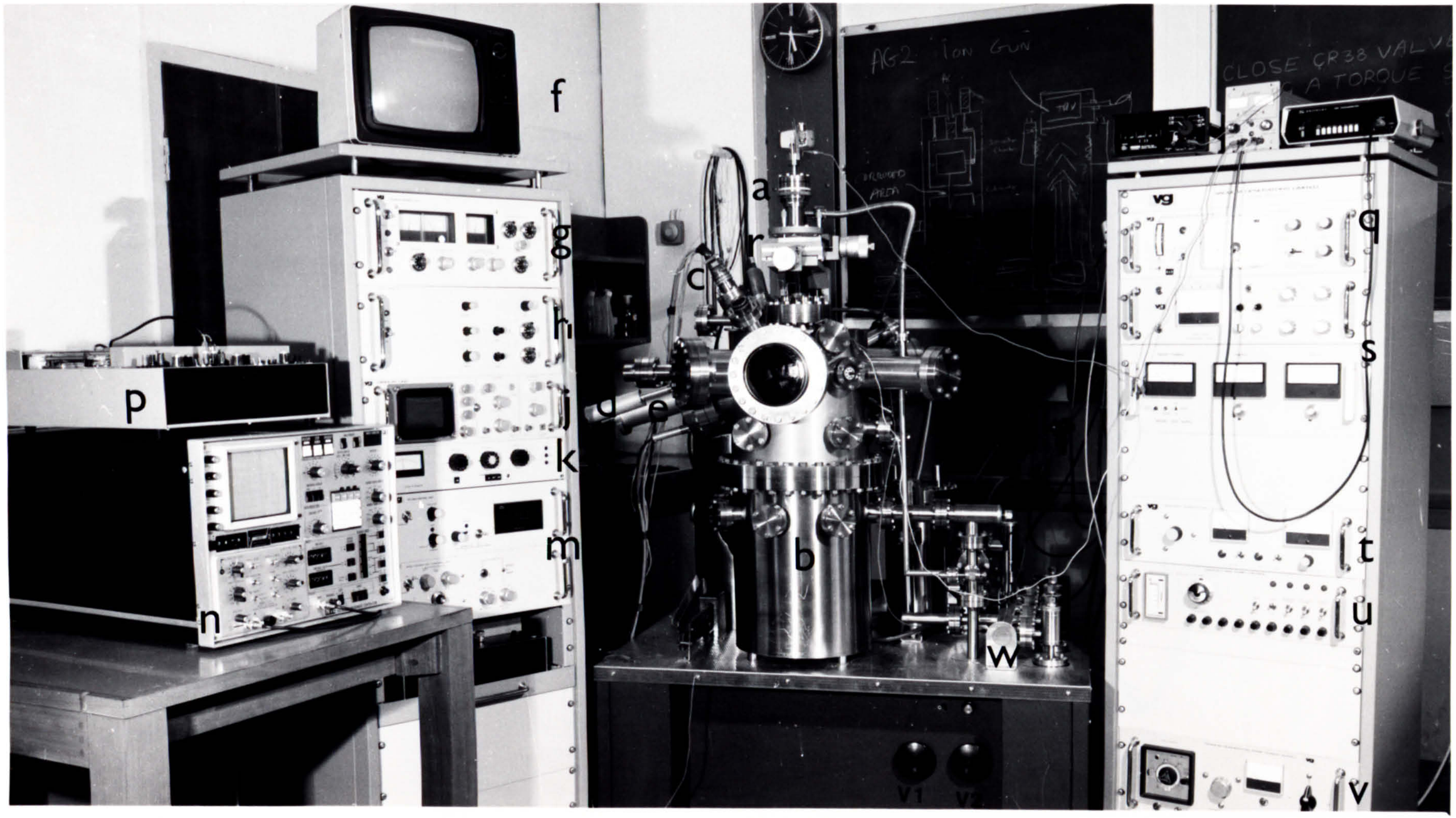
AG2 ION GUN
CLOSE CR38 VALVE
vg
V1
V2
a
b
c
d
e
f
g
h
i
j
k
m
n
p
q
r
s
t
u
v
w

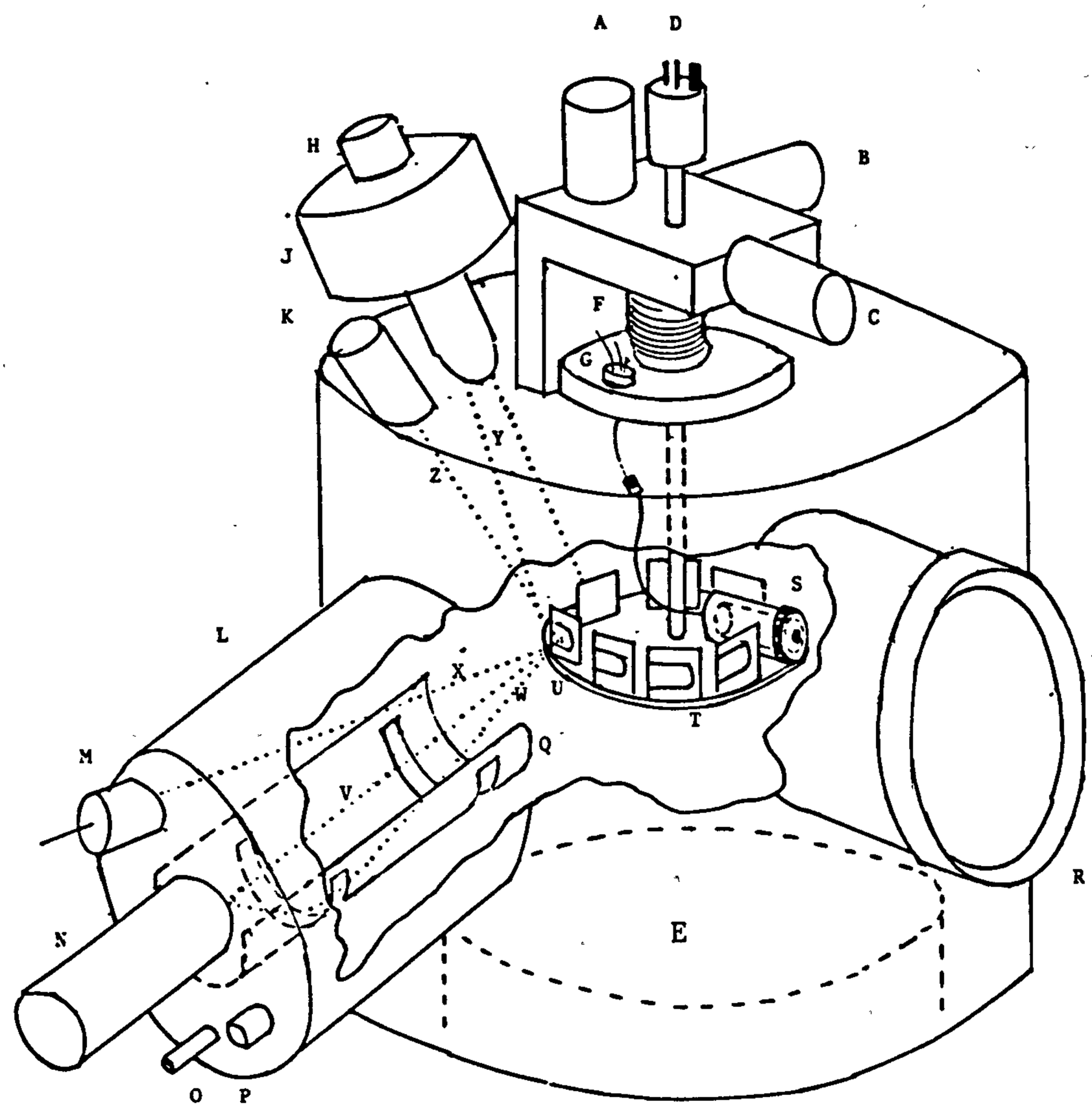

A,B,C: Y,Z,X micrometers respectively; D: liquid air (cooling) and electrical (heating) connections; E: to pumps; F: Manipulator bellows; G: thermocouple and Faraday cup lead-through; H: Argon ion gun; J:Toroidal magnet; K: Glancing incidence electron gun; L: CMA housing; M: Normal incidence electron gun; N:Photomultiplier tube; O: Video connection; P: Outer cylinder biassing; Q: Inner cylinder; R: Viewing port; S: Faraday cup; T: Sample carousel; U: Analyte; V: Axis of CMA; W: Path of transmitted electron; X: Normal incidence beam; Y: Ion beam; Z: Glancing incidencebeam

The outer cylinder of the CMA is not shown

Fig.(7.6b): An isometric sketch of the CMA assembly

'Vacuum generators' cylindrical mirror analyser (CMA) chamber, as shown in Fig. 7.6a and in diagrammatic form in Fig. 7.6b. The chamber, spectrometer and the majority of the electronic back-up and signal processing were identical to those used by Pollard (7.34) and described in detail by him.

7.6.1 Outline of system

The chamber was constructed according to the usual UHV techniques (7.36), being pumped by an oil vapour diffusion pump with a liquid air vapour trap, and a rotary, backing pump. A titanium sublimation pump (TSP) was available, and the entire chamber could be baked to a temperature of 180°C, to remove adsorbed water. Final pressures achievable were better than 10^{-8} Pa.

Samples were mounted on a carousel with a capacity of 8, having micrometer controls for movement in three orthogonal directions: vertical, and two in a horizontal plane. Also, the sample holder could be tilted on its mountings and rotated.

Two electron guns were available, one at normal incidence, (VG LEG 61) and one at 60° to the normal, referred to as the glancing incidence gun (Elvants). Accelerating voltages up to 5 keV were provided for either gun by a VG (326) supply unit.

Electrons issuing from the CMA (section 7.6.2) are deflected into a phosphorescent screen, the light from which was collected by a photo-multiplier tube (EMI 9524B). The output signal enters a lock-in amplifier (see subsection 7.8.2) and is displayed on an oscilloscope screen (VG model 132) and pen recorder (Bryans model 2600A4). During the later stages of the study, a multichannel analyser (MCA) was used to store and display the spectra (Nicolet 4 x 1024 bit memory).

The pass energy of the CMA is displayed by a DVM and is ramped

downwards; the amplitude, speed and starting voltage being controlled by a VG CMA control unit (Model 318). Spectra are therefore taken with the higher energy at the left, contrary to the usual practice, and this is the way they are displayed in this thesis.

An AGS2 argon ion gun was fitted, and was used for sputter etching the surface of the samples. The effect that this has upon their surface composition has been discussed in Chapter 3, and the following chapter contains the results obtained using this technique.

It should be recalled, throughout the following analysis of the action of the CMA, that the instrument employed has only 120° of rotational symmetry; that is, the entrance and exit slits subtend only 120° at the axis. The designers, Bishop et al (7.35), find that this reduces the necessary manufacturing tolerances, and consequent expense, and that the spectrometer resolution is not seriously worsened.

An indispensable feature of the apparatus is a video image of the sample, furnished by a VG physical imaging unit (model 346). The primary electron beam is restored over the surface of the sample by sawtooth waveforms applied to the X and Y deflect plates of the gun, and the secondary electron current collected by a positively biassed electrode, mounted on the axis of the CMA, is used to control the brightness of the spot in an ordinary TV tube. The line and frame scans of the TV display are synchronised with the X and Y deflect signals, and in this way an image is generated which is very similar to the optical appearance of the sample, as can be seen in Fig. 8.9, for example. The TV picture is used for locating the sample prior to analysis and can be used as a crude electron microscope by reducing the amplitude of the X and Y rasters.

7.7 Theory of the CMA

The CMA is a band pass analyser; an electron passing through the

entrance slit will be transmitted if its energy is within a certain interval ΔE of the pass energy E_o. The signal to noise ratio of a CMA is therefore inherently superior to spectrometers of the retarding field type (7.37). The magnitude of ΔE determines the resolution, and E_o is set by the negative voltage applied to the outer cylinder to deflect the electrons through the exit slit.

A complete theoretical treatment of the CMA can be developed surprisingly quickly from first principles. The outline given below is based upon the work of Zashkvara et al (7.38) and Sar-El (7.39), with nomenclature as shown in Fig. 7.7.

7.7.1 Electronic trajectory

It is easily shown, by considering the electric field between the cylinders, that the Lagrangian for the motion of the electron in that space is:

$$\frac{m\dot{r}^2}{2} + eA\ln(r/r_1) = B, \text{a constant} \qquad 7.11$$

where $$A = \frac{V}{\ln(r_2/r_1)} \qquad 7.11a$$

V being the voltage between the cylinders, r_1 and r_2 the radii of the inner and outer cylinders respectively, m and e are the mass and charge of the electron, and r is the radial position. The radial component of the initial velocity can be written $\cos\alpha \frac{\partial r}{\partial z}$ so that we have from equation 7.11:

$$E\cos^2\alpha\left(\frac{\partial r}{\partial z}\right)^2 = B - eA\ln(r/r_1) \qquad 7.11'$$

if the initial energy be E. Using the boundary conditions at the entrance slit,

$$\frac{\partial r}{\partial z} = \frac{1}{s}\left\{p^2 - \ln(r/r_1)\right\}^{\frac{1}{2}} \qquad 7.12$$

where $$s^2 = \frac{E}{eA}\cos^2\alpha = \frac{p^2}{\tan^2\alpha} \qquad 7.12a$$

The maximum excursion r_m is found by equating $\frac{\partial r}{\partial z}$ to zero, whereupon

$$r_m = r_1 e^{p^2} \qquad 7.13$$

and the distance between the slits z_{12} is found by integrating thus:

$$z_{12}(p) = 2\int_{r_1}^{r_m} dz = 2s\int_{r_1}^{r_m} \frac{dr}{\left\{p^2 - \ln\left(\frac{r}{r_1}\right)\right\}^{\frac{1}{2}}} \qquad 7.14$$

By substituting 1/y for the integrand, we have

$$z_{12}(p) = 4r_1 e^{p^2}\, s \int_0^p e^{-y^2}\, dy = 4r_1 s e^{p^2}\, \phi(p) \qquad 7.14'$$

where $\phi(p) = \int_0^p e^{-y^2}\, dy = \frac{\sqrt{\pi}}{2}\, \mathrm{erf}(p)$

The position at which the electron crosses the z-axis, the axis of the spectrometer, is given by:

$$L(p(\alpha)) = 2r_1 \cot\alpha + z_{12} = r_1\left\{\frac{2}{\tan\alpha} + 4se^{p^2}\,\phi(p)\right\} \qquad 7.15$$

7.7.2 Focussing

Differentiating L(p) with respect to α, noticing that $\frac{\partial p}{\partial \alpha} = s$, $\frac{\partial s}{\partial \alpha} = -p$ and that $\frac{\partial \phi}{\partial p} = e^{-p^2}$, gives:

$$\frac{\partial L}{\partial \alpha} = r_1\left\{\frac{-2}{\sin^2\alpha} + 4\left[s^2 + pe^{p^2}\,\phi(p)(2s^2 - 1)\right]\right\} \qquad 7.16$$

It is possible now to appreciate the remarkable focussing properties of the CMA. For first order focussing, $\frac{\partial L}{\partial \alpha} = 0$, and equation 7.16 yields:

$$\tan^2\alpha = \frac{2p^2 + 4p^3\, e^{p^2}\, \phi(p) - 1}{1 + 2pe^{p^2}\, \phi(p)} \qquad 7.17$$

showing that first order focussing occurs at all angles and corresponding distances L(p). These are shown in Fig. 7.8. It is clearly seen from the figure that at $\alpha = \alpha_o = 42.3^o$ ($p = 0.77$, $\phi = 0.6418$) there is a minimum focal length $F_o(\alpha_o)$ of $6.1r_1$. The second derivative of equation 7.15 is zero at this angle, $\left[\frac{\partial^2 L}{\partial \alpha^2}\right]_{\alpha_o} = 0$, producing a 'second order' focus at F_o. The third derivative is also shown in the figure, reaching a maximum at $\alpha = \alpha_o$ of $-92.4\ m^3 rad^{-3}$, and the fourth derivative is consequently zero at that point.

7.7.3 Pass energy

From the definitions of p and A, the energy of electrons focussed at F_o must be given (in eV) by

$$E_o = \left[\frac{Ap^2}{\sin^2\alpha}\right]_{F_o} = \frac{1.309\ V}{\ln\left\{\frac{r_2}{r_1}\right\}} \qquad 7.18$$

Thus, E_o is proportional to V, and at $r_2 = 3.702r_1$, $E_o = V$.

7.7.4 Minimum trace width

Expanding small changes in crossing point L as a series in $\Delta\alpha$ gives:

$$\Delta_\alpha L = \frac{\partial L}{\partial \alpha}\Delta\alpha + \frac{1}{2!}\frac{\partial^2 L}{\partial \alpha^2}(\Delta\alpha)^2 + \frac{1}{3!}\frac{\partial^3 L}{\partial \alpha^3}(\Delta\alpha)^3 + \frac{1}{4!}\frac{\partial^4 L}{\partial \alpha^4}(\Delta\alpha)^4 + \ldots \qquad 7.19$$

The results of subsection 7.7.2 show that at F_o this can be written:

$$\left[\Delta_\alpha L\right]_{F_o} = -15.4\ r_1\ (\Delta\alpha)^3 + 0\left\{(\Delta\alpha)^5\right\} \qquad 7.19'$$

Hafner et al (7.40) recognised that the negative sign in equation 7.19' implies an 'envelope' of trajectories with a 'waist' slightly short of the focus. This is the 'minimum trace width' whose size is $7.76r_1\ (\Delta\alpha)^3$ and position is $5.28r_1\ (\Delta\alpha)^2$ off axis, using approximations valid for an acceptance angle $\Delta\alpha$ of less than 6^o.

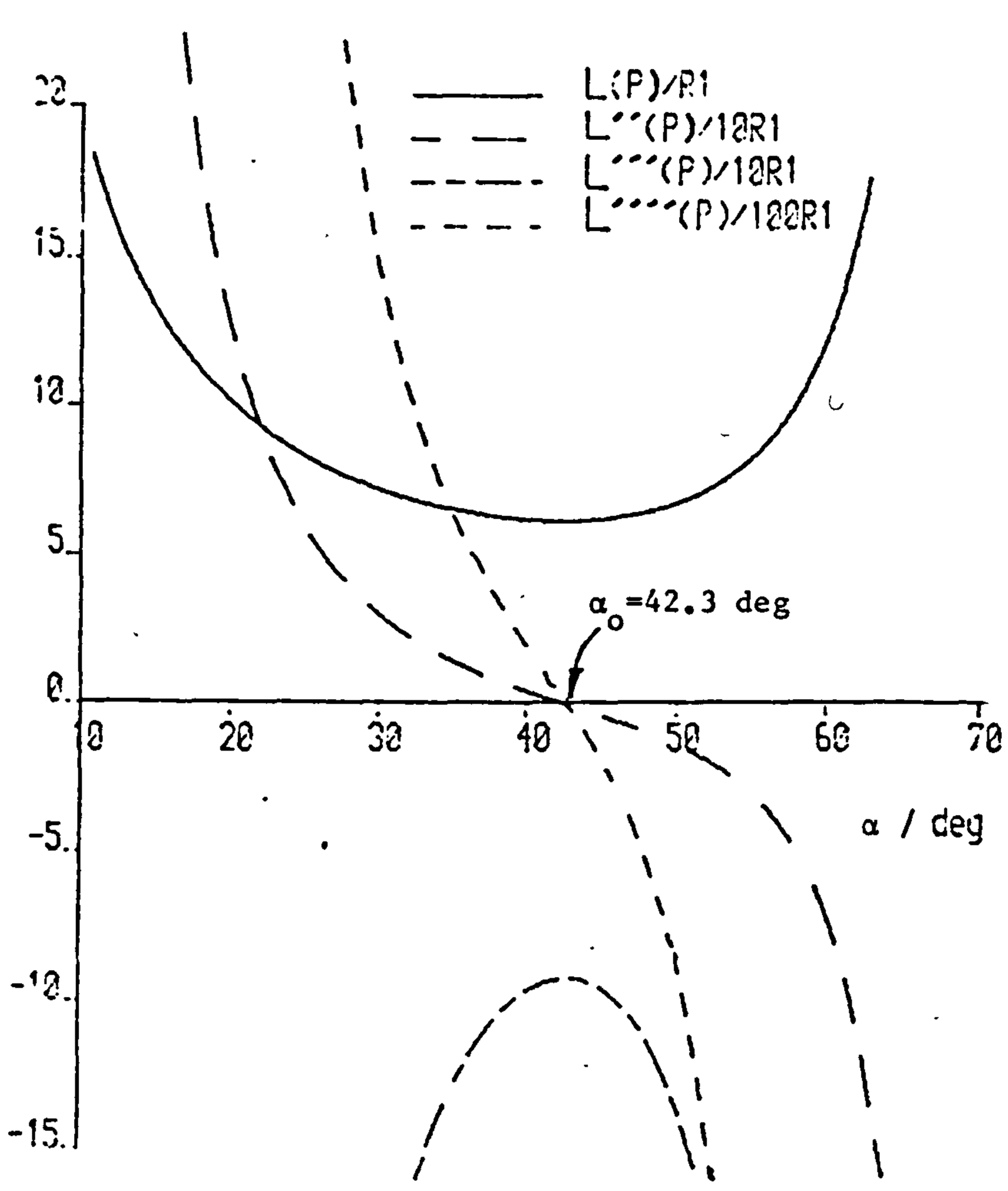

Fig.(7.8): The second order focussing of the CMA

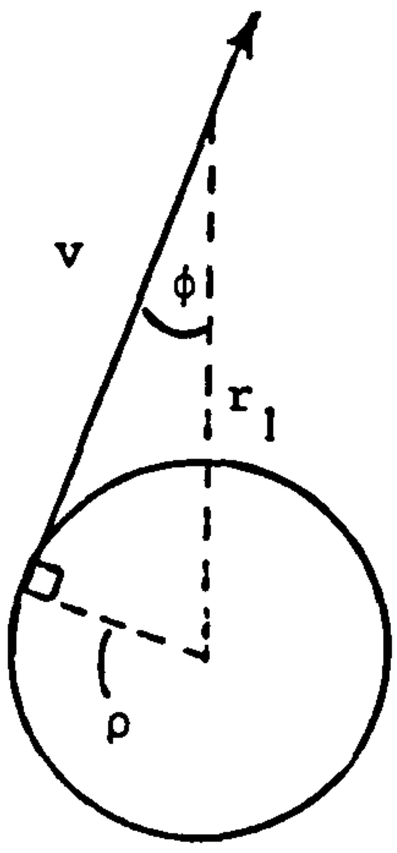

Fig.(7.9): Large spot geometry

7.7.5 Energy dispersion and resolution

The extent to which small changes ΔE in the energy of the electron alter L is given by

$$\left[\Delta L\right]_\alpha = \frac{\partial L}{\partial p}\frac{\partial p}{\partial E}\Delta E \qquad 7.20$$

and using equation 7.15 and $\frac{\partial p}{\partial E} = {}^{p}/_{2E}$ we obtain

$$\left[\Delta L\right]_\alpha = \frac{2r_1 p}{\tan\alpha}\left\{p + \phi(p)\ \ e^{p^2}\ (2p^2 + 1)\right\}\frac{\Delta E}{E} \qquad 7.20'$$

At F_o, from this equation,

$$R = \frac{E}{\Delta E} = \frac{5.61 r_1}{\left[\Delta L\right]_{\alpha o}} \qquad 7.21$$

The resolution is improved by minimising ΔL, but the signal current will reduce also. Positioning the detector aperture coincident with the minimum trace width allows a resolution better than is achievable at F_o and avoids excessive loss of signal. Using $\Delta L = 7.76 r_1 (\Delta\alpha)^3$ from section 7.7.4, equation 7.21 gives a base resolution of $R_o = 0.72 (\Delta\alpha)^{-3}$ or better than 600, with $\Delta\alpha = 6^o$.

7.7.6 Finite spots

In the treatment so far, particularly the resolution result above, the electrons have been treated as issuing from a point source on the axis of the spectrometer, at exactly the correct distance from the entrance slit ($1.099 r_1$). These conditions do not in general prevail, and practical resolutions are less than half the theoretical best. Chapter 8 describes the effects that electron beam irradiation has upon the samples, but broadly it is clear that reducing the incident current density will reduce the beam damage, and hence much of the spectroscopic work was done with a deliberately defocussed primary beam.

The effect of a large spot upon the base resolution has been

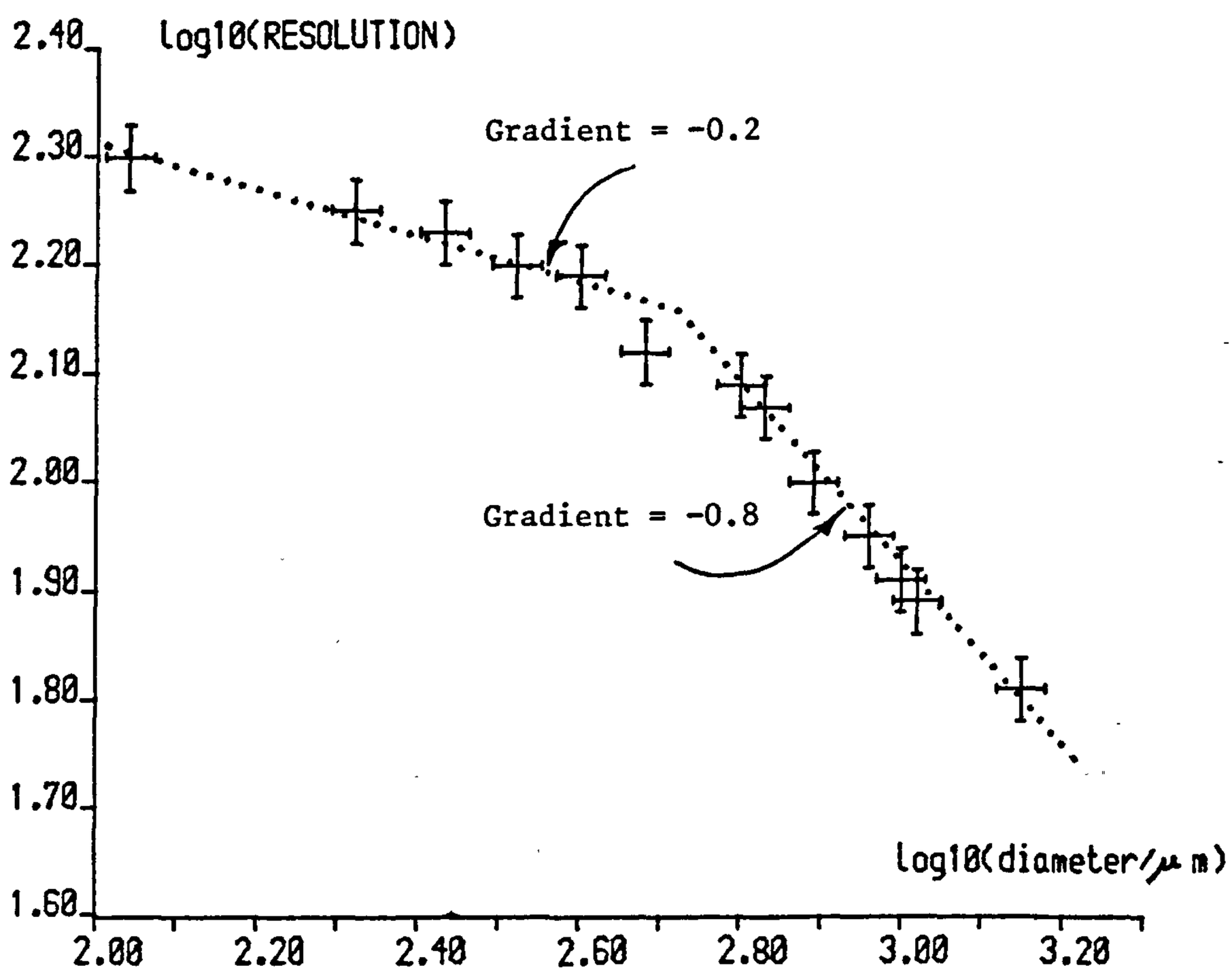

FIG(7.10):CMA resolution against spot size

considered by Risley (7.41), by writing

$$R = \frac{E}{\Delta E} = \frac{v_o^2}{v^2 - v_o^2} = \left[\cos^{-2}\phi - 1\right]^{-1} \qquad 7.22$$

where v is the true velocity of the electron transmitted at a pass energy of E_o and ϕ the off-radial angle shown in Fig. 7.9. Making the approximation for small ϕ,

$$\cos\phi = \left[1 - \left(\frac{\rho}{r_1}\right)^2\right]^{\frac{1}{2}} \qquad 7.22a$$

where ρ is the radius of the spot, thus:

$$R = \left(\frac{r_1}{\rho}\right)^2 = 4\left(\frac{r_1}{d}\right)^2 \qquad 7.22'$$

where d is the spot diameter. Zashkvara et al however, published without proof (7.37) the relation:

$$R = 4\,\frac{r_1}{d} \qquad 7.23$$

and consequently it was considered necessary to attempt to determine experimentally the way in which the spot size affected the resolution of the CMA. Defining ΔE as the separation of the two minima of a doubly differentiated 3 kV elastic peak, which is 2.35 times the 'standard deviation' of a Gaussian profile, and having calibrated the gun focus settings in terms of the beam diameter, as described in the following chapter, it was possible to plot the resolution curve of Fig. 7.10. Two regimes can be identified, which may be because the uncertainty in the energy is derived from two contributions:

$$(\Delta E)^2_{total} = (\Delta E_o)^2 + (\Delta E_{spot})^2 \qquad 7.24$$

where ΔE_{spot} is the error deriving from the finite spot size. The second term dominates only at a spot diameter above about 500 μm, (log d = 2.7), as is seen in Fig. 7.10.

We can extrapolate the second slope from this plot to yield:

$$R = 6.5 \left(\frac{r_1}{d}\right)^{0.8} \qquad 7.25$$

which is approximately the relation found by Zashkvara in equation 7.23.

At beam diameters above about 350 μm, signal sizes were found to be severely reduced, and the S/N ratio rose rapidly. Hence, to determine more precisely the dependency of R upon d was considered unnecessary.

7.8 Signal recovery

7.8.1 Noise

The advantages of the CMA include particularly the ability to scan a spectral feature sufficiently rapidly for the signal to be displayed on an oscilloscope. This requires a typical amplifier bandwidth Δf of the order of 1 kHz. The shot noise current in the detector is given by (7.37)

$$I_N = \sqrt{2eI_c \ \Delta f} \qquad 7.26$$

and the signal is

$$I_s = I_c T \qquad 7.27$$

where the collected signal current $I_c = \frac{\Omega}{4\pi} I_A$, Ω being the solid angle of collection, and I_A the emitted total Auger current. T is the transmission ratio of the CMA.

Using $I_A = 10^{-10}$ A, $\Omega = 7 \times 10^{-2}$sr ($\Delta\alpha = 6^o$), T = 10% (7.37) and Δf = 1 kHz:

$$I_S = 6 \times 10^{-13} \text{ A} \qquad 7.28a$$

$$I_N = 4 \times 10^{-13} \text{ A} \qquad 7.28b$$

so that the signal to noise ratio is of order unity, and phase sensitive detection is required. This also removes the large background slope of true secondaries on which the peaks are superimposed (Fig. 7.1) as is seen below.

7.8.2 Phase sensitive detection

If a small sinusoidal signal is added to the potential V on the outer cylinder of the CMA, the output current from the analyser $I_S(V)$ becomes I_S (V +asinωt) which can be expanded as a series thus:

$$I\ (V + a\sin\omega t) = I(V) + \frac{a^2}{4} I''(V) + \frac{a^2}{96} I''''(V) + \ldots$$

$$+ a\left\{I'(V) + \frac{a^2}{12} I''''(V) + \ldots\right\} \sin\omega t$$

$$- \frac{a^2}{4}\left\{ I''(V) + \frac{a^2}{12} I''''''(V) + \ldots\right\} \cos 2\omega t \qquad 7.29$$

where the subscript S has been dropped for clarity.

$$\text{Now, } I(V) = \frac{\Omega}{4\pi} TI_A(E) = \frac{\Omega}{4\pi} Te\,\Delta\, EN(E) \qquad 7.30$$

where N(E) is the number of electrons leaving the sample per second in the energy interval ΔE at E. At constant resolution $\Delta E = RE$, so that

$$I(V) = \frac{1}{4\pi}\Omega\, TeREN(E) \qquad 7.30'$$

and from equation 7.29, the component modulated at ω is given by:

$$I(\omega) = aI'(V) \qquad 7.31$$

for small a, so that differentiating equation 7.30' with respect to E gives:

$$I(\omega) \sim\ a\left\{EN'(E) + N(E)\right\} \qquad 7.32$$

and since N(E) has no turning points in the region of interest,

$$I(\omega)\ \sim\ aEN'(E), \text{ at high E} \qquad 7.32'$$

showing that $I(\omega)$ is proportional to the first derivative of the spectrum. Further,

$$I(2\omega) = -\frac{a^2}{4}\ I''(V) = -\frac{a^2}{4}\ \frac{\Omega}{4\pi}\ TeR\ \frac{d^2}{dE^2}\ (EN(E)) \qquad 7.33$$

and similarly,

$$I(2\omega) \sim -\ a^2\ EN''(E) \qquad 7.33'$$

and $I(2\omega)$ is proportional to the second derivative.

These components are recovered by convolving the total signal $I(V + a\sin\omega t)$ with a reference square wave, centered at zero volts, before passing it into the amplifier. If the reference channel is coherent with the modulation, then $I(\omega)$ will be detected, and all other frequencies (particularly the non-periodic noise) will be eliminated. If the reference channel frequency is 2ω (and a $\pi/2$ phase shift added) then $I(2\omega)$ will be detected.

The magnitude of $I(\omega)$ and $I(2\omega)$ are proportional to a and a^2 respectively but the amplitude a cannot be increased arbitrarily without detriment to the resolution since ω will be outside the bandwidth of the amplifiers, and the signal would be lost. The optimum modulation is of p-p height equal to the breadth of the spectral feature, i.e. less than about 5 V.

7.9 Electron loss spectroscopy

To augment the results obtained from Auger spectroscopy a small quantity of reflection electron energy loss spectroscopy (ELS) (7.42) was performed. Transmission ELS, which involves recording the energy of electrons emerging from the far side of the specimen, was clearly impossible, first, since the idential experimental system was used for this work as for the Auger spectroscopy, with the gun and the spectrometer on the same side of the specimen, as in Fig. 7.6b), and second because the thickness of the samples far exceeds the penetration depth of the electrons. This is unfortunate because, in the transmission mode, ELS yields information on the properties of the bulk solid, which in the case of sputter-deposited films would perhaps have been of greater interest than those of the extreme surface. It will be seen, notwithstanding, that ELS spectra can demonstrate features of glass surfaces which Auger spectra cannot.

As has been mentioned in the introduction to this chapter, primary electrons may lose energy in discrete amounts during their interaction with a solid surface, and spectra are therefore taken close to the elastic peak. Primary energies between 100 to 500 eV are generally used, since with a constant resolution spectrometer the elastic peak is sharper at low energies and loss peaks may be observed closer to the primary energy. Customarily, the PSD is used in the 2ω mode, doubly differentiated signals being recorded, because of the very low signal to noise ratio obtaining at the low beam currents necessarily employed.

As Pollard (7.34) has described, very little literature is available concerning ELS of glasses. Underhill (3.8) has recently completed an experimental investigation using a concentric hemispherical analyser, and provides extensive theoretical interpretation. Two main processes dominate the interactions causing energy loss, and they are described in the following subsections.

7.9.1 Single particle processes

The primary electrons may cause interband transitions, or excitations of core electrons in a very similar manner to that of incident light. The approach of the electron causes a time dependent electric polarisation wave in the material, the damping of which is the mechanism by which the primary energy is reduced. Since the intensity of the wave is proportional to ε^{-2} and the damping to ε_2, where the complex dielectric constant of the medium is written

$$\varepsilon = \varepsilon_1 + i\varepsilon_2 \qquad 7.34$$

it is reasonable that the magnitude of the energy loss can be shown to be of the form:

$$E_b \sim \frac{\varepsilon_2}{|\varepsilon|^2} = -\,\mathrm{Im}\left\{\frac{1}{\varepsilon}\right\} = \frac{\varepsilon_2}{\varepsilon_1^{\,2} + \varepsilon_2^{\,2}} \qquad 7.35a$$

for bulk loss effects, and

$$E_s \sim \frac{\varepsilon_2}{|\varepsilon + 1|^2} = - \mathrm{Im} \left\{ \frac{1}{\varepsilon + 1} \right\} = \frac{\varepsilon_2}{(\varepsilon_1 + 1)^2 + \varepsilon_2^2} \qquad 7.35b$$

for the surface loss function.

In consequence of treating the incident electron as an EM disturbance, it is possible directly to compare features of ELS spectra with data from optical spectroscopy. The theoretical basis of UV spectroscopy is described by Brown (7.44), using Koster-Kronig analysis (7.45, 7.46), giving the refractive index of a medium in terms of the linked equations:

$$n(\omega) - 1 = \frac{2}{\pi} \mathbb{P} \int_0^\infty \frac{\omega' k(\omega')}{\omega'^2 - \omega^2} \, d\omega' \qquad 7.36a$$

and

$$k(\omega) = \frac{-2\omega}{\pi} \mathbb{P} \int_0^\infty \frac{n(\omega') - 1}{\omega'^2 - \omega^2} \, d\omega' \qquad 7.36b$$

where $n(\omega)$ and $k(\omega)$ are the real and imaginary parts of the refractive index at a frequency ω, and $\mathbb{P}$ indicates the Cauchy principal value of the integral excluding the point at $\omega' = \omega$. Only recently, since the advent of the synchrotron, has the energy range of optical data been sufficient for interesting comparison with ELS data to be made.

The creation of excitons is also observed in ELS. As Kittel describes (7.47), the weakly bound (or Wannier) exciton is an electron-hole pair with the electron in the valence band and the hole in the conduction band. The Coulomb attraction between the pair lowers the exciton energy to below that of the band gap. The tightly bound (or Frenkel) exciton is localised to an atom, and has energy levels similar to those of the free ion.

7.9.2 Plasmons

In contrast to these processes, the oscillations of the electron gas cannot be observed optically. It can be quite simply shown (7.48) that

under the influence of a time varying field, the electrons of a solid will resonate collectively and can absorb energy in quanta known as plasmons. The electrons of the surface can support their own plasmons, whose energy is reduced by a factor of $\sqrt{2}$ from the three-dimensional case.

7.10 Interpretation of the Auger and loss spectra

In the light of the foregoing description of the techniques of Auger and energy loss spectroscopy, it is clear that while a qualitative assessment of a surface composition can be relatively simply obtained, a quantitative determination of the ratios of constituent elements is more difficult.

It has been mentioned in section 7.5 that whereas the heights of the peaks in the N(E) spectrum may be interpreted by the use of standards, as in equation 7.10, the magnitudes of features in the differentiated spectra are affected strongly by the peak shape, which may differ strongly between samples, and which introduces further difficulty. Hence, the size of N'(E) and N''(E) features may not be used as an indicator of elemental concentrations except in a crude comparative way.

Errors introduced into N'(E) spectra have been studied by Underhill (3.8) whose computer program mimics the action of the PSD and who suggests that some of the features in the ELS spectrum of glass may have been introduced by the modulation process.

7.11 Summary

The principles of Auger spectroscopy have been described with a brief treatment of its theoretical basis. Attention has been paid to the problems attaching to dielectric analytes, particularly glass. The reason for the extreme surface sensitivity of the technique has been emphasised, as has the qualitative nature of AES.

The small quantity of ELS carried out merits only the briefest

introductory theoretical discussion, which is contained in section 7.9. Once again, quantitative interpretation is fraught with difficulty.

The apparatus with which the films and glasses were analysed has been described. The experimental technique and results are given in the following chapter.

CHAPTER 8

ELECTRON BEAM SPECTROSCOPY : EXPERIMENTAL

Obtaining spectra from glass surfaces in a reproducible and consistent manner is attended with special problems in addition to the general theoretical pitfalls described in the preceding chapter. It is found very quickly, for example, that certain spectral features are not stable, but reduce in intensity as irradiation proceeds. This chapter contains a description of a theory of ionic electromigration to explain the time-dependency of sodium signals in glass. Also, an experimental method is described by which reproducible spectra from glass may be obtained, and the results of depth profiling using the argon ion gun shown in Fig. 7.6b are presented.

The samples analysed were either glass films RF sputter deposited on to various substrates (usually microscope slides), or fragments of the glasses from whose surface the sputtering took place, that is 'targets' in the terminology of Chapter 4. As both types of sample were DC sputtered with the ion gun, confusion would arise if this terminology were continued. Throughout the following, therefore, the latter type of sample, the glasses used to create the films, will be referred to as 'source glasses'. Films will be labelled according to the nature of their source glass and the particular sputtering run as well as a specimen index. The source glasses are indicated thus: A, ordinary window glass; B, three component glass; and C, four component glass. A film C2/3 is hence identified as the third sample in the chamber during sputtering run C2, whose conditions are set out in the appropriate log sheet, Fig. 6.2. The source in this case was the four component glass, of composition given in Table I. No variation of deposition rate was observed with changes in position on the substrate table, and it is hence legitimate to refer to the thickness of film C2, the second film to be deposited from that source.

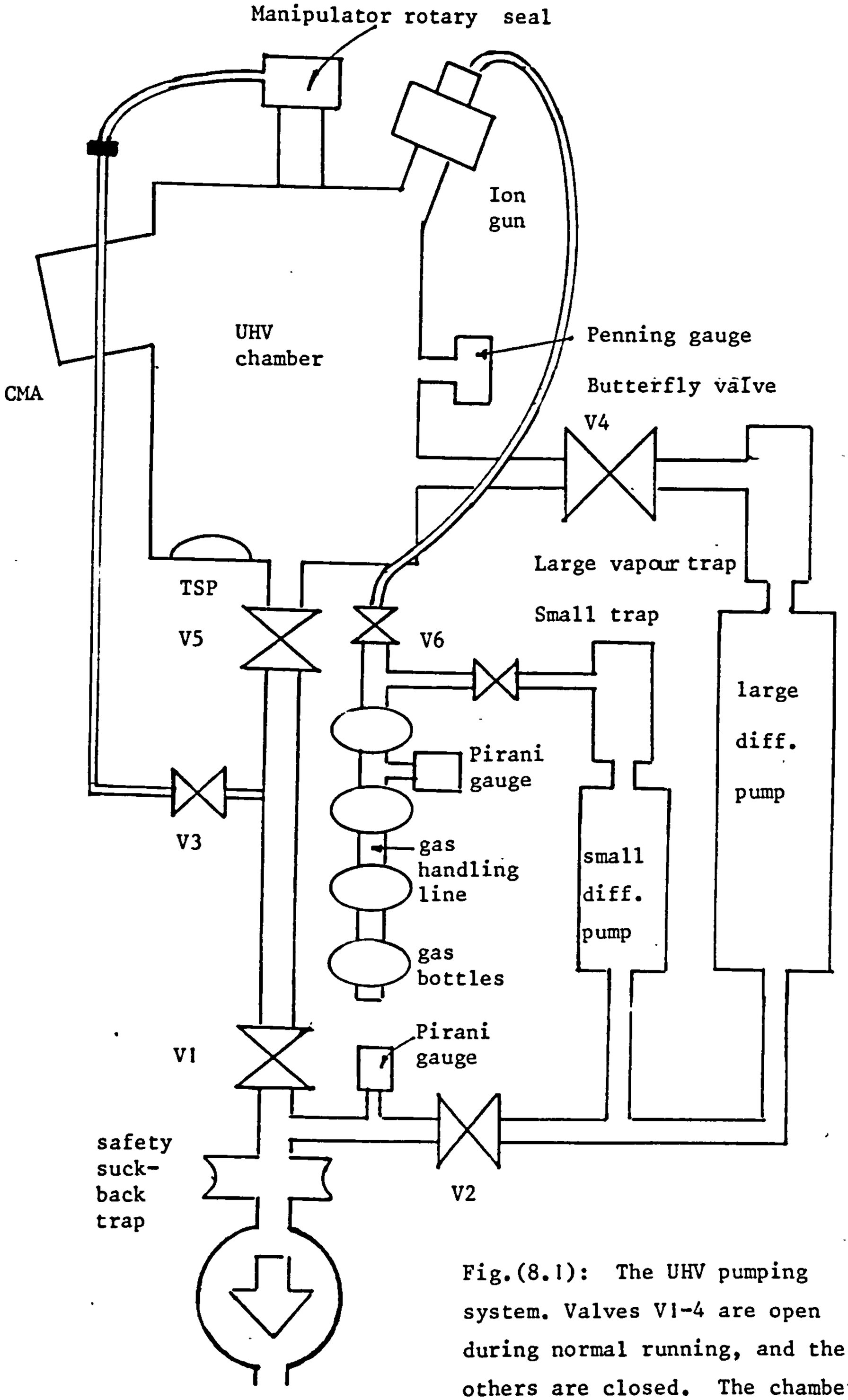

Fig.(8.1): The UHV pumping system. Valves V1-4 are open during normal running, and the others are closed. The chamber is roughed out with the even numbered valves closed and the others open.

8.1 Experimental technique

8.1.1 Vacuum practice

The samples to be analysed were first cleaned with a weak solution of detergent in water, and then briefly with ether. The vacuum chamber was brought to atmospheric pressure following the usual procedure of admitting air vaporised from the laboratory liquid air supply (to reduce the contamination of the chamber by water), and the large access plate at the rear was removed. The circular sample holder was disconnected from its rotary support and electrical contacts, and extracted from the chamber. Used samples were replaced with fresh ones, and care was exercised throughout to avoid touching the surfaces.

After replacing the vacuum seals the chamber was evacuated to about 10 Pa with the rotary pump and thereafter with the oil vapour diffusion pump. The pumping system is shown in full in Fig. 8.1. Usually, all the external connections were removed and the chamber was baked at 180°C overnight to remove water vapour and adsorbed gases. It was found that if the period for which the chamber was open to the atmosphere was no longer than about 10 minutes, final pressures in the good UHV region ($\sim 10^{-8}$ Pa) could be achieved without bakeout, although not repeatably.

8.1.2 Sample positioning

The singular importance of the correct positioning of the analysed spot with respect to the axis and entrance slits of the spectrometer is apparent from the analysis of the previous chapter. As Fig. 7.6b shows, the position of the spot is determined in general by the X, Y and Z micrometer settings, the angle between the normal to the sample surface and the plane defined by the electron beam and the CMA axis, the three tilt micrometer settings, and the electron beam deflect voltages. It is impossible correctly to orientate the specimen unless these variables are reduced in

number. If the analyte has a flat surface, and is mounted vertically, and if the carousel is rotated such that the surface normal is contained in the electron beam-CMA axis plane, the spot position is determined only by the Z-micrometer and the beam deflection conditions.

Elastic peak signals, usually at 3 kV, were used for orientation. The energy range from 3050 to 2550 eV, was scanned rapidly and the shape as well as the recorded energy of the differentiated peak (displayed on the CRT) was used as the basis for the adjustment of the Z-micrometer. With experience, a sample could be positioned in less than a minute.

Uncharacteristically, glass samples have an advantage over other materials in this regard, as cathodoluminescence causes the irradiated spot to emit a blue light which is easily visible to the naked eye, and which can be used as a rough guide if the alignment is so bad that no signal at all can be seen.

8.1.3 Electron beam characterisation

The glancing incidence (GI) gun was used almost exclusively for the study, because of the behaviour of the secondary electron coefficient with the incident angle of the primary beam. At normal incidence, a charge cloud builds up just proud of the surface of the sample, preventing the penetration of the beam. At glancing incidence, the effect is reduced, and electrons may reach the sample, but Auger emissions from glass surfaces generally show a 10-12 eV downward shift because of the positive charge on the surface.

The electron beam current, which was ostensibly set and stabilised by a feedback control loop in the power supply was found to be better measured by making use of a Faraday cup mounted on the carousel in the position of the sample. The electron beam was directed into the inner can through a 2 mm hole in the cap. Biassing the can at +40 V ensured the

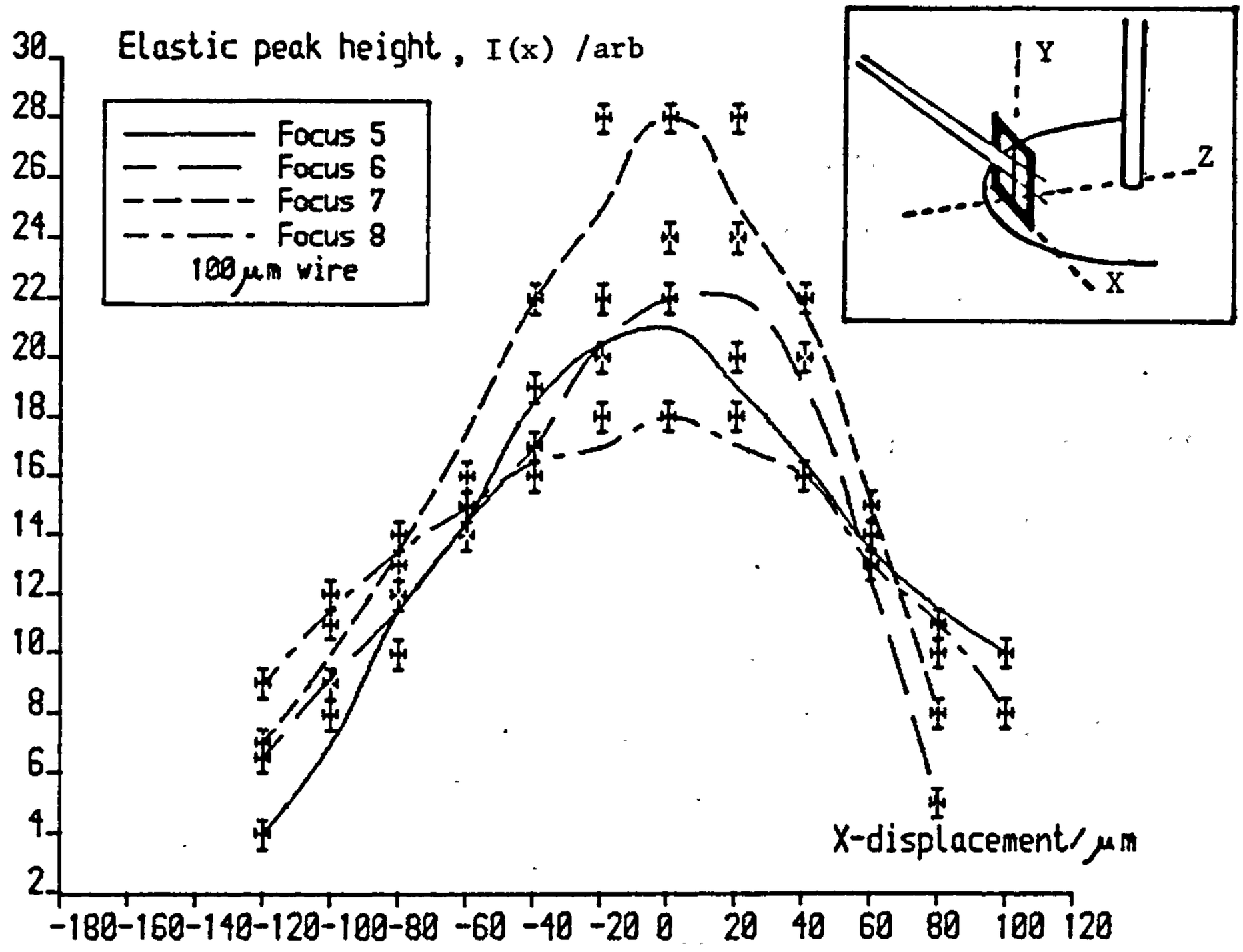

FIG(8.2a):3kV Elastic peak size versus wire position

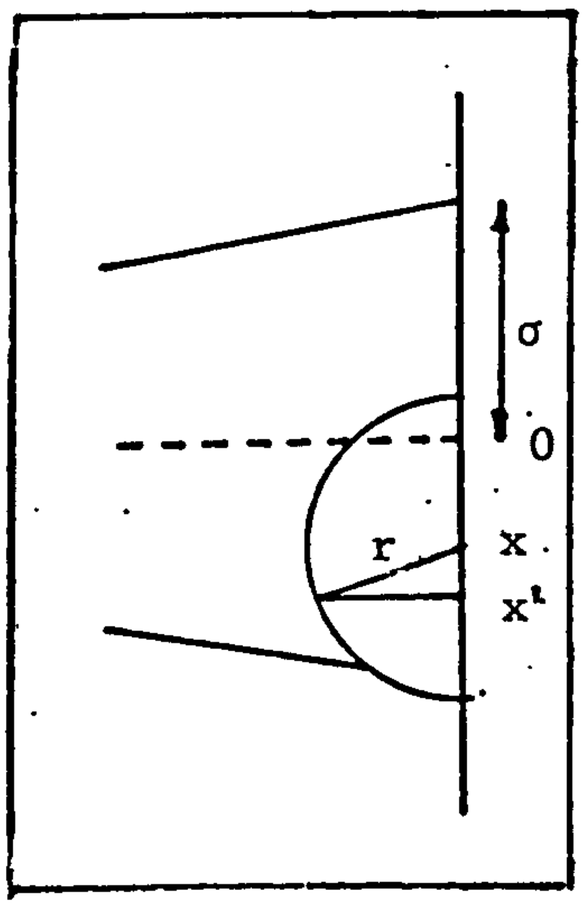

Fig(8.2b):
Nomenclature of convolution expression 8.1

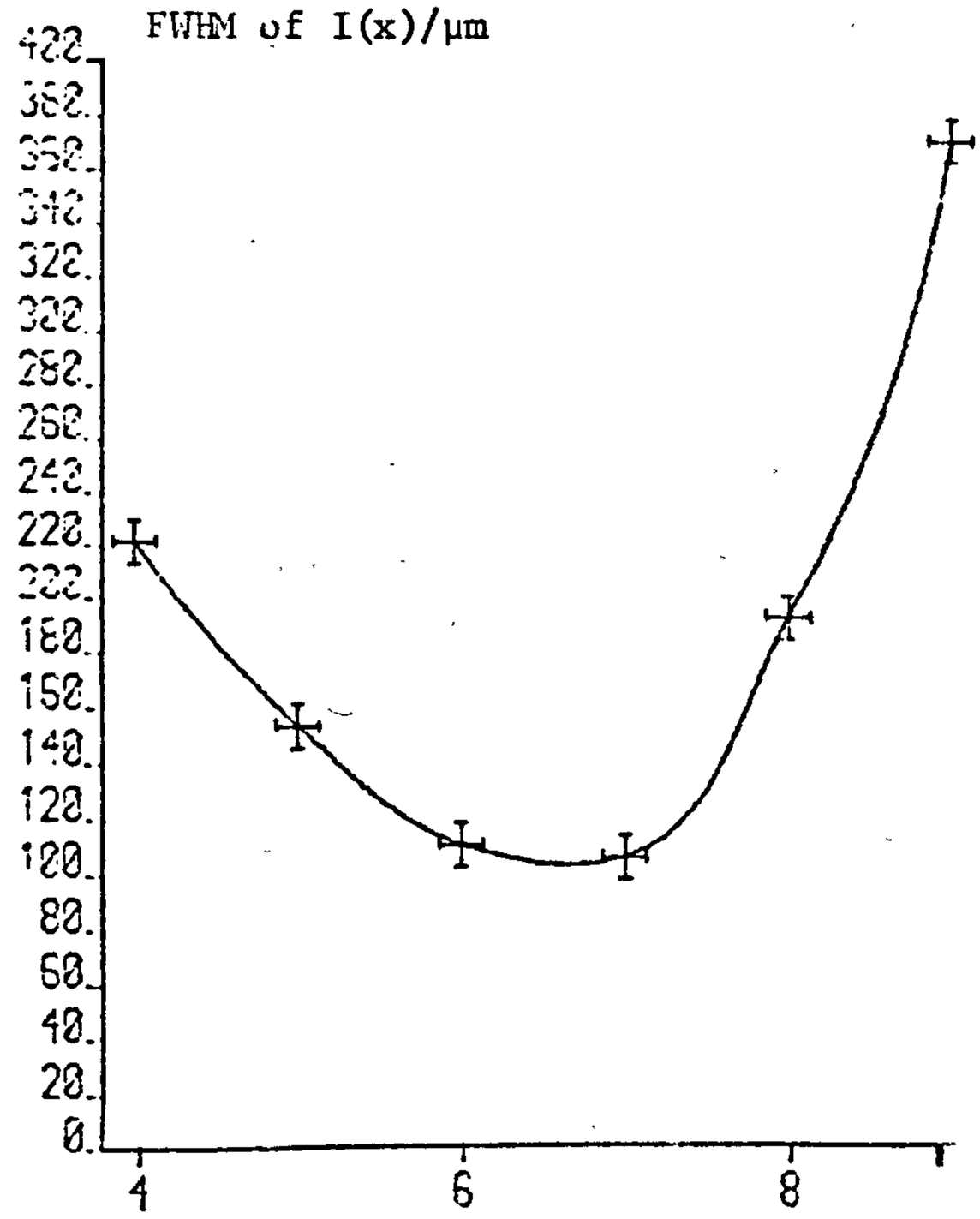

Fig.(8.2c): Electron beam breadth as a function of setting of fine focus control

collection of all the secondaries, and the current flowing in the bias line was measured with a Keithley picoammeter. At an accelerating voltage of 3 kV, the GI gun was found by this method to emit beam currents in the range from 1 to 10 μA, controllable by the filament current setting.

The spatial extent of the electron beam at the sample is determined by the focussing voltage, and was measured by mounting a fine gauge wire on a small frame in the sample position and tracking it in the X-direction, as shown in Fig. 8.2a. This figure also indicates the intensity I(x) of the 3 kV elastic peak, measured as a function of the wire position, x. The function I(x) is a convolution of the response function of the wire and the current density distribution in the beam, as shown in Fig. 8.2b. If we assume that this distribution is Gaussian of standard deviation σ and that the wire responds according to the angle presented to the beam at a position x', we may write

$$I(x) = \left(\frac{A}{\sigma} \int_{x-r}^{x+r} \exp\ (-x'^2/2\sigma^2)(r^2 - (x-x')^2)^{\frac{1}{2}}\, dx' \right)^2 \qquad 8.1$$

where 2r is the diameter of the wire.

The value of the constant of proportionality A was discovered from Fig. 8.2a by solving equation 8.1 numerically, using a σ of 40 μm obtained simply from the half width of the focus 7 curve. Hence it was possible to calculate the 'spreads' σ produced by the other focus settings. Values of 48 μm (focus 5), 73 μm (focus 6) and 72 μm (focus 8) were obtained, but there are profound systematic errors inherent in this approach (the wire has been taken as normal to the beam, for example) and it was not pursued in the course of this study. Estimating the half widths of the I(x) curves was found sufficiently accurate to obtain the calibration of the fine focus control of the gun supply shown in Fig. 8.2c.

8.1.4 Recording spectra

After the sample has been correctly positioned, and the primary energy set (in the range from 0 to 5 keV in 100 eV steps), spectra were recorded in the following manner.

It has been mentioned in subsection 7.6.1 that the spectrometer control unit ramps the pass energy downwards. The procedure for recording spectra was therefore to set the starting ('pedestal') voltage well above the region of interest. A range of 0 to 4 kV in 1 V steps was available. The amplitude of the scan was chosen from 1, 3, 10, 100, 300 or 1000 V and the duration of the scan from 30, 100, 300, 1000 or 3000 s. It was possible to scan the entire range in 0.8 s ('rep. slow') or at rate which gave a continuous display on the CRT ('rep. fast'). The 'rep. slow' mode was used in conjunction with the MCA where the CRT fly-back blanking signal was used to initiate each new data acquisition scan.

Regarding the PSD, the sensitivity (10 μV to 1 V), the DC offsets and the time constant (250 μs to 100 s) were arranged to avoid overloading the amplifier and to eliminate as much as possible of the background noise without filtering out any of the desired signal. The modulation voltage was continuously variable from 0 to 14 V p-p, and was constant throughout all scans, eschewing the automatic facility for background suppression by reducing the modulation at low energies.

The electron beam focus setting was adjusted according to the calibration scheme above, to provide whatever spot size was required, and the beam current was monitored frequently with the Faraday cup, to check for any instability in comparison with the total emission current displayed on the control unit.

The photomultiplier voltage was variable in 1 V steps in the range from 100 to 1000 V. Trial scans on an oxygen peak at different voltages quickly showed that the signal to noise ratio was greatest at a setting of

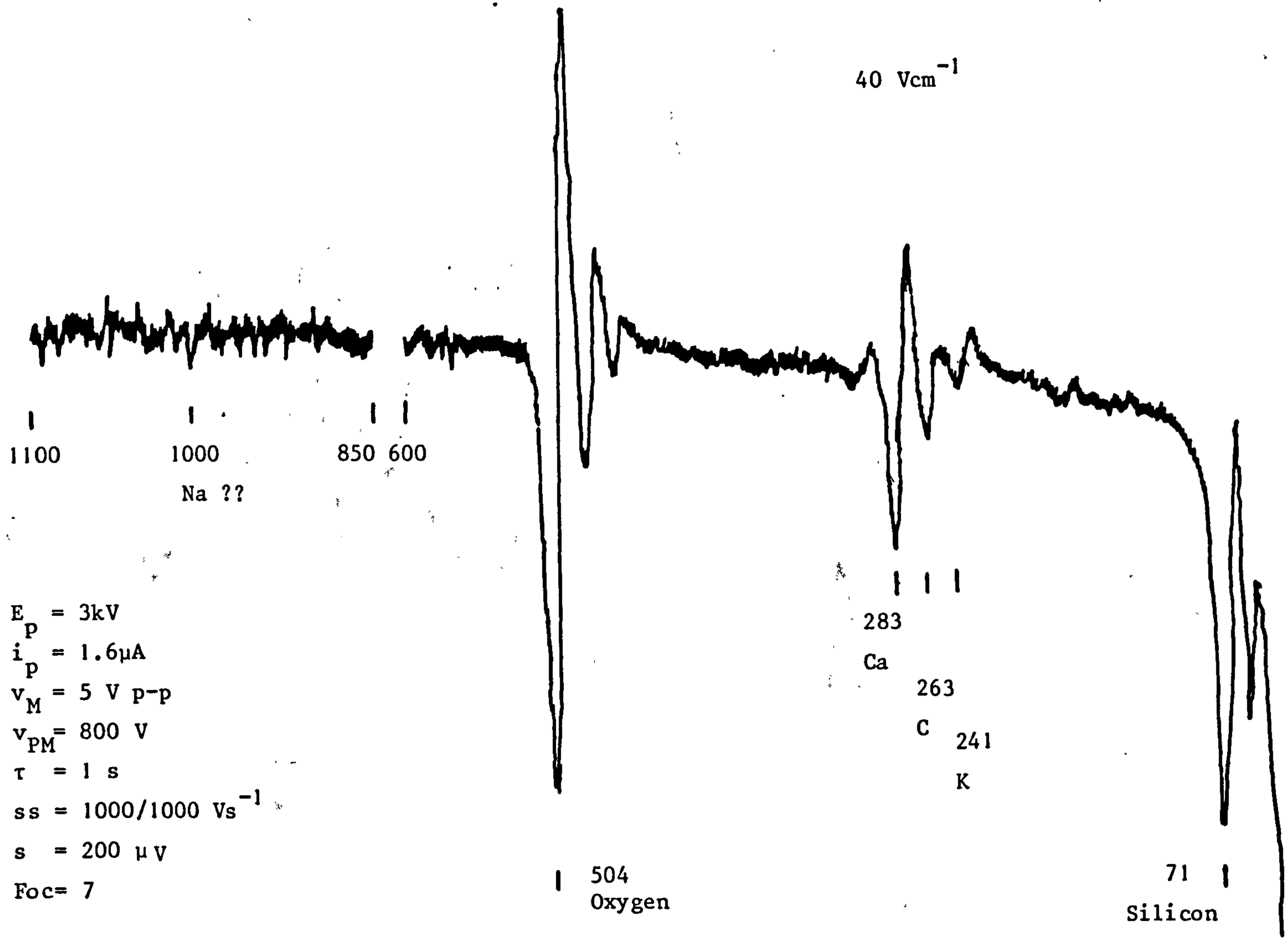

Fig.(8.3a): A typical Auger spectrum from soda glass, after extensive electron beam irradiation

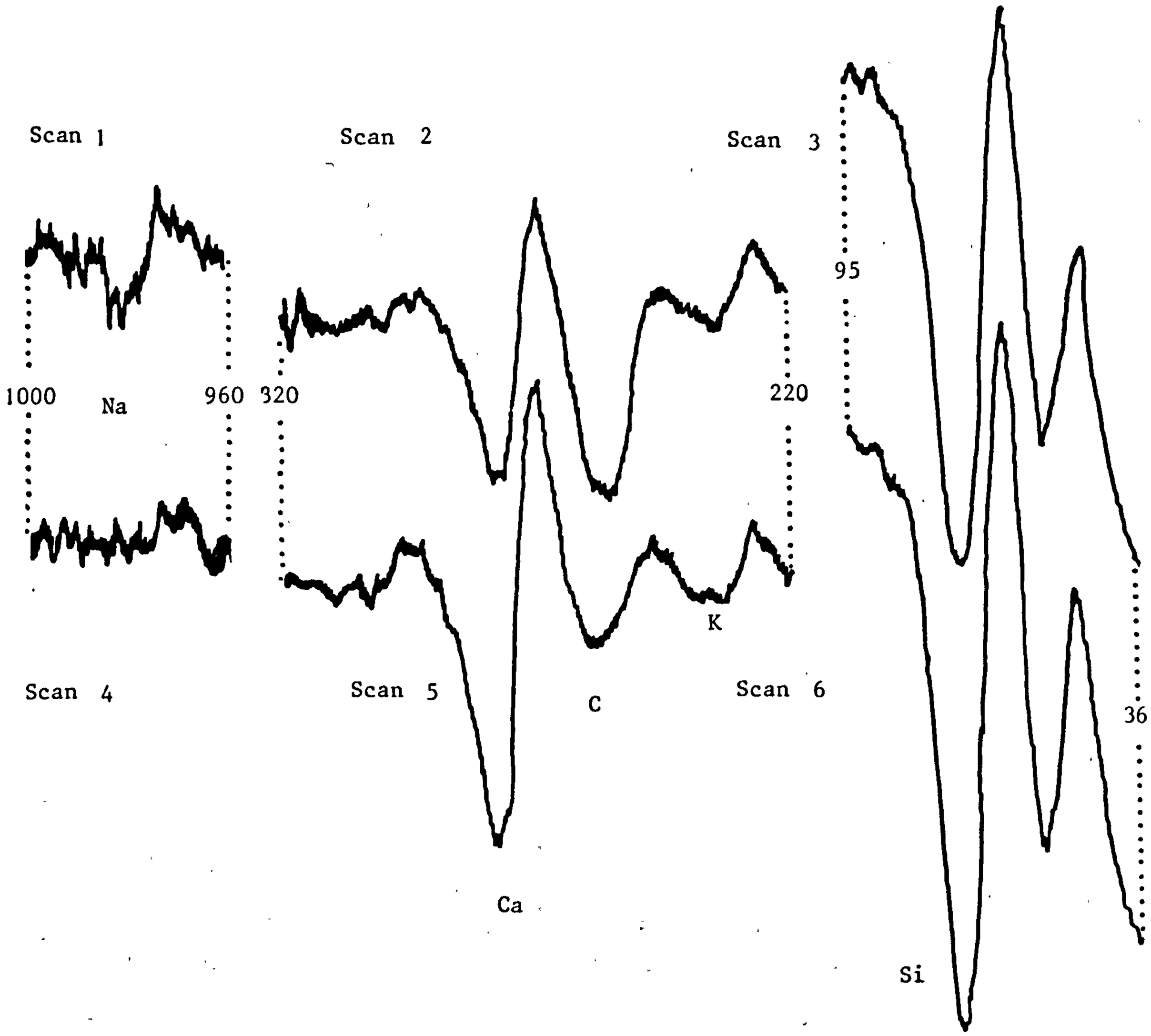

E_p = 2 kV
v_M = 5 V p-p
v_{PM} = 800 V
i_p = 1.0 μA
s = 100 μV
ss = 300/1000 Vs^{-1}
τ = 3 s
defocussed spot
12 Vcm^{-1}

Fig.(8.3b): A fresh area of the same soda glass sample as in Fig.(8.3a), showing increasing damage effects in successive scans.

800 V, and this was used throughout.

For comparability between scans it is essential to record all the settings mentioned above. They will be given individually for each spectrum presented herein, with the abbreviations E_p (primary energy), i_p (beam current), v_M (modulation voltage), v_{PM} (photo-multiplier setting), s (amplifier sensitivity), τ (time constant of amplifier), and ss (scanning speed expressed as the total range divided by the time taken to scan it). The usual convention of labelling differentiated peaks by the energy of the turning point of their higher energy wing will be followed.

8.2 General features

A typical full scan of a window glass surface is given in Fig. 8.3a. The beam was fully focussed (breadth approximately 100 μm) when this spectrum was taken, and although calcium, potassium carbon and silicon may easily be seen, convincing evidence of sodium signals is absent.

For Fig. 8.3b, the same sample was scanned again, this time using lower values of E_p and i_p and a defocussed beam. A sodium peak at 990 eV may easily be seen, showing that the spectra recorded are very dependent on the conditions obtaining at the time of the scan, and the history of the irradiated spot. Indeed, the successive scans given in the figure demonstrate the elusive nature of stable Auger peak sizes. The following sections deal with the processes active here.

The rapid background fall-off at about 100 eV is due to the increasingly negative slope of the secondary emission curve shown in Fig. 7.1. This gradient distorts the shape of the low energy silicon peak and reduces its energy, but using the facilities of the MCA, the background can be subtracted, as shown in Fig. 8.4. The silicon N'(E) peak in glass is seen to be a doublet of energy 75 and 58 eV. Once the slope has been subtracted, the peak may be integrated numerically to yield N(E), as in the

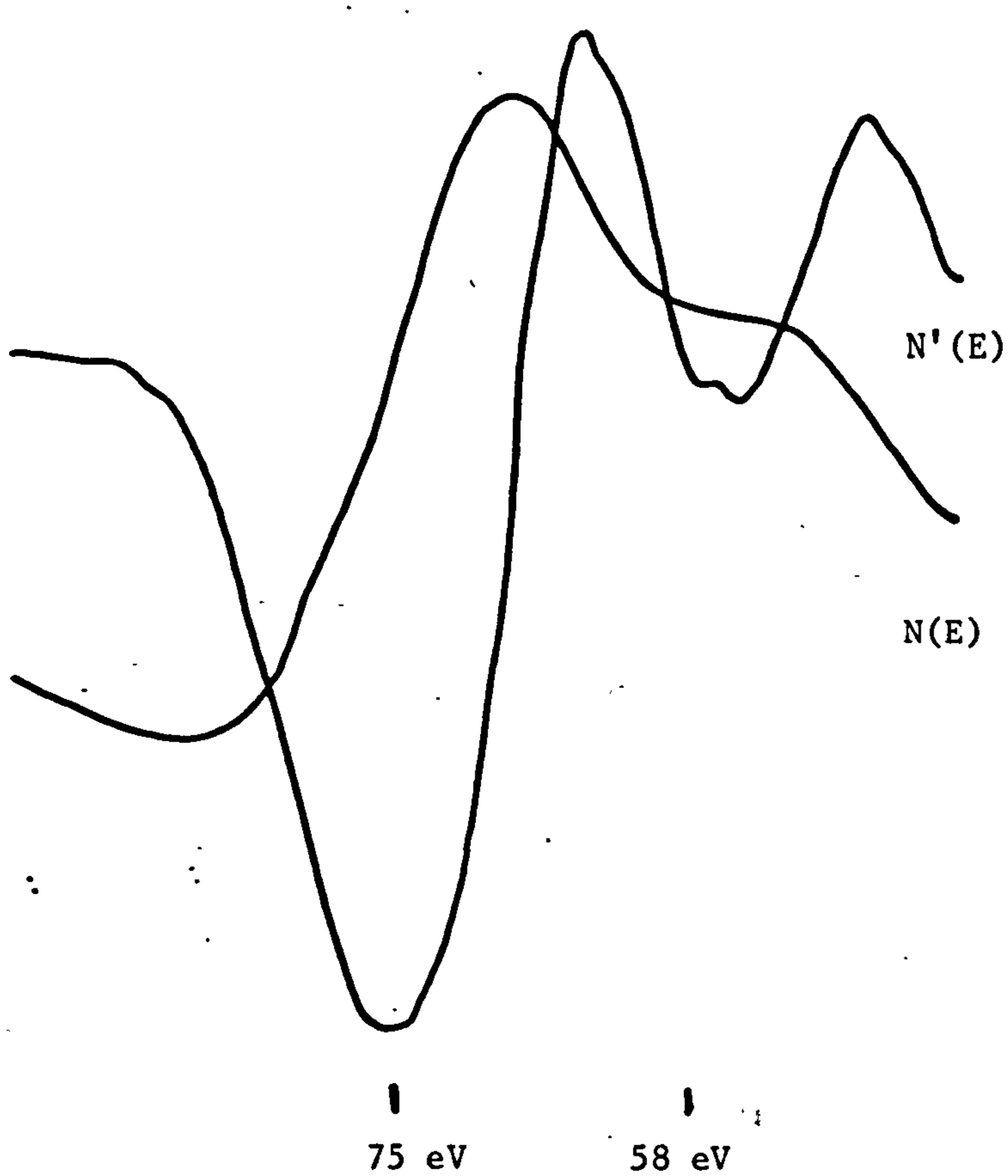

Fig.(8.4): Silicon Auger peak in glass, with sloping background subtracted using the MCA. The N(E) curve is the N'(E) curve integrated numerically.

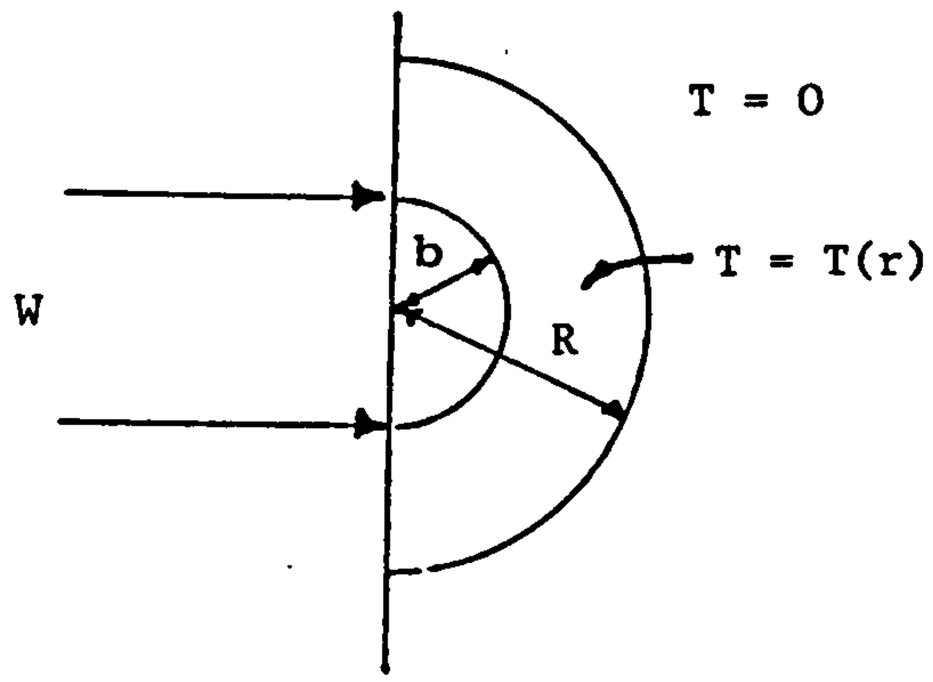

Fig.(8.5): Hemispherical heat flow geometry, after ref.8.2.

figure, but peak shapes obtained by this method are contingent on the nature of the polynomial used for the background subtraction, and cannot be reliably reproduced.

Traces of carbon may be detected on almost all surfaces not created in UHV conditions by cleavage or by sputtering. The highly assymetric shape of the carbon N'(E) peak, as shown in Figs. 8.3,is characteristic of a graphitic surface layer, presumably deriving from environmental contamination.

8.3 Beam damage

The various mechanisms by which an electron beam may alter a glass surface have been discussed briefly by Pollard (7.43) and Ohuchi et al (8.1). They may be described semi-quantitatively as follows:

8.3.1 Surface heating

Using an electron beam of 2 μA at 3 kV, the power density incident upon a 100 μm diameter spot is as high as 1 MWm^{-2}, and the temperature of the material in the spot will rise. The heat flow problem has been studied by Friskney and Haworth (8.2), by solving the equation:

$$W = -2\pi r^2 \kappa \frac{dT}{dr} \qquad 8.2$$

where W is the beam power, κ the thermal conductivity and dT/dr the temperature gradient in the material, for the hemispherical case shown in Fig. 8.5. Appendix VIII provides the few steps necessary to obtain, for the maximum temperature elevation $T_m/^{o}C$, the expression:

$$T_m = \frac{3W}{4\pi\kappa b} \simeq 0.239 \frac{W}{\kappa b} \qquad 8.3a$$

As a consequence of the radial heat flow in this treatment, the beam radius b must be taken as much smaller than the region being heated.

The result for T_m of equation 8.3a is similar to that obtained by Baker and Sexton (8.3) for the maximum temperature attained at the surface

of a sample bombarded with an electron beam of uniform power density. If the sample is much thicker than the heated layer, these workers show that:

$$T_m = \frac{W}{\pi \kappa b} = 0.378 \frac{W}{\kappa b} \qquad 8.3b$$

Alternatively, the problem may be approached from first principles, by summing over the whole sample surface solutions to the diffusion equation

$$\nabla^2 T = \frac{1}{K} \frac{\partial T}{\partial t} \qquad 8.4$$

for point sources of heat. In this equation, the diffusivity K is given by $\kappa/\rho c$, where ρ is the density and c the specific heat of the medium. It has been shown by Pittaway (8.4) that for a Gaussian incident power density profile of standard deviation σ, the rise in temperature ΔT at a time t after the start of irradiation may be calculated from equation 8.4 as:

$$\Delta T(t) = \frac{W}{\pi^{3/2} \kappa \sigma} \arctan \left(2\sqrt{Kt}/\sigma\right) \qquad 8.5$$

This function is plotted in Fig. 8.6 for the heating of a glass sample by a 1μA beam at 3 kV, using parameters K and κ from standard texts (8.5), and it can be seen how very quickly the maximum temperature:

$$T_m = \Delta T(\infty) = \frac{W}{2\sqrt{\pi} \kappa \sigma} = 0.282 \frac{W}{\kappa \sigma} \qquad 8.6$$

is approached. The similarity of equations 8.3 and equation 8.6 allows us to identify the standard deviation of a Gaussian beam profile with the radius of the uniform beam.

It can be seen that for beam diameters above 200 μm the rise in temperature is restricted to below 10°C. It is difficult to associate changes in the properties of a glass analyte with temperature differences as slight as these.

8.3.2 Descrption

An impinging electron beam causes an alteration of the local charge distribution in a material. In the case of a predominantly ionic solid, it

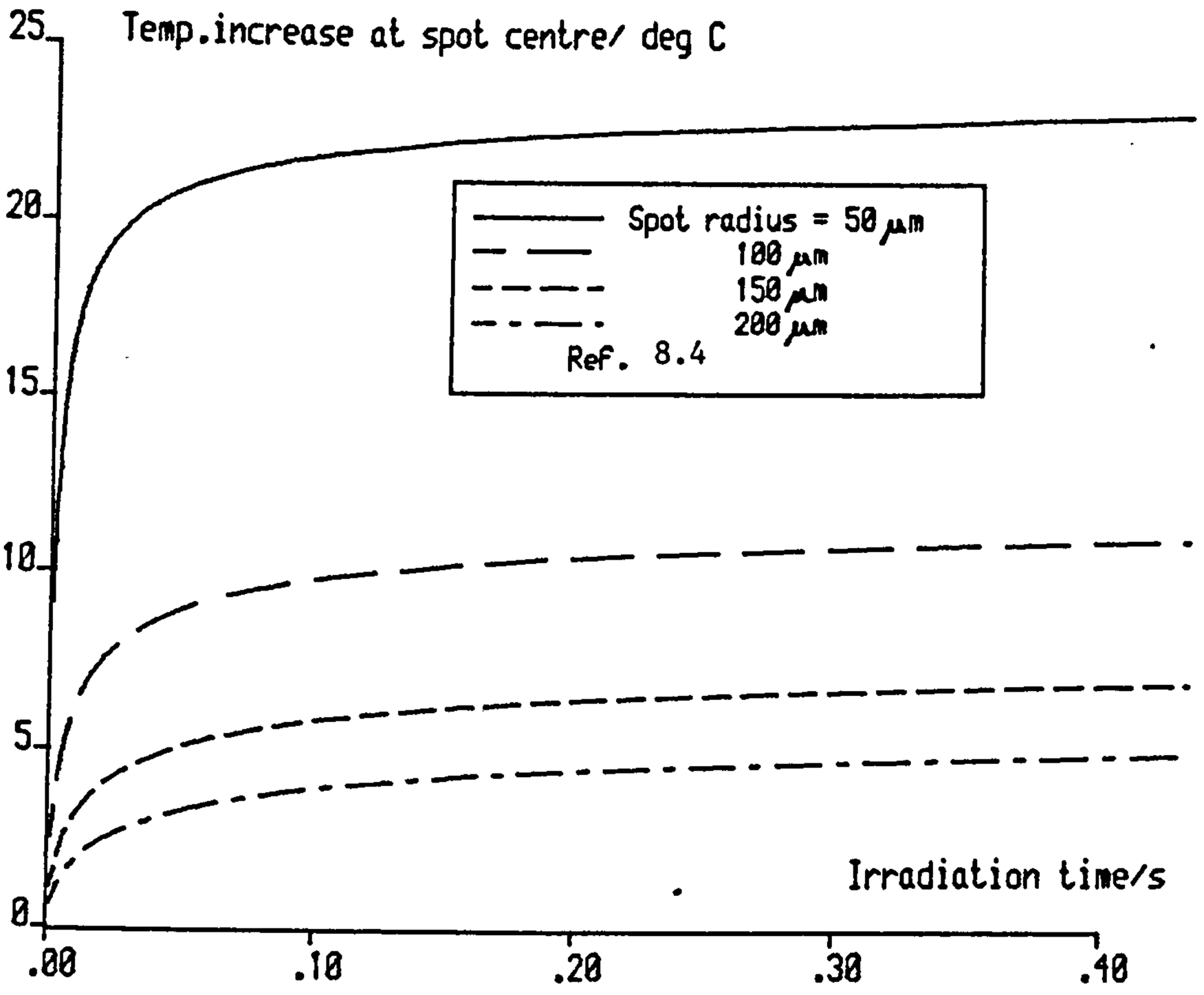

FIG(8.6): Glass heating by electron beam

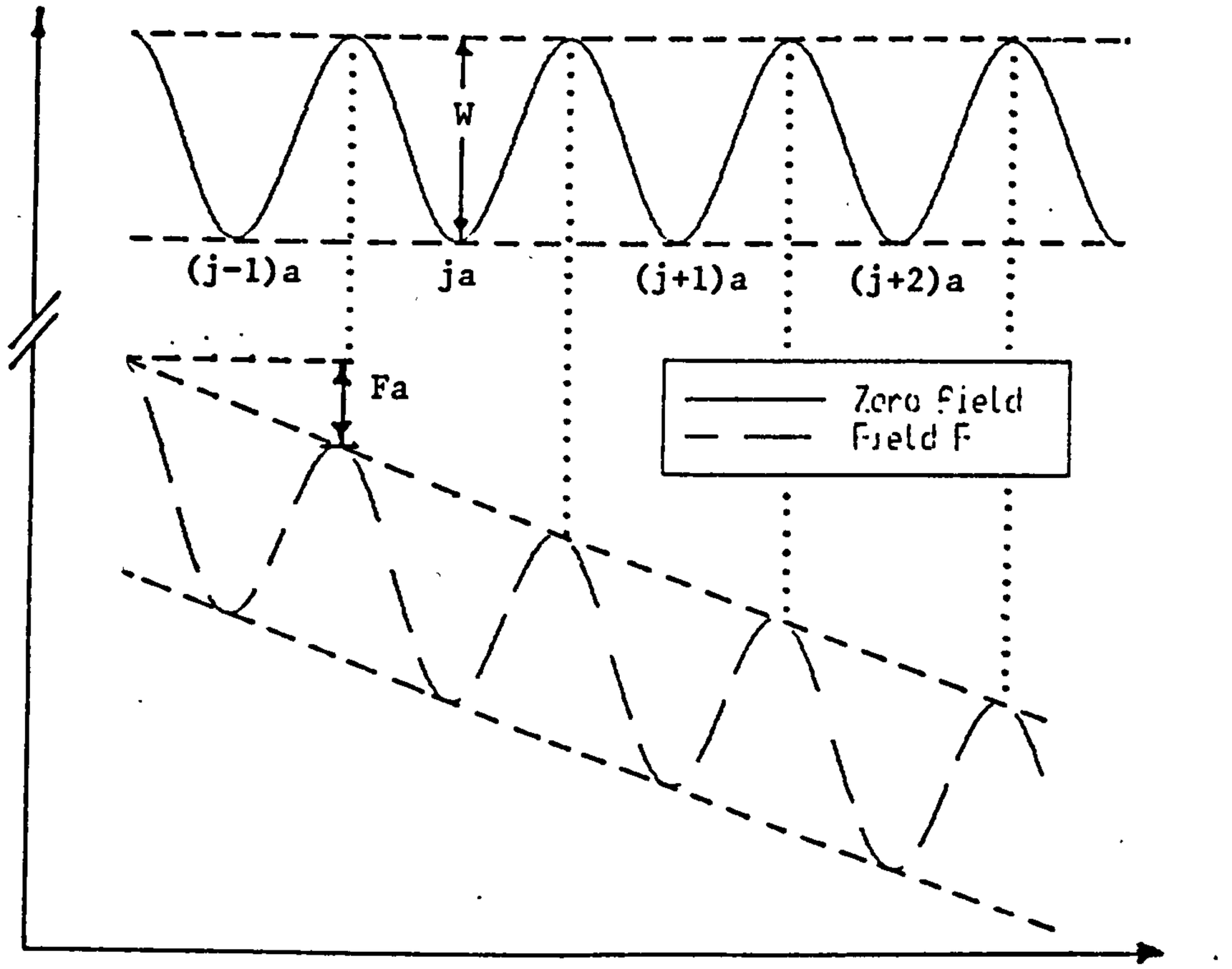

Fig:(8.7): Periodic potential wells in glass, showing the effect of an applied electric field.

is possible that the Madelung binding energy for a particular ion might be altered substantially, or indeed temporarily reversed in sign. Such an occurence, which would expel the ion from its site and perhaps from the bulk, is known as electron stimulated desorption (ESD).

Ohuchi et al (8.1) consider ESD a contributory factor in the decay of the sodium Auger signal from glass samples.

8.3.3 Ion migration and diffusion

As discussed in detail in section 1.1, the network modifying ions of a glass are considered to be scattered throughout the lattice in interstitial sites as shown in 2-dimensional analogy in Fig. 1.2b (1.2). Such electrical conductivity as can be measured in glasses is explained by postulating an ionic migration between these sites, under the impressed electric field. The experimental evidence for this effect is provided by Douglas and Isard (8.6) in their study of the correspondence between the activation energies for electrical conductivity and for ionic diffusion in glasses. In this reference, the temperature dependence of the diffusion constant D is shown to be given by:

$$D(W,T) = D_o \exp(-W/kT) \qquad 8.7a$$

where T is the absolute temperature, k is Boltzmann's constant, and W is both the 'activation energy' for diffusion and the depth of the potential wells between which the ion are considered to move. Assuming the modifying ions to be distributed with a broadly uniform concentration (the existence of a minimum separation makes the term 'random' inappropriate), we can conceive of a 'periodic glass' with potential wells of constant depth and separation as shown in Fig. 8.7.

The effect of an applied electric field upon such a system is to raise one side of the well and to lower the other by the same amount, $\frac{Fa}{2}$, where F is the field strength, and a the average separation. This increases

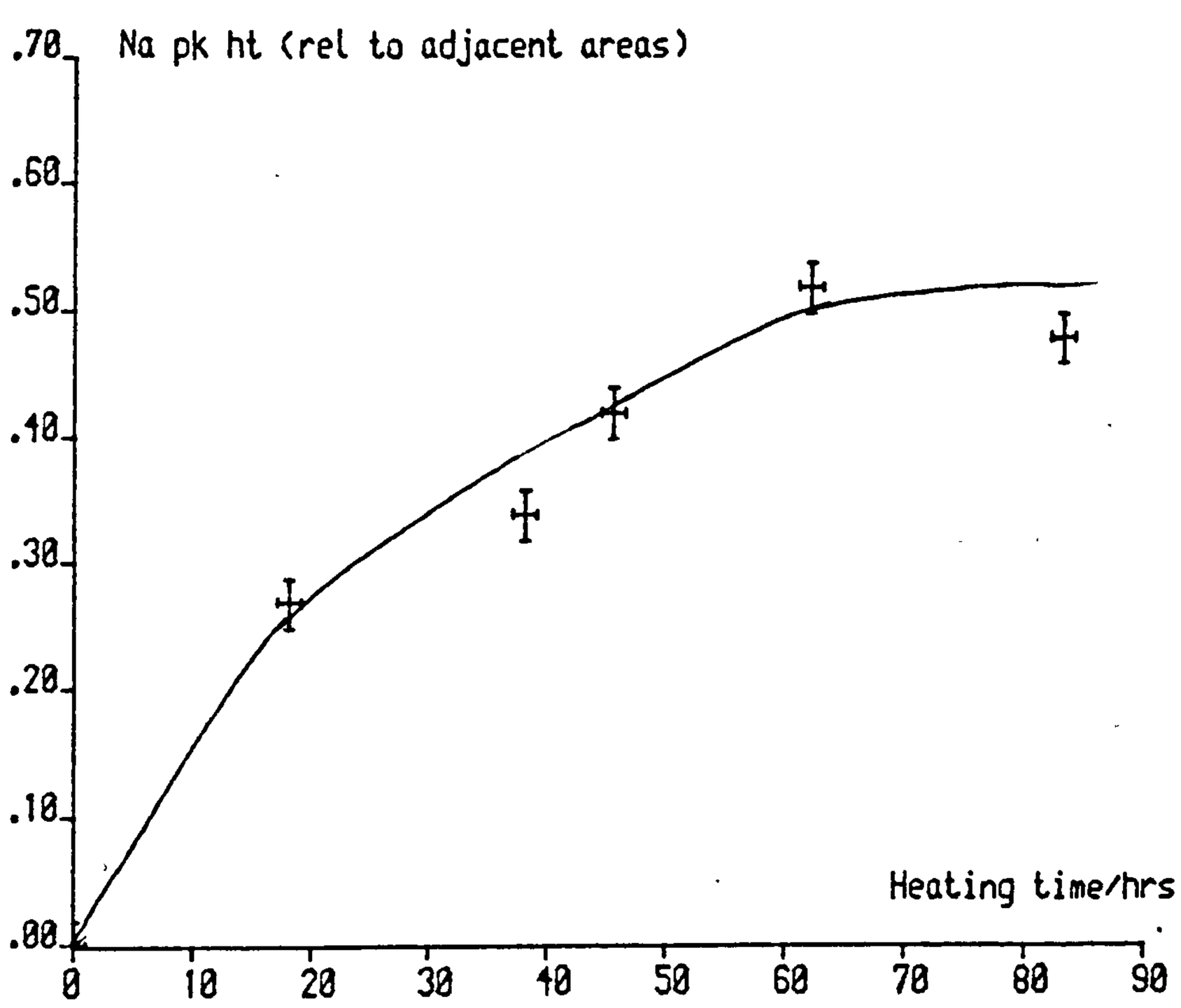

FIG(8.8): Sodium rediffusion in glass at 700 K

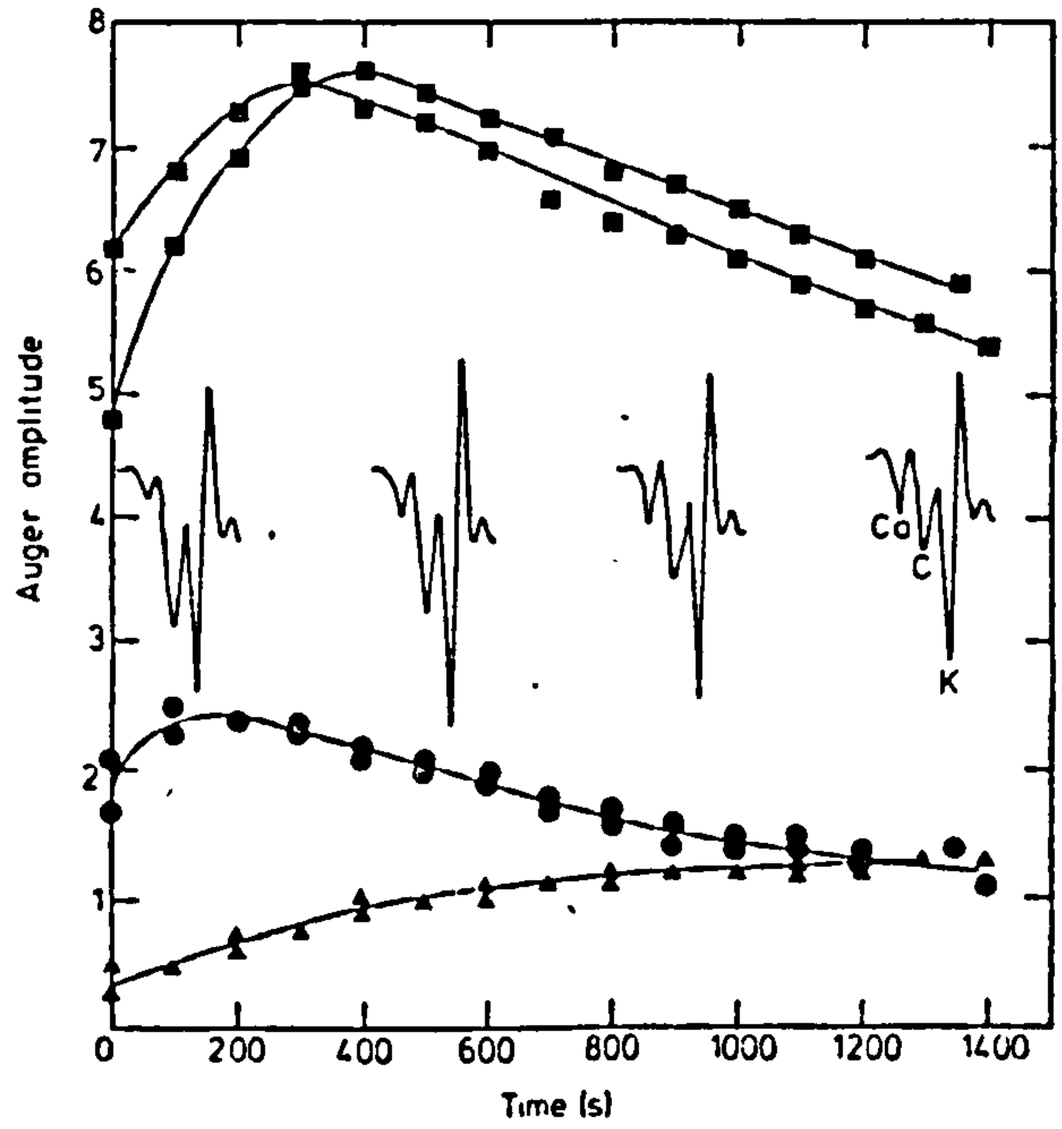

The variation in the calcium (▲), carbon (●) and potassium (■) Auger signals with exposure time to the electron beam for simulated mediaeval glass. The results of two separate experiments are shown, both for primary beams of 3 keV and 1·5 μA. Also shown in the figure are the Auger scans for Ca, C and K at 100, 500, 900 and 1300 seconds.

Fig.(8.10): Time dependence of Auger signals from glasses. Ref.8.8.

the probability of the escape of the ion in one direction at the expense of the other, resulting in an ion current which may be used to determine the trap depth, W. For sodium ions, W is found to be 0.774 eV by this method (8.6), and from diffusion measurements alone (using the rate of the surface reactions with water discussed in Chapter 1) a result of 0.994 eV is obtained.

Another method of measuring W has been to study the diffusion of sodium from a thin surface layer, using radioactive tracers (8.7). In this case the results can be described by the equation:

$$D/m^2s^{-1} = (8 \pm 3) \times 10^{-8} \exp\left(\frac{-0.707 \pm 0.022}{kT}\right) \qquad 8.7b$$

where the energies are in eV, a result not dissimilar to those of Douglas and Isard. We can conclude that in sodium silicate glasses, the average depth of the wells in which the sodium ions are usually to be found is between 0.7 and 0.9 eV.

When the sodium had been completely expelled from an irradiated spot, so that its Auger signal had become unmeasurable, an experiment was done to determine whether it could be recovered. It has been reported (7.43), and is very easily shown, that no reappearance of sodium signals from beam damaged glass is observed at room temperature. However, Fig. 8.8 shows that after about 60 hours at 700 K (kT = 0.06 eV) the sodium concentration in the analysed volume has regained half its initial value. Further heating could not recover the full signal.

The data points in this experiment were obtained by irradiating an identifiable area of the glass surface (one marked with a cross) and noting the Auger signal size from it relative to adjacent areas chosen at random. This required that the sample be maintained at room temperature or below during analysis, that the sodium concentration of the glass be constant, that the carbon contamination of the surface be constant, that the electron beam

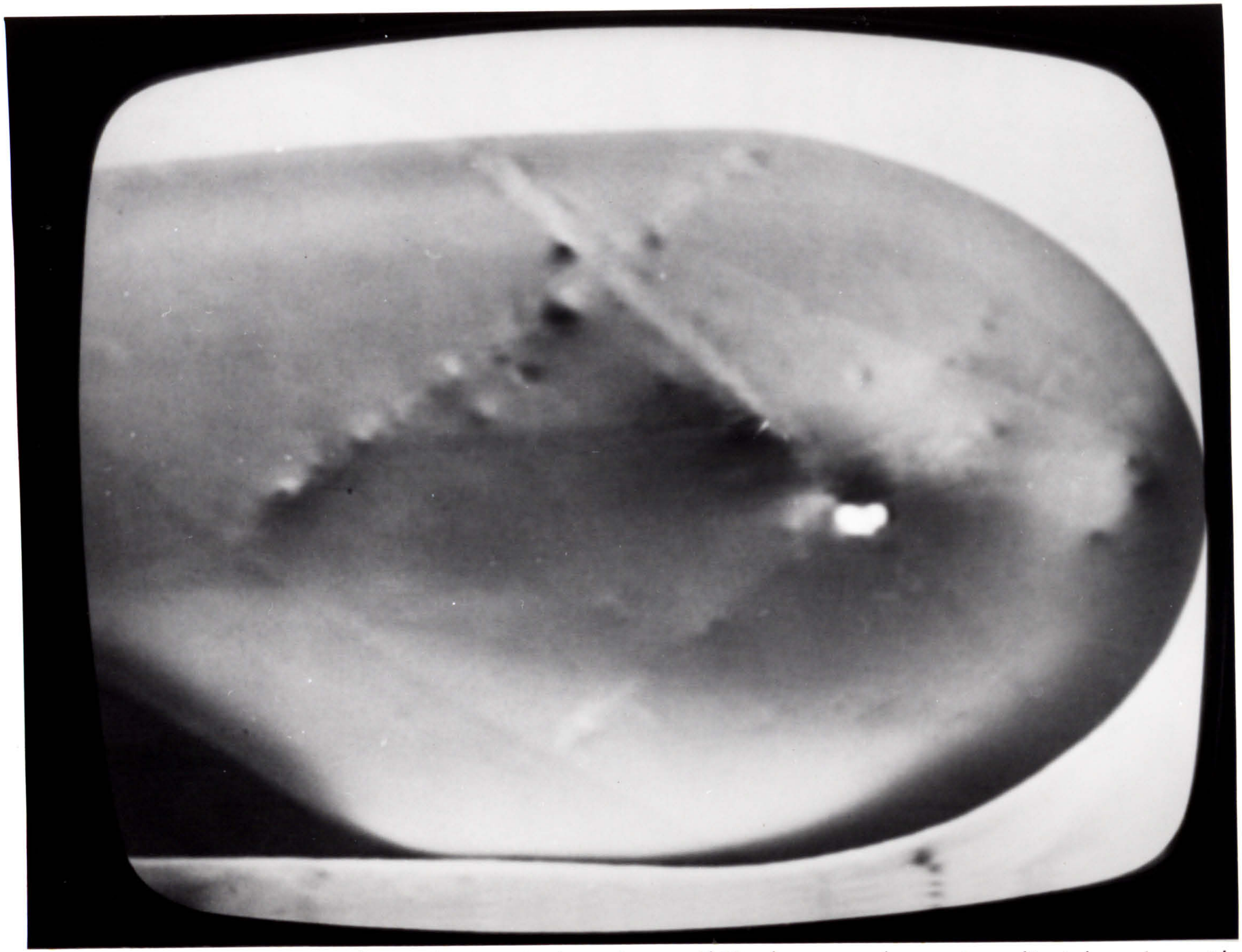

Fig.(8.9): Photograph of the video display during the re-diffusion experiment described in sub-section 8.3.3. The analysed spot, at the intersection of the scribed lines, has a greatly modified secondary electron image.

current suffer no drift with respect to its calibration, that the successive heating and cooling of the sample and holder have no effect upon the signal size, and that no further beam damage to either the spot or to adjacent areas should occur. The results shown in Fig. 8.8 are therefore attended with uncertainty. Fig. 8.9 is a photograph taken of the video display showing the spot used for this experiment, and the effect of the irradiation on the secondary electron image of the sample, which is considerable.

The failure to re-diffuse all of the original sodium into the depleted volume despite very considerable heating could be interpreted as showing that the quantity of sodium in a volume of glass larger than that originally irradiated (and surrounding it) has been permanently reduced. This might have occurred through desorption (see subsection 8.3.2) or by migration through the surface caused by a rising electric field in the bulk of the glass, an effect to be described fully below. Conversely, the results might imply the existence of a very wide distribution of trap depths, the probability of emptying some of which, by a thermal energy of only 60 meV, is extremely small. Heating to a higher temperature would, in this case, increase the quantity of re-diffused sodium. Unfortunately, time did not permit an investigation of the temperature dependence of the phenomenon.

8.3.4 Induction time, T_i

The time dependence of the Auger intensities from ions in glasses has been studied by Pollard (7.34), Dawson et al (8.8) and Pantano et al (8.9, 8.10). Some of the results of Dawson et al, which were obtained using the equipment described in this thesis, are shown in Fig. 8.10. It can be seen that the absolute magnitude of the carbon and potassium signals rise sharply before declining, and that the signals from calcium show a slight

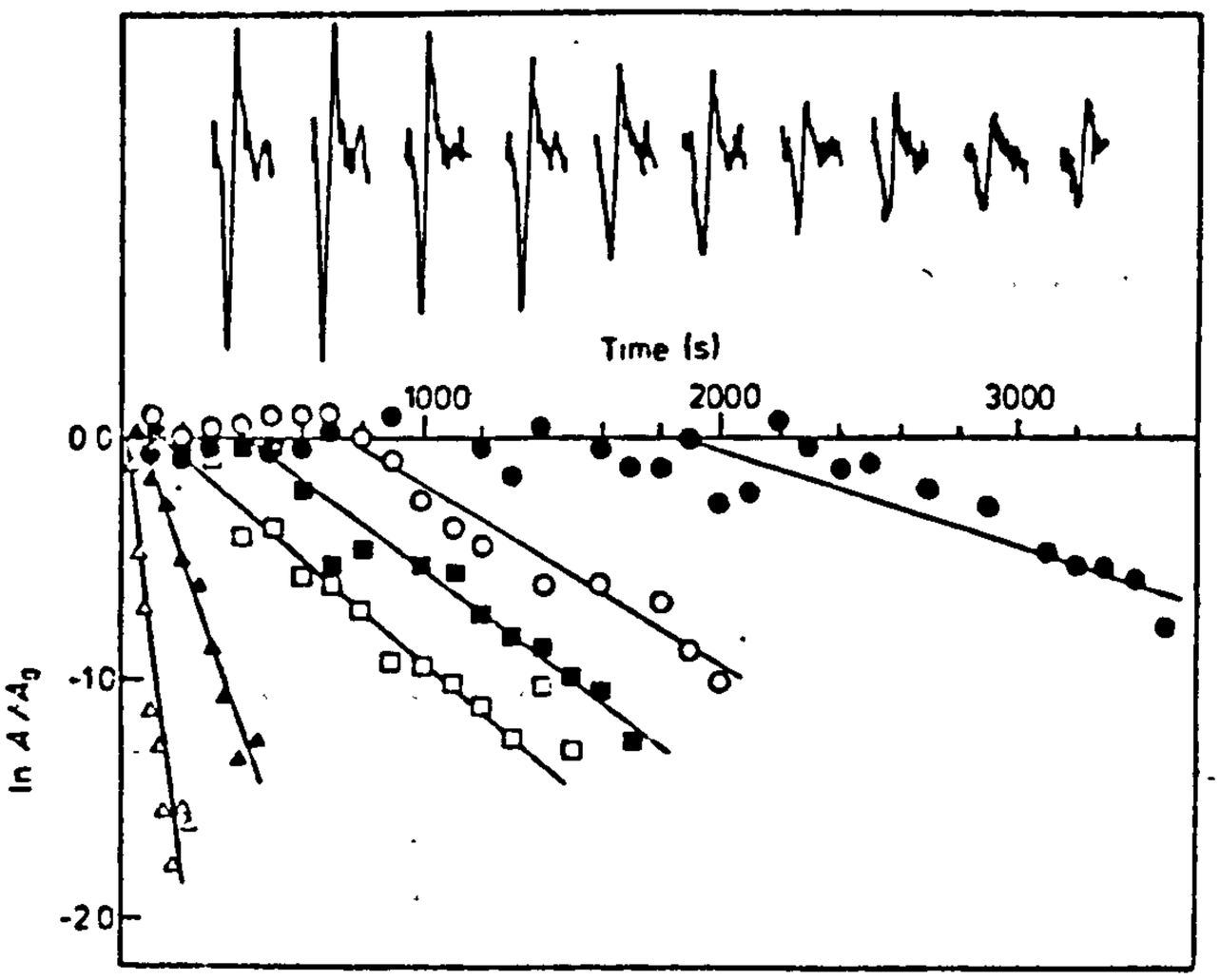

The decay of the sodium Auger signal of sample with exposure time to the electron beam, plotted as the natural logarithm of the ratio of the Auger amplitude at a given time to the initial amplitude. The inset shows a typical data set obtained for a beam current of 2 μA at 3 keV. The sodium 990 eV peak was scanned continuously with scan starts separated by 50 seconds. Δ 10·0 μA, ▲ 2·0 μA, □ 1·0 μA, ■ 0·75 μA, ○ 0·5 μA, ● 0·25 μA

Fig.(8.11a): Sodium signal decay at room temperature
Ref. 8.8

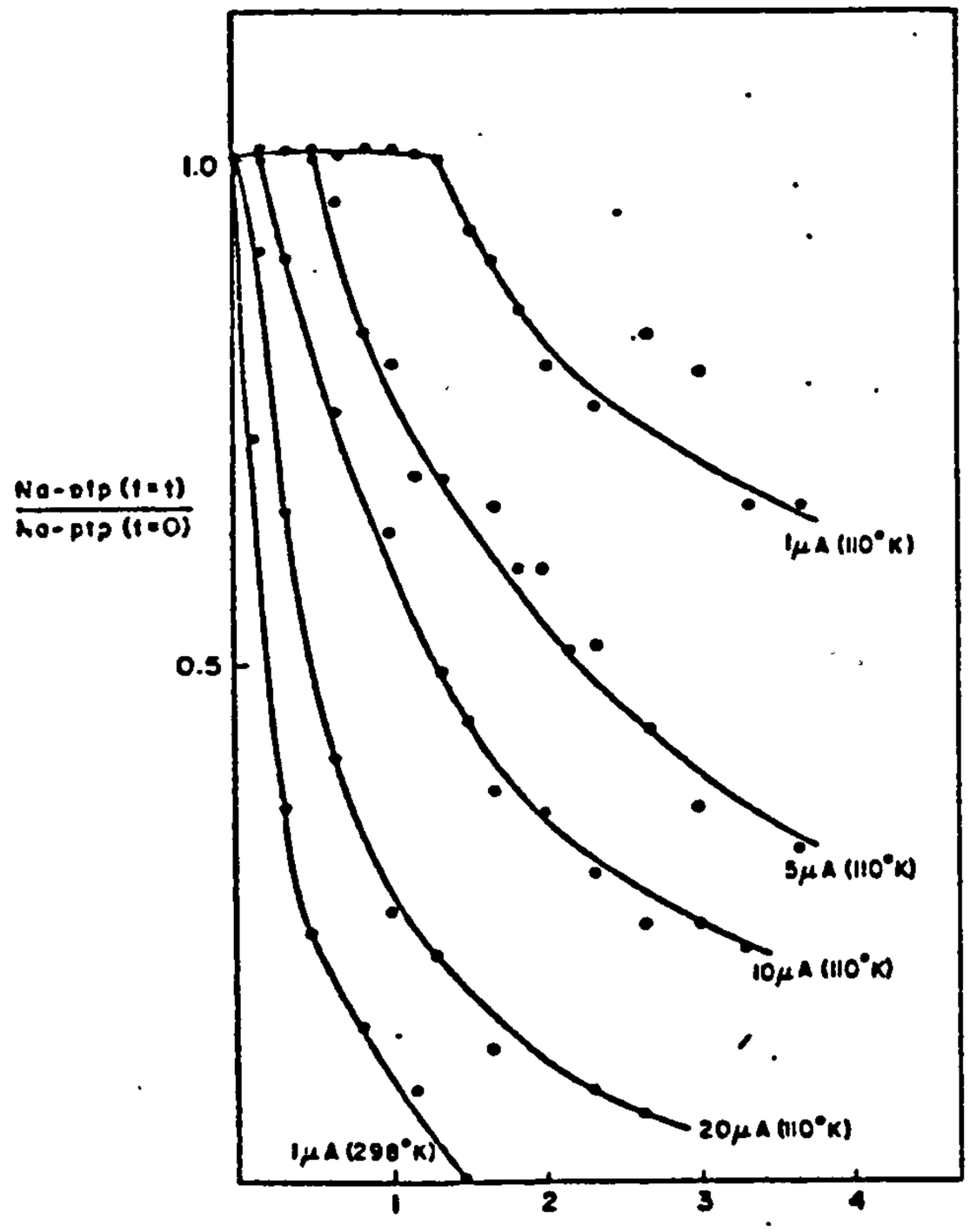

The decay at 110 K of the Na peak-to-peak height, normalized to the peak-to-peak height at zero time, as a function of the time of electron irradiation for beam currents of 1, 5, 10, and 20 μA. A decay curve measured at room temperature and 1 μA is also shown.

Fig.(8.11b): Sodium signal decay at 110 K. Ref.8.9

rise overall. A change in absolute peak size can be attributed to many factors; in this case to the decline in the density of the surface carbon layer. No significant increases in signal intensities were observed in the present investigation when the peak sizes relative to that from the silicon in the sample were recorded. The practice of recording only relative peak sizes only was adopted to reduce the effect of the changing carbon layer, although since Auger electrons from the sodium are attenuated less by a carbon layer than are those from silicon, because of their higher energy, the effect is not eliminated.

Calcium was found not to exhibit decay, which is probably attributable to its larger ionic radius reducing its mobility.

The case of sodium is particularly interesting. The signals begin to decrease only after the elapse of a period of time, determined by the conditions of the irradiation. This time is known variously in the literature as the 'residence time', 'incubation time' or 'induction time', T_i. The latter term will be used, as by Dawson et al (8.8) whose results are shown in Fig. 8.11a. The induction time is found by these workers to be inversely related to the beam current according to:

$$T_i/s = 200\ (i_p/\mu A)^{-1} \qquad 8.8a$$

The results of Pantano et al (8.10), shown in Fig. 8.11b, were taken at liquid nitrogen temperature and fit a similar equation:

$$T_i \sim 150\ i_p^{-1} \qquad 8.8b$$

except in the case of a beam current of 1 μ A. These workers find, somewhat surprisingly, that at room temperature the induction times are unchanged, except for the 1μ A value.

After T_i, the decay of sodium signals S(t) is described by the equation:

$$S(t > T_i) = S(t < T_i)\left\{1 - 0.3\ \ln\ (t/T_i)\right\} \qquad 8.9a$$

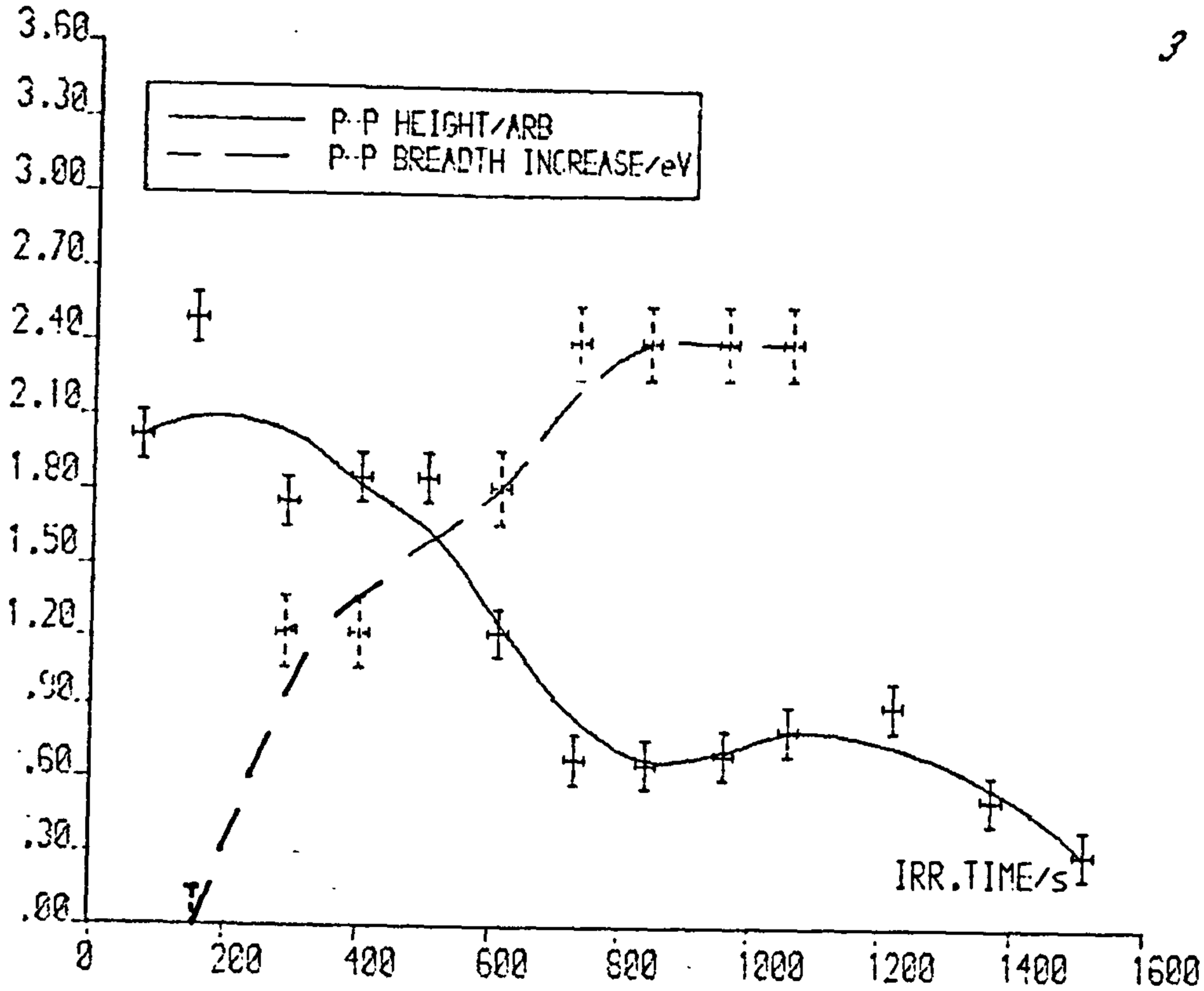

FIG(8.12):SODIUM 990eV AUGER PEAK DECAY

Fig.(8.13a): Time dependence of Na Kα intensity I(t) for glass containing 24 wt% NaO. Ref.8.11

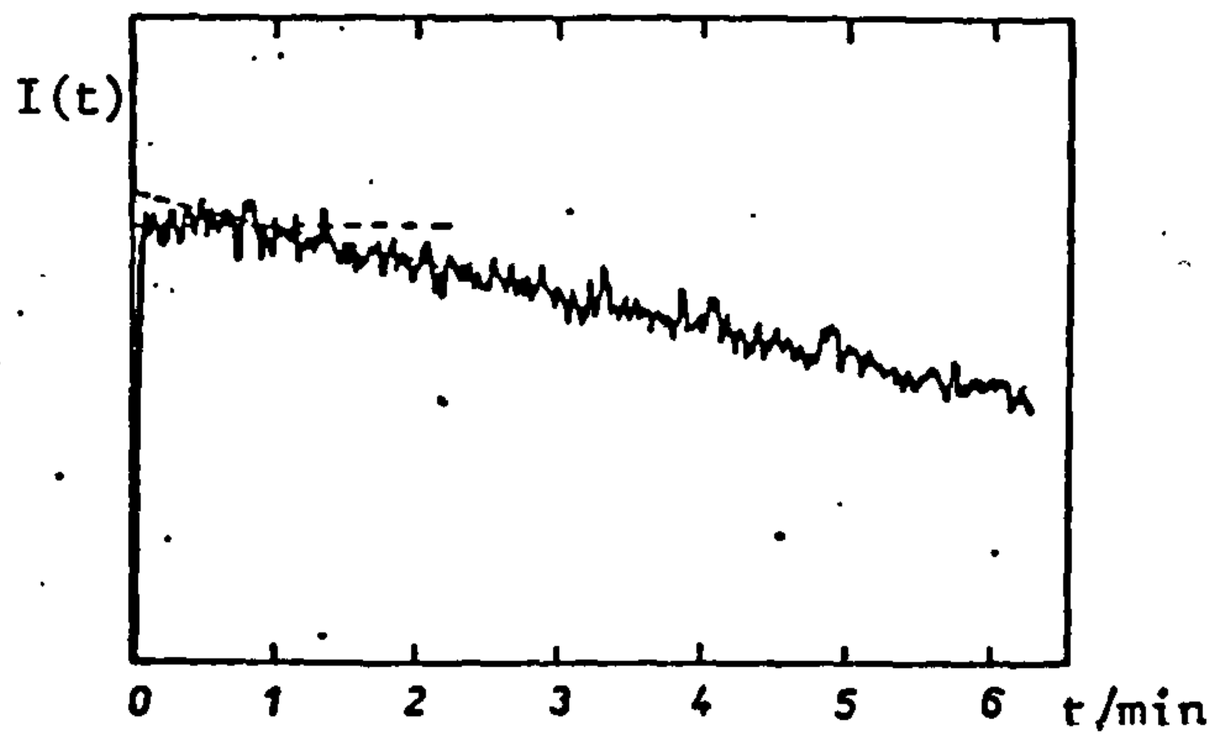

Fig.(8.13b): Induction time T_i against current density $j/mAcm^{-2}$. The two glasses used were coated with a copper layer. Ref.8.11

at both room temperature and at 110 K, according to Pantano et al (8.9), but by:

$$S(t > T_i) = S(t < T_i) \exp(-2 \times 10^{-3} i_p t) \qquad 8.9b$$

according to Dawson et al (8.8).

Fig. 8.12 shows the relative intensities of the sodium to the silicon signals from a microscope slide, and the change in the separation of the extrema of the peaks (or peak 'breadth') as a function of time. The sodium signal is seen to broaden by as much as 2.4 eV (~40%), and the broadening can be seen to set in well before the decay has become apparent. The rather large scatter of points in the figure might be explained in terms of the low bulk concentration of sodium in the glass causing a lower S/N ratio than is usual in such plots.

A satisfactory theoretical description of the decay of alkali ion signals during electron beam spectroscopy of glasses must encompass the time dependence of both intensity and peak breadth.

That the induction time phenomenon is not an artifact of Auger spectroscopy is shown by the work of Vaskova et al (8.11) using sodium K_α emission from electron beam bombarded glasses. Figs. 8.13 show these workers' results and it is notable that the inverse behaviour in Fig. 8.13b is with primary current density j and not simply with the current i_p.

8.4 Electromigration

During a discussion of the oxygen outgassing of electron bombarded glasses in 1963, Lineweaver (7.29) states that the incident electrons "dissipate their energy by ionization and excitation of the atoms of the glass structure" and "come to rest at some depth within the glass producing a net negative charge". This charge is considered to set up a field in the glass layer "in a direction necessary to move the positive sodium ions toward the negative charge region". This is the Lineweaver mechanism for the electro-

migration of ions in glasses which has been widely quoted. Thomas (8.12), while accepting that electric fields are created in glass surfaces, criticises this simplistic view of the final states of the electrons, and denies that sodium migration is responsible for oxygen release.

Lacharme and Champion (8.13) attribute the decay of sodium Auger intensity from irradiated glasses to the existence of a positive charge density in the bulk away from which the ions are considered to move. No model for the production of this charge distribution is proposed, nor explanation of the induction times given.

In a recent conference paper (8.14), Heavens and Usher indicated that the polarity of the electric field and the consequent direction of motion of the ions can be deduced from the change in Auger line shape as the irradiation proceeds. A paper describing this work has been accepted by the Journal of Physics C (8.15), and it is the substance of the remainder of this section.

8.4.1 Dielectric breakdown in glasses

The discussion of conductivity in subsection 8.3.3 was based upon the periodic structure of Fig. 8.7. Continuing the analysis, we can write the probability of an ion leaving the potential well in a positive direction as being proportional to:

$$\exp\left[-(W-Fa/2)/kT\right] \qquad 8.10a$$

and for the other direction:

$$\exp\left[-(W+Fa/2)/kT\right] \qquad 8.10b$$

if the field is as shown in the figure.

The net flow is therefore in the positive direction and contains a term:

$$e^{-W/kT}\left[\ e^{Fa/2kT} - e^{-Fa/2kT}\ \right] \qquad 8.11$$

which is large only if:

$$\tfrac{1}{2}Fa - W > kT \qquad 8.12$$

As we have seen, $kT \ll W$ at room temperature, and therefore the field F_B necessary for large ionic flow is given by:

$$F_B \sim 2W/a. \qquad 8.13$$

Equation 8.13 is crudely derived but serves to predict the order of magnitude of the dielectric strengths of glasses. The quantities W and a, as has been stressed, are distributed over a wide range.

Reported values of F_B from the literature are in the region of 10^8 Vm^{-1} (8.16), and depend strongly upon the experimental conditions, in particular the thickness of the sample. Dignam (8.17) develops the theory of ionic transport under large electric fields, showing that higher fields are possible in thin films than in bulk samples. Evaluating equation 8.13 with W = 0.7 eV and a = 3.5 $\mathring{A}$ yields $F_B = 4 \times 10^9$ Vm^{-1}, which is rather higher than observed breakdown fields, but it must be realised that breakdown in real glasses is often the result of conduction in surface discontinuities (micro-cracks), or of Joule heating effects, and not necessarily caused by the homogeneous bulk ionic motion described above.

We will consider satisfaction of equation 8.13 a criterion for ionic conduction, and hence will regard F_B as the maximum attainable field in glass.

8.4.2 Space-charge effects

High energy incident electrons are slowed by a dielectric through a diversity of processes, the eventual result of most of which is the emission of an electron, leaving the sample in an electrically neutral state. However, alterations will be made to local charge distributions and energy levels, and what are known as 'damage centres' may be created (see for example, 8.17). The literature concerning centres in crystals is too extensive to review here, but Bishay (8.18) and Lell et al (8.19) have

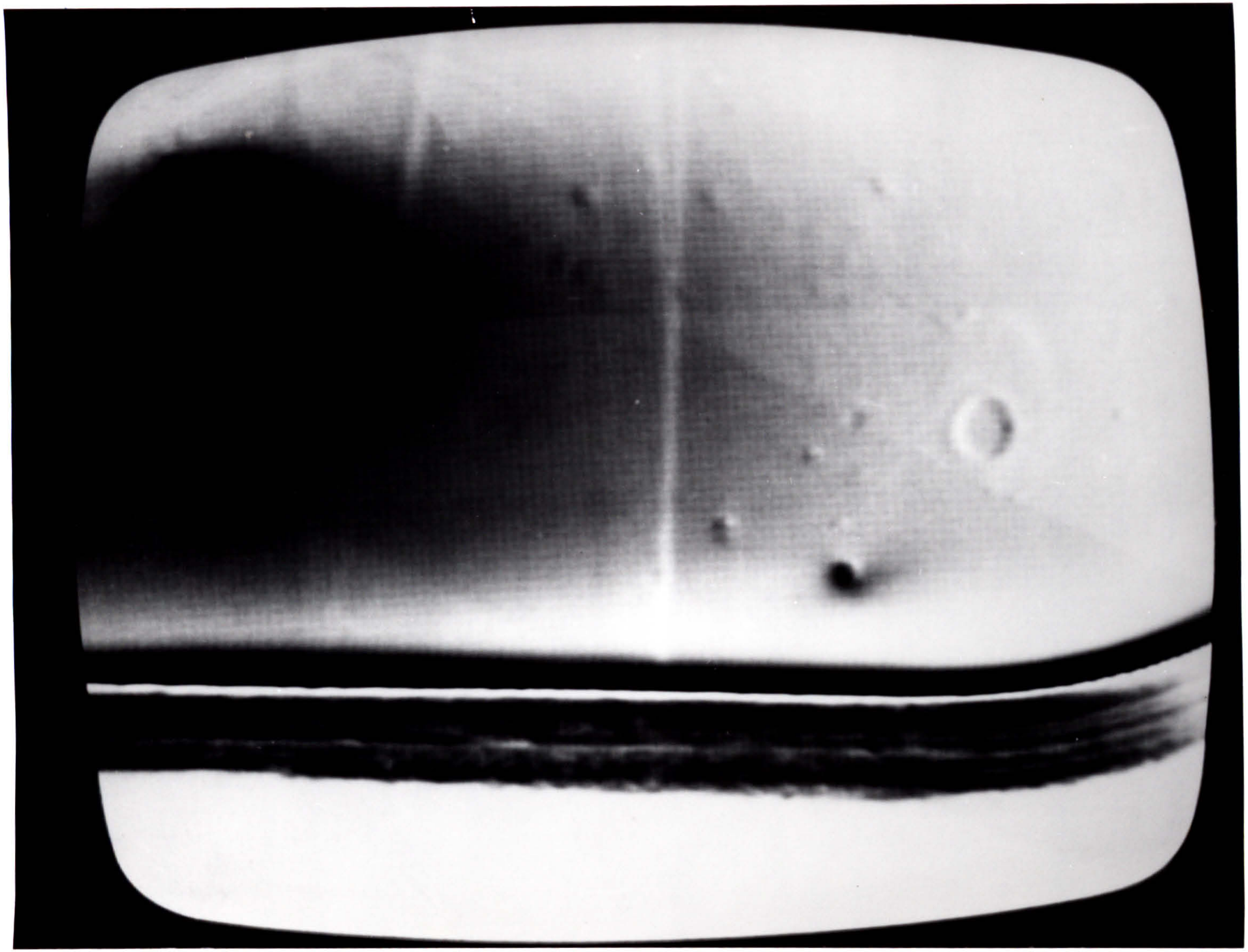

Fig.(8.14): Beam damage made visible. The secondary electron image of a sample after extensive irradiation at the centre of the crater. The edge of a sputter-deposited film may also be seen.

described comprehensively the centres created by irradiating glasses. Some of these have been modelled by Weeks (8.20) and Petrovskii and Yudin (8.21).

The radiation induced effects which would introduce a space-charge into the glass include the following:

(a) the creation of damage centres of both electron and hole types (8.18, 8.22) with a slow decay,

(b) the filling of meta-stable trapping states by electrons generated in the collision casca de,

(c) the promotion of electrons from the valence band or mid-gap trapping states into the conduction band (8.23) to leave behind positive hole centres, as exemplified by the ionization of traps in SiO_2 (8.24), and

(d) the alteration of local charge distributions at existing defects (8.25).

Two types of existing defect are found to be relevant for glass (8.26): E'-centres, which are caused by an electron filling an empty silicon orbital, and H-centres, consisting of electrons missing from neighbouring oxygen ions due to a local oxygen deficiency. Irradiation of an E'-centre may remove the electron, causing a positive space-charge; alternatively an H-centre may be filled, producing the opposite result.

Thus the magnitude and sign of the space-charge established in the glass will depend on which of the processes (a) to (d) dominates.

The ability of glass to store charge has been recognised for a considerable period. In 1957, Gross (8.26) irradiated borosilicate glass with 2 MeV electrons and showed that the fields produced could be so high that touching the surface of the sample with a "pointed piece of metal" initiated a visible discharge, centered at the point of contact. Gross used the production of colour centres in the glass to estimate the beam

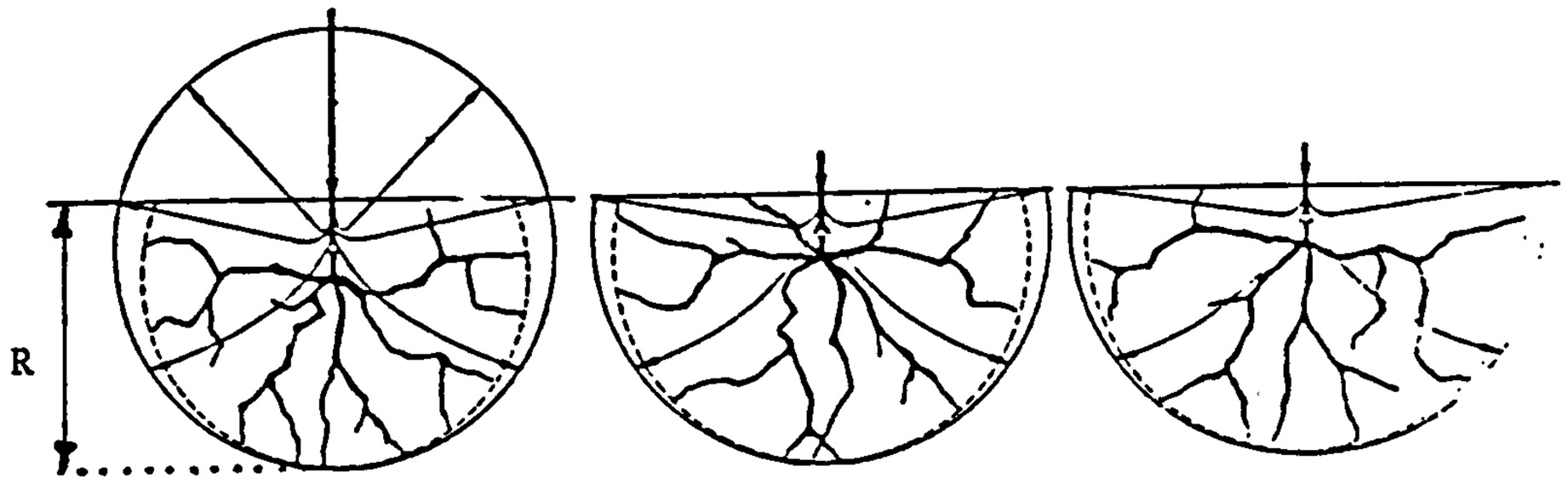

Fig.(8.15a): Modified diffusion model of inelastic electron scattering by solid targets. (Ref.7.26)

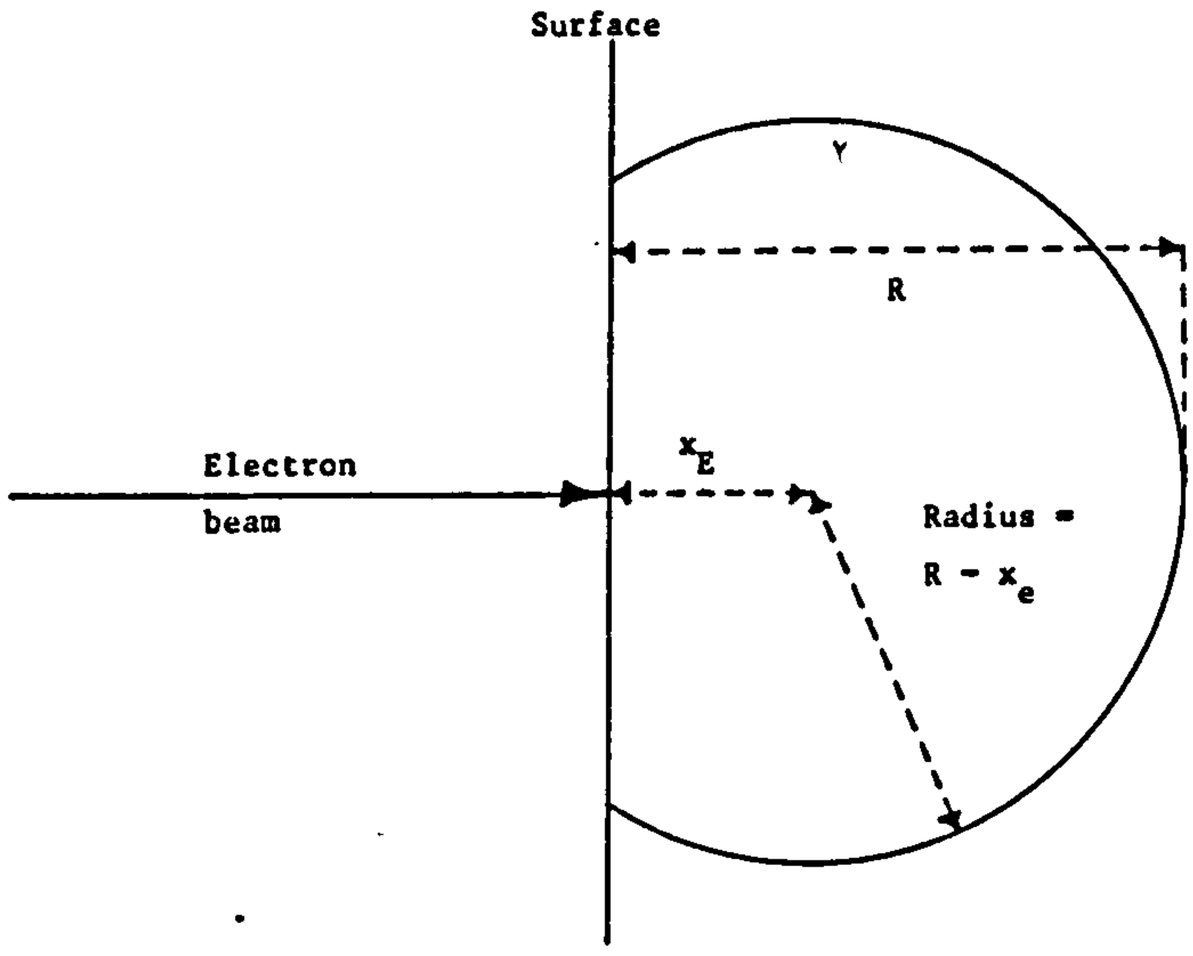

Fig.(8.15b): Diffusion model of ref.7.26 (as in Fig.8.15a) showing nomenclature, particularly the maximum range, R.

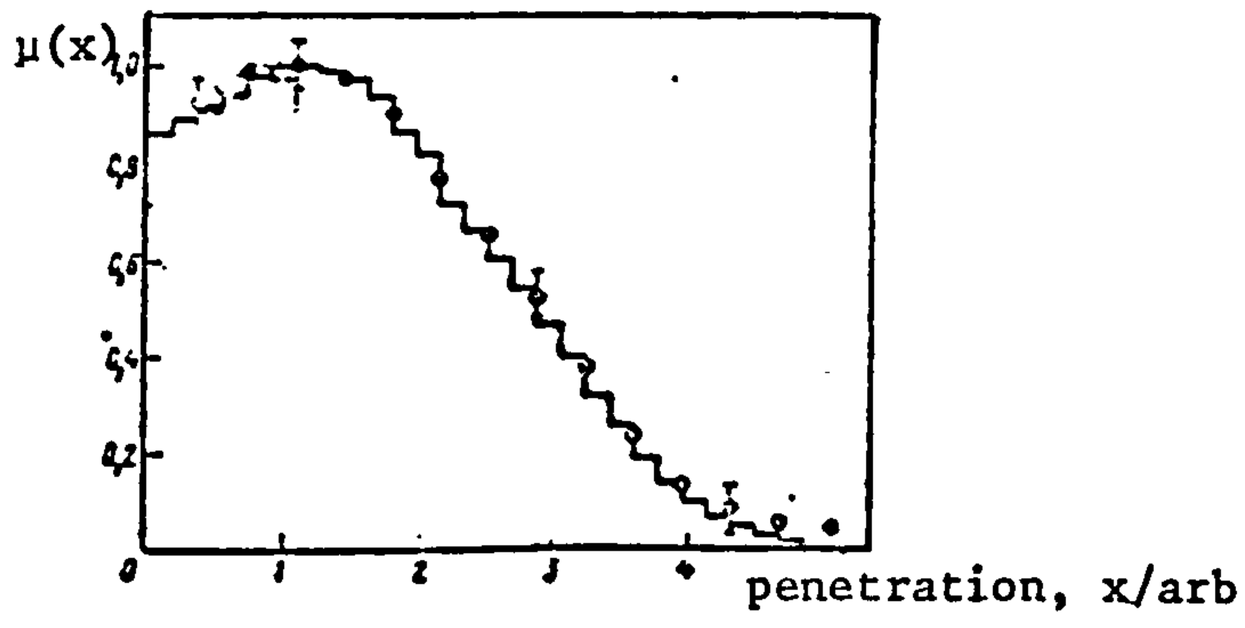

solid line: computer prediction

Fig.(8.16a):Depth distribution of the dose and the optical density μ of a glass sample irradiated with 8.5 MeV electrons. Ref.8.27

penetration distance, and discoloration was observed in many heavily irradiated samples in the present study.

Fig. 8.14 is a photograph of the video display showing the effect of long term irradiation by a defocussed beam on the secondary electron image. The photograph demonstrates the existence of charged centres, of one polarity or the other. It was found that such features could be observed for many days after their creation and that they could be removed by heating the sample. The edge of a sputter-deposited film is also to be seen in the figure.

8.4.3 Charge distribution

In their application of scattering theory to which reference was made in subsection 7.4.4, Kanaya and Okayama (7.26) show that the paths of scattered electrons can be regarded as emanating from a depth X_E in the glass equal to the position of the maximum in the curve of their energy loss versus distance. The model is depicted in Figs. 8.15 for very high energy electrons whose penetration is very much greater than the diameter of the beam. In the present case, the beam is wider than the range R and we are concerned only with the one-dimensional variation of the deposited charge density with the depth of penetration. The work of Balashov et al (8.27), shown in Fig. 8.16a, compares computer generated distributions with the variation of optical absorption (as a function of depth) in glass samples irradiated with high energy electrons. The agreement is found to be excellent, and the distribution is seen to have a form approximating to a truncated Gaussian of the type introduced previously in Fig. 2.5 as the depth distribution of deposited energy in sputtering (2.13).

The concentration of absorbing centres N_c is related monotonically to the intensity μ/m^{-1} of a Gaussian absorption band through Smakula's equation (8.28, 8.29) in the form:

$$N_c/m^{-3} = 8.7 \times 10^{20}\, \mu U \, \frac{N}{(N^2+2)^2} \, f^{-1} \qquad 8.14$$

where U/eV is the FWHM and f the oscillator strength of the band, and N is the number density of atoms in the sample. Assuming a constant proportion of these centres to be charged, we may consider the charge density $q(y,y_p)$ deposited in irradiated glasses to be distributed as shown in Fig. 8.16b. The convenient parameter the 'reduced depth' $y = x/R$ is used in this figure, in references 7.26 and 8.14 and in the following. A value of $x_E \sim 0.3R$ for glass is obtained by interpolating the homogeneous glass composition discussed in subsection 3.3.1 in the table provided in Ref. 7.26. The Gaussian curve of the figure is centred at $y_p = \frac{1}{3}$ for this reason.

To simplify further the present treatment, we will approximate the distribution by the two linear portions indicated, which have equal and opposite slope. This final approximation is not made in Ref. 8.14, but it permits the behaviour of the various functions to be seen more clearly with little loss of accuracy.

For unit irradiated area of surface, the total area under the curve of q versus y represents the total charge Q produced by electron bombardment. If the position of the maximum of the distribution occurs in the region $0 < y_p < \frac{1}{2}$, it is shown in Appendix IX that the electric field in the region $0 < y < y_p$ is given by:

$$F(y) = \frac{Q}{2\varepsilon_o\varepsilon_r}\left[1 - D(y,y_p)\right] \qquad 8.15$$

$$\text{where} \quad Q = \frac{(1-2y_p^2)q_{max}}{2(1-y_p)} \qquad 8.15a$$

$$\text{and} \quad D(y,y_p) = \frac{4}{(1-2y_p^2)}\left[\frac{y^2}{2} + (1-2y_p)y\right] \qquad 8.15b$$

The function $D(y,y_p)$ takes account of the opposing effects of the

charge situated on either side of a depth y, and increases from zero at y=0 to unity at $y=y_p=\frac{1}{2}$, reducing F(y) accordingly.

Initially, the quantity of the trapped charge and hence the field F(y), will increase linearly with time t and with current density, J. If η_k^+ is the probability of creating a trapped charge of hole type k, and η_k^- the corresponding probability for E'-centres, then the charge density Q accumulated at a time t is given by:

$$Q = \eta J(1 - r)t \qquad 8.16$$

where r is the backscatter ratio and:

$$\eta = \sum_k (\eta_k^+ - \eta_k^-) \qquad 8.16a$$

The sign of Q can therefore be either positive or negative according to the magnitudes of the two terms. From equations 8.15 and 8.16 we obtain:

$$F(y) = \frac{nJ(1-r)t}{2\varepsilon_o\varepsilon_r} \left\{ 1 - D(y,y_p) \right\} \qquad 8.15'$$

for the field in the glass.

8.4.4 Time-dependence of alkali concentration

Since ionic migration begins only when a critical field F_B is reached, and since the value of the field is a function of the depth y, then the time before which motion is induced will also be a function of the depth, $t_i(y)$. Assuming a constant initial ion concentration N_o at t=0 for all y, and the vacation of the potential wells above a given depth y when $t > t_i(y)$, we may write directly from equations 8.15' and 8.13:

$$t_i(y) = \frac{t_o}{1 - D(y_i,y_p)} \qquad 8.17$$

where $$t_o = \frac{4W\varepsilon_o\varepsilon_r}{Ja\eta(1-r)} \qquad 8.17a$$

8.4.5 Ion concentration in the analysed region

If the space charge is negative, cations will move away from the surface towards the centroid of the distribution, y_c. The depth y_A sampled

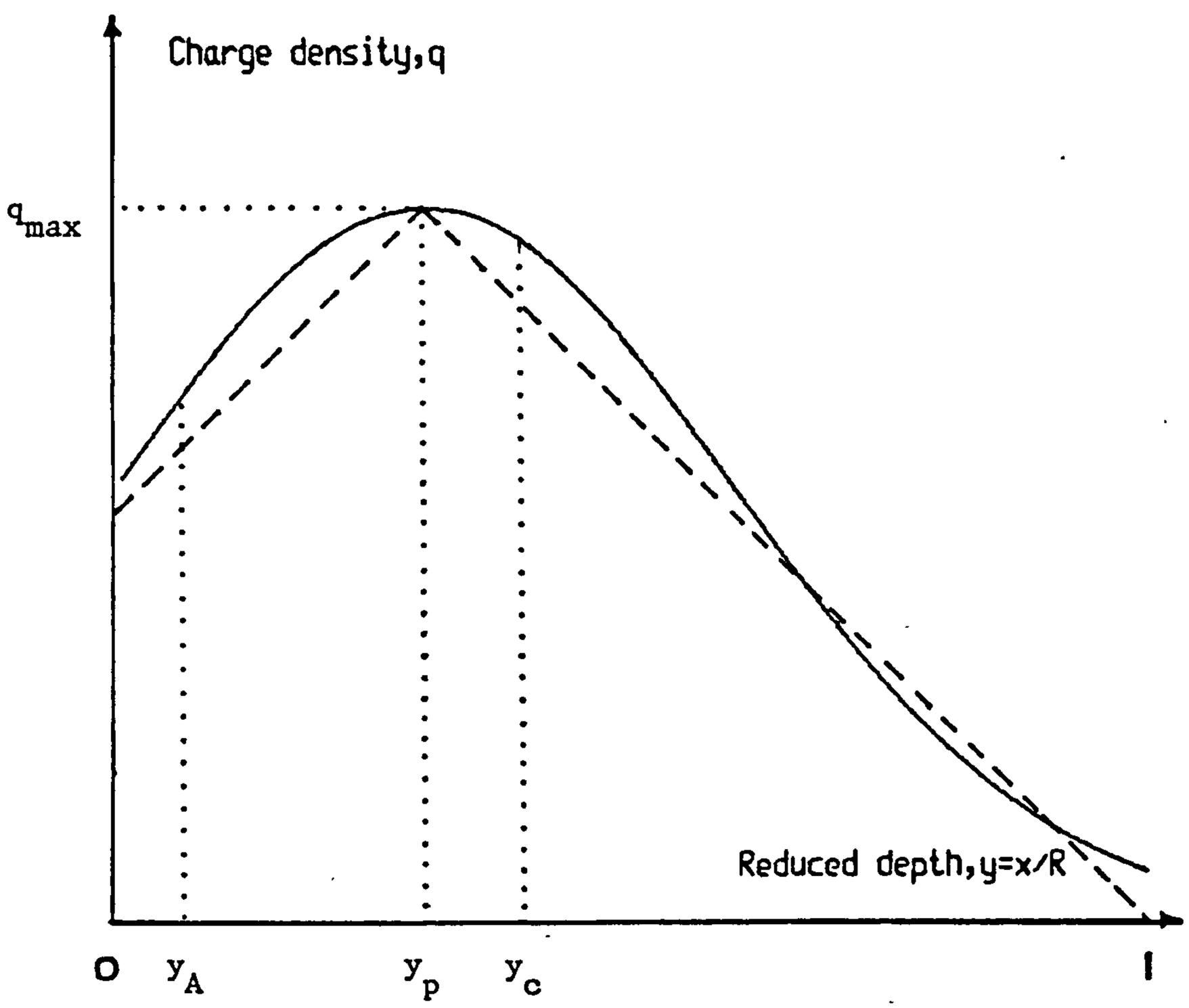

Fig.(8.16b):Truncated Gaussian distribution (full line) with linear approximation (dashed line)

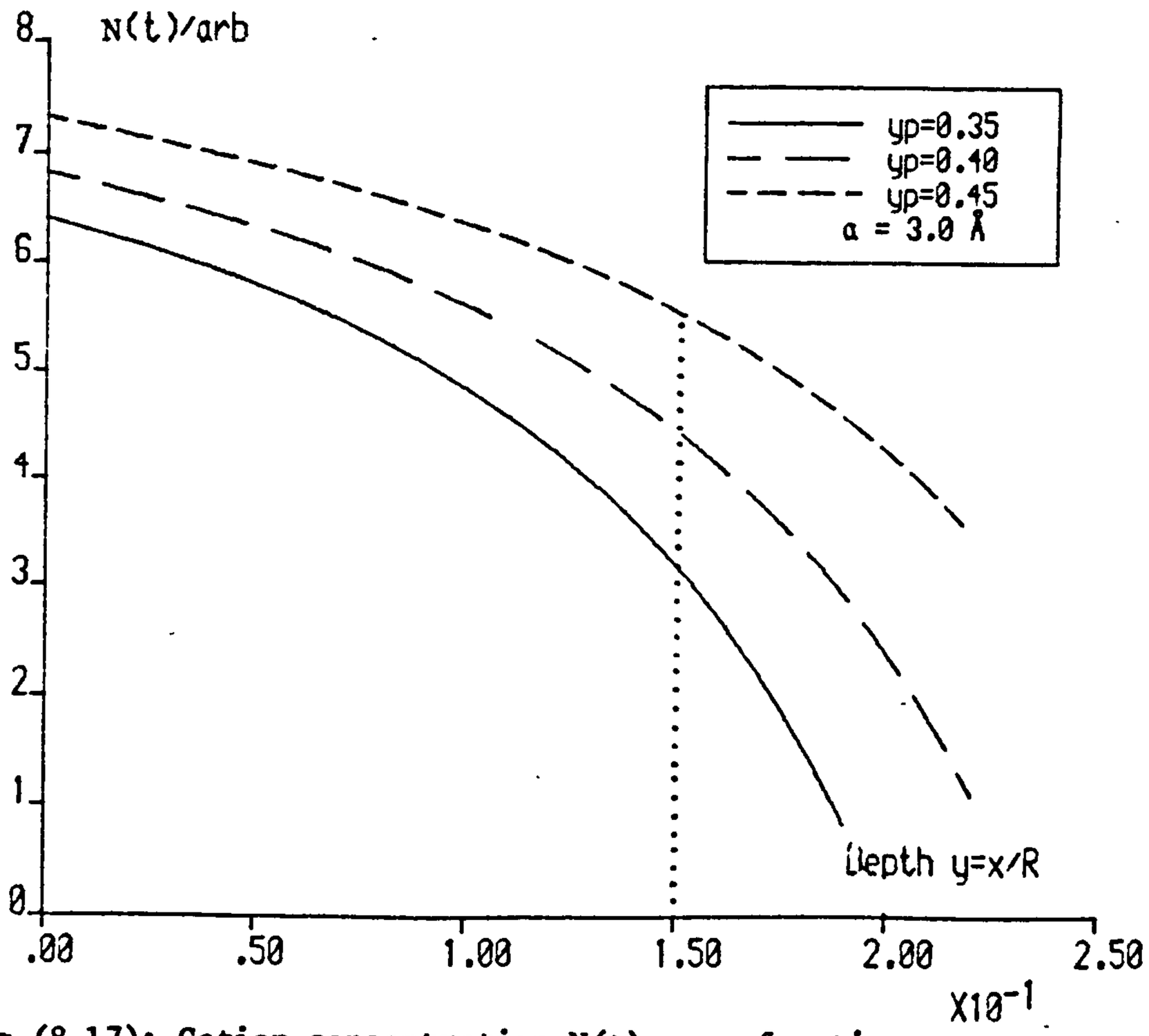

Fig.(8.17): Cation concentration N(t) as a function of reduced depth,y

by the observed Auger line is smaller than y_c so that the intensity of the signal will begin to decrease after the induction time of a depth y_A has elapsed, and an induction time can be defined for the case of negative charge centres according to:

$$T_i^- = t_i(y_A) = \frac{t_o}{1 - D(y_A, y_p)} \qquad 8.18a$$

All the mobile ions will have left the region $0<y<y_A$ after T_i^-.

The case in which the space-charge is positive is more complicated, but rewards closer inspection. The ionic motion is now away from the centroid, y_c, and ions originally beyond it will accumulate in the interior. This would explain in a different way the concentration of sodium found by Ohuchi et al (8.1) at the interface of a glass film and a metal substrate, after electron bombardment. For ions in the region $0<y<y_c$, the motion will be towards the surface, as suggested by Lacharme and Champion (8.13), and desorption will occur. The transient increase in signal intensity which has been observed (8.8, 8.13) could perhaps be accounted for by the effect of the surface potential barrier U_o discussed in section 3.3. The concentration of ions in the analysed region will be a balance between the rate of desorption and the rate of field migration from layers below the surface. The observed constancy of the Auger signal before T_i suggests that initially these two rates are roughly equal. However, as seen from equation 8.17, the time after which ions begin to migrate increases non-linearly with depth and there is a consequent reduction in the rate at which ions reach the analysed layer as the depth from which they originate increases.

The change in the concentration of the mobile species can be found by considering the spacing of the layers during migration. The j^{th} layer will have no motion until a time $t_i(ja/R)$ but after a time $t > t_i(ja/R)$ it will have reached a position $y_j(t)$ where:

$$y_j(t)R = ja - \mu F_B \left[t - t_i(ja/R)\right] \qquad 8.19a$$

if the field is considered to remain constant at F_B between the original depth ja and the surface, and μ is the ionic mobility. The adjacent layer will have assumed a position given by:

$$y_{j+1}(t)R = (j+1)a - \mu F_B \left[t - t_i(a(j+1)/R)\right] \qquad 8.19b$$

from which we can see that the layer spacing $(y_{j+1}(t) - y(t))R$ has become a function of time, a(t), and also from equations 8.17 and 8.19 that the change in spacing caused by the migration has a behaviour given by:

$$\begin{aligned}\Delta a(t) &= a(t) - a \\ &= \mu F_B \left[t_i(a(j+1)/R) - t_i(ja/R)\right] \\ &\sim \frac{1}{1-D(a(j+1)/R, y_p)} - \frac{1}{1-D(ja/R, y_p)} \\ &\sim \frac{dD}{dy}\left[1-D(y,y_p)\right]^{-2} \qquad 8.20\end{aligned}$$

The concentration of ions N(t) falls when $\Delta a(t)$ becomes large since:

$$N \sim a^{-3}$$

and we may write, approximately:

$$\Delta N(t) \sim -3a^{-4}\,\Delta a(t) \qquad 8.21$$

The function $\Delta N(t)$ is plotted in Fig. 8.17 for three values of y_p, evaluated using equation 8.15b and 8.20 with an arbitrary N_o.

The curves of Fig. 8.17 show that the Auger signal from the alkali ions, which is proportional to N(t), will fall significantly only when layers from about 0.15R have begun to migrate. This enables the induction time caused by a positive charge distribution to be defined approximately as the time taken for these layers to reach the surface.

$$T_i^+ = t_i(0.15) + \frac{0.15R}{\mu F_B}$$

$$= \frac{t_o}{1 - D(0.15, y_p)} + \frac{0.15R}{\mu F_B} \qquad 8.18b$$

It is impossible to determine which is the dominant term of the two in equation 8.18b since the quantity η in the definition of t_o (eq.8.17a) is completely unknown at present. The inverse behaviour of the induction times T_i with current density J (8.11, 8.8) indicates that the second term is small; the layers move quickly once migration has started.

It is clear that an induction time T_i may be defined by equations 8.18 for both the positive and negative space-charge case. Close inspection of the peaks themselves will distinguish the two, as demonstrated below.

8.4.6 Peak asymmetry

If there is present in the glass a field F_B then Auger electrons from adjacent layers will have their energy E altered by an amount $F_B a$ in a direction according to the polarity of the field, that is, the sign of η.

Defining the escape depth $y_A R$ in the usual way (7.6), the signal from the jth layer will be of intensity given by:

$$I_j = I_o \exp(-ja/y_A R) \qquad 8.22$$

and considering the peak shape to be Gaussian of spread σ, we can write for the emission from a layer j:

$$I_j(E) = I_o \exp\left\{-ja/y_A R\right\} \exp\left\{-(E \pm 2jW)^2/2\sigma^2\right\} \qquad 8.22'$$

where the sign chosen is the same as that of η.

The peak shape observed therefore, at the end of the induction time T_i, will be the sum of such expressions for $0 < ja < y_A R$:

$$I(E) = \sum_J I_j(E) \qquad 8.23$$

It is clear that I(E) will be an asymmetrical function of E, and the differentiated signal I'(E) is shown in Figs. 8.18 to 8.21 for the two directions of field, and various values of the parameters within

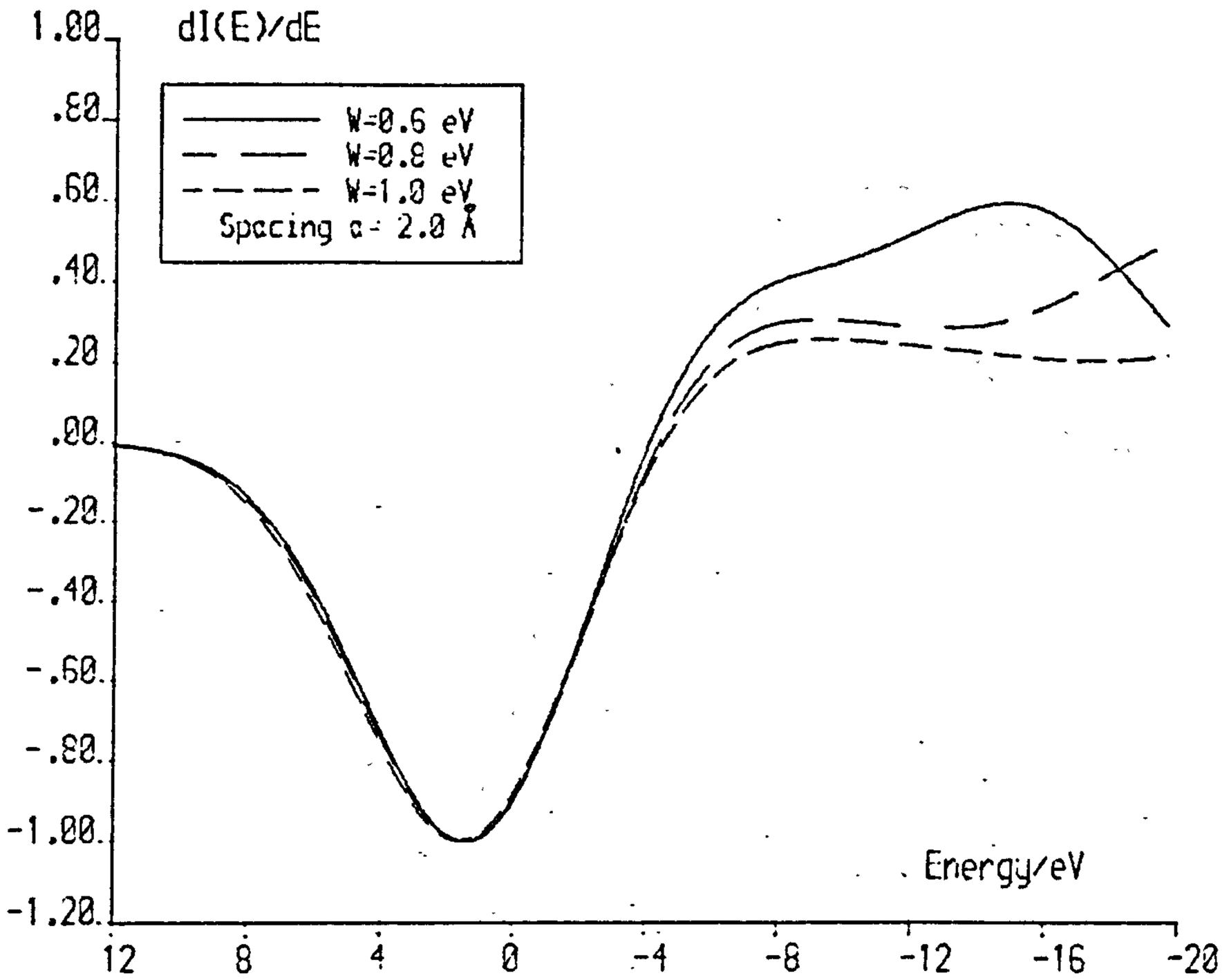

Fig(8.18a)Positive charge density

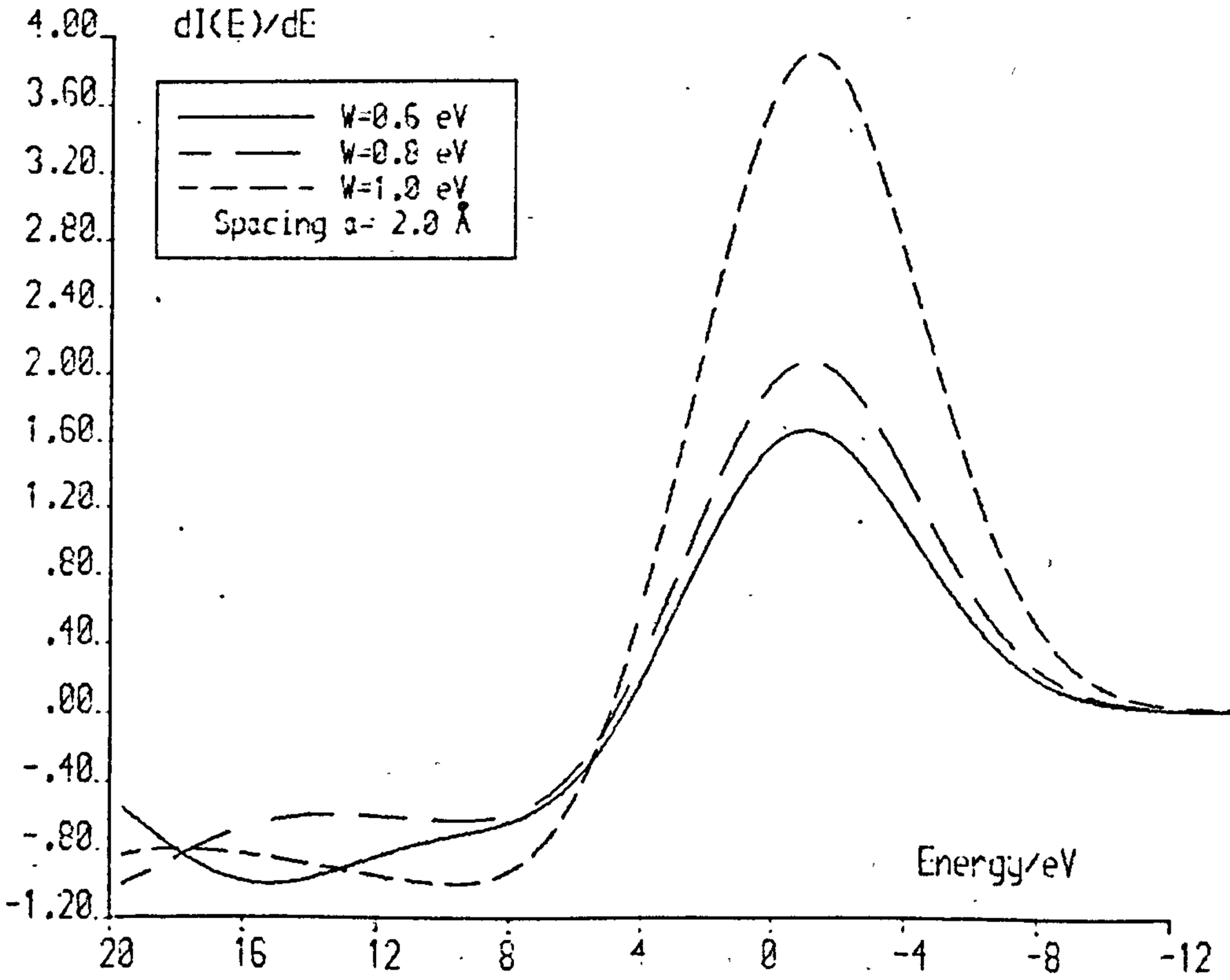

Fig(8.18b):Negative charge density

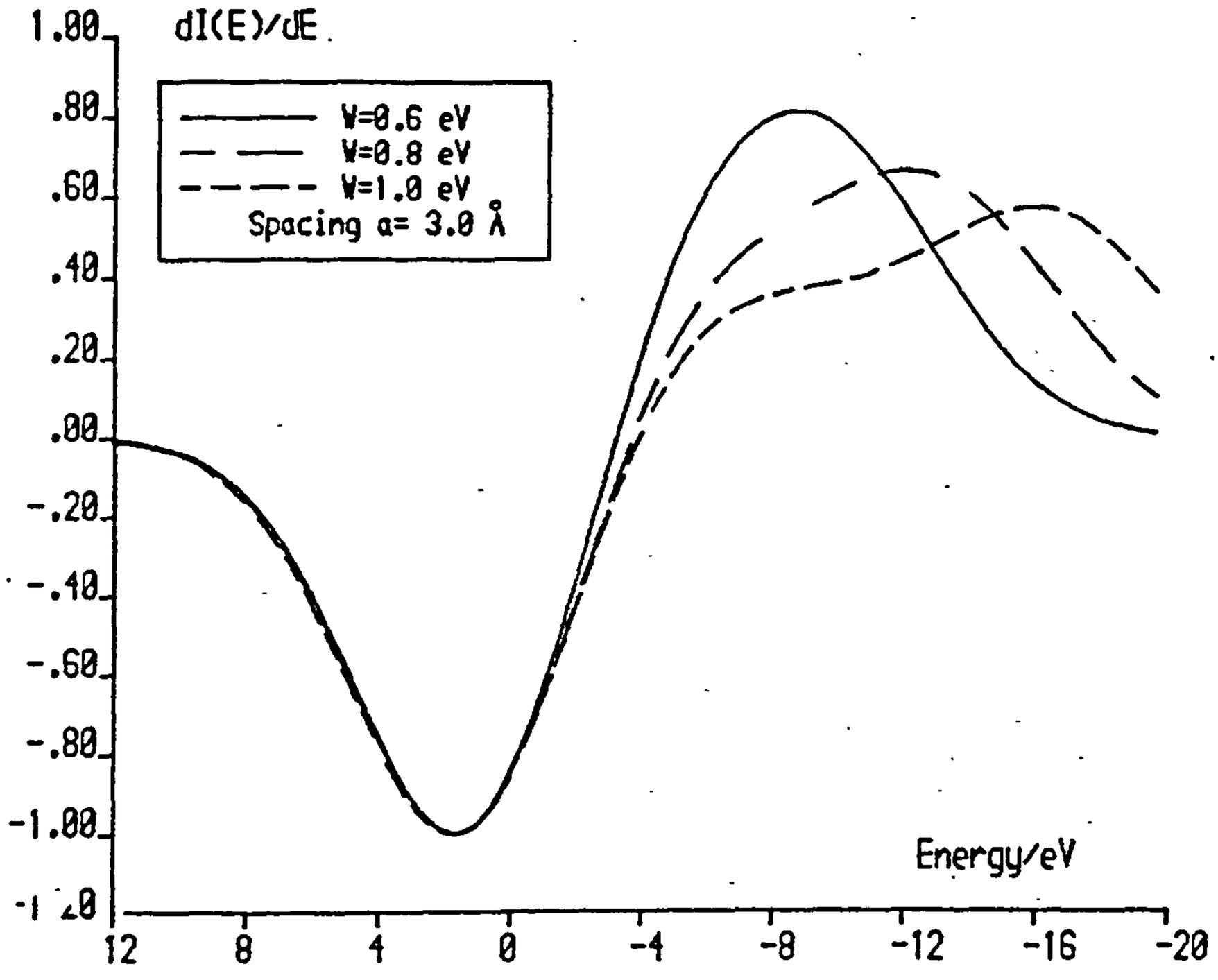

Fig(8.19a)Positive charge density

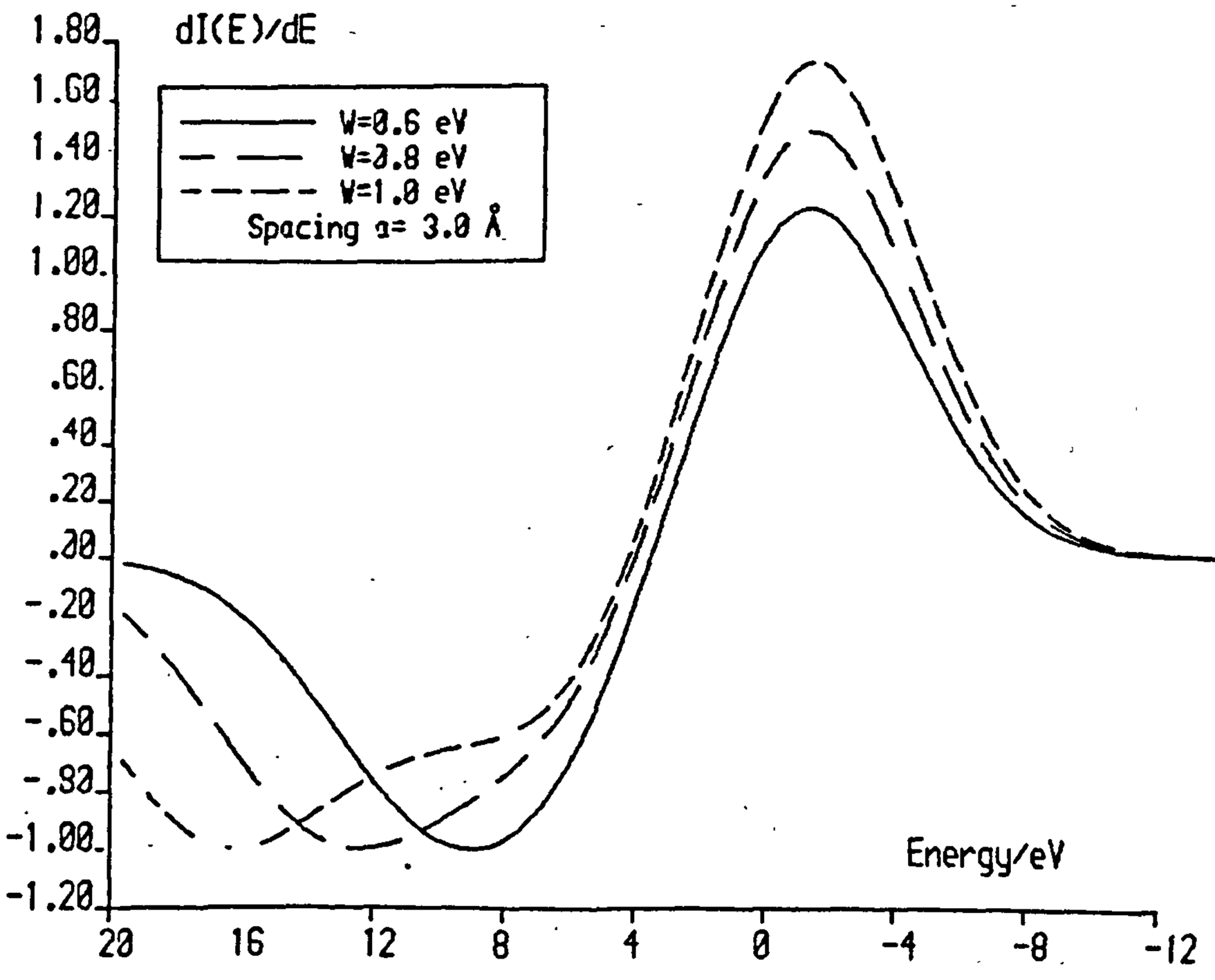

Fig(8.19b): Negative charge density

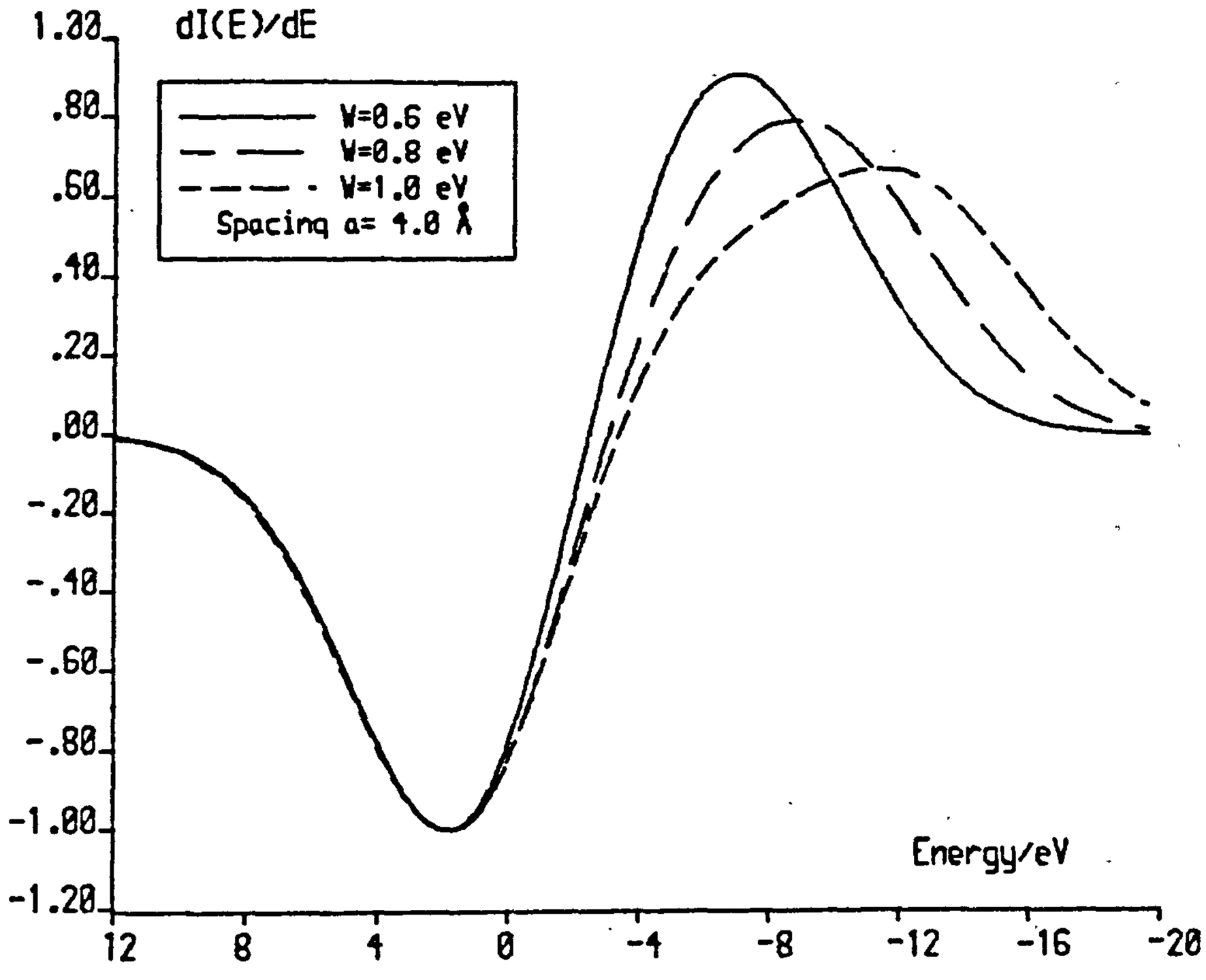

Fig(8.20) :Positive charge density

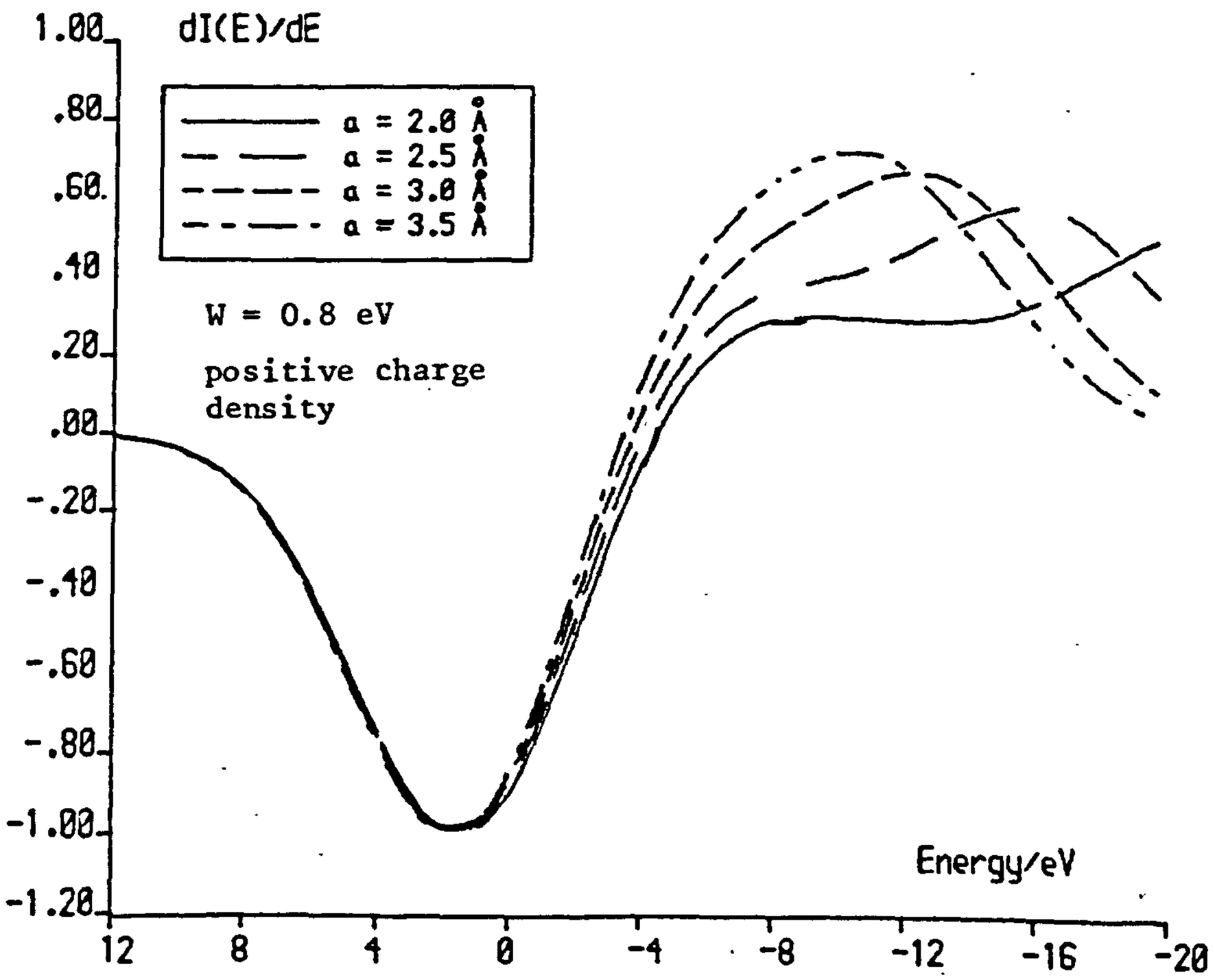

Fig(8.21) : Peak shape against cation separation

physically reasonable limits appropriate to sodium in glass (8.7). The curves are plotted in the reverse direction for easy comparison with experimental spectra. In the computation of these curves, the 28 Å used for the escape depth was obtained from equation 7.9b (7.32) using E_A = 990 eV, the value of 7 eV for the peak breadth was the p-p length of the initial signals from sodium such as in Figs. 8.12 and 8.22, and each curve was normalised to unity at its most negative excursion. Fig. 8.21 indicates the effect of the layer separation on the peak shape with positive η and W = 0.8 eV.

8.4.7 Experimental peak shapes

As can be seen from Fig. 8.22a, showing the time development of the 990 eV KLL line from sodium in a glass film RF-sputter-deposited on to SiO_2, and from Fig. 8.22b showing the same line from ordinary soda glass, the shapes correspond very much more closely to those caused by positive charge densities than to those caused by the other trapping state. This implies that the field is such as to cause the analysed cations to migrate towards the surface and out of the sample.

Figs. 8.22 show the time-development over a period $0 < t < T_i$ and the maximum asymmetry is seen to occur near T_i, when the field in the glass is considered to have reached its maximum, F_B.

Interpreting the experimental lineshapes in terms of the model proposed in this section, we can conclude that the decay of the alkali ion signals on electron beam irradiation is due to the accumulation of a positive space charge in the bombarded volume which causes the ions in the region above the centroid of the charge distribution to migrate to the surface through the analysed region. This view is supported by the experimental work of Lacharme et al (8.13), and is not in conflict with results of Ohuchi et al (8.1).

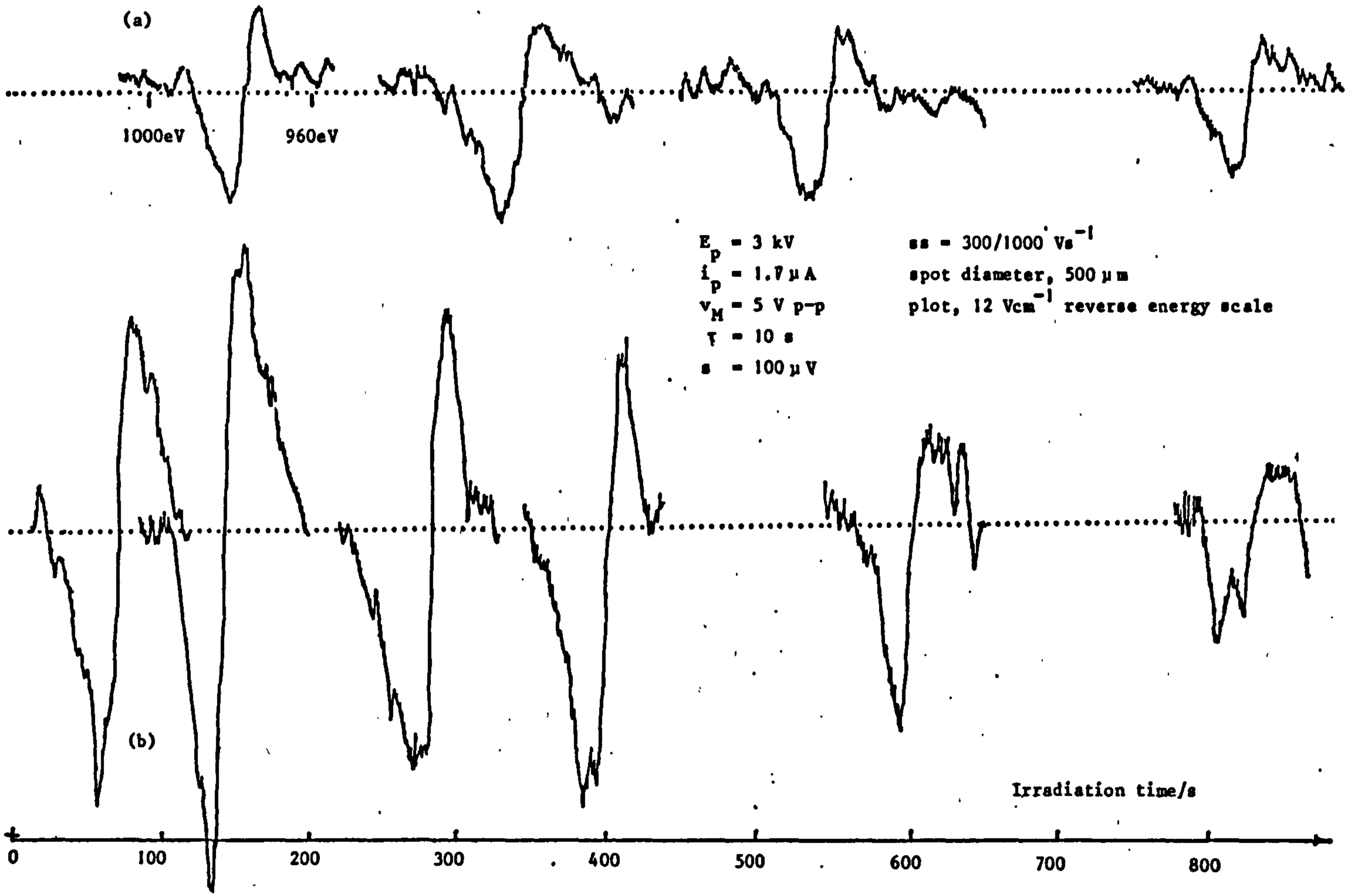

Fig 8.22: Time development of 990 eV Auger peak from sodium in (a) a glass B23 on silica (b) soda glass

8.5 Sample translation

When the Auger intensity ratio Na/Si was measured at 46 points chosen at random on the surface of a fragment of the ternary glass (whose composition is given in Table II, Chapter 1) the distribution shown in Fig. 8.23 was obtained. It has the large standard deviation of 0.037, which may be due to a combination of a lack of homogeneity in the glass itself ('phase separation') and possible variations in Auger efficiency as a function of the surface topography, but differences in the extent of the beam damage probably have the most effect since it is very difficult to be sure that each area has been irradiated equally. Thus, the success of any attempt to quantify the composition of a glass (or film) surface depends upon the extent to which beam damage is reduced.

The other distribution of results shown in Fig. 8.23 was obtained using the Nicolet MCA to sum 64 100 eV scans taken whilst the sample was being translated in the x-direction (see Fig. 7.6b) at a speed of roughly 0.3 mm s^{-1} by manual rotation of the micrometer. This was done separately for the sodium and the silicon signals. The standard deviation of the 8 such measurements recorded was 0.018, half that of the previous distribution, with a mean differing by only 4%.

Two of the sodium spectra recorded using this technique are to be seen in Fig. 8.24. Not only is it easy to see the second sodium peak (at ~ 946 eV) which is usually obscured by noise, but the asymmetry discussed above is completely absent.

Sample translation causes the irradiated surface area of the sample to be increased by a factor of about 50, which reduces the deposited charge density and the field present in the glass and increases the induction times. Asymmetric peak shapes very similar to those of Fig. 8.22 were recorded using this signal averaging technique when the sample was left stationary.

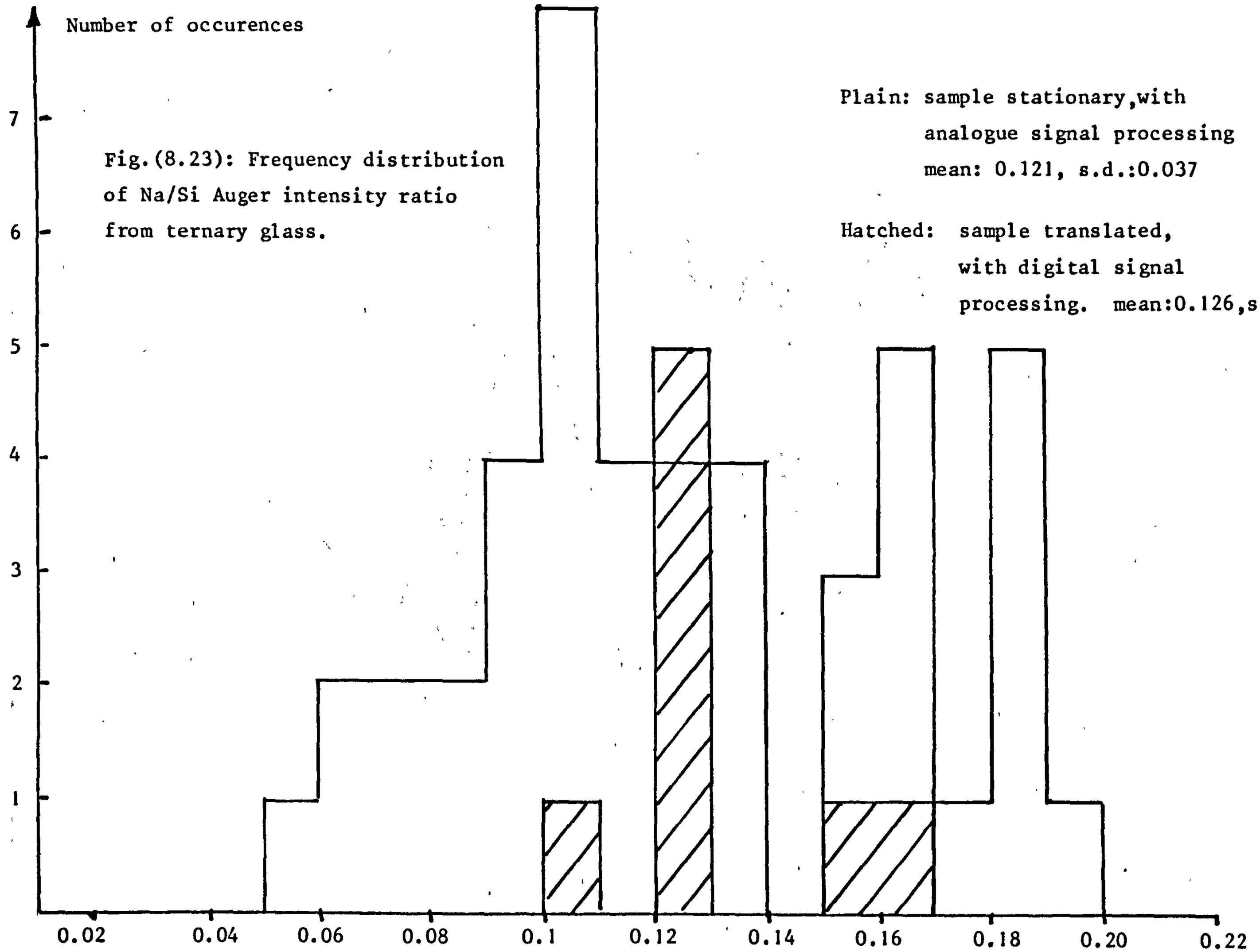

Fig.(8.23): Frequency distribution of Na/Si Auger intensity ratio from ternary glass.

Plain: sample stationary,with analogue signal processing mean: 0.121, s.d.:0.037

Hatched: sample translated, with digital signal processing. mean:0.126,s.d:0.018

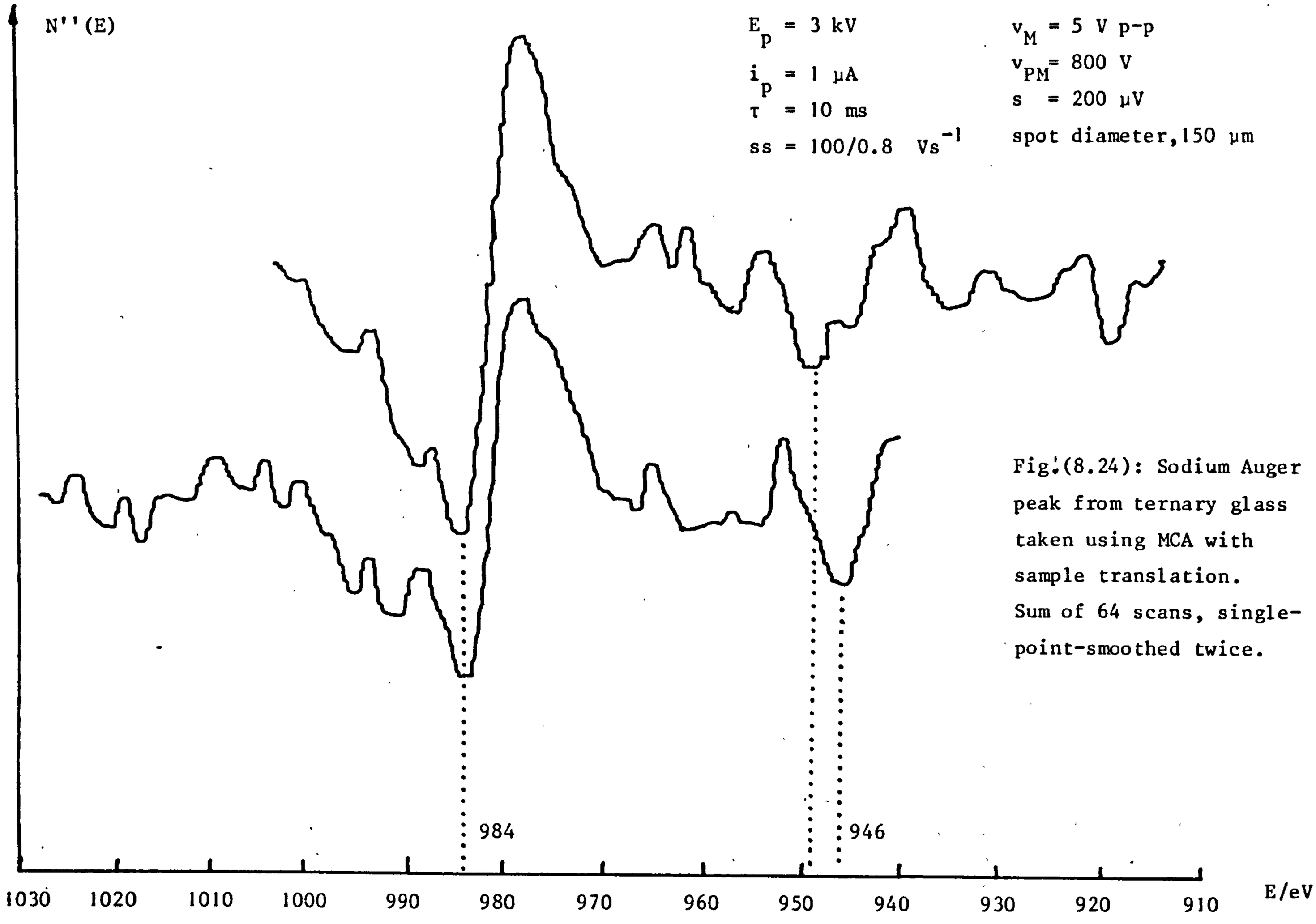

Fig. (8.24): Sodium Auger peak from ternary glass taken using MCA with sample translation. Sum of 64 scans, single-point-smoothed twice.

Thus, it has been shown that slow translation of the glass sample during bombardment combined with rapid data acquisition and signal averaging can reduce beam damage during AES, and quantitative results are made slightly more accessible. We can tentatively associate a Na/Si Auger intensity ratio of 0.125 with a compositional ratio of 21.0 mol% (21.5 wt%).

The glass films produced from the ternary glass were examined briefly and Na/Si Auger intensity ratios of less than 0.125 were in general recorded, but as the MCA was available only at the end of the period of study, extensive investigation of the quantitative results was not possible.

8.6 ELS spectra of glasses and films

The theoretical basis of electron spectroscopy has been set out in section 7.9, and the small literature concerning ELS of glasses has been mentioned. Pollard (8.33) made a study using the present equipment which identified certain of the peaks but emphasised the difficulty of interpretating ELS glass spectra.

Beam currents used for ELS are extremely low, in the region of 0.01 to 0.05 μA, and primary accelerating voltages are usually between 100 and 500 eV. Damage to the sample of the type described above is hence reduced from that cause in AES despite the necessity of using well focussed beams. This is one of the reasons that ELS has been suggested as an improved technique for glass surface analysis (8.14, 8.34), but evidence of beam damage has been observed in this study.

8.6.1 Experimental technique

The equipment used was identical to that described in section 7.6 except for the addition of a voltage divider network and DVM to permit continuous monitoring of the difference between the pass energy E_o and the primary energy E_p. The pass energy was obtained from the terminals of the spectrometer DVM and E_p from the gun H.T. line. There is 1000:1 internal

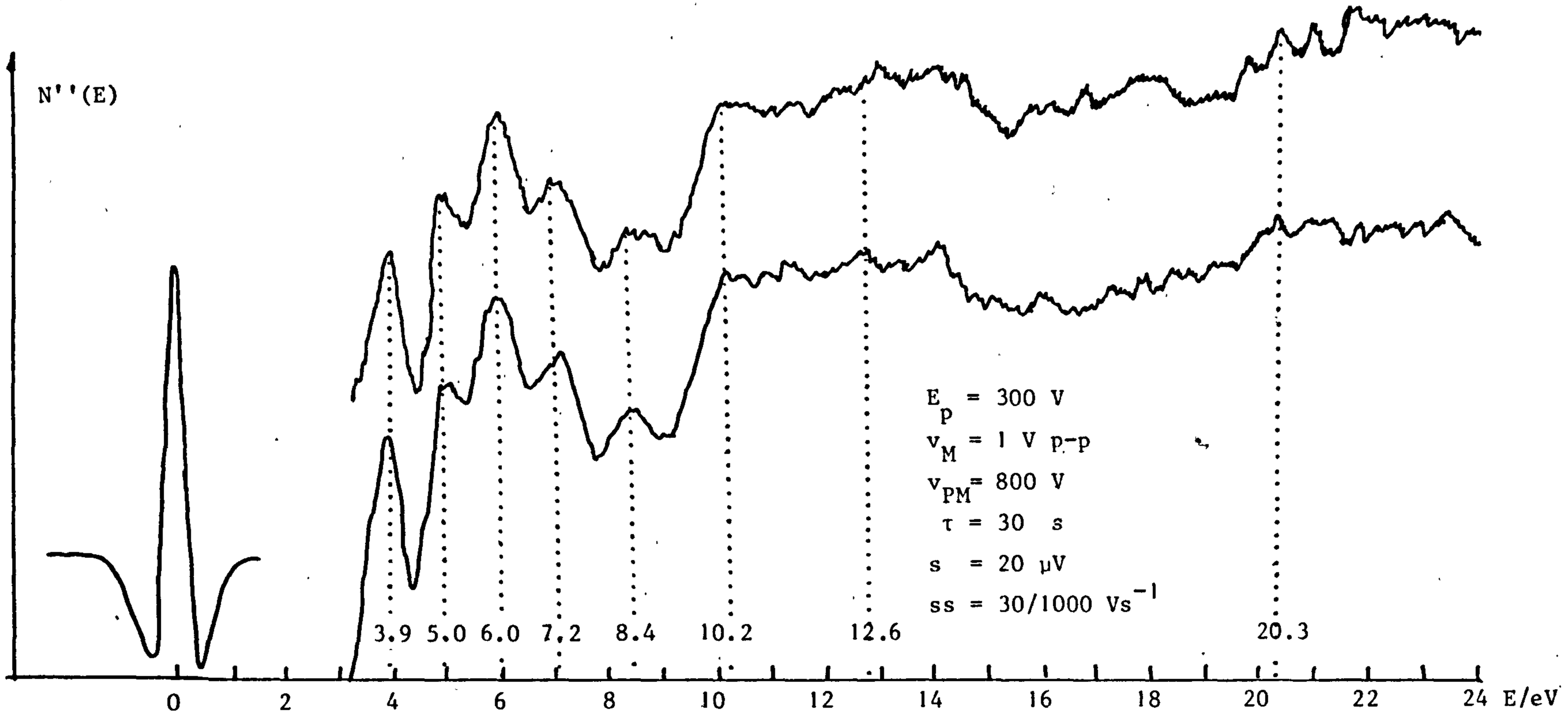

Fig.(8.25):: ELS spectra from RF sputter-deposited glass film A14.

voltage division in the spectrometer (the DVM is a millivoltmeter) and it was necessary to drop the H.T. accordingly. When conditions had been adjusted such that the N''(E) elastic peak was symmetrical about E_p as in Fig. 8.25, the display was set to zero with offset potentiometers. Although this technique was very useful, there was evidence of drift over a period of a few hours, probably due to resistor heating, and there was a suggestion that spectra were affected by the presence of the tapping in the HT line.

Since ELS signals are extremely weak, the spectra were recorded in the doubly differentiated mode (see subsection 7.8.2) with very long time constants, high sensitivity, and scanning speeds as slow as 30 mVs^{-1}. Two typical scans from a glass film are shown in Fig. 8.25 and it can be seen that the main features of the spectra occur in the first 10 eV, losses smaller than 3 eV being off-scale. The amplifier DC offsets were in fact pre-set so that the flat portion above 12 eV could just be recorded without overload, and this determined the limit of approach to E_p.

Fig. 8.26 is provided as an aid to interpreting doubly-differentiated traces. It shows that small changes in the background level are manifested as double winged features, and that symmetrical peaks become triple winged as, for example, in Fig. 8.25. It was necessary regularly to maximise the signal by adjusting the phase of the modulating signal.

8.6.2 Modulation amplitude

The effect of the modulation amplitude upon spectral features is nowhere more clearly demonstrated than in ELS. It has been indicated (subsection 7.8.2) that v_M should be roughly equal to the breadth of the feature, and the three consecutive scans of Fig. 8.27 show how features may be obscured whether the amplitude of the modulation is too large or too small. A value of 1 V p-p was preferred, since features of this extent were

Fig.(8.26):
Single and double differentiation of an illustrative trace. Negative functions are shown for easy comparability with experimental spectra which are taken from high to low energies.

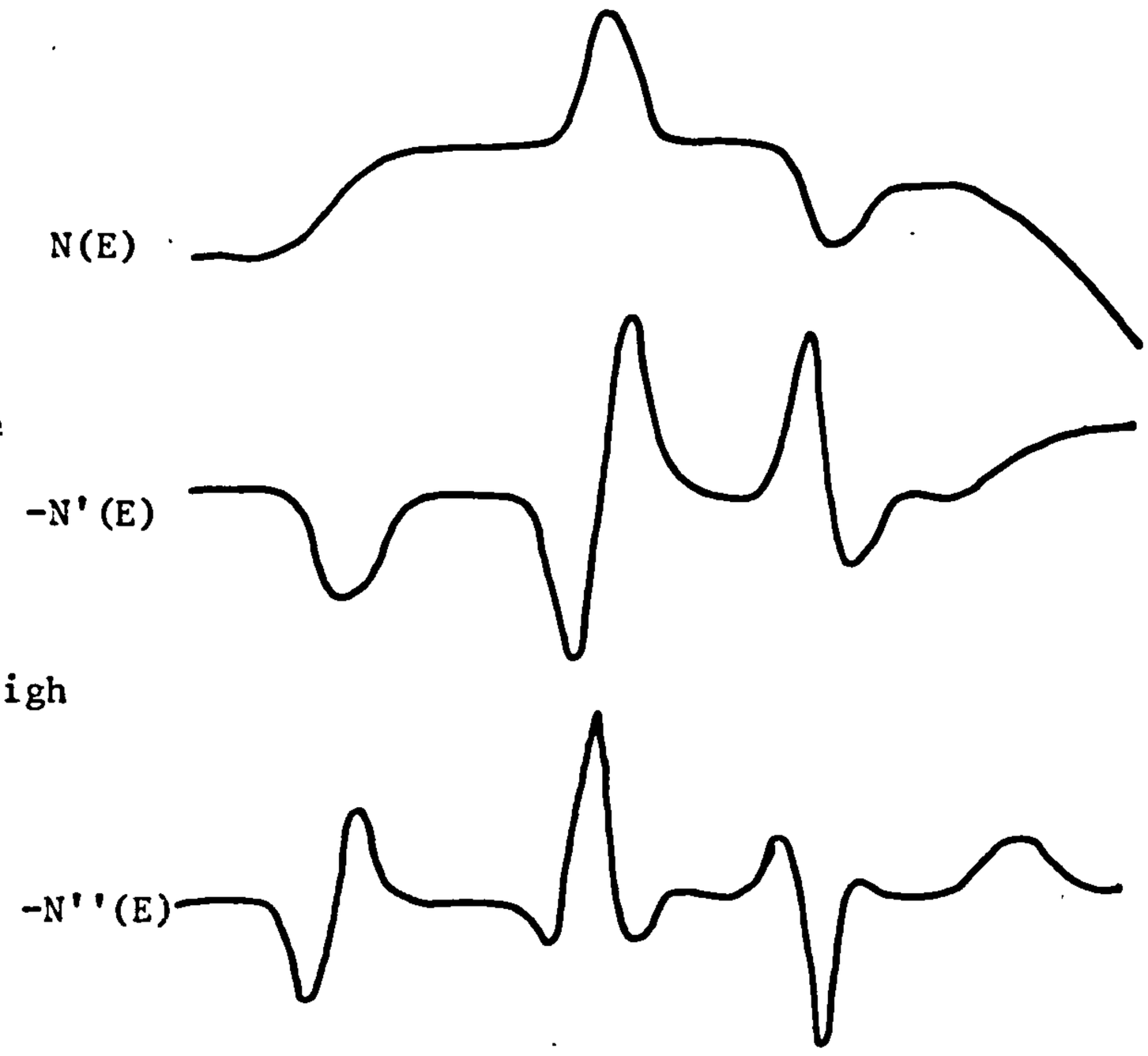

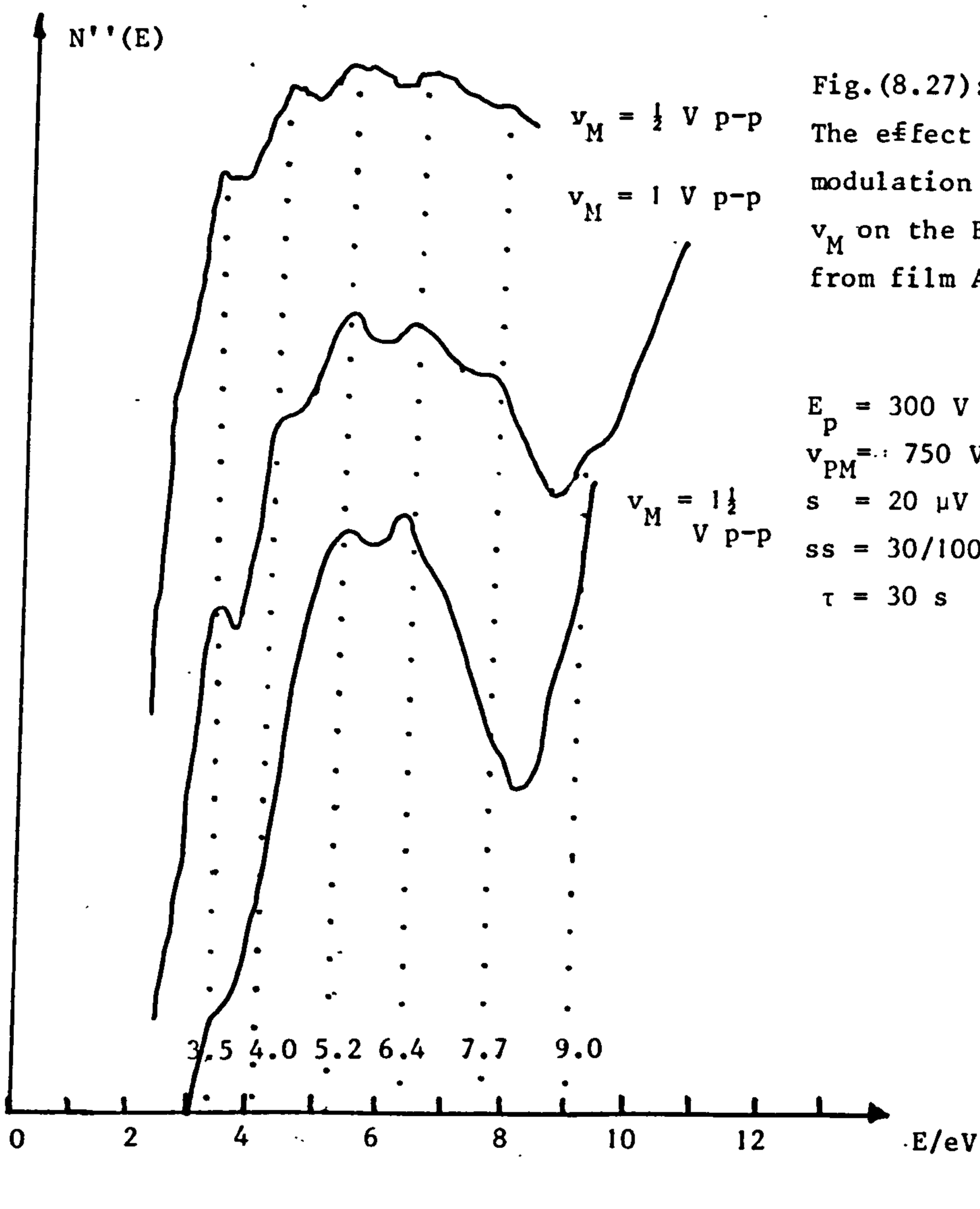

Fig.(8.27):
The effect of the modulation amplitude v_M on the ELS spectrum from film A13.

E_p = 300 V
v_{PM} = 750 V
s = 20 μV
ss = 30/1000 Vs^{-1}
τ = 30 s

predominant; different values are appropriate for other tasks (3.8).

8.6.3 Identification of peaks

Our present imperfect understanding of the electronic states in glasses has been reviewed by Mott (8.23, 8.30) and Stephenson et al (8.31). Some of the energy levels are well established in the literature (8.32, 8.36), but there continues to be difficulty in assigning many of those remaining.

Rowe (8.35) and Pollard (8.33) have published ELS spectra of silica, as shown in Figs. 8.28. Both workers assign the features below 10 eV to non-bridging oxygen atoms in the surface of the material, and designate the surface stoichiometry SiO_x, where $x \sim 1$. The peaks coincide well in the two references, but their relative intensities are different. It is clear, however, that the peak intensities in doubly differentiated spectra are sensitive to so many variables that it is the similarity of the scans of Figs. 8.28 which is surprising. The peak positions reported are indicated in Table IV.

The portion below 10 eV of the spectrum of glass film A14 (Fig. 8.25) shows the silica peaks and additional ones at 6.0 and 8.4 eV. The spectra of film A13 in Fig. 8.27 show peaks in similar positions and also one at 3.5 eV, as found by Rowe (8.35). The veracity of the 3.5 eV peak has been questioned by Underhill (3.8), as mentioned in section 7.10, although a clear peak at this energy was found by Ibach and Rowe (8.37) in the spectrum of oxygen adsorbed on to silicon. In the analysis of soda-lime-silica glass (8.33), the three peaks visible below 10 eV in the silica spectrum reduce to two (at 5.0 and 7.0) or just one (at 4.0 eV). It is easy to see from Table IV that RF sputter-deposited films show the characteristic loss peaks of both glass and silica, with additional features previously observed only with UV reflectance spectroscopy.

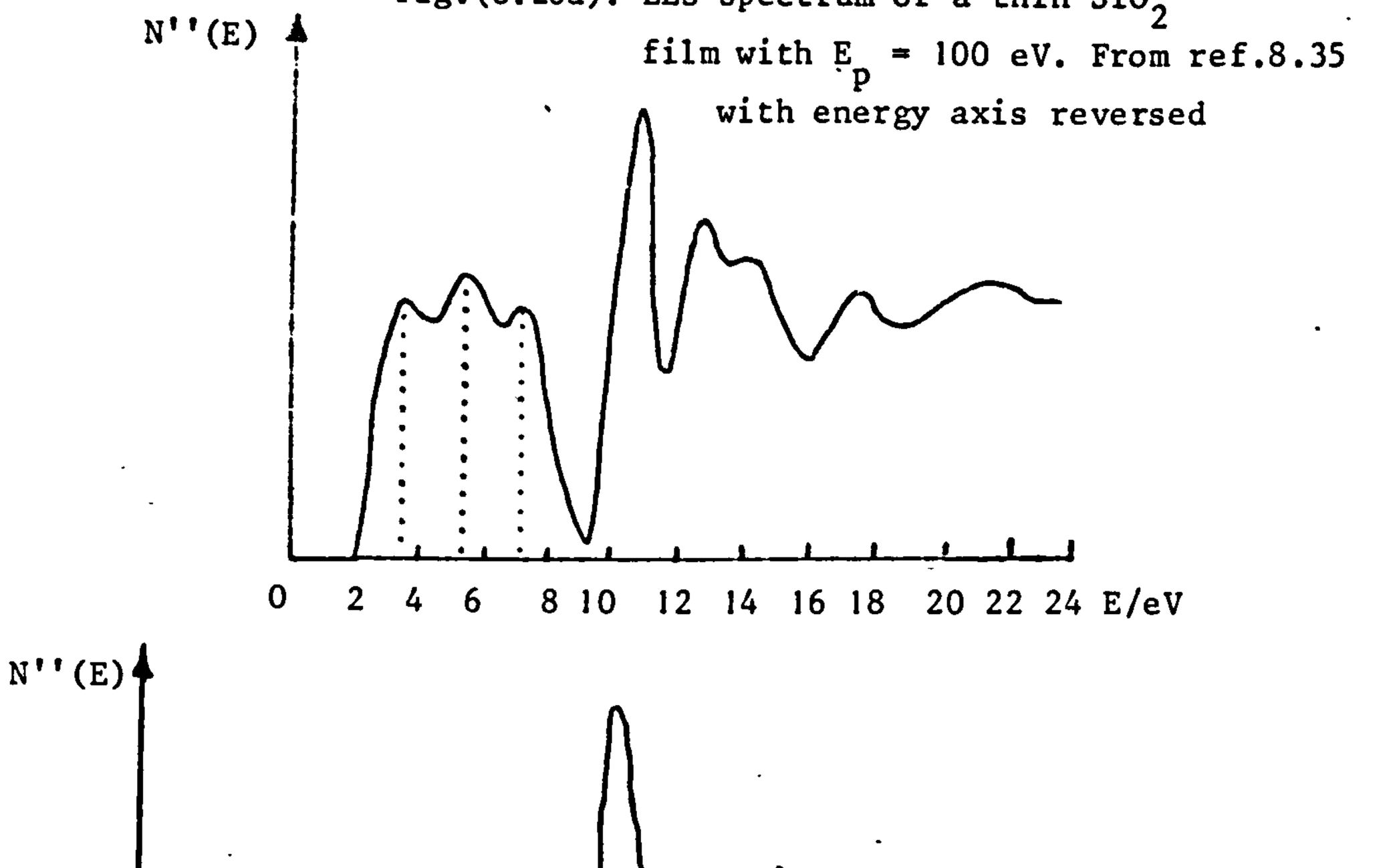

Fig.(8.28a): ELS spectrum of a thin SiO_2 film with E_p = 100 eV. From ref.8.35 with energy axis reversed

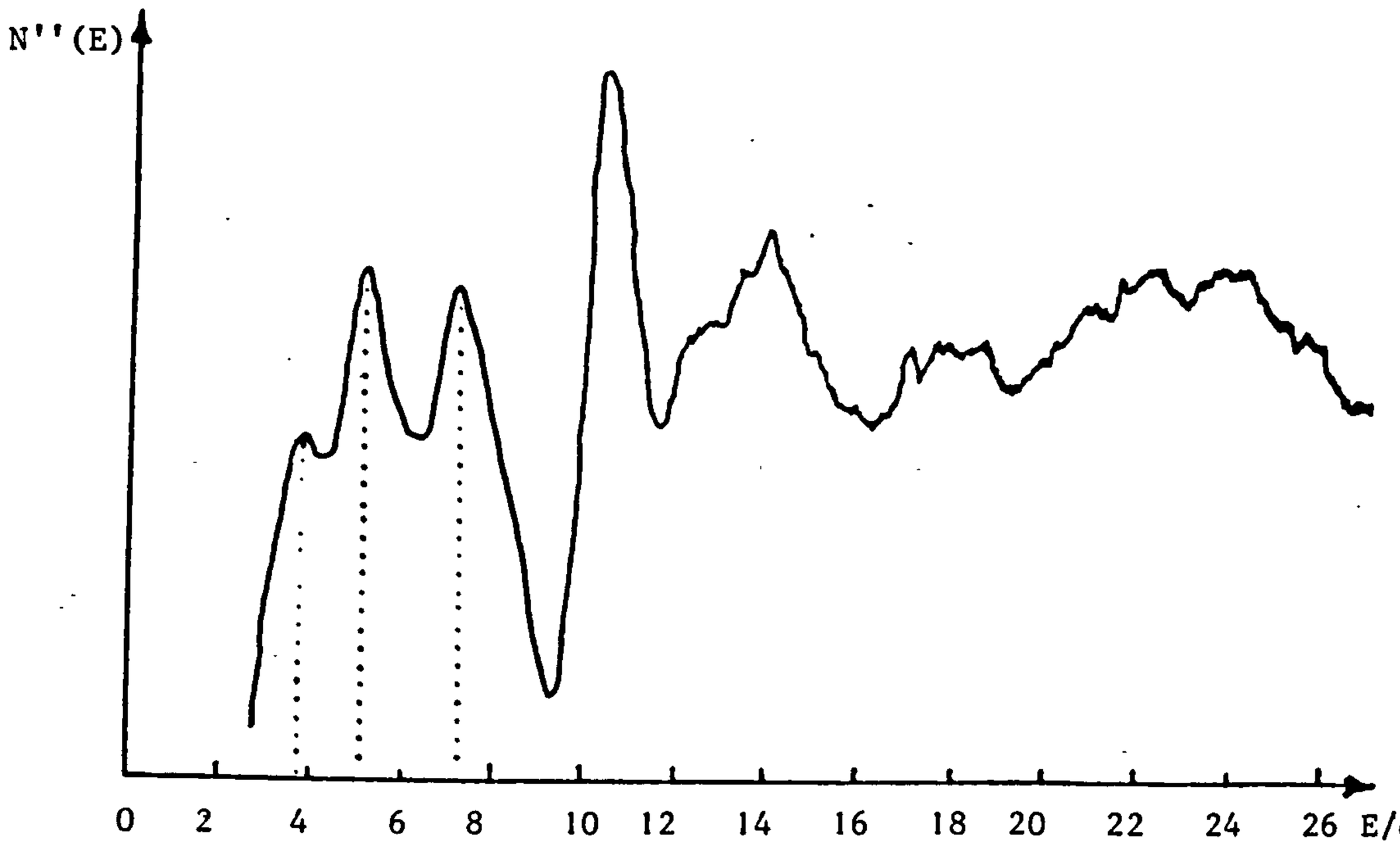

Fig.(8.28b): ELs spectrum of solid silica from ref.8.33. E_p = 200 eV.

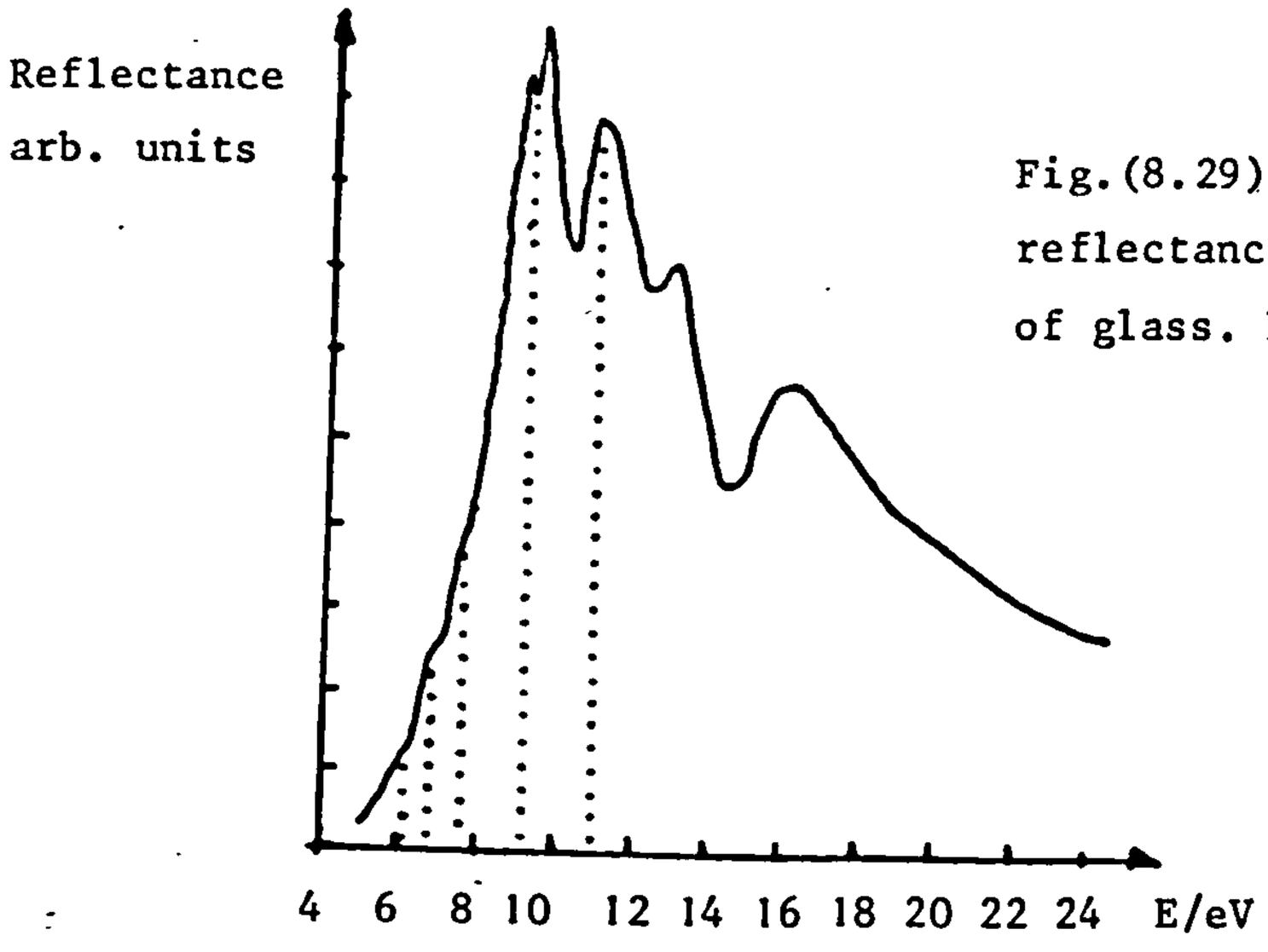

Fig.(8.29): Ultraviolet reflectance spectrum of glass. Ref.(8.36).

As yet, no detailed model of the formation of the SiO_x peaks has been suggested, and so the introduction of further losses in this part of the spectrum can only be attributed to other interactions involving non-bridging atoms at the surface. The mode of deposition of the films does not preclude adsorbed oxygen, but the 3.5 eV peak was not always present, and cannot be positively identified.

Shown in Fig. 8.29 is the UV reflectance spectrum of glass from the work of Bagley et al (8.36) from which the UV data of Table IV was taken. The prominent feature close to 11 eV has been observed in glass by Ellis et al (8.32) (at 10.2 eV) and attributed to excitonic absorption (possibly to a state 1.3 eV below the conduction band). This assignment is supported by Ibach and Rowe (8.37) but disputed by Kana and Ludeke (8.38). The peak is to be seen in Fig. 8.25 and particularly clearly in Fig. 8.30. A peak at 12.4 eV is attributed to the presence of network modifiers (8.36) and Pollard shows that its magnitude correlates with the quantity of potassium in the glass. The peak at 12.6 eV which can be discerned in Fig. 8.25, may have the same origin. Peaks at 20, 28-29 and 32-33 eV are possibly due to cationic excitons (8.33); one such may be seen amongst the several peaks in the region of 20 eV in Fig. 8.25.

The spectrum of calcium enriched glass in Fig. 8.30 was obtained using the MCA according to the technique described in the previous section. It shows a large feature centred at 28 eV, which energy is close to the Ca^{2+} 3p-4s or 3p-3d transition (8.39) and we can identify this energy loss with a calcium exciton (8.33). There is also a compositional correlation since no peak is found here unless the surface of the specimen has been calcium enriched by sputtering.

8.6.4 Beam damage

Although the incident power densities used for ELS ($\sim 1\ kWm^{-2}$) are typically a thousandth of those in Auger work, spectra frequently show

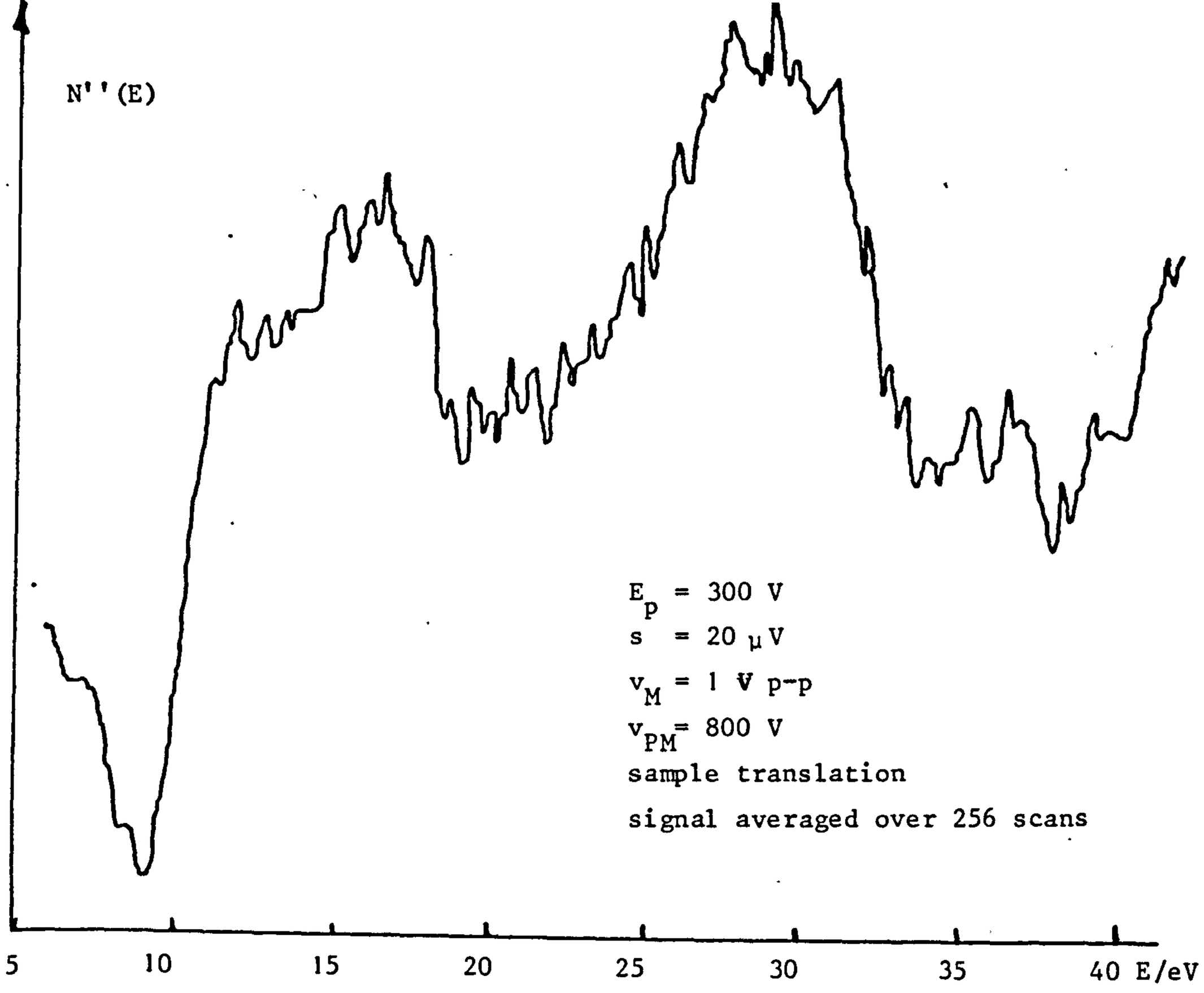

Fig.(8.30): ELS spectrum of a calcium enriched glass surface showing the calcium exciton at 28 eV

Fig.(8.31): ELS spectrum of silica showing beam damage.

E_p = 200 V
v_M = 1 V p-p
v_{PM} = 840 V
ss = 30/3000 Vs^{-1}
speed, 100 sV^{-1}
25 mins /scan

The three traces were obtained consecutively in the order shown

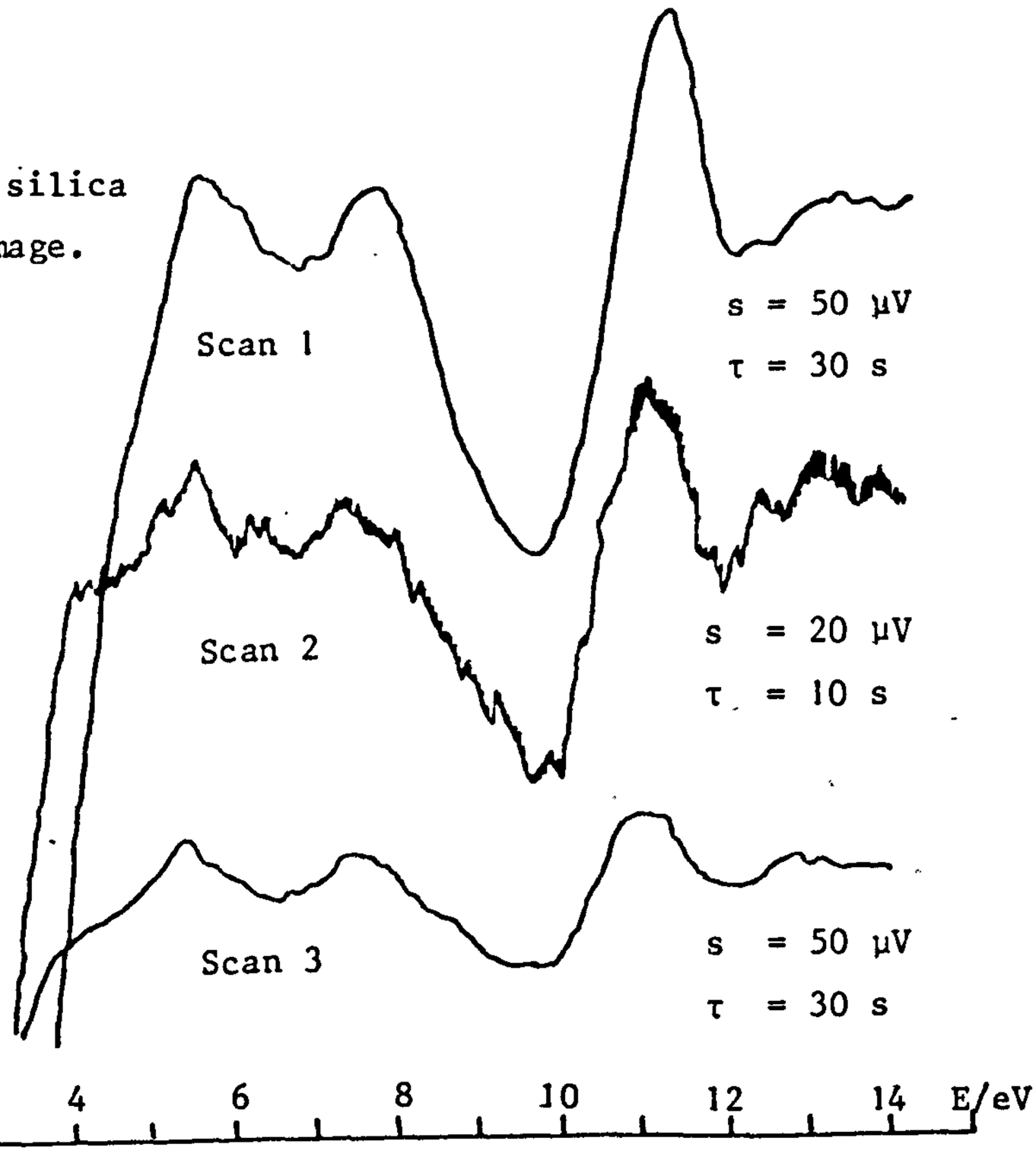

a time dependence which can only be attributed to beam damage. Fig. 8.31 exemplifies the reduction in the intensity of the structure in the SiO_x region of amorphous SiO_2 as irradiation proceeds. Continued exposure of the same part of the specimen to the beam results in a completely structureless spectrum. No detailed explanation of this phenomenon is available at present, but it should be recognised that the primary electrons' interaction cross-section with atomic bonding electrons increases as E_p approaches their bond energies, as it does in the case of ELS. Hence, the damage to the sample is likely to be a result of many processes different from those occurring in Auger analysis which have been described in sections 8.3 and 8.4.

8.6.5 Remarks

The study of glass surfaces using ELS is in its infancy. This is the first occasion of the analysis of RF sputter deposited glass films using the technique, and their spectra show similarities to those of both silica and bulk glass. It is unfortunate that relatively little may be learnt about the composition of the films and that more questions are raised by each scan than are answered.

8.7 Depth profiling by sputtering

This section unites the two halves of this thesis. The account of sputtering theory given in Chapters 2 and 3 is now applied to the prediction of etch rates and the time-development of surface composition, during sputtering in an ion beam.

8.7.1 The ion beam

The ion gun shown in Figs. 7.6 and 8.1, a Vacuum Generators AGS2, was used to bombard the surface of the sample with energetic argon ions. The 99.999% pure argon, admitted through leak valve V6 from the gas handling line (shown in Fig. 8.1) is ionised in the high toroidal magnetic field

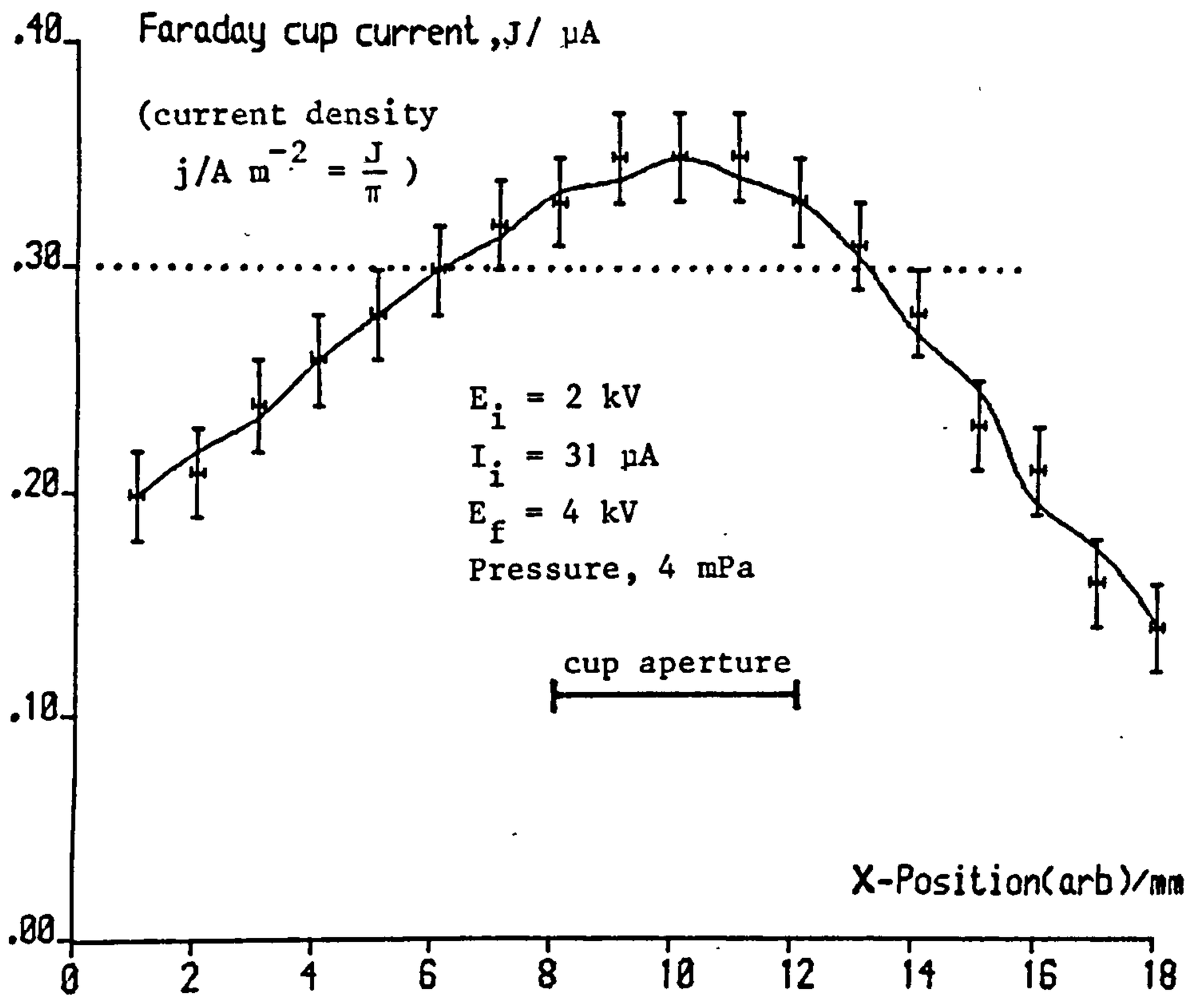

FIG(8.32) Argon ion current entering cup against position

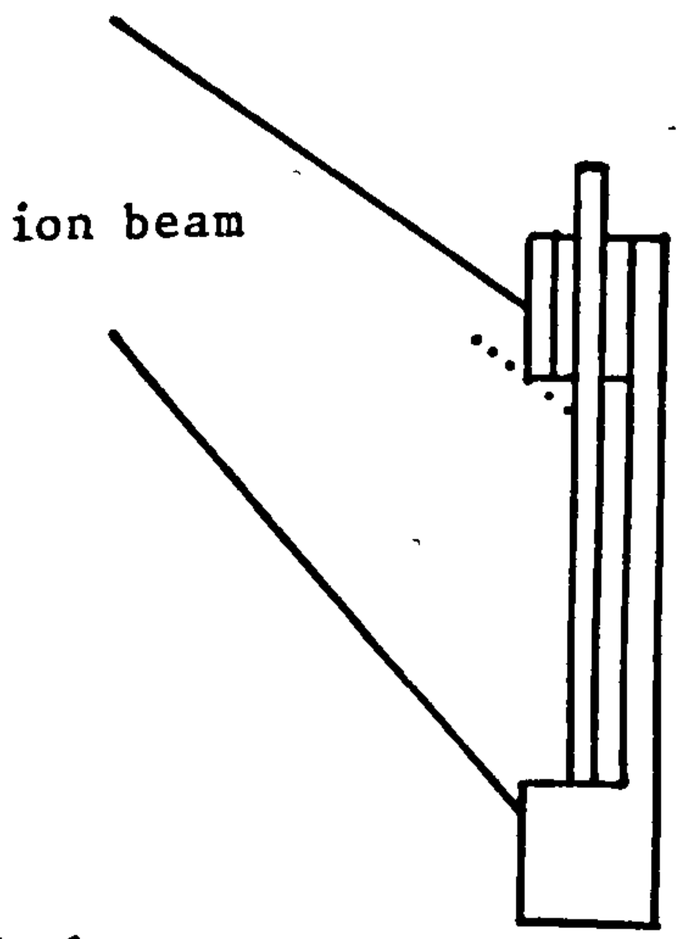

E_i = 2 kV
E_f = 1.6 kV
j_{av} = 0.095 Am^{-2}
I_i = 30 μA

Fig.(8.33):
Etch rate of glass
experiment.

Talystep traces

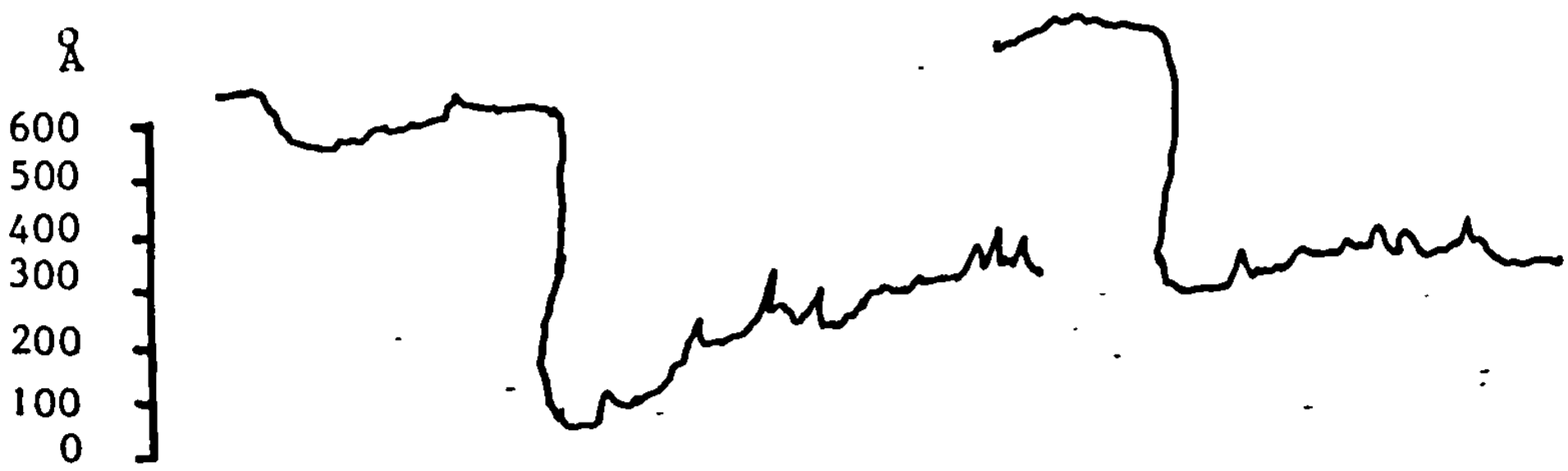

created by the permanent magnet surrounding the gun, and the ions are accelerated into the chamber by an electrode biassed at up to 15 kV. Although the axis of the beam is directed to permit 'in situ' bombardment of the analyte, the stray fields from the magnet prevent electron spectroscopy, and it must be removed during analysis.

After protracted trials with various gas flow rates, it was found that a stable beam could be attained only by reducing the aperture of the butterfly valve V4 and admitting argon slowly until the pressure in the chamber began to rise. Ion beam currents were measured by the current in the bias line which was displayed on the control unit. The current readings I_i were found to be affected by the chamber pressure and the gas flow rate, but at a butterfly valve setting of $1\frac{1}{2}$ turns of the control wheel from the closed position, and at pressures around 4 mPa ($\sim 3 \times 10^{-5}$ Torr) this dependence was reduced, and a fairly stable current could be obtained.

The beam profiles were investigated using the Faraday cup with the inner can biassed until saturation, at about -20V. Fig. 8.32 shows the ion current J entering the cup as a function of position in the x-direction. Since the Faraday cup aperture has a radius of 1 mm, the current density j in Am^{-2} is given by J/π where J is measured in μA. A somewhat asymmetric profile is found because the gun is mounted at 60° to the y-z plane and at 50° to the x-z plane, and the Faraday cup is not tracked normal to the beam in this experiment. The full angle made by the ion beam axis with the surface normal of the analyte is 71.2°.

The current density j_{max} in the centre of the beam, calculated from plots such as Fig. 8.32, was used in combination with I_i to determine the effect of the focus voltage E_f on the divergence of the beam. The total current is given by:

$$I_i = j_{max}\ 2\pi \int_0^{\infty} \exp(-r^2/2\sigma^2)\ r^2\ dr = 2\pi\sigma^2 j_{max} \qquad 8.24$$

assuming a Gaussian profile of spread σ, and using $I_i = 31\,\mu A$ and $j_{max} = 0.11\ Am^{-2}$ from the figure, we obtain $\sigma = 6.6$ mm. This is consistent with the extent of the reddish glow to be seen on the surface of the samples as discussed in section 6.4. It was found that the beam was focussed to this (its minimum) divergence, with a focus potential E_f of $0.8E_i$.

The sample surface available for analysis was usually about 10 x 10 mm, which is small compared with the beam. Thus, if we consider that the beam produces a cup current of $J_{av} = 0.3\,\mu A$ over its central region (as shown in Fig. 8.32), we may write:

$$j_{av} = \frac{J_{av}}{\pi} = 0.095\ Am^{-2} = 86\%\ j_{max} \qquad 8.25$$

and substituting $\sigma = 6.6$ mm in equation 8.24 yields the useful relation:

$$j_{av}/Am^{-2} = 3.1 \times 10^{-3}\ I_i/\mu A \qquad 8.25'$$

An accuracy of only 15% may be claimed for the constant of proportionality in the above equation considering all the approximations made.

8.7.2 The etch rate

The rate at which the glass surface was eroded by the ion beam was determined by the height of the step produced in the surface of a glass slide caused by the shadow of the sample holder as shown in Fig. 8.33. The Talystep instrument (6.5) was used to measure the height at 19 points along the length of a step produced by an hour's continuous sputtering at the settings shown in the figure. A mean etch rate of 5.7 $\mathring{A}\ min^{-1}$ was calculated. Whereas during this experiment the beam current was kept close to $30\,\mu A$, it was found on other occasions that I_i could not be stabilised at this value. The etch rate was therefore expressed per unit beam current thus:

$$R(I_i)/\mathring{A}\ min^{-1} = 0.19\ I_i/\mu A \qquad 8.26$$

which was the relation used to calibrate the depth profiles. Using equation 8.25', we may obtain the equation:

$$R(j_{av})/\mathring{A}\ min^{-1} = 60.0\ j_{av}/Am^{-2} \qquad 8.26'$$

used below, in the context of RF sputtering.

These results may be used to determine the sputter yield S(E) at E = 2 keV and at an incident angle of 71.2°. The etch rate R(E) may be written:

$$R(E) = S(E)j_{av}/Ne \qquad 8.27$$

which, using the typical number density N = 0.072 $\mathring{A}^{-3}$ (from subsection 3.3.2) represents a rate of:

$$R(2\ keV)/\mathring{A}\ min^{-1} = 52.14\ S\ j_{av}. \qquad 8.27'$$

Using j_{av} = 0.095 Am^{-2} and R = 5.7 $\mathring{A}\ min^{-1}$, we obtain the approximate result:

$$S(2\ keV) = 1.2 \qquad 8.28$$

at an angle of 71.2°.

It is unfortunate that the geometry of the apparatus causes the range of validity of the angular dependence of the sputtering yield (equation 2.23a) to be exceeded by 1.2°. We may add, however, that pursuing the $\eta^{-5/3}$ relationship nevertheless (with η = cos 71.2) and using equation 4.2' for the ion current density in a 3 kV p-p RF discharge sheath of 15 mm thickness, we can calculate the rate of erosion of a target glass in the sputtering rig of the first part of this thesis. A result of 20 $\mathring{A}\ min^{-1}$ is obtained from equation 8.26', which is some 25% higher than the deposition rate of films established in Fig. 6.4, but the similarity of the two results is surprising in view of the gamut of approximations made.

8.7.3 Auger signal profiles

The time development of the composition of a multi-component surface under sputtering was described in Chapter 3, with particular reference to the work of Liau et al (3.4). Figs. 3.2 show how the ratio of

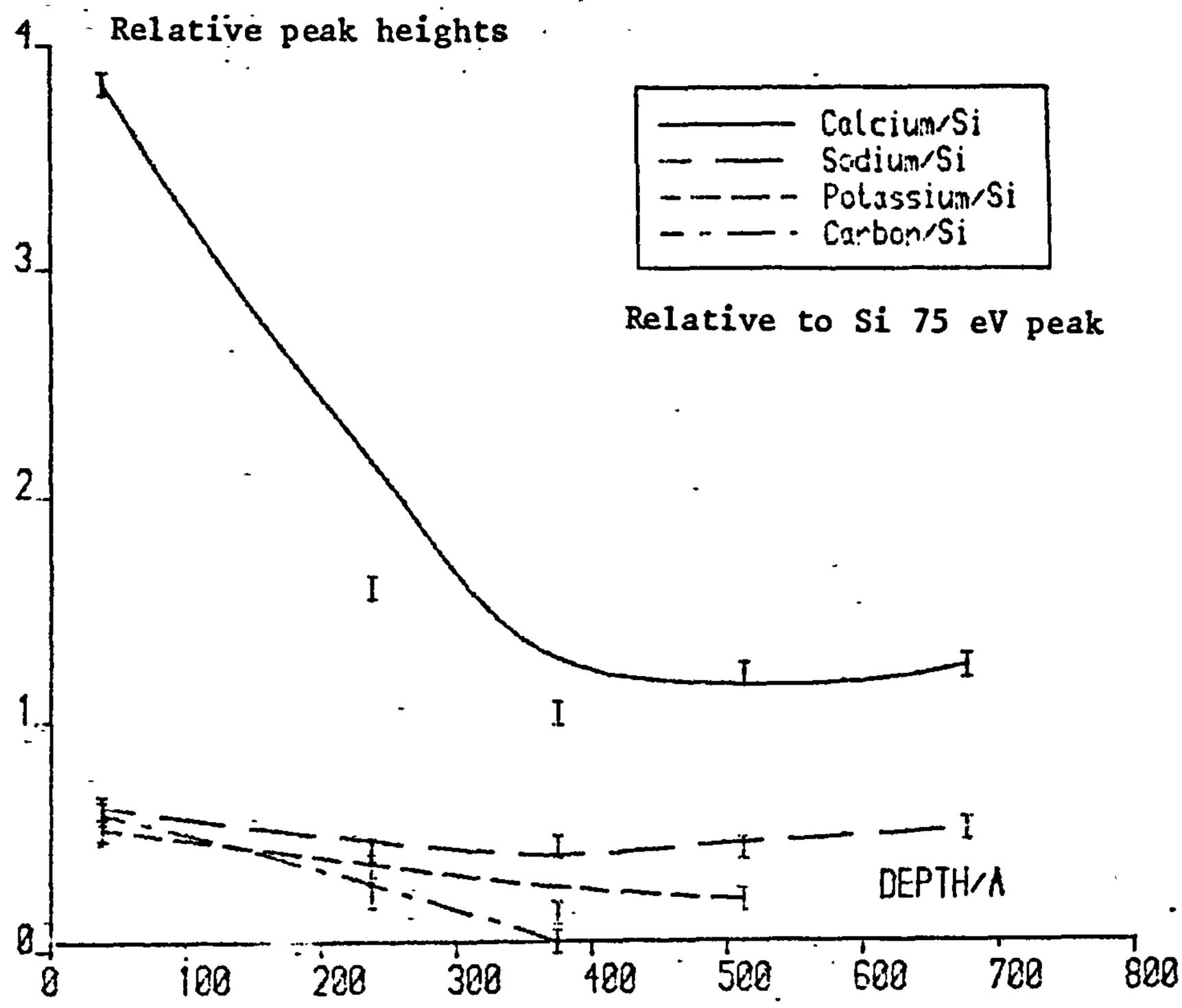

Fig(8.34a)DEPTH PROFILE SOURCE GLASS SURFACE B

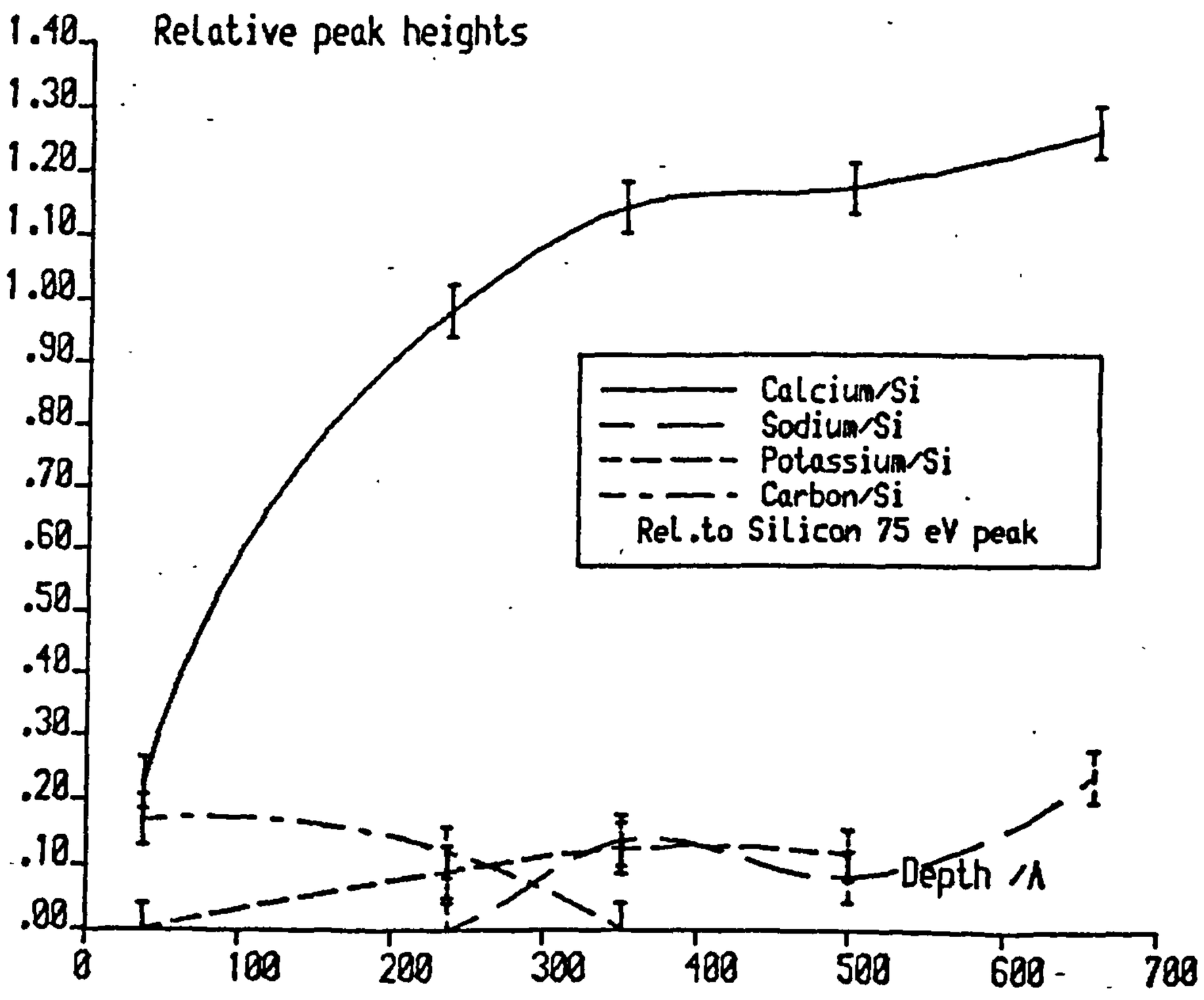

Fig(8.34b): Depth profile of film B53

the surface concentrations of two components approaches a constant (r) whatever was its original bulk value. Using the results above ($S = 1.2$, $j_{av} = 0.095\ Am^{-2}$, $N = 0.072\ \mathring{A}^{-3}$), the abscissa of these plots, defined in equation 3.6, may be partially evaluated thus:

$$D(t) \sim \frac{0.098\ t}{W} \qquad 3.6'$$

The remaining parameter W, the depth at which the steady state composition ratio r is attained, may be inferred from plots such as Figs. 8.34. These figures show the p-p Auger heights of signals from four atomic species (relative to the silicon 75 eV peak) as a function of depth, calibrated using equation 8.26. Since each data point was obtained with the sample translation method described in section 8.5, the production of depth profiles was a very arduous occupation. It is seen that after a depth of $\sim 400\ \mathring{A}$ had been sputtered away, the signal intensities show a distinct constancy, and we may hence set $W = 400\ \mathring{A}$, and write:

$$D(t) \sim 2.45 \times 10^{-4}\ t/s \qquad 8.29$$

No indication of the accuracy of the depth determination is given in these and similar plots for reasons of clarity. Since the error is contained in the estimation of the etch rate, an error of perhaps $\pm$ 15% may be attached to each depth measurement.

It is preferable in many ways simply to use the sputtering time as a parameter to eliminate this large uncertainty, following Malm et al (8.40), but use of the depth allows comparability between the results of workers who may have used different beam current densities and energies.

An ion beam energy of 2 keV was used for all depth profiling work, with $E_f = 1.6$ kV and a pressure in the region of 4 mPa ($\sim 3 \times 10^{-5}$ Torr). Beam currents of 30 μA were typical (the effect of variations being nullified by recording I_i and using equation 8.26).

The profiles of calcium, sodium, potassium and carbon in glass

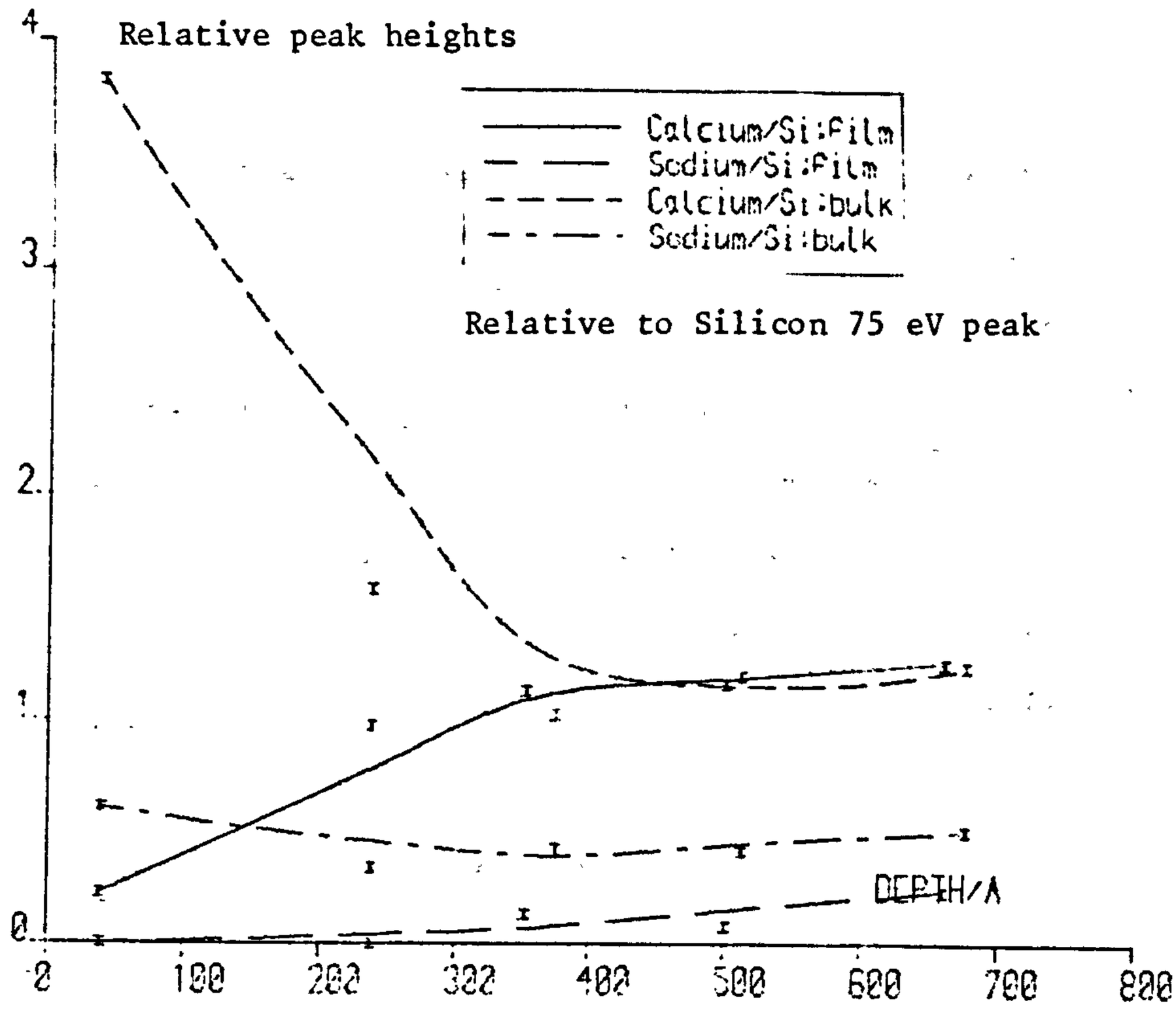

Fig(8.34c): DEPTH PROFILES FILM B53 AND SOURCE B

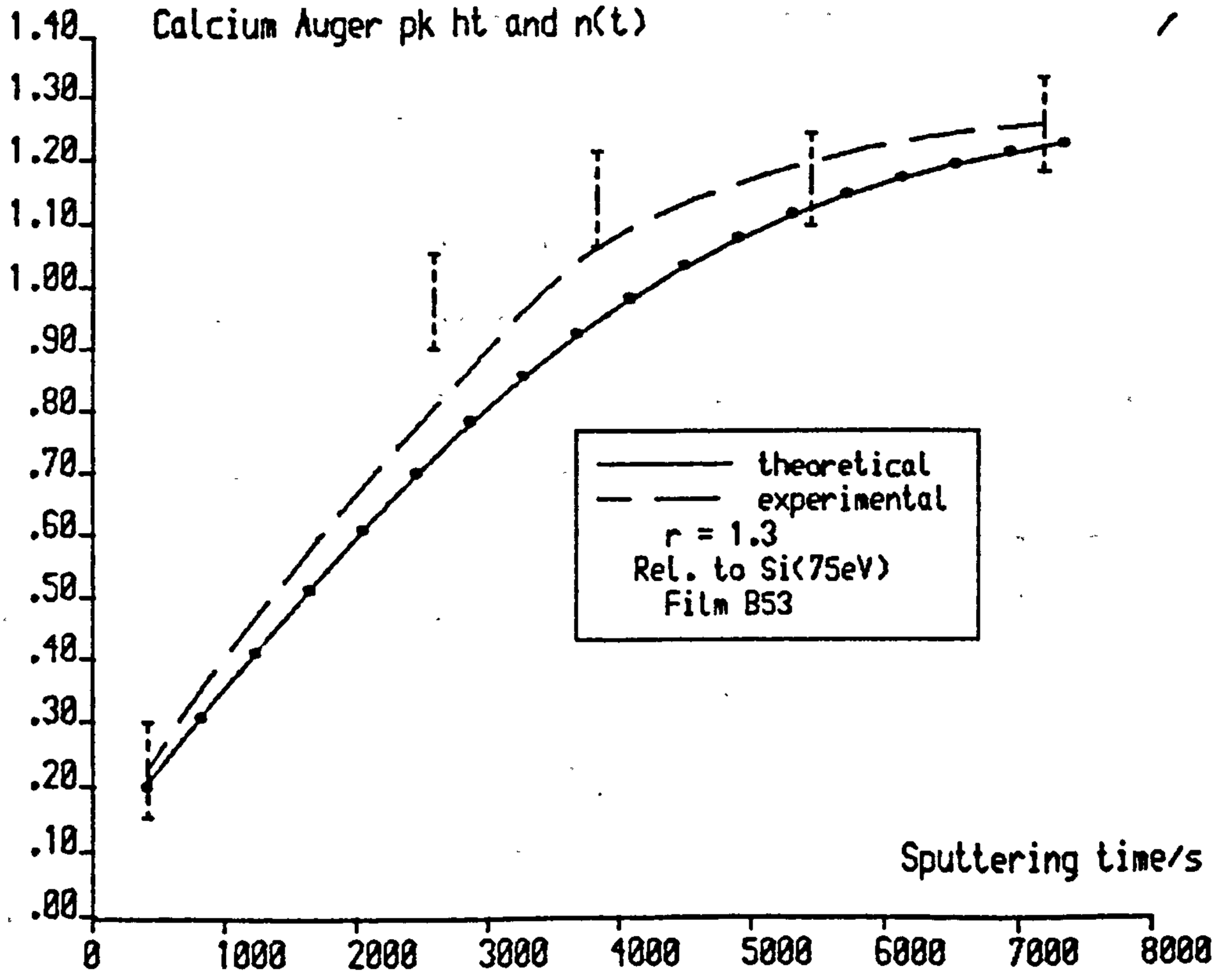

Fig.(8.35): Calcium sputter-time profile and surf. conc., n(t)

are shown in Figs. 8.34. The Ca/Si ratio varies most markedly with depth (i.e. dose, D), and is seen to stabilise at approximately 1.3 whether its initial value was very high or very low. The high surface concentration of Ca seen in the ternary source glass is surprising because the surface was that from which the film B53 was deposited and as such should be of the steady state composition. The probable explanation is that the carbon layer, by which the silicon signals are very strongly attenuated, was thicker in the initial stages of the profiling of the bulk than in the case of the film.

The carbon signal decays to zero in both cases at a depth of 350 Å. Collisional reimplantation effects (2.12) are probably responsible for extending the apparent depth of the surface carbon (which is usually little more than a monolayer), since intrinsic carbon at this depth in the glass matrix is unlikely (8.33). Some of the data of Figs. 8.34a, 8.34b are replotted in Fig. 8.34c where the Ca and Na signal ratios from both source glass and film are seen to approach $r_{Ca} \sim 1.3$ and $r_{Na} \sim 0.3$ respectively. Figs. 8.34 also yield $r_K \sim 0.1$.

Equation 8.29 can be used to rescale theoretical profiles such as in Fig. 3.2 against time instead of dose, and hence enable them to be compared with the experimental profiles. Solutions n(t) of equation 3.6, with r = 1.3, and the Ca/Si data from Figs. 8.34 are plotted in Fig. 8.35 against sputtering time. The experimental points appear to rise slightly faster than predicted; if W had been set at 300 Å, the theoretical curve would have passed through the experimental points, but there is no justification for such an alteration. Equation 3.6 is based upon the assumption that the material has a uniform composition, but this is probably incorrect in the case of a glass film exposed to air for a long period of time. The Auger signal profile to be expected from sputtering glasses is a convolution of n(t) and the chemically altered surface described by

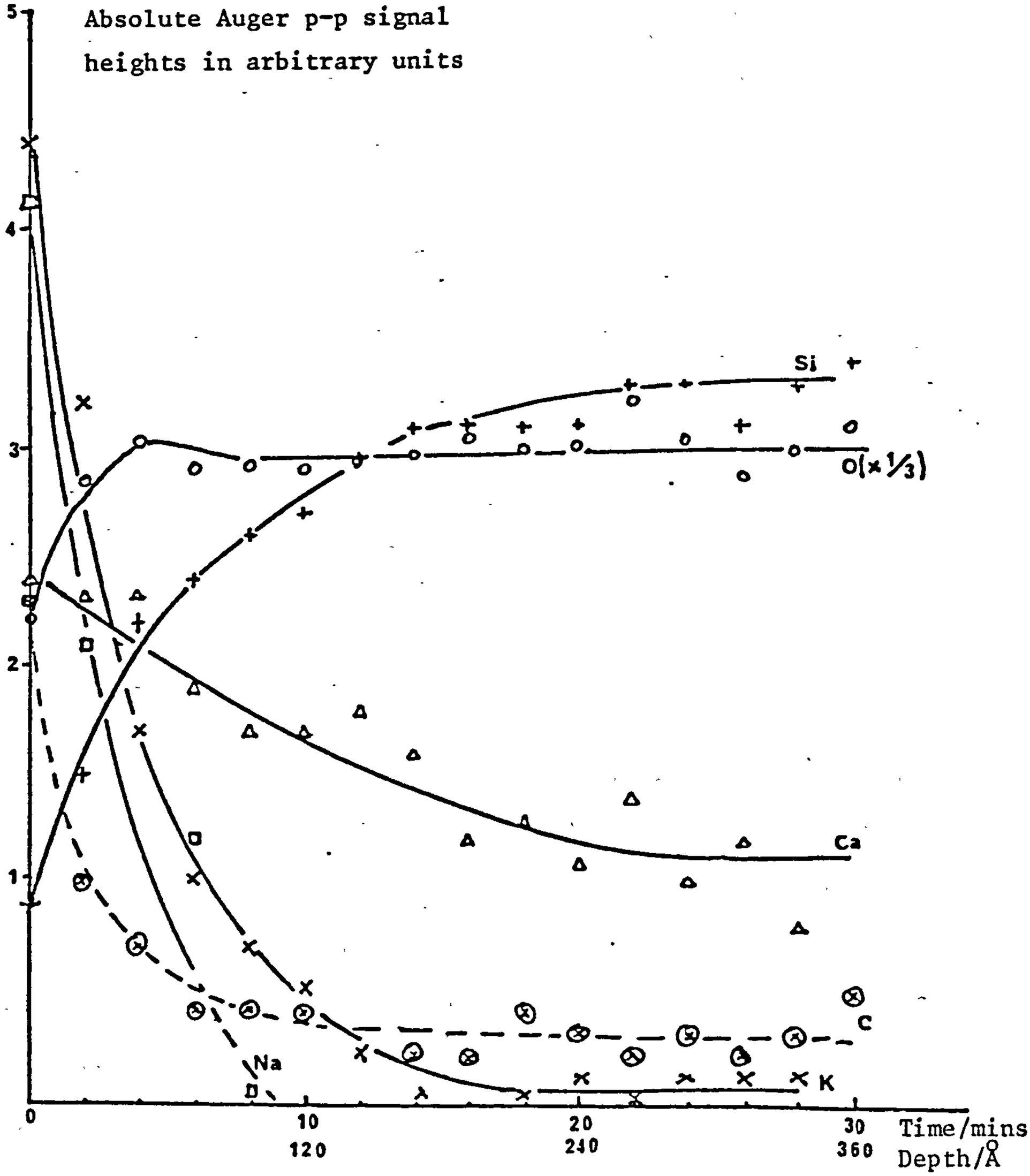

Fig.(8.36): 30 minute depth profile of window glass, Ref. 8.33

Hlavac (1.11), Hench and Clark (8.41) and Pollard (8.33). Pollard performed profiling experiments on various glasses (without making use of relative intensities or sample translation) and obtained results as shown in Fig. 8.36. The trend is very similar in most cases, with the steady state composition ratio being established at a depth of about 360 Å, although this depth appears to depend upon the length of the experiment.

In Fig. 8.37 are the results of depth profiling the calcium in a window glass film and its source surface. The steady state seems to have been reached at W~100 Å, a quarter of the previous value. This anomaly must be due to a deliberate difference in the experimental technique: the samples were not translated during analysis, as they were not in Fig. 8.36 from the work of Pollard (8.33). The difference can be attributed to a further manifestation of electron beam damage, unless a continuation of the experiment would have revealed the levelling off of the profile to have been transient.

The effect of sputtering away the entire thickness of a ternary glass film deposited upon silica is shown in Fig. 8.38. The film was measured after deposition to be 1000 Å thick and the figure can be used as a guide to the accuracy of the etch rate calculation, since the carbon signal which reappears at a depth of 950 Å is taken as contamination on the substrate surface buried beneath the film. The calcium rises to rather above the usual 1.3 in this case, but is seen to fall again as the interface is approached. The fall is less sudden than might be expected, which may be explained by the re-implantation effects mentioned above or by a failure to wait for the establishment of a stoichiometric flux at the beginning of the deposition, but is more probably due to the rough surface of the silica substrate causing an apparent spread in the depth as the sample was traversed.

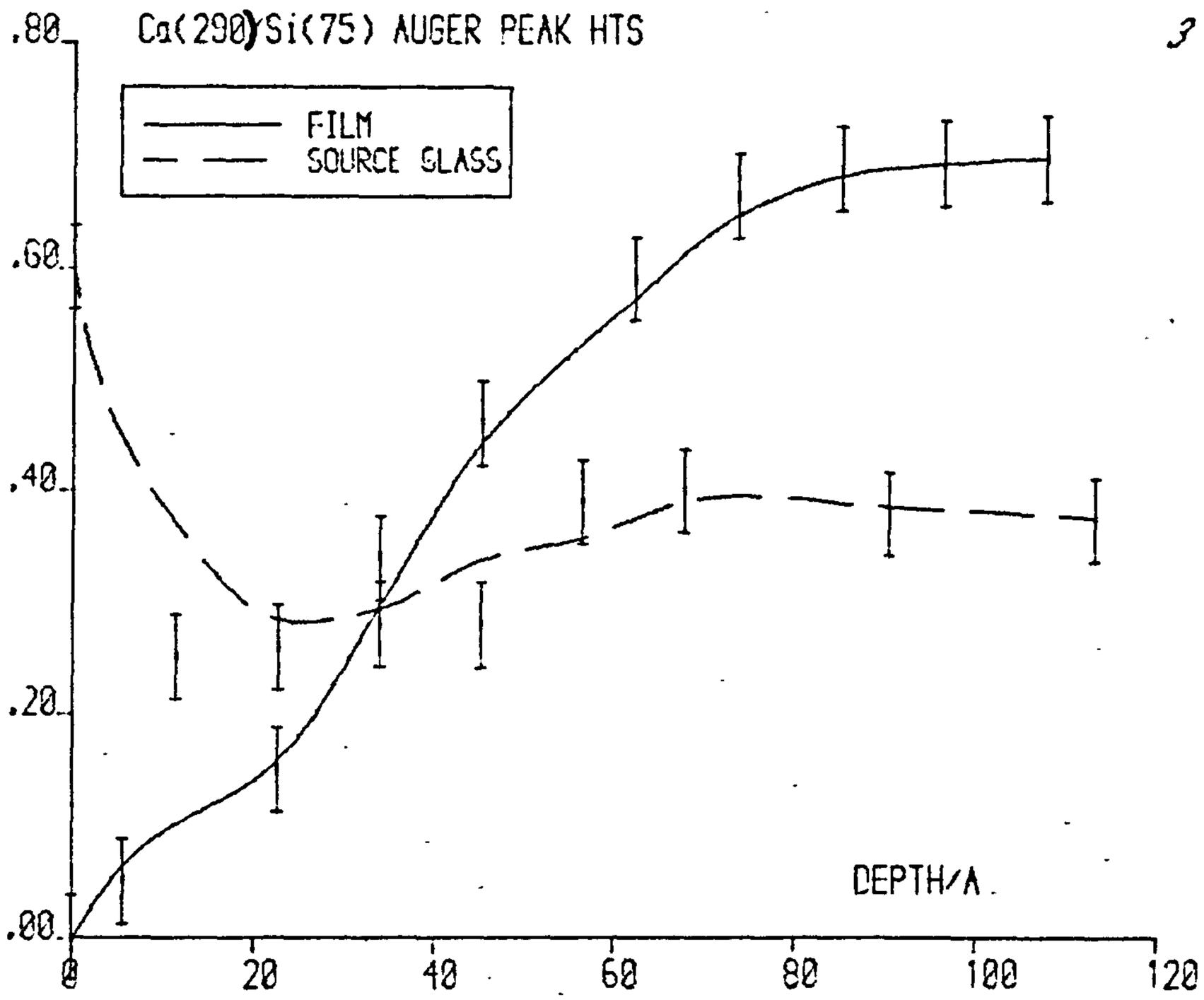

FIG(8.37):Ca PROFILE OF WG AND FILM

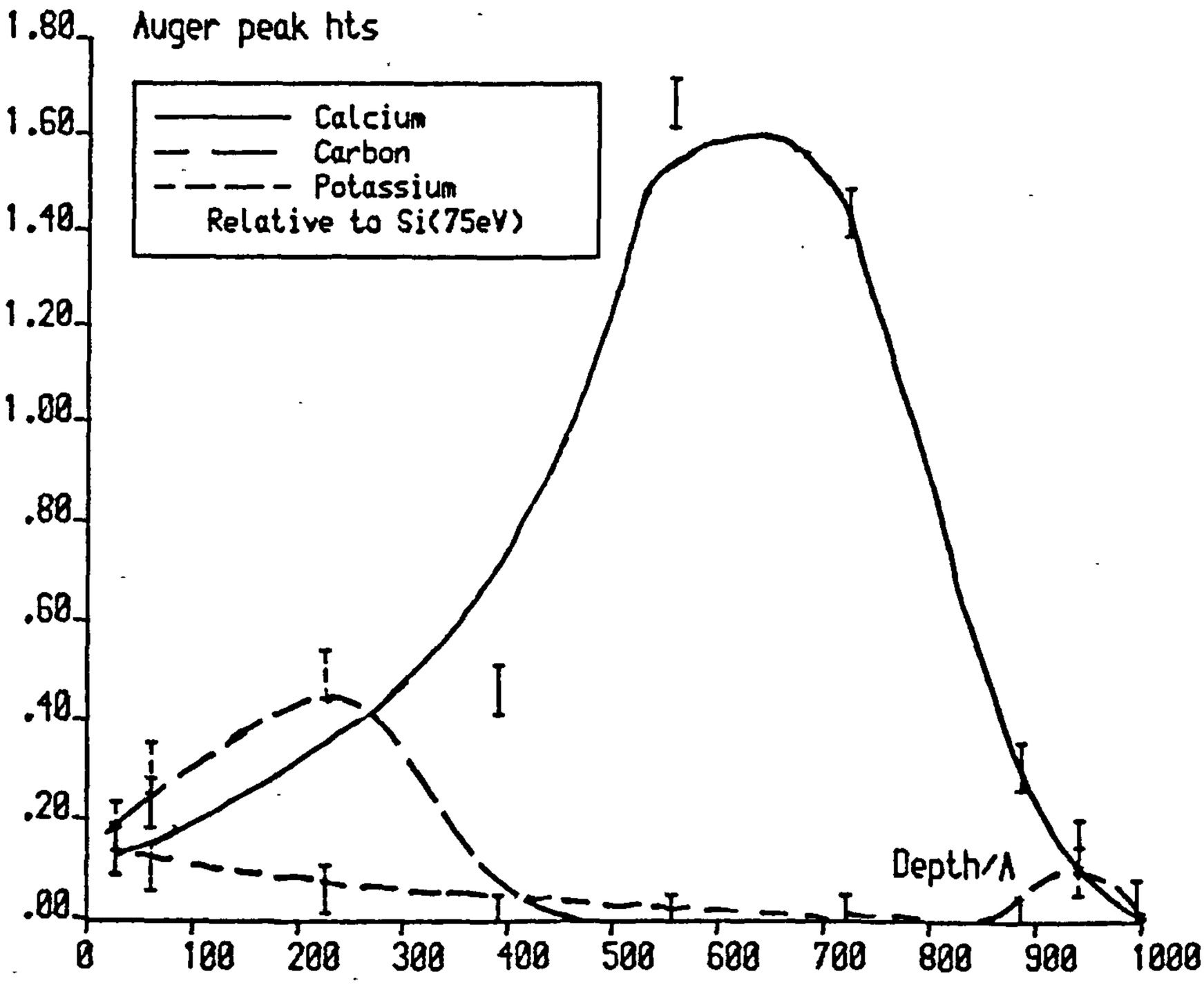

FIG(8.38):Depth profile of Film B41 on silica

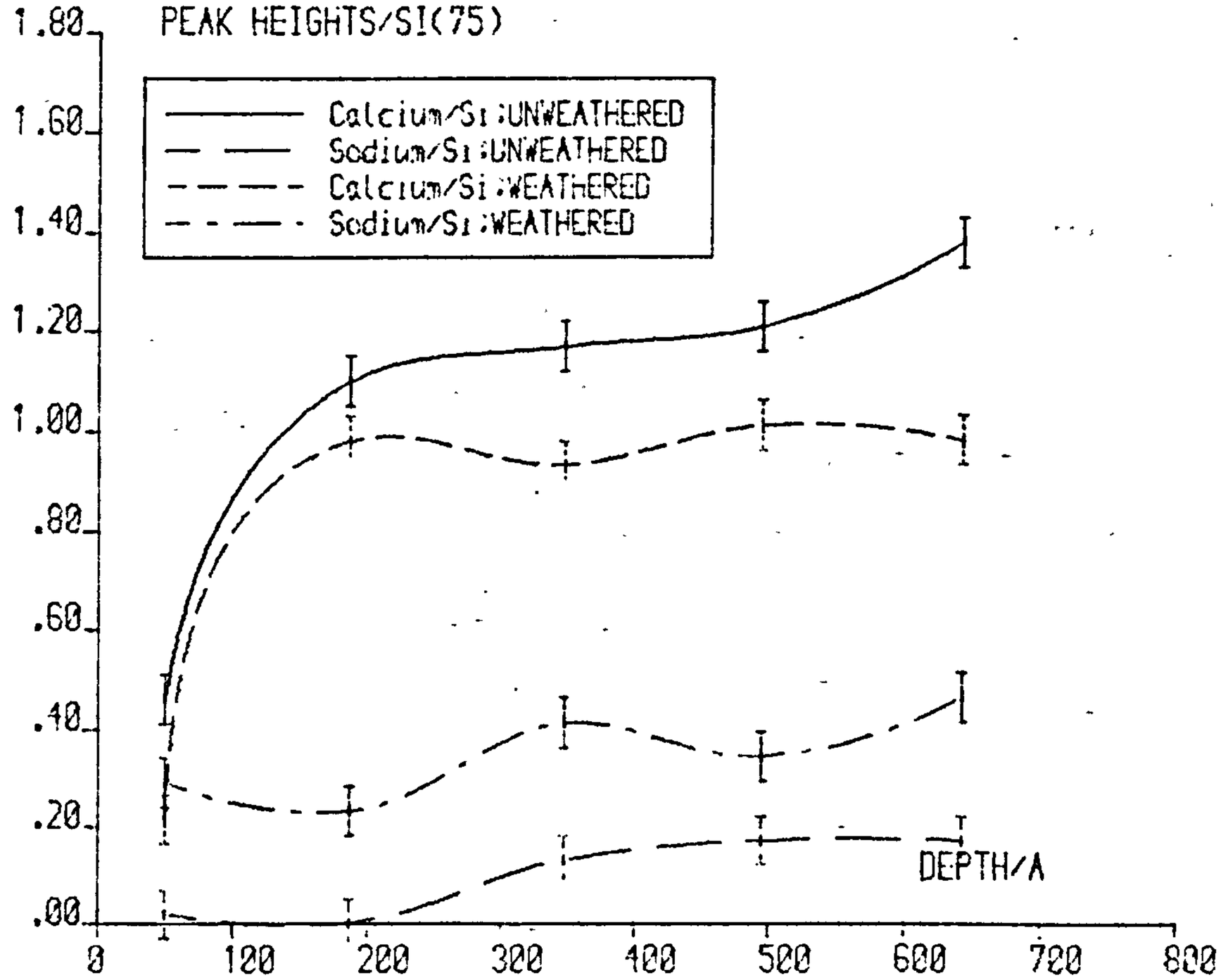

FIG(8.39):WEATHERING EFFECT ON MICROSCOPE SLIDE

Shown in Fig. 8.39 is a depth profile of a microscope slide before and after weathering for 5 hours in the laboratory unit described in Appendix II. As before, W ~400 Å, r_{Ca} is in the region of 1.3 (in the unweathered case) and r_{Na} is close to 0.3 (in the weathered case), but the other two steady state ratios appear anomalous. No explanation of this can be provided at the present stage.

8.8 Summary

In this chapter, we have explored the difficulties attaching to AES and ELS of glasses. Particularly, the electron beam damage effects have been described in detail, and a theory of ionic migration has been set out. Finally, the results of sputter-profiling glass surfaces are compared with the predictions of the work on the time-dependence of the surface composition of multi-component materials developed in Chapter 3.

CHAPTER 9

RAMAN SPECTROSCOPY OF GLASSES

The results obtained from electron beam spectroscopy are interesting because of the light shed on the processes involved, but it is clear that neither AES nor ELS can be recommended as a technique for the quantitative determination of the composition of either glass films or bulk glass, primarily because of their extreme surface sensitivity. Therefore, during the final stages of the study, attention was turned to optical techniques, which penetrate the bulk of the sample, and to Raman spectroscopy in particular because of the excellent facilities available at the Department of Chemistry of the University of York.*

Raman spectroscopy (9.1, 9.2) consists of illuminating a sample with monochromatic light of high intensity and examining the emitted spectrum. Lasers are invariably used for the primary light source in modern practice. The chemical bonds present in the sample vibrate in their characteristic modes, the intensity and frequency of which identify the type and concentration of the bond.

This chapter consists of a very brief account of the theoretical basis of the technique, followed by the experimental results obtained from examining bulk glass, RF sputter-deposited glass films and silica.

9.1 The Raman effect

The treatment set out in this section is based upon those of Colthup et al (9.3) and Chantry (9.4), and will be restricted to the classical case, by which means most Raman effects may be explained. Long (9.2) provides a quantum mechanical derivation of considerable thoroughness.

* The author is indebted to Dr. R.E. Hester for his invaluable advice, assistance and encouragement.

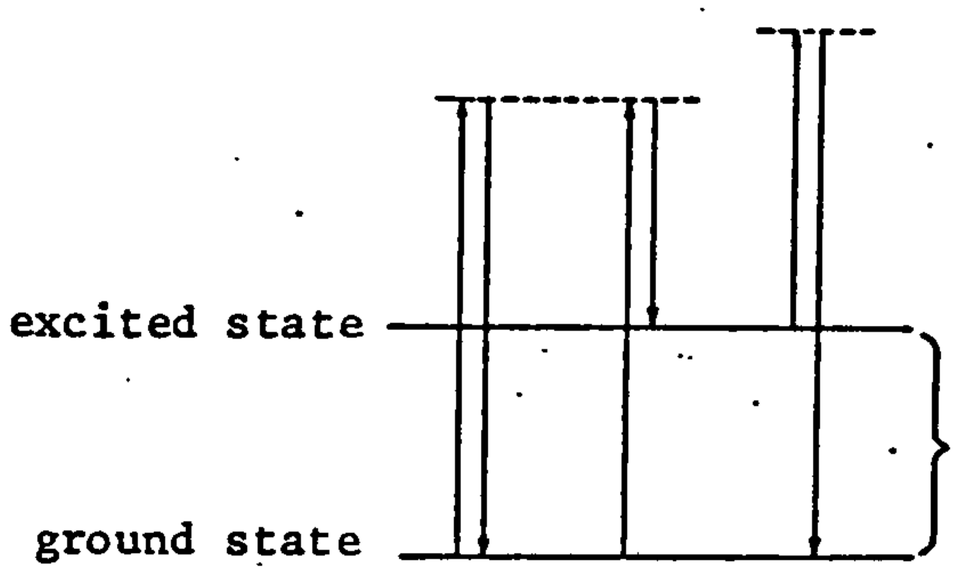

Fig.(9.1): Energy level diagram of the Raman effect. (Ref.9.3)

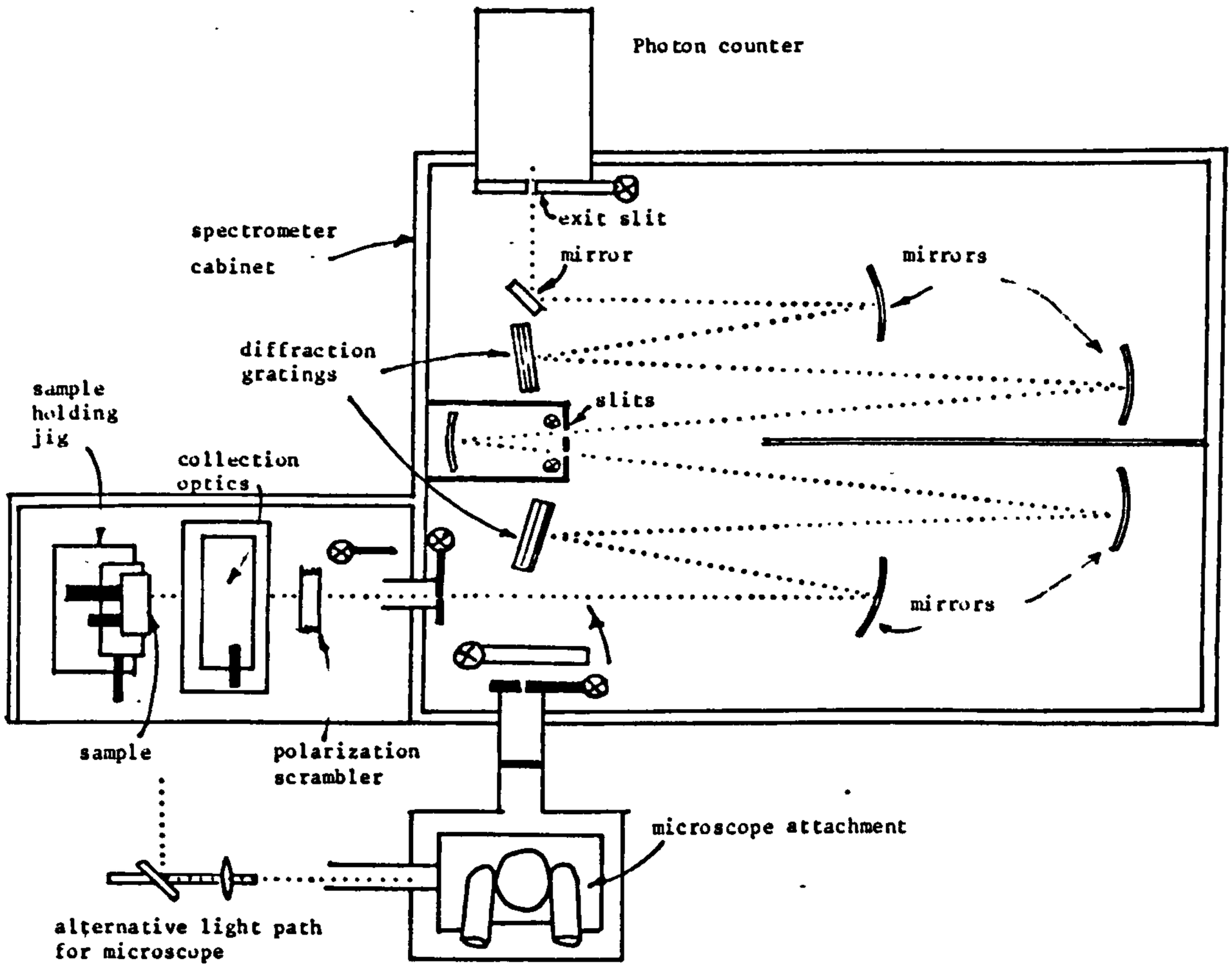

Fig.(9.2): Diagram of Spex spectrometer used in study

9.1.1 Polarizability

The Raman effect is due to changes in the polarizability of a molecule as it deforms in an electric field. In the equation

$$\underline{\mu} = \underline{\underline{\alpha}} \cdot \underline{E} \qquad 9.1$$

the matrix $\underline{\underline{\alpha}}$ relates the magnitude and direction of the dipole moment $\underline{\mu}$ to the applied field vector $\underline{E}$. The matrix $\underline{\underline{\alpha}}$ is symmetric, and we can transform to a special coordinate set in which its off-diagonal elements disappear. Equation 9.1 may then be written in the form:

$$\mu'_i = \alpha'_{ii} E'_i \qquad 9.1'$$

where the components are expressed in terms of the principal axes i = 1, 2 and 3, and α'_{ii} are the three elements of $\underline{\underline{\alpha}}'$.

The polarizability of the molecule may be considered as an ellipsoid whose surface is $|\underline{\underline{\alpha}}'|^{-\frac{1}{2}}$ from the origin, and whose symmetry reflects that of the molecule. The extent to which the polarizability ellipsoid is deformed by a small vibration or rotation of magnitude x may be written $\frac{\partial \alpha}{\partial x}$ giving:

$$\alpha = \alpha_o + \frac{\partial \alpha}{\partial x} x \qquad 9.2$$

Now, if the deformation occurs sinusoidally, at a frequency ω_v, we have:

$$\alpha = \alpha_o + \frac{\partial \alpha}{\partial x} x_o \sin \omega_v t \qquad 9.2'$$

and combining this equation with equation 9.1' applied to an incident light wave of amplitude E_o and frequency ω_i, we obtain:

$$\mu = \alpha_o E_o \sin \omega_i t + x_o E_o \frac{\partial \alpha}{\partial x} \sin \omega_v t \sin \omega_i t$$

$$= \alpha_o E_o \sin \omega_i t + \frac{x_o}{2} E_o \frac{\partial \alpha}{\partial x} \left\{ \cos(\omega_i - \omega_v)t - \cos(\omega_i + \omega_v)t \right\} \qquad 9.3$$

Classical EM theory indicates that the power radiated by an oscillating dipole is proportional to μ^2, and it can be seen from equation 9.3 that therefore energy will be emitted not only at ω_i, the

frequency of the incident radiation (Rayleigh scattering) but at frequencies $(\omega_i - \omega_v)$ (the Stokes line) and $(\omega_i + \omega_v)$ (the anti-Stokes line). The cross terms are not detectable with present equipment (9.4).

If the polarizability ellipsoid does not deform as the molecule vibrates $(\frac{\partial \alpha}{\partial x} = o)$, no Raman activity is possible. The bond may, however, be detectable by its infra-red activity, which is determined by the change in dipole moment on deformation. The two techniques are hence complementary.

9.1.2 Energy levels

The physical basis of the effect is made more accessible through considering the energy levels of a molecule, as seen in simplified form in Fig. 9.1. An incoming photon may interact with a molecule in three ways. First, a molecule in the ground state may be raised to an unstable level (a "virtual state") and return immediately to the ground state. This is Rayleigh scattering, since the energy of the emitted photon is equal to that of the incident one. Second, the excited molecule may decay to an intermediate level above the ground state, which results in Stokes scattering, as the energy of emission is below that of the incident radiation. Finally, the excited molecule may be raised to a higher level and thence decay to the ground state. The emission is of higher energy than the primary photon and anti-Stokes scattering is seen.

By means of this approach we see that the intensity of the anti-Stokes line must be very much less than that of the Stokes line, because at room temperature few molecules are excited thermally above the ground state. Hence, Raman spectroscopy is concerned with photons below the primary frequency.

Wave number units are used universally in optical spectroscopy, defined by:

$$\nu/cm^{-1} = \frac{10^7}{\lambda/nm} \qquad 9.4$$

where λ is the wavelength of the radiation. Raman shifts are designated $\Delta\nu$.

9.2 Experimental equipment

The primary light source was an argon ion laser which was tuned to either λ = 488 nm (ν = 20487 cm^{-1}) or λ = 514.5 nm (ν = 19436 cm^{-1}). A power of approximately 300 mW was available in each case. The laser beam was directed into the spectrometer by a combination of lenses and prisms with a long optical path (~10m), to provide frequency filtering.

The spectrometer was a Spex 1403/4 (9.5) which is a double pass monochromotor instrument with 2 gratings, each of 1800 lines mm^{-1}, as shown in Fig. 9.2. The scanning speed and dwell time were determined by a Spex Scamp controller and data processor (Model 3400) and the detector was a Spex DPC2 digital photon counter. The Scamp allowed spectra to be stored on floppy discs (a Diskette unit was used) and to be displayed both on the monitor (a Tektronix 620) and on a graph plotter in raw or smoothed form.

Figs. 9.3 show the optics and orientation of the sample in the two arrangements used. In Fig. 9.3a the sample is illuminated in the cabinet of the spectrometer by focusing the laser beam on its surface with a lens of focal length 50 mm and diameter 10 mm. The scattered light enters the collection optics, passes through a polarization scrambler and thence into the spectrometer itself. The second method was to focus the beam through a x40 microscope objective (focal length, 3.9 mm; diameter 9.0 mm) and to collect the scattered light with the same lens. This latter facility has the advantage that very small volumes of sample can be analysed, and that the analyte may be inspected visually with high magnification, but no rise in Raman intensity is to be expected since the irradiated volume reduces with the beam diameter and leaves the signal unchanged.

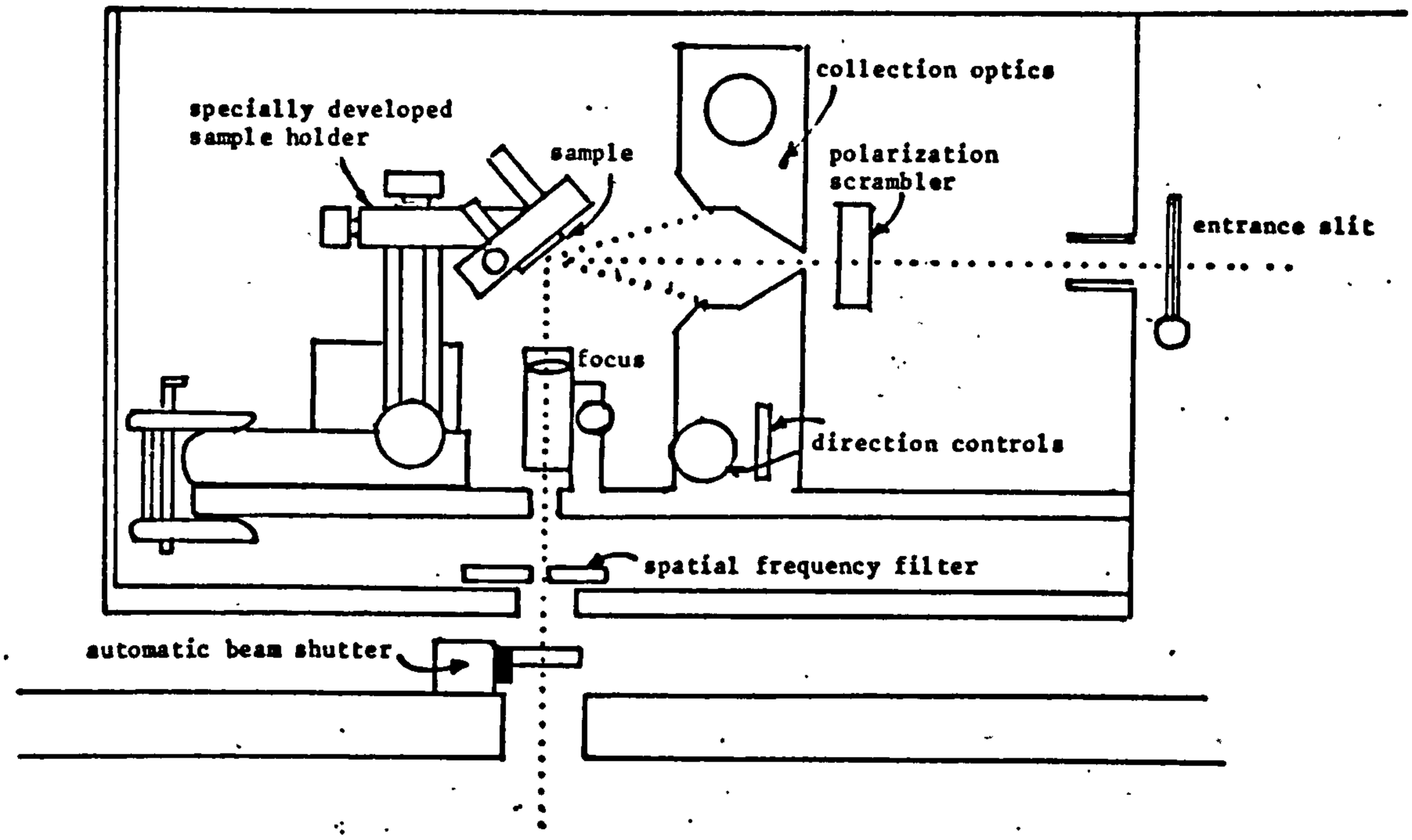

Fig.(9.3a): Sectional view of sample orientation in compartment

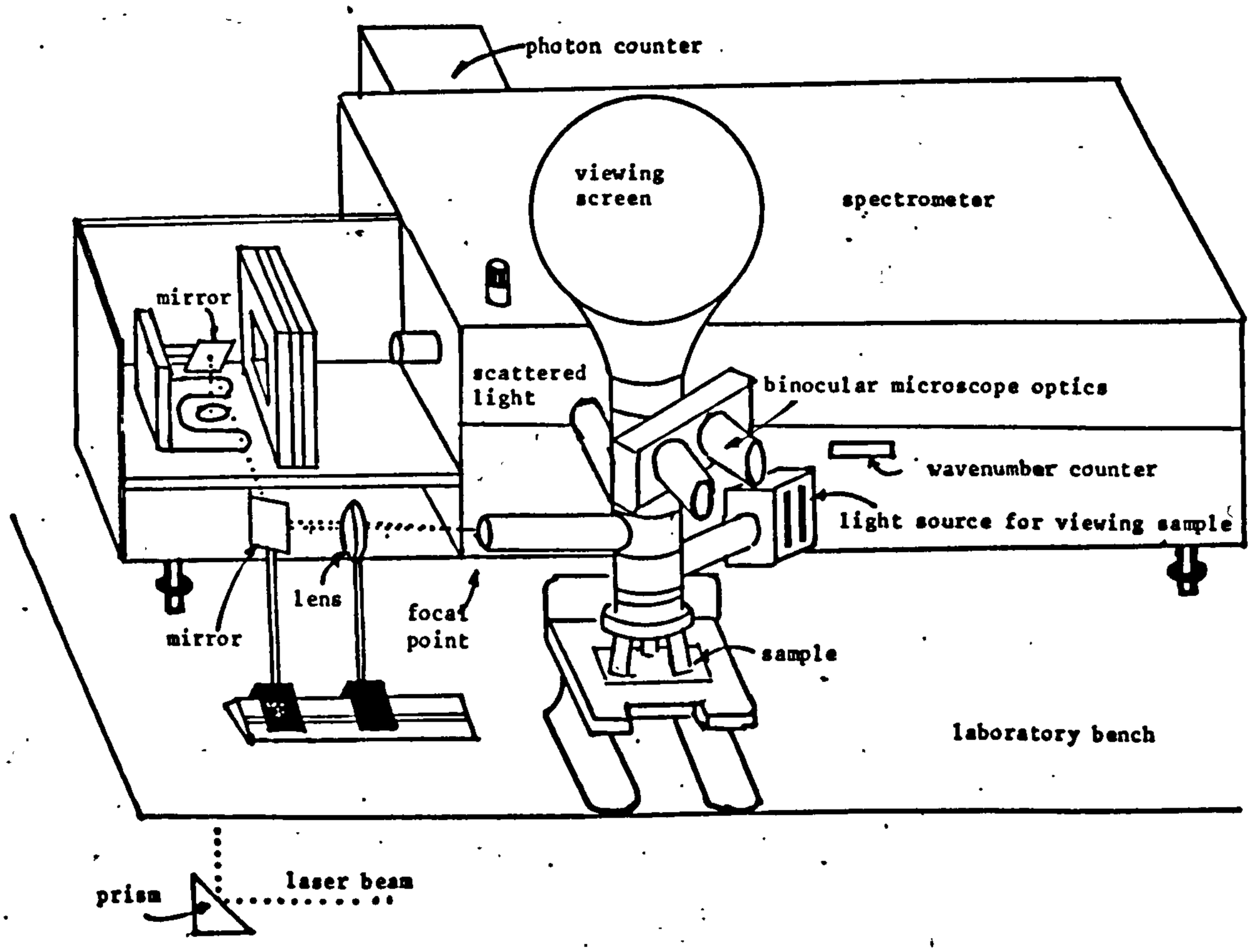

Fig.(9.3b): Isometric sketch of spectrometer with microscope attachment. The sample compartment lid (necessarily open) has been omitted.

The minimum diameter d to which a parallel beam of light of diameter D can be focused by a lens of focal length f is given by (9.2):

$$d = \frac{4\lambda f}{\pi D} \qquad 9.5$$

where λ is the wavelength of the light. In the present case, the relation becomes:

$$d = 0.62 \frac{f}{D} \qquad 9.5'$$

or $d \sim 3.1\ \mu m$ for the configuration of Fig. 9.3a. The heating effect of a beam of this intensity cannot be neglected, but the expressions for the temperature attained in irradiated spots given in sub-section 8.3.1 cannot be used as they are based upon the heating of a very thin surface layer. Sample damage in the high power densities involved must be considerable, and probably contributes to the difficulties of this method of analysis.

9.3 Raman spectra of glasses

Fundamentally, it must be stated that glass has a Raman signal which is so weak that it is usually entirely neglected. Glass or silica vessels are used universally for containing chemical solutions during analysis, without regard to their influence on the spectra.

In consequence, if a Raman signal is to be seen from glass samples, very high levels of illumination are required, the slits of the spectrometer must be unusually wide (with deleterious effect on the resolution), and low scanning speeds must be used. Figs. 9.4 show the spectra obtained by Simon (9.6) and Hass (9.7) from glasses of different compositions. As the concentration of Na_2O in the glass is increased, the Raman bands at 1100 cm^{-1} and 500 cm^{-1} are easily seen to gain in intensity. The explanation of this is in terms of the stretching vibration of the $Si-O^-$ non-bridging oxygen bonds (9.6) which tend to increase in concentration as the glass matrix is disrupted by network modifiers.

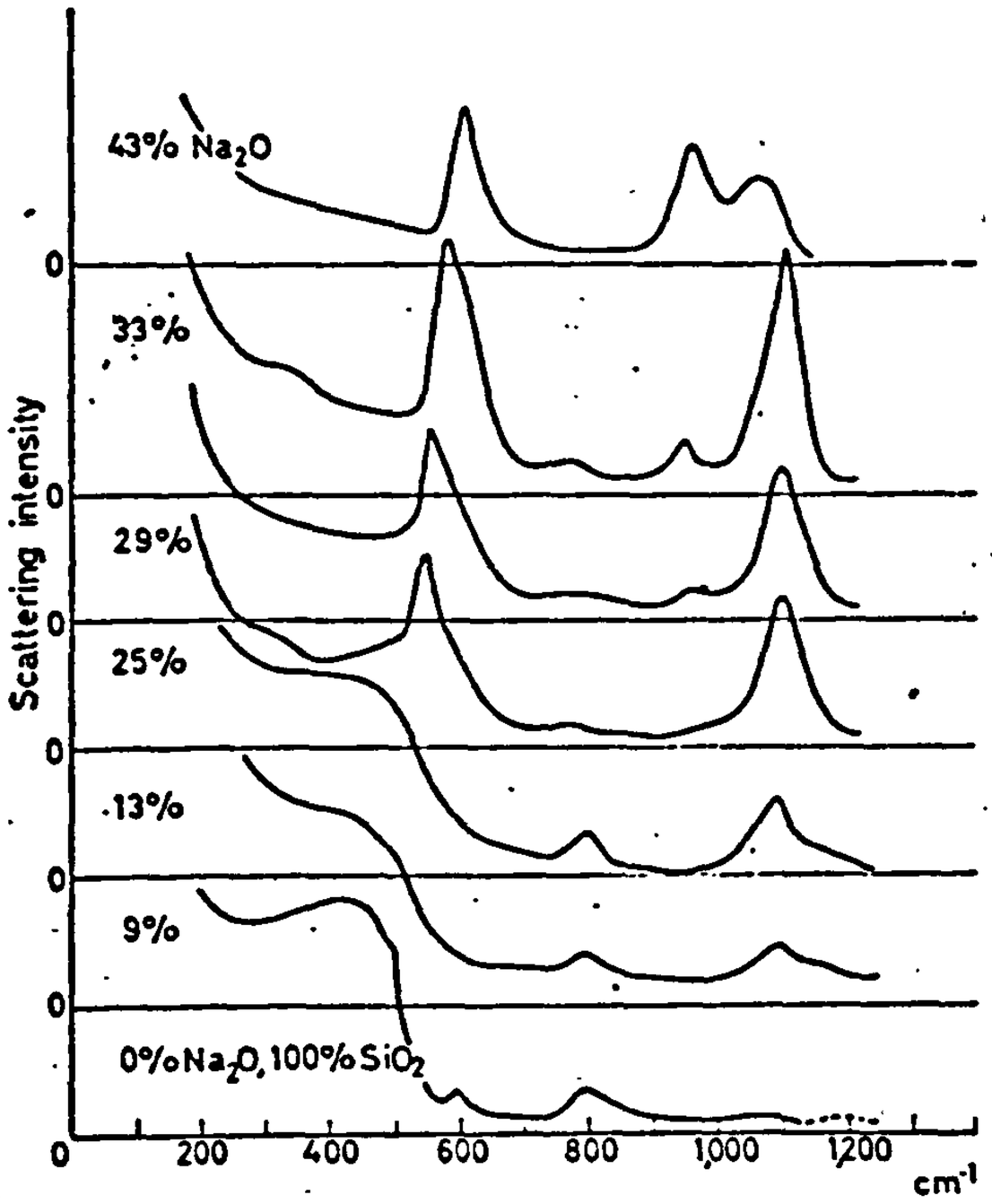

Fig.(9.4a): Raman spectra of soda glasses. Ref.9.6

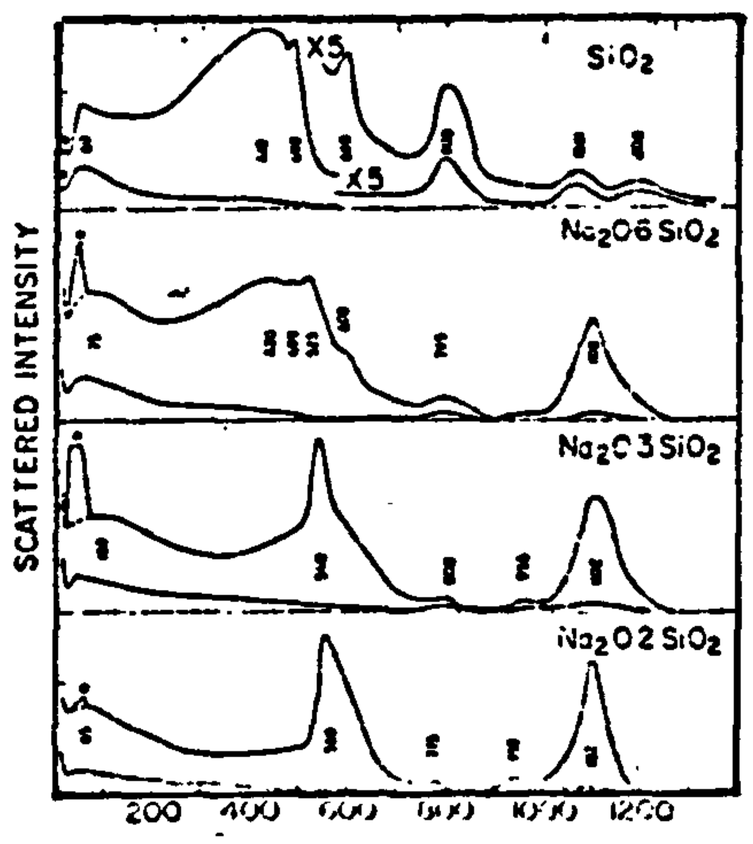

Fig.(9.4b): Raman spectra of soda glasses Ref.9.7

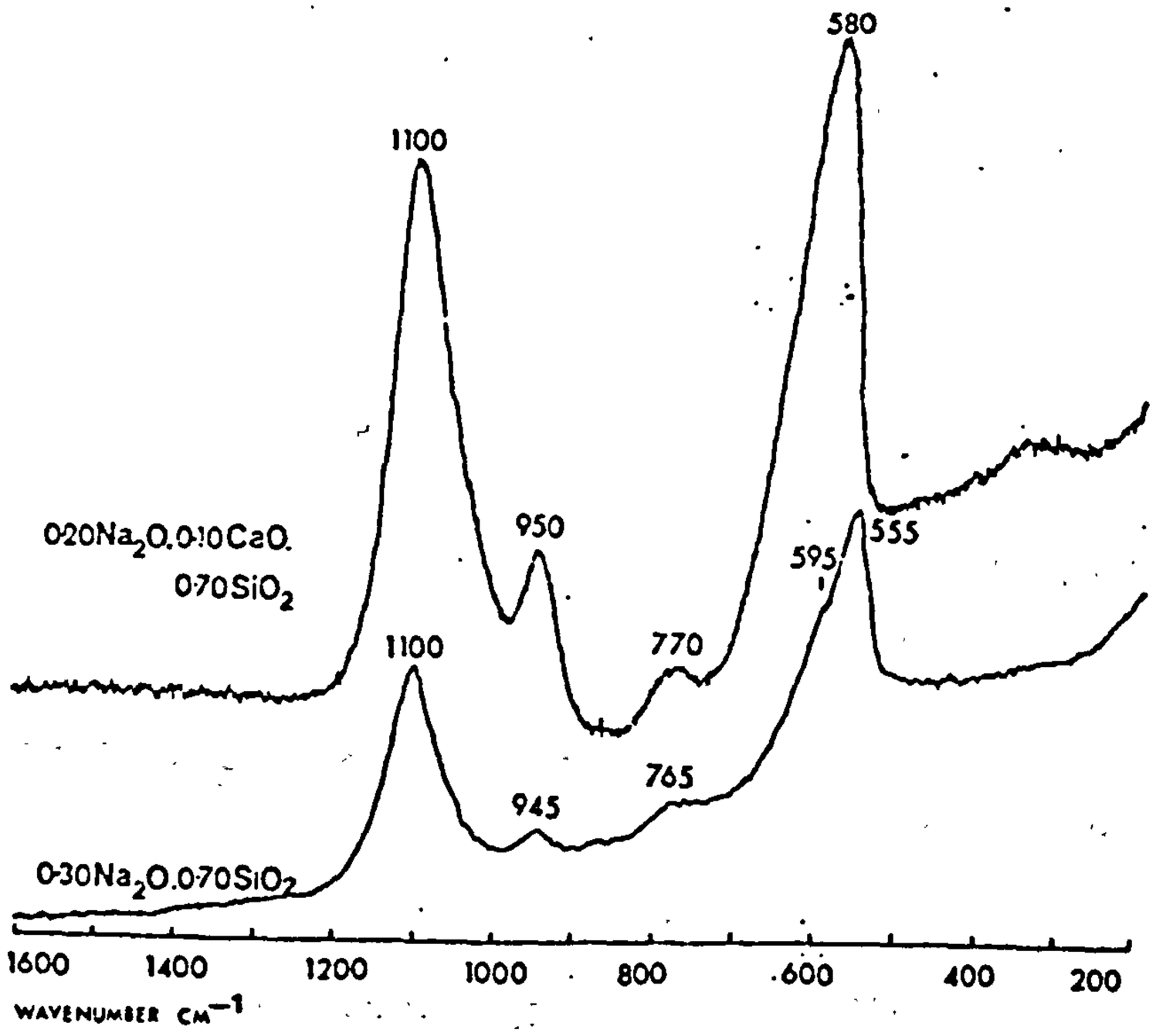

Fig.(9.5a): Raman spectra of silicate glasses

Ref.9.8

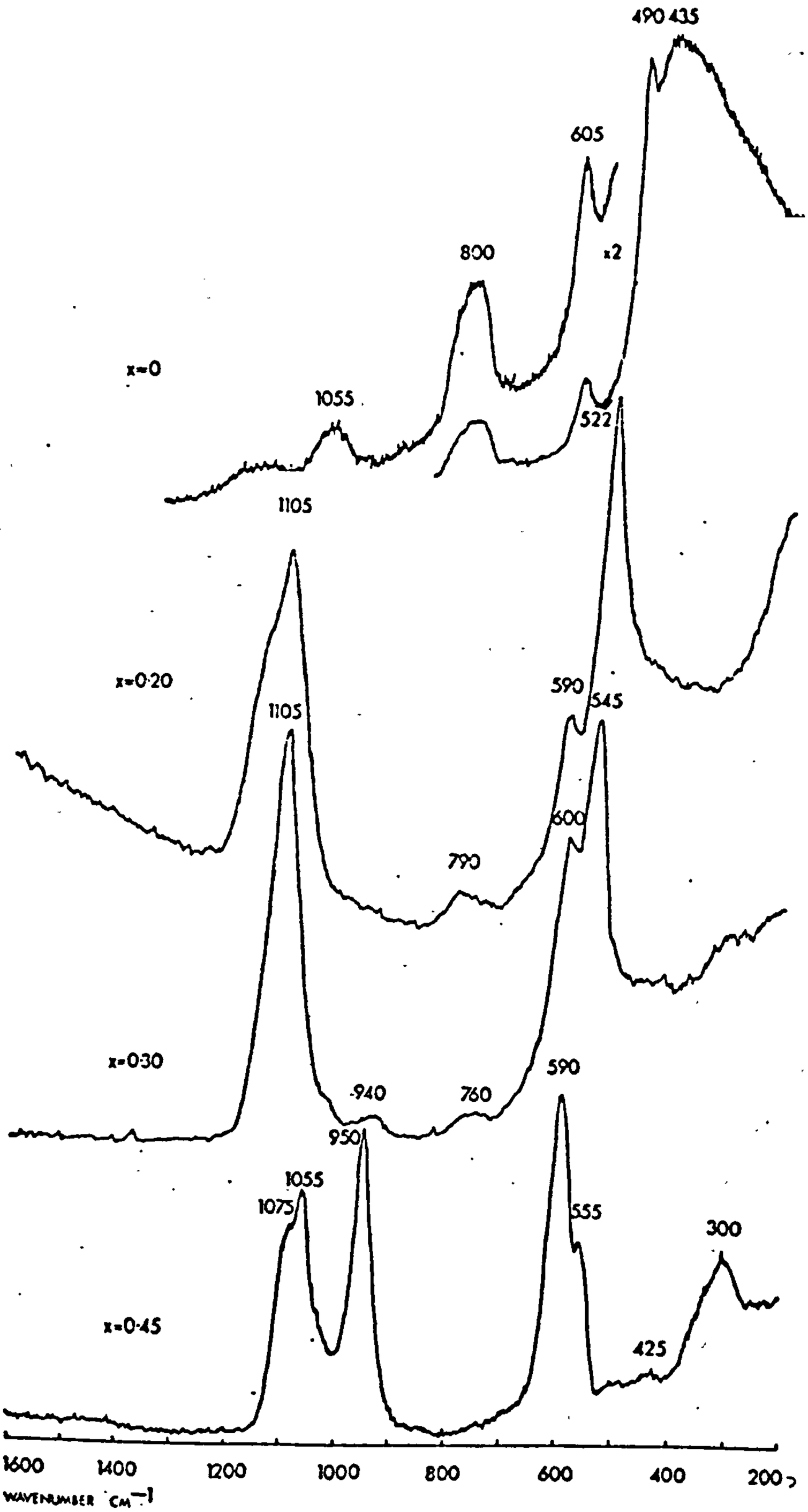

Fig.(9.5b): Raman spectra of silicate glasses in the system $xK_2O.(1-x)SiO_2$. Ref.9.8

The influence of the potassium content of silicate glasses on their Raman spectra has been investigated by Konijnendijt and Stevels (9.8), whose work is Figs. 9.5. In Fig. 9.5b can be seen large differences in intensities according to composition: as the quantity of potash increases, the 100 cm^{-1} band grows sharply and the 800 cm^{-1} band diminishes. At a composition of 30% K_2O, a band at ~ 940 cm^{-1} is seen which, as the potash is further increased, grows so as to overwhelm the 100 cm^{-1} band. At 45 mol% K_2O, a distinct band is found at 300 cm^{-1}. A gradual increase in the frequency of the band at about 500 cm^{-1} is correlated with the increase in the potash concentration. In Fig. 9.5a the effect of replacing 10 mol% of the soda with CaO is shown: the 1100 cm^{-1} band, from non-bridging oxygen bonds, increases very markedly.

The importance of this particular reference is that Konijnendijt and Stevels consider that Raman spectroscopy enables the composition of a glass to be determined to within 5%. Hence, an extension of the technique should provide a means of characterising glass films to the accuracy required to assess their durability.

9.4 Comparison with IR spectra

The complementary technique of infra-red spectroscopy has been used extensively in the past for glass analysis, and good correspondance is found between spectra taken in reflectance and transmittance (9.9). The modes at 1100 cm^{-1} and 500 cm^{-1} are also revealed, but their frequency is seen to depend somewhat upon the sodium content of the glass. Fig. 9.6, from the work of Ferraro and Manghnani (9.10), gives the attributions of the principal IR bands in glasses and indicates that those above 600 cm^{-1} tend to reduce in frequency with increasing soda content, while the frequency of the Si-O-Si bonding mode increases very slightly. Simon (9.6) has complied the published spectra of silica, as shown in Fig. 9.7. The band frequencies in this figure are weighted averages of those in the

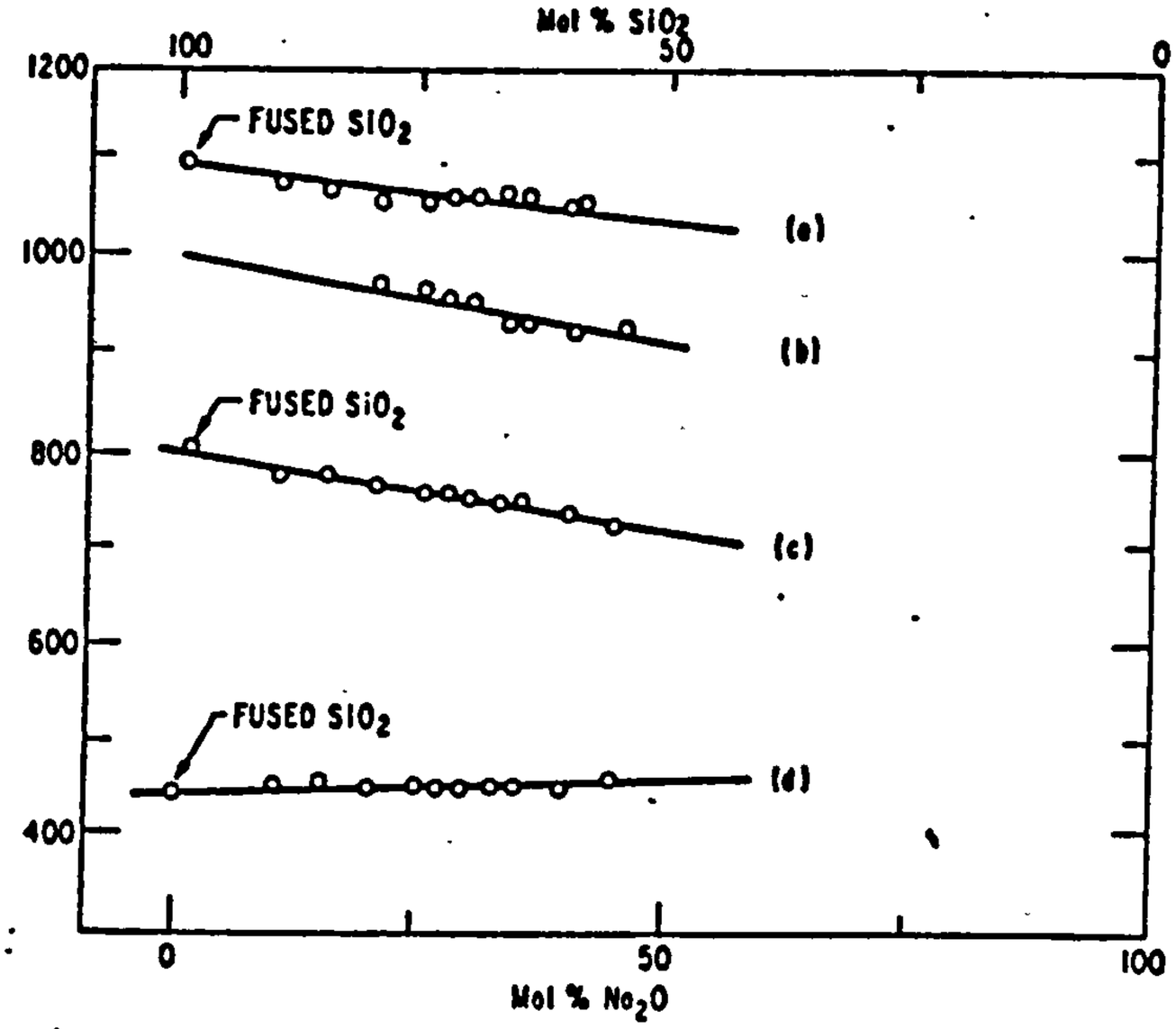

Fig.(9.6): IR Band frequencies versus mol% Na_2O in sodium silicate glasses. (a) Si-O-Si stretching mode; (b) terminal Si-O stretching mode (oxygen nonbridging); (c) O-Si-O bending mode; (d) Si-O-Si bending mode.

Ref.9.10

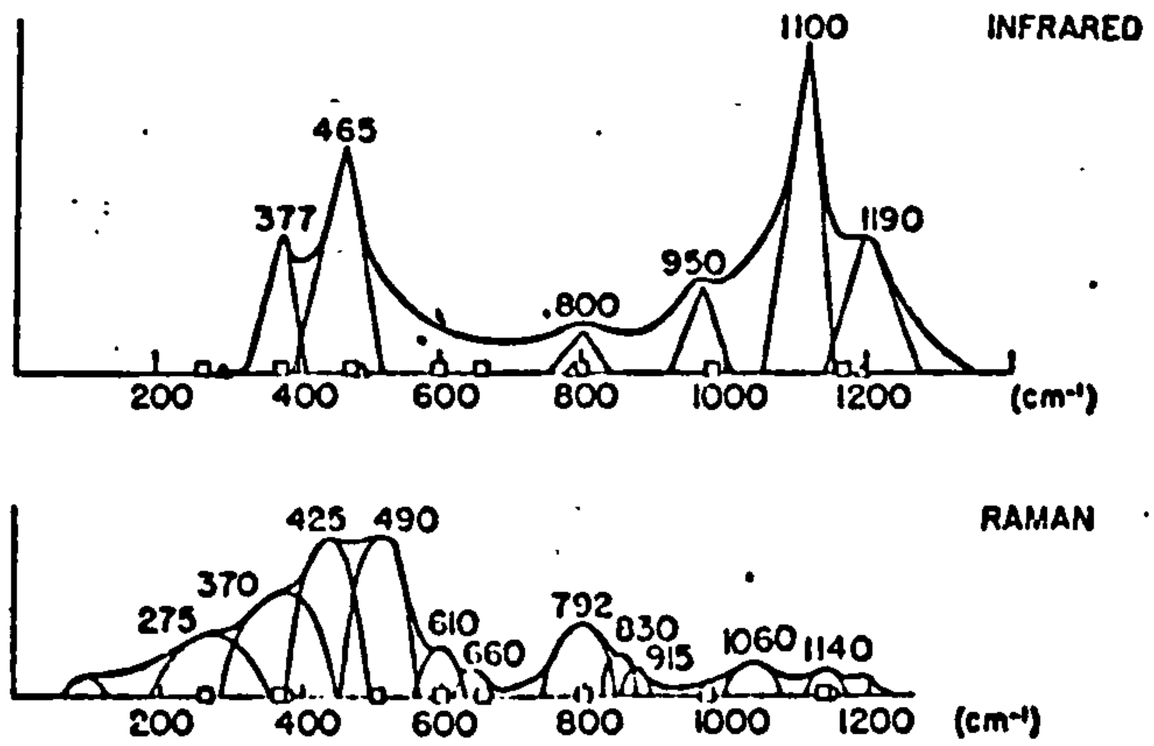

Fig.(9.7): Compilation of spectra from silica

Ref.9.6

literature. Bock and Su (9.11) have attempted to assign symmetry groups to the features of the spectra in Fig. 9.7, but although some success is achieved, the details of the force constants and symmetry obtained are by no means certain and need not be described here.

The work of Pliskin et al (9.12) is singular in its presentation of the IR spectra obtainable from glass films. Traces A and C of Fig. 9.8a show transmittance spectra of a sample consisting of a glass film (809 nm thick) sputter-deposited upon a silicon substrate at about 100°C, before and after annealing in nitrogen. A comparison is made with the spectrum of a film formed by fusing a sedimented powder of the source glass (GSC-1, an alumina borosilicate glass) on to the silicon substrate. Both the 1100 cm^{-1} and the 500 cm^{-1} bands are easily seen and at 1390 cm^{-1}, a new feature occurs (which increases in intensity on annealing the sample) attributed to a B–O stretching mode.

Surprisingly little description of experimental apparatus and technique is provided by Pliskin et al (9.12) in this reference. It is not clear for example whether the substrate possessed a measurable IR signal, and if so whether any alteration is made to it by annealing. Notwithstanding, the results obtained may be used to demonstrate the great similarity in structure between RF-sputter-deposited films and their source materials. Fig. 9.7b indicates the effect of the target surface composition on the spectra of films. Trace C was obtained from a film deposited after a 'run-in' period had been allowed to elapse, and the film is shown to contain an increased concentration of B–O bonds (the 1390 cm^{-1} band) over the films deposited directly from a fire polished glass surface (trace A) and a ground glass surface (trace B). Large differences may be seen in the magnitude of the signal from the B–O bonds, and trace C shows the greatest similarity to the spectra of Fig. 9.7a. This is of course explicable in terms of the approach of the target surface composition to the steady state

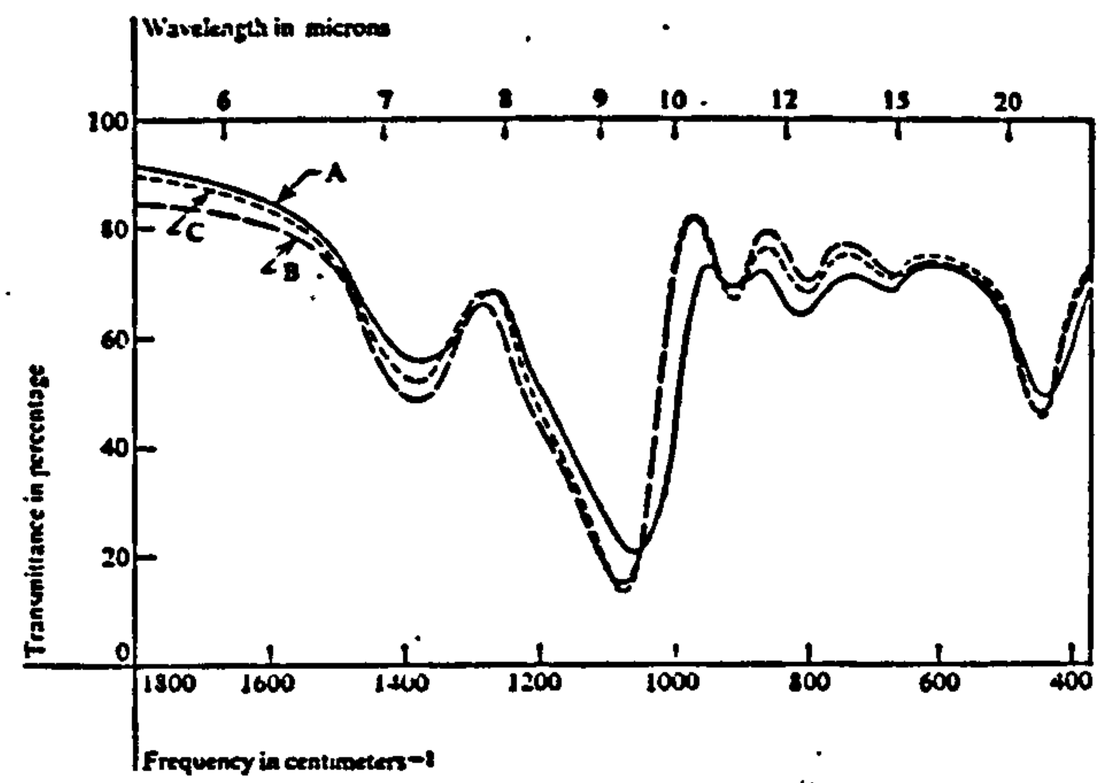

Fig.(9.8a): IR spectra from (A) RF sputter-deposited glass (GSC1) on 100°C silicon substrate, (B) glass film of fused sediment, (C) glass film as in (A) after annealing in N_2 for 5 min at 965°C

Ref.9.12

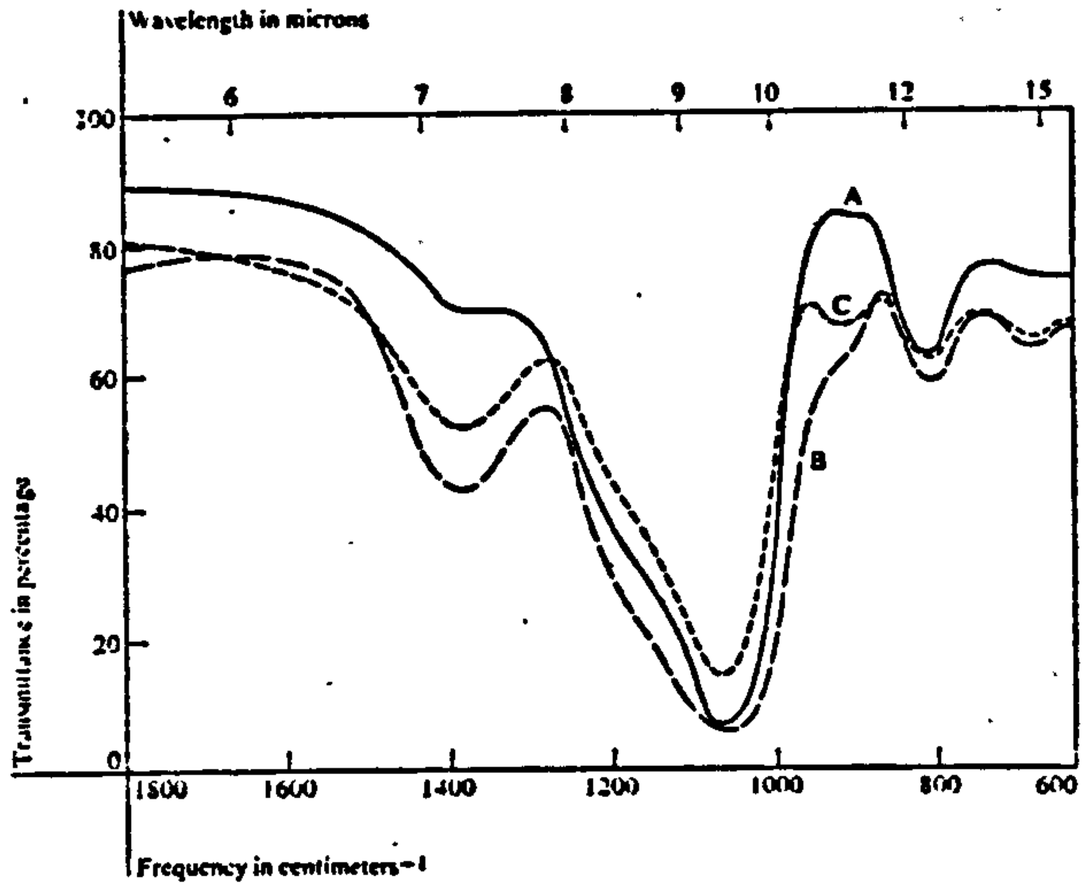

Fig.(9.8b): IR spectra showing effects of target surface removal and 'run-in' time on mixed composition glass films:

(A) Glass film (GSC1) RF sputter-deposited from fire polished GSC1 surface,

(B) film sputtered from same plate after removal of the outer layer of the plate by grinding,

(C) film sputter-deposited from same plate after grinding and 'run-in'period

Ref.9.12

values described in Chapters 3 and 8, and the gradual attainment of stoichiometric sputtered flux.

9.5 Experimental method

The usual practice in Raman spectroscopy is to admit into the spectrometer only the scattered light from the sample. However, the scattered Raman intensity in this case is so small that it was quickly found impossible to achieve the correct alignment of the sample surface with respect to the collection optics. Consequently, the spectrally reflected beam was directed into the entrance slit and the sample position was adjusted to maximise the photon count at $\Delta\mu \sim 400$ cm^{-1}. Damage to the photon detector will occur using this technique if the spectrometer passes the primary frequency; in this case the approach was limited to $\Delta\mu \sim 200$ cm^{-1}.

It is presupposed that the spectrum contains a 400 cm^{-1} band, which is not necessarily the case when analysing films. The difficulties experienced in obtaining spectra from films might be attributed to this fact. The laser line, the scanning speed and the number of scans will be indicated on each spectrum presented below. No recommendations will be made regarding these parameters, the channel dwell time or the slit widths which depend largely upon the resolution required, the signal intensity and the time available. All four slits were opened to the same width, following the usual practice, to give resolutions of 5 - 10 cm^{-1} (3 - 5 channels).

9.6 Results

Raman spectra obtained from a sample of ordinary silica plate using the configuration of Fig. 9.3a are shown in Figs 9.9. The 800 and 600 cm^{-1} peaks (9.6, 9.7) may be distinguished, and there is evidence of a small feature at 1050 cm^{-1}. The spectra are generally similar to those shown in Figs. 9.4 for glasses with zero soda content, except for the very great variability below about 450 cm^{-1}. This poor reproducibility is

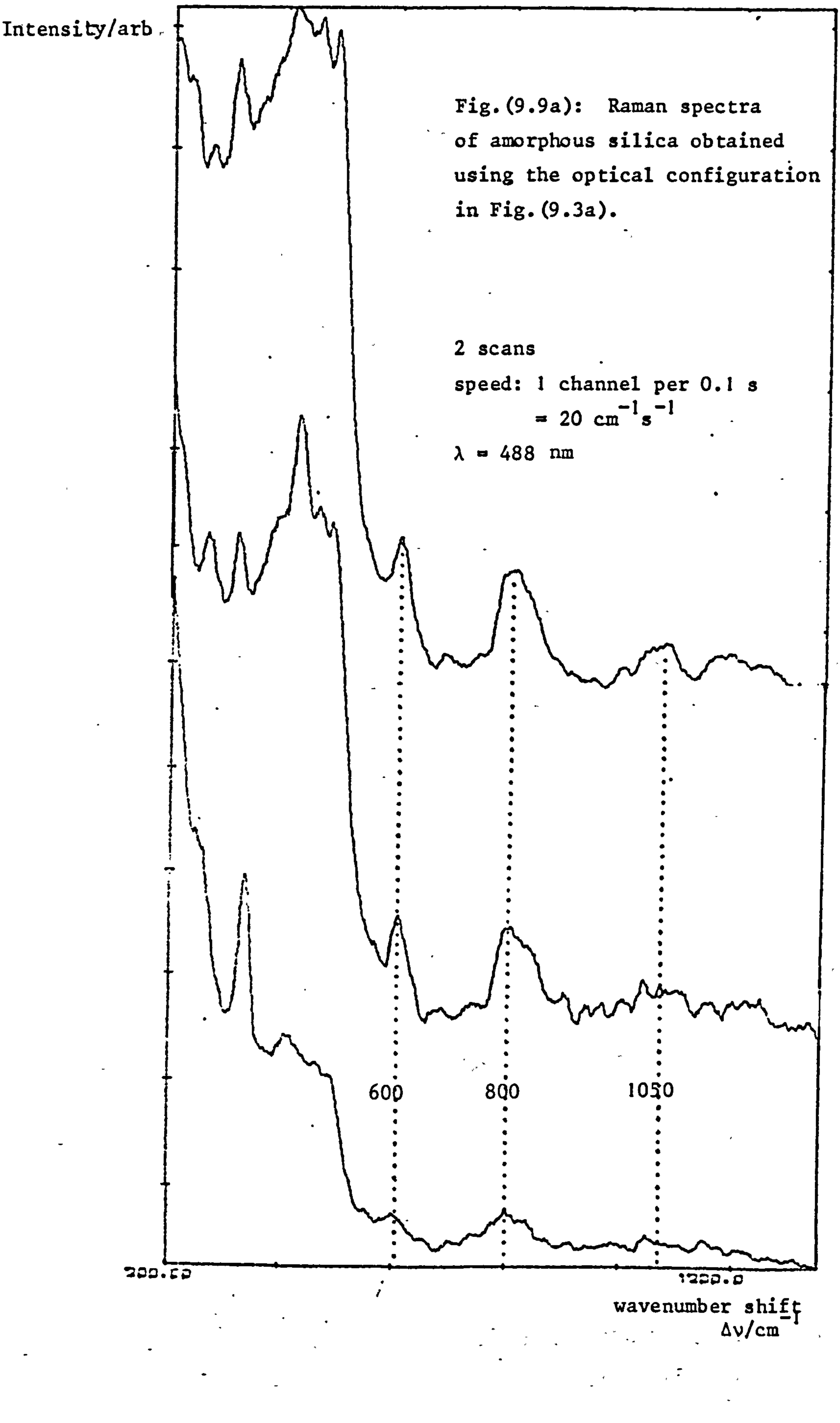

Fig.(9.9a): Raman spectra of amorphous silica obtained using the optical configuration in Fig.(9.3a).

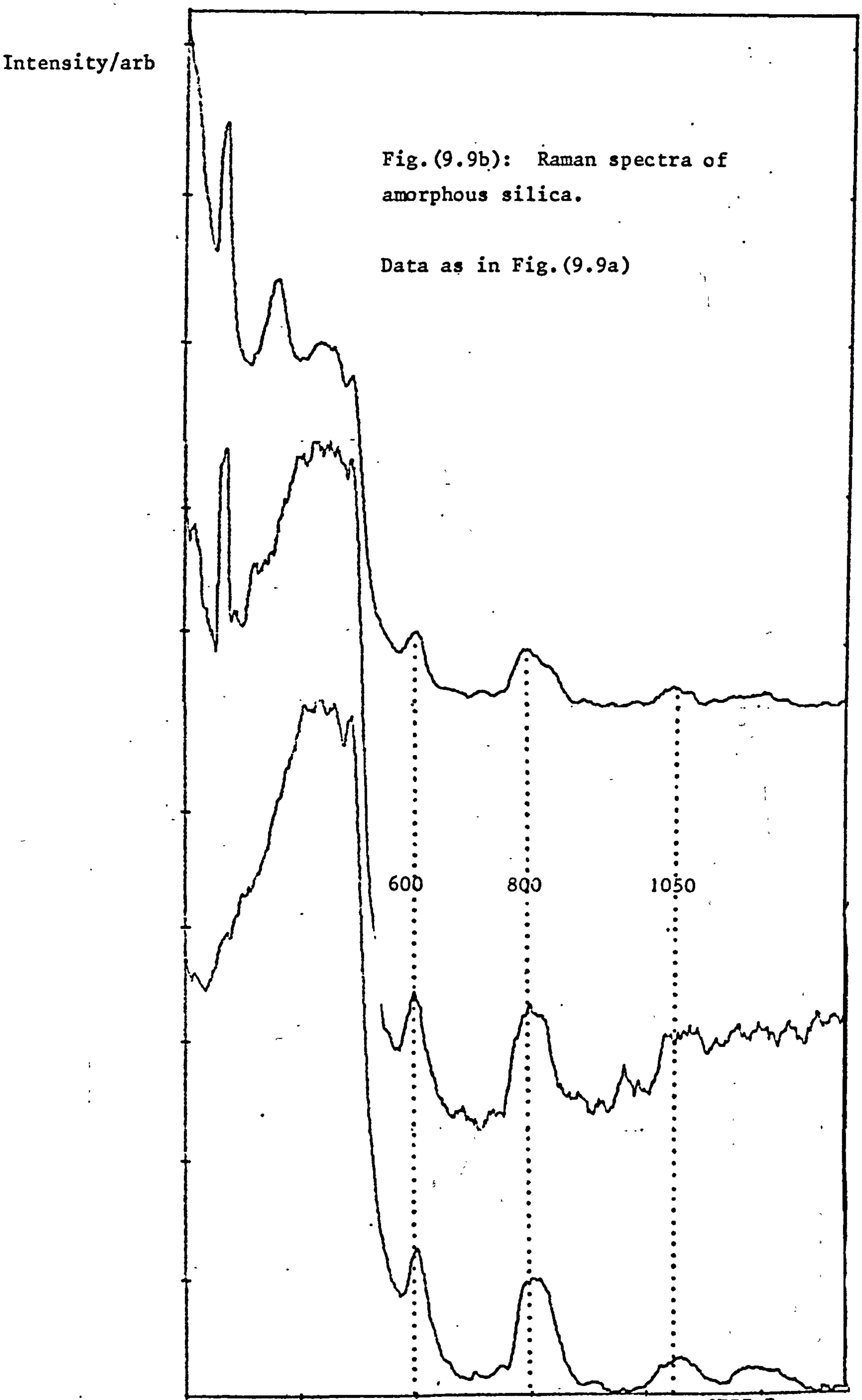

Fig.(9.9b): Raman spectra of amorphous silica.

Data as in Fig.(9.9a)

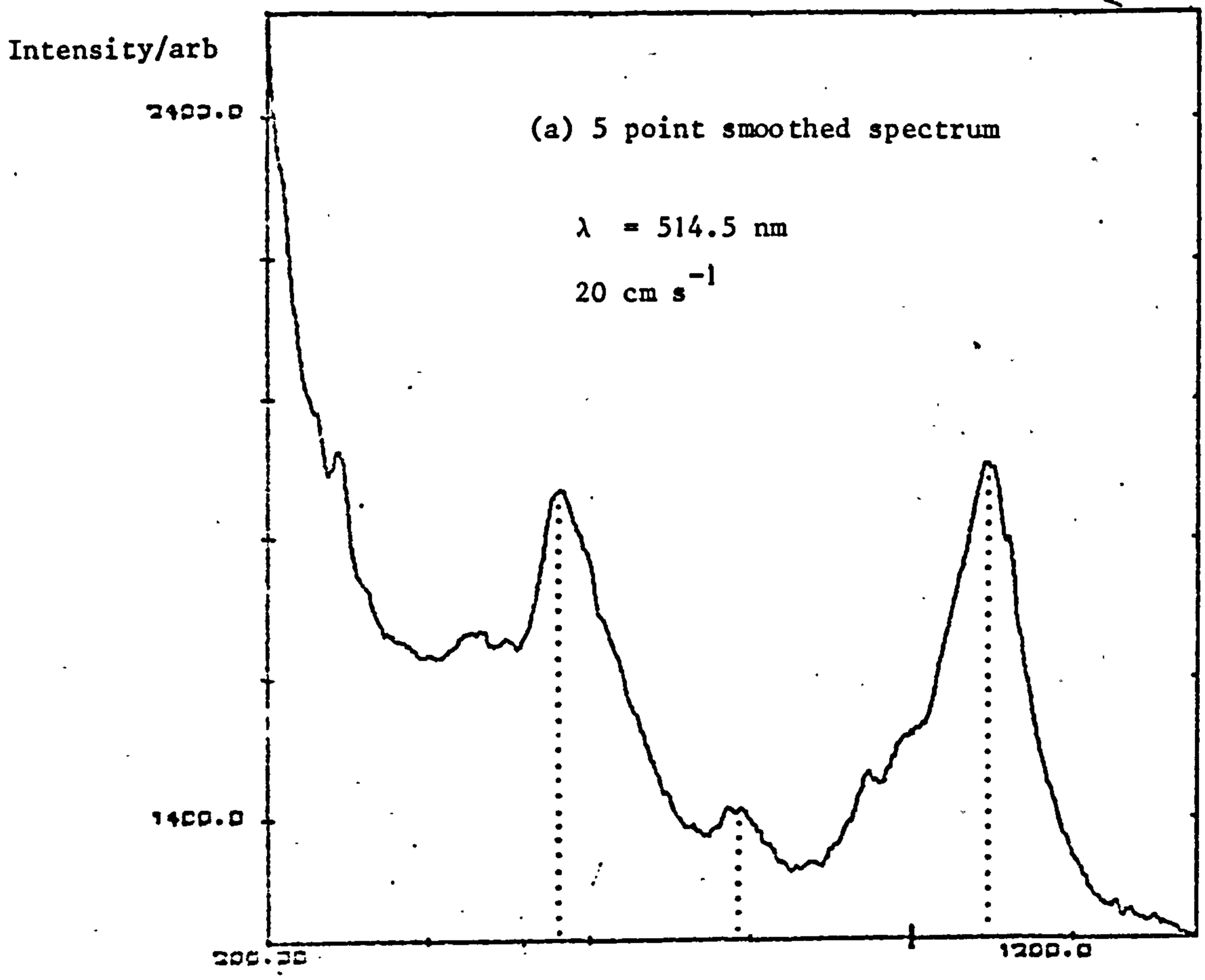

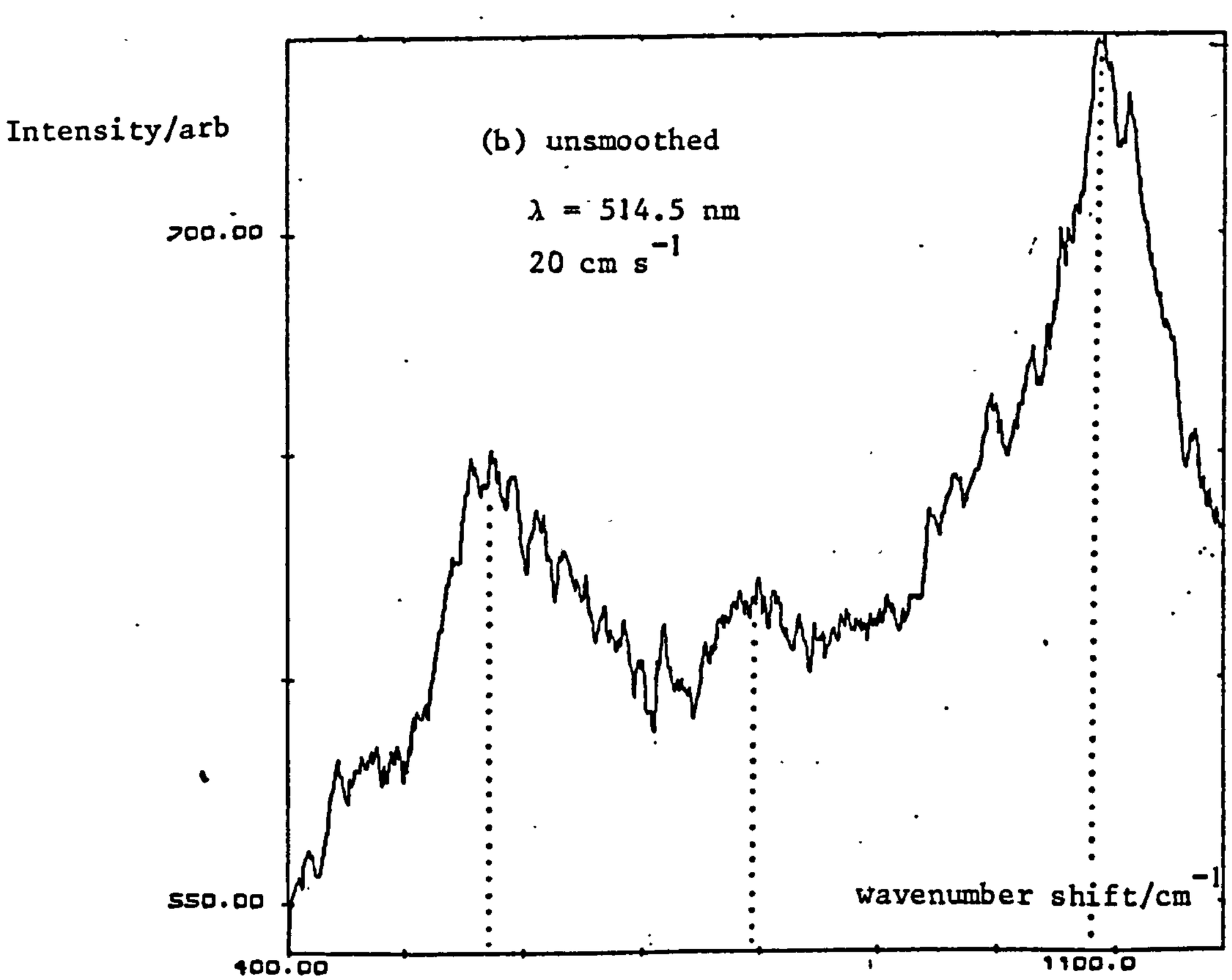

Fig.(9.10): Raman spectra of window glass

probably due to inhomogeneities in the sample, although it is not clear why the higher region should be less affected. It has been mentioned that no improvement in signal to noise ratio would be expected by making use of the microscope optics of Fig. 9.3b; indeed, the spectra obtained from this silica sample were very similar to those shown in Fig. 9.9 but with reproducibility reduced still further because of the greater effect of impurities on a smaller analysed volume. The microscope facility was eschewed for this reason.

Figs. 9.10 show spectra obtained from an irregularly shaped sample fractured from a 10 mm thick window glass plate. The characteristic peaks of glass at 500 cm^{-1} and 1100 cm^{-1} dominate the spectrum; their relative sizes are somewhat similar to those of the 30% K_2O sample in Fig. 9.5b, but the correlation is not close. The exact frequency of the band close to 800 cm^{-1} (768 cm^{-1} from Fig. 9.10a) may be used, in conjunction with Fig. 9.6 to yield a soda concentration of ~10%. It is to be regretted that time did not permit an analysis of the composition of this glass by another method, but a composition of $0.3K_2O \cdot 0.1Na_2O \cdot 0.6SiO_2$ would not be exceptional in an ordinary modern window glass of this kind.

The dramatic change in the Raman spectrum caused by the introduction of non-bridging oxygen bonds ($\Delta\nu$~1100 cm^{-1}) to an amorphous silicon lattice is shown in Fig. 9.11, where traces from Figs. 9.9 and 9.10 are redrawn for easier comparison. The silica spectrum in this figure (which is the middle one of Fig. 9.9a) was obtained using the microscope.

9.7 Examination of glass films

9.7.1 Results

Using the method described above, samples of nominally identical materials yield Raman spectra with large differences; even consecutive scans of the same sample are not always similar. Considering the case of a

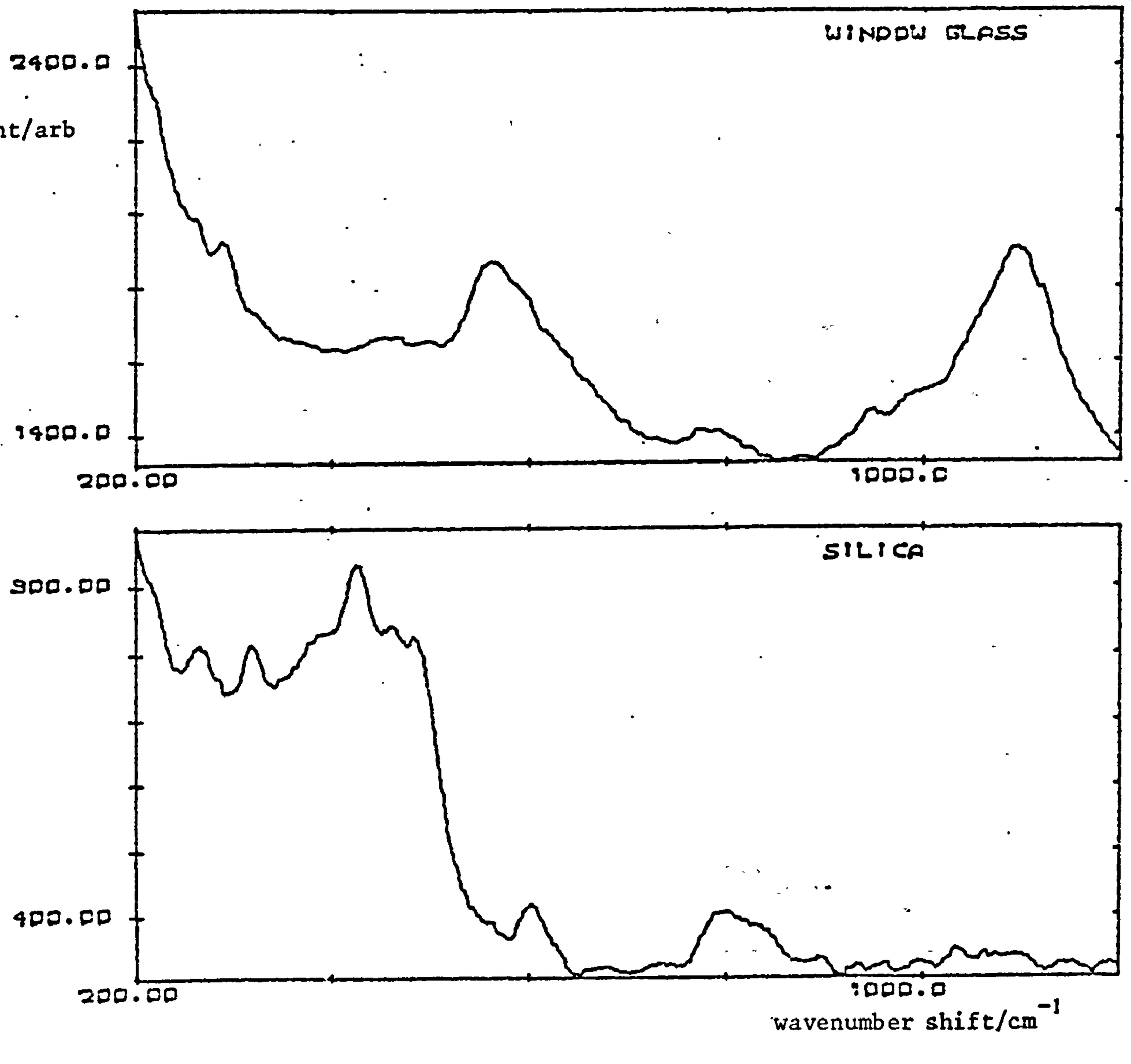

Fig.(9.11): Raman spectra of silica and glass (taken from previous two figures)

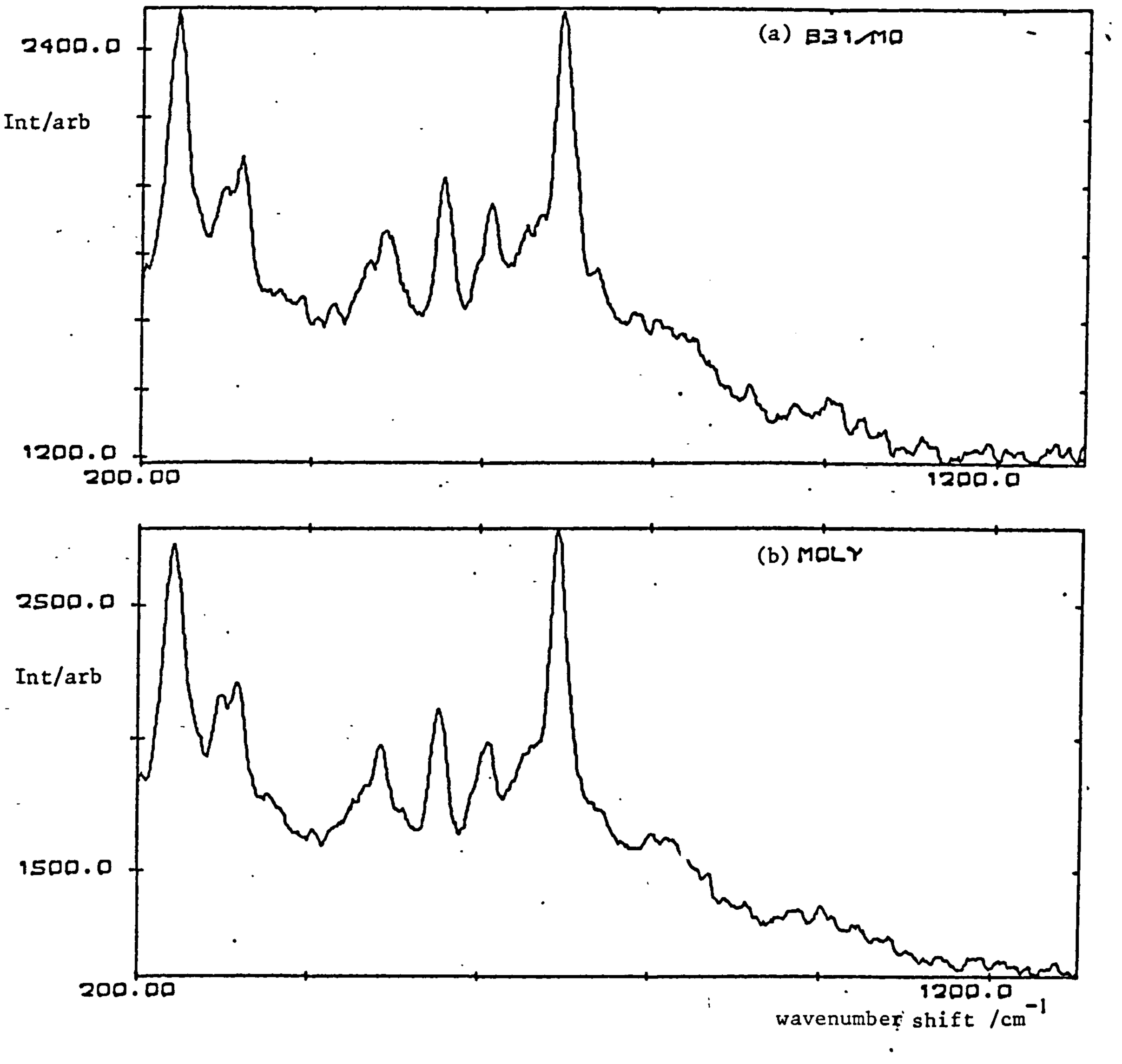

Fig.(9.12): Raman spectra obtained from a molybdenum sample
(a) coated with a 500 Å glass film B31, and
(b) uncoated.
λ = 488 nm, speed: 10 cm^{-1} s^{-1}

transparent sample coated with a film, we can see immediately that since the sample volume is completely dominated by the substrate (even for 'thick' films of 1000Å), it will be difficult to identify spectral features originating in the film. No consistently observable differences were found between the spectra of silica slides coated with soda glass and those obtained from uncoated specimens.

In an attempt to obviate the problem, films deposited upon metal substrates were examined. The spectrum shown in Fig. 9.12a is from a molybdenum sheet coated with a ternary glass film. The direct method was used; no success whatever was achieved with the microscope. It is probable that the structure to be seen in both this and Fig. 9.12b (of the substrate) is spurious. In addition to the primary line, small amounts of power are emitted from the laser at several discrete frequencies known as 'plasma lines'. Since to obtain these spectra the spectrometer slits needed to be opened to 1000 μm, it is probable that unwanted plasma lines were admitted. In any case, it is clear that no differences in the spectra are to be seen; the film cannot be observed.

9.7.2 Guided wave method

An interesting method of obtaining Raman spectra from thin films has been developed recently by Rabolt et al (9.13). In this work, the primary laser light is coupled to a polymer film by a prism and enters it at an angle to the surface greater than the critical, as shown in Fig. 9.13. The beam is internally reflected from each interface and continues to travel in the film suffering as many as 100 reflections each millimeter (the exact number depending upon the mode of the wave). The Raman light is emitted isotropically, and passes through the film surface to be collected by a lens and focused into the spectrometer.

This method has been shown to be successful for polymer films of

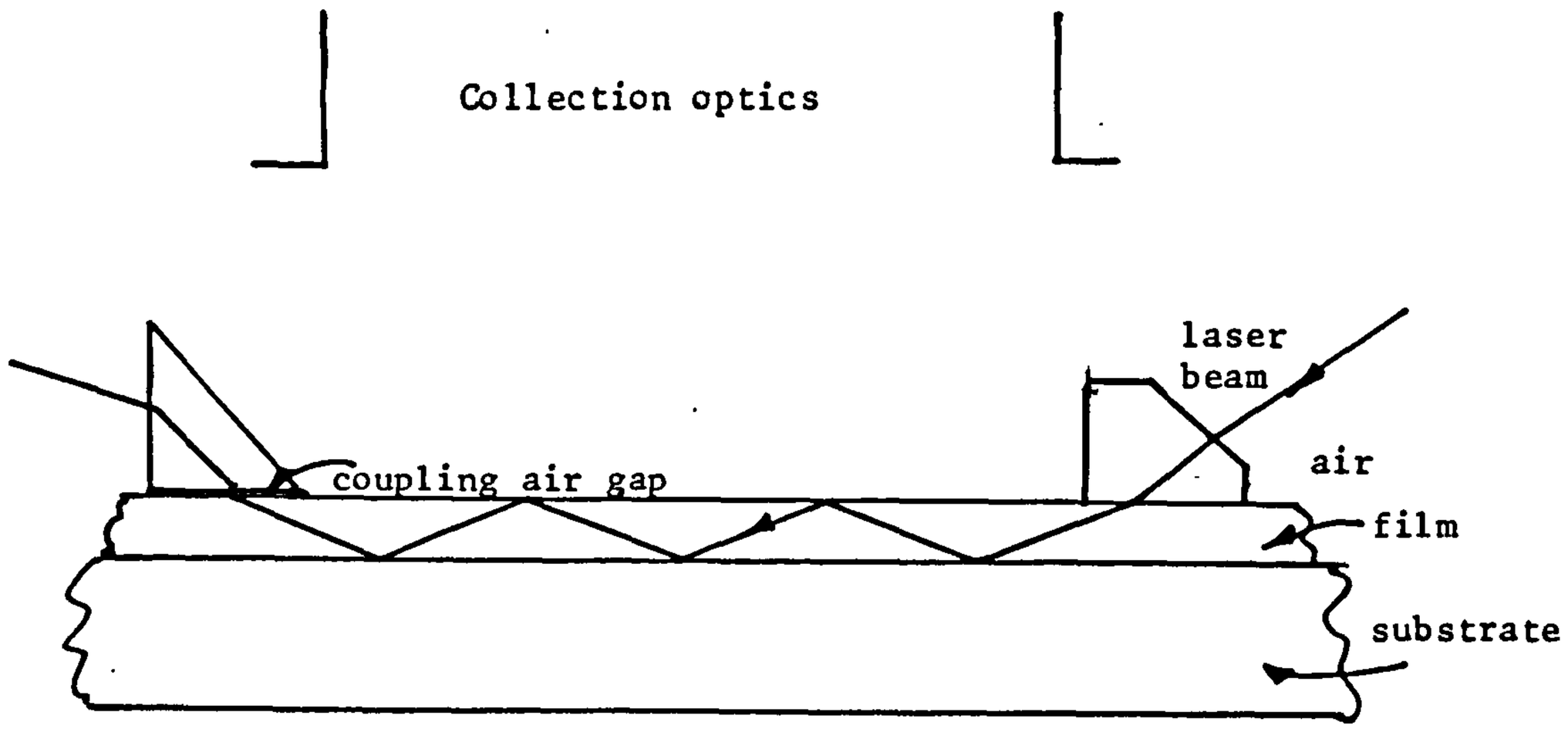

Fig.(9.13): Guided wave method. Ref.9.13

a few micrometers in thickness, increasing the signal to noise ratio by as much as two orders of magnitude. Whether or not it might have been adapted for use in the analysis of much thinner films made from glass, time did not permit us to discover. It is a promising avenue of approach.

9.8 Summary

A classical derivation of the Raman effect has been provided, and the type of experimental equipment used for Raman spectroscopy has been described. The very small literature on the Raman spectra of glasses has been reviewed exhaustively, and spectra have been obtained from both silica and bulk glass that bear great similarity to those obtained by other workers.

Unfortunately, the reproducibility was not such as to enable this experimental technique to be recommended for glass analysis, although the Raman effect itself might be utilized in the characterization of films provided that the sample volume can be increased. The guided wave method of Rabolt et al (9.13) shows great potential in this respect.

Infra-red spectroscopy can clearly provide complementary information on the chemical bonding of glass, and the literature is larger and more detailed than for Raman spectroscopy. The IR spectra of glasses are more fully understood. Hence, future workers in this field would benefit from studying also the infra-red spectra of the glass films, particularly in reflectance, in addition to their Raman spectra as described above.

CHAPTER 10

CONCLUSIONS AND FUTURE WORK

In this brief final chapter are set out the conclusions that may be drawn from the wide-ranging work described in the present volume. Each chapter is summarized in its final section, but to provide a basis for a short discussion of possible future work in this field it is convenient to recapitulate the principal results.

10.1 Conclusions

In Chapter 1, which predominantly reviews the nature of aqueous attack of glass, it is found that a composition may be calculated which would provide a glass with high durability and also a high thermal expansivity. Such glasses are shown to be appropriate for use as the source material for durable films on ancient glasses.

Chapter 2 shows in purely theoretical terms how argon ion sputtering of materials takes place, and in Chapter 3, the method is applied to glass. Many approximations are made in the rather complex manipulation inevitable in collision cascade theory, and in some cases their effects on the accuracy of the final results are not completely assessable. However, the sputtering yield prediction (S(2keV) = 1.2) is shown to be accurate to better than an order of magnitude by the experimental results of Chapter 8, and to a lesser extent by those of Chapter 6. Also, Chapters 2 and 3 demonstrate the extremely superficial provenance of the sputtered flux, and that the flux is expected to achieve a stoichiometry identical with that of the target or 'source glass'. Hence, sputter-deposition should be intrinsically superior, in terms of reproducibility and reliability, to evaporation techniques (10.1, 10.2, 10.3), which can be prone to differential fractionation problems. Recent work (10.4) has implied, however, that glass can be successfully electron-beam evaporated. This technique is of great interest because of its very high deposition rates, and should be investigated, but

it is doubtful whether the composition specification for film durability can be met sufficiently closely.

Chapters 4 and 5 (and ref. 4.36) supply criteria by which an RF sputtering plant may successfully be constructed. No special techniques are found necessary in welding or machining (Chapter 4), but care must be taken at the design stage of the field coils. By the correct choice of winding wire gauge it is seen that the coils may be wound quickly and inexpensively to provide magnetic fields of the strength, and over volumes, appropriate to sputtering plants.

RF power matching methods are discussed in Chapter 5, for both the balanced electrode and the single-ended systems. A matching technique is suggested for the balanced mode, but it is concluded that more power may be transmitted to the sputtering plasma in the single ended case. The modified Hartley oscillator design of Fig. 5.7 emerged successful from trials of various RF power circuits. The extent of modification necessary to increase its output power is a subject for future study.

Three points are clear from the discussion of plant performance in Chapter 6. First, the deposition rates were lower than those achieved by other workers, for reasons adumbrated in subsection 6.7.3. This prevents the assessment of the economic viability of the process. Second, the problem of glass shattering was found to be severe for the disc and annulus system, but less so for the single-ended mode. Overall, indeed, the single-ended diode method is shown to be more successful for sputtering glass targets. Deposition rates were limited principally by target vulnerability and the breaking down of the tuning capacitor air gap. Third, the bias sputtering facility of the laboratory apparatus is as yet untried. The impedance matching problems attaching to coupling RF power to the substrate table are formidable, but film adherence and homogeneity are reported to be improved under bias conditions (4.20), and these are vital qualities for

durability. Thus, investigating bias sputtering effects is a priority on the film deposition side.

10.2 Future work

The most important front for future work is in analysing the films. The results obtained from electron beam spectroscopy (Chapter 8) are confined to qualitative aspects of electron bombardment of glasses. The hypothesis is made that a high electric field is induced by the creation of charge centres in the bombarded volume of the glass. Alkali ions (particularly sodium) are caused to migrate out of the analysed volume under the influence of the field. Their motion explains the time-dependent reduction in their Auger intensities, and from the increasing symmetry of the peaks themselves it is argued that the damage centres must be positive in sign. The migration of the analysed sodium ions in glass is hence towards, and through, the surface.

Electron energy loss spectroscopy is found to be no more quantitative; its results are even more sensitive to the state of the extreme surface than those of AES. It is shown that electron spectroscopy inevitably samples an unrepresentative surface because the removal of the obstructive surface carbon layer (by ion bombardment) in itself alters the surface composition. Calcium and silicon atoms are shown to sputter from glass in the approximate ratio 1 : 1.3.

10.2.1 Spectroscopy

Chapter 9, however, contains the seeds of the most promising methods of analysing deposited films. The internally reflected wave technique of Rabolt et al (9.13) has great potential if the problem of coupling the laser beam into a glass film proves surmountable. The film probably would need to be of increased thickness, which is contingent on increased deposition rates being achievable and on the improved reliability

of the sputtering plant itself. These are not remote possibilities. Also, the infra-red techniques used by Pliskin et al (9.12) should be closely investigated as IR spectroscopy has much to recommend it in the study of glasses (9.9).

X-ray fluorescence could also be attempted. A brief exploratory trial was performed during the project in an attempt to quantify the sodium content of a glass film on silica. Electron beam stimulated XRF (10.6) was employed and signals from all the components of the film were identified, but no meaningful data could be obtained. 'Matrix effects' in glasses, or the influence of the surrounding atoms upon the recorded intensities of X-ray emissions, have been investigated extensively by Cox and Pollard (1.15,1.16) during the first stages of the project at York. This work would need profound modification for use in the quantitative analysis of thin films, because the X-ray penetration depth is too great to permit the effect of the substrate to be neglected, and the sample has previously been considered homogeneous. Molybdenum was used as a substrate (Fig. 9.12) because of its few XRF bands in the region of interest.

Another potentially very useful technique is X-ray induced electron spectroscopy (or 'ESCA'), whose advantages include a large sampling volume to average the inhomogeneities of composition,combined with a failure to cause sample damage. It is as surface sensitive as AES.

10.2.2 Deposition

The methods by which the sputtering plant might be improved have been indicated in Chapter 6. An increased deposition is the aim, and greater power to the plasma is the means, but extensive modifications to the rig are probably a requirement. Attention is better concentrated on the single-ended arrangement, because the target shattering problem remains

unsolved, indeed, unexplained. A simple investigation of whether thick glass targets shatter more or less readily than thin ones could form very useful work.

10.2.3 Weathering

The recent work in Austria by Kny and Nauer (10.5) has shown that 80 nm sputter deposited tetra-ethyl tin coatings can withstand harsh artificial weathering conditions better than their simulated Mediaeval glass substrates. The assessment of durability was made primarily by microscopy, and the films were shown to have corroded far less severely than the glasses. The reasons for the choice of tetra-ethyl tin ('organotin') as a material are not specified in the reference.

Immediately a satisfactory analytical technique is evolved, it is necessary that the artificial weathering unit (Appendix II) be used to determine the durability of films of various thicknesses deposited under a range of pressures, electrode voltages, powers and temperatures.

10.3 Summary

The possibilities for research in this field are limited only by time, money and imagination. The hope of the author is that, if only in a negative manner, the work contained in this volume will be of assistance to those people scattered worldwide actively concerned with ameliorating the decay of our beautiful and irreplaceable stained glass windows.

APPENDIX I

Model of glass corrosion

The model due to Hlavac (1.11) is presented.

The process is considered in two parts, in which

(1) glass cations are exchanged for H_3O^+ by diffusion through the leached layer, and

(2) the leached layer is dissolved by surface reaction.

The approximations made are that there is (a) a linear concentration gradient in the leached layer, (b) a constant rate of erosion of the leached layer, (c) a planar interface and (d) a single alkali component in the glass

The notation is as follows: Q, the quantity of alkali extracted; A, the area of reaction; D, the diffusion coefficient; C_o, the original concentration; x, the thickness of the layer; and B, the rate of reaction expressed as a velocity of progress of the interface into the glass.

The total amount of alkali extracted after a time t is written

$$Q(t) = AC_o(x(t)/2 + Bt)$$

thus
$$\frac{dQ}{dt} = AC_o(\tfrac{1}{2} \frac{dx}{dt} + B)$$

but also
$$\frac{dQ}{dt} = \frac{ADC_o}{x} \text{ , by the definition of D and approximation (a).}$$

So that
$$\frac{dx}{dt} = 2(D/x - B)$$

$$\tfrac{1}{2} \int \frac{x\ dx}{D - Bx} = \int dt$$

and
$$t + c = \frac{1}{2B^2} \left\{(D-Bx) - D\ \ln(D-Bx)\right\}$$

The constant of integration c is given as $(D-D\ln D)/2B^2$ by x=0 at t=0, which yields

$$t = \frac{D}{2B^2} \ln\left(\frac{1}{1 - Bx/D}\right) - \frac{x}{2B}$$

and expressing t in units of D/B^2 and x in units of D/B we have the form shown in Fig.1.6

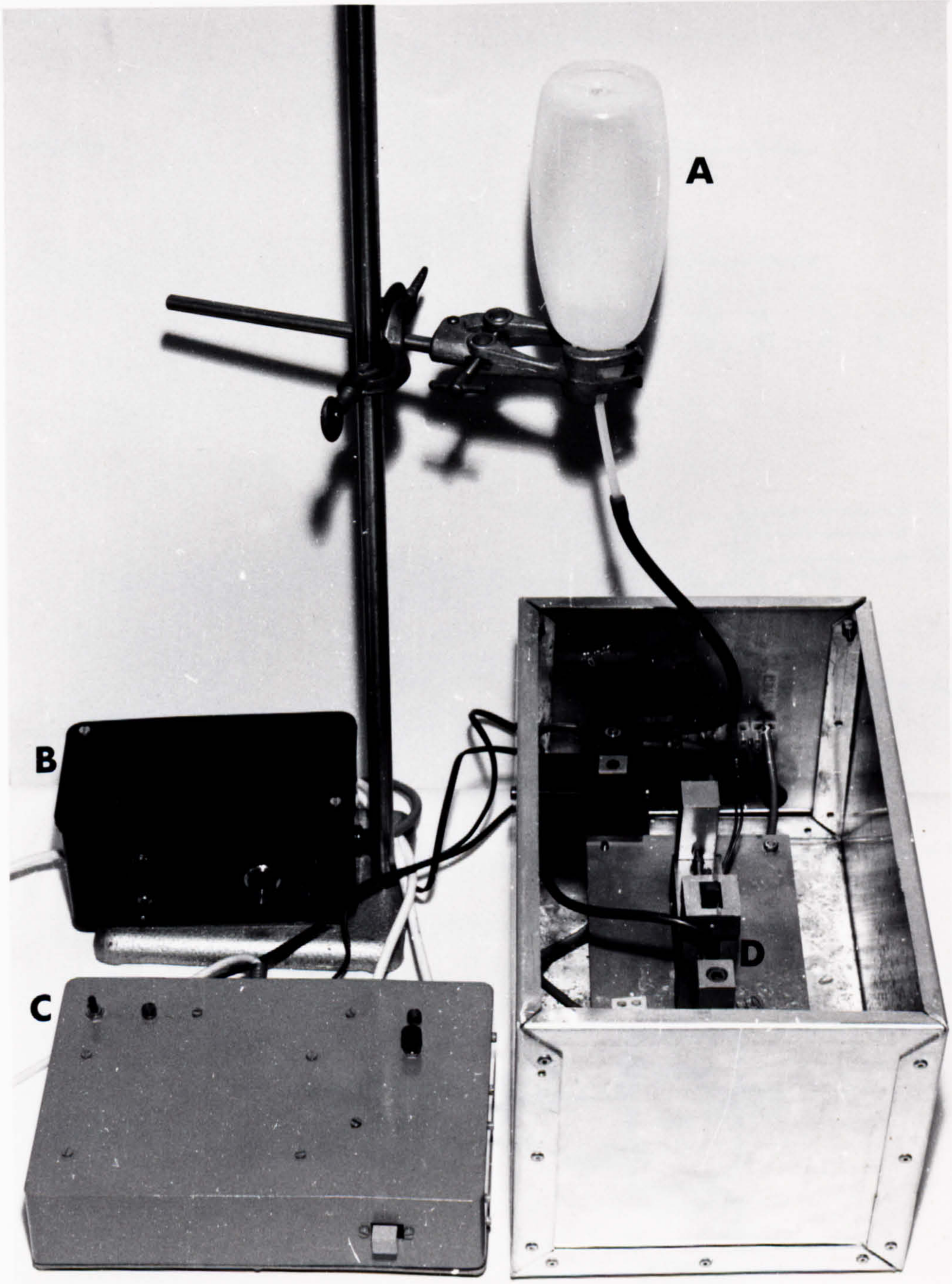

Fig.(1.10): Artificial weatering unit

A: Dionised water supply

B: 12 V power supply

C: Controller

D: Sample

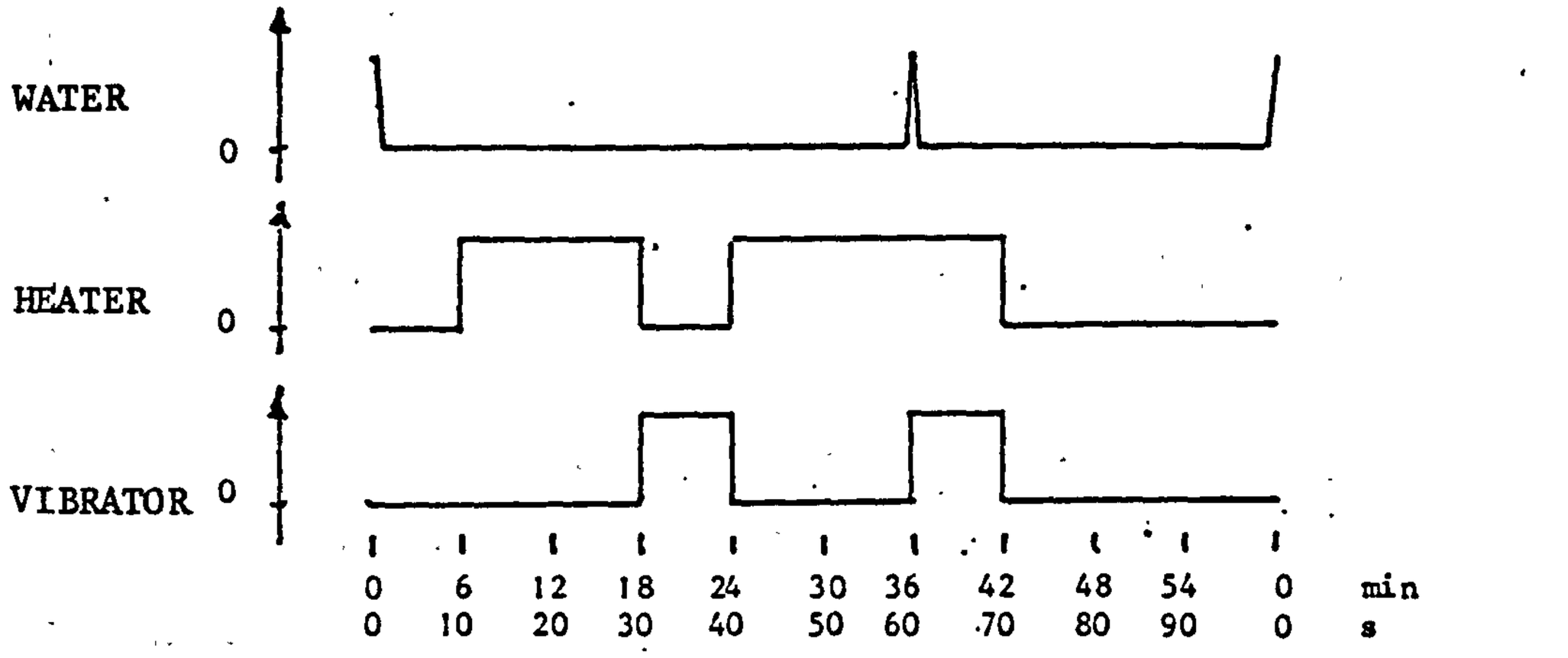

Fig.(1.11a): Weathering cycle

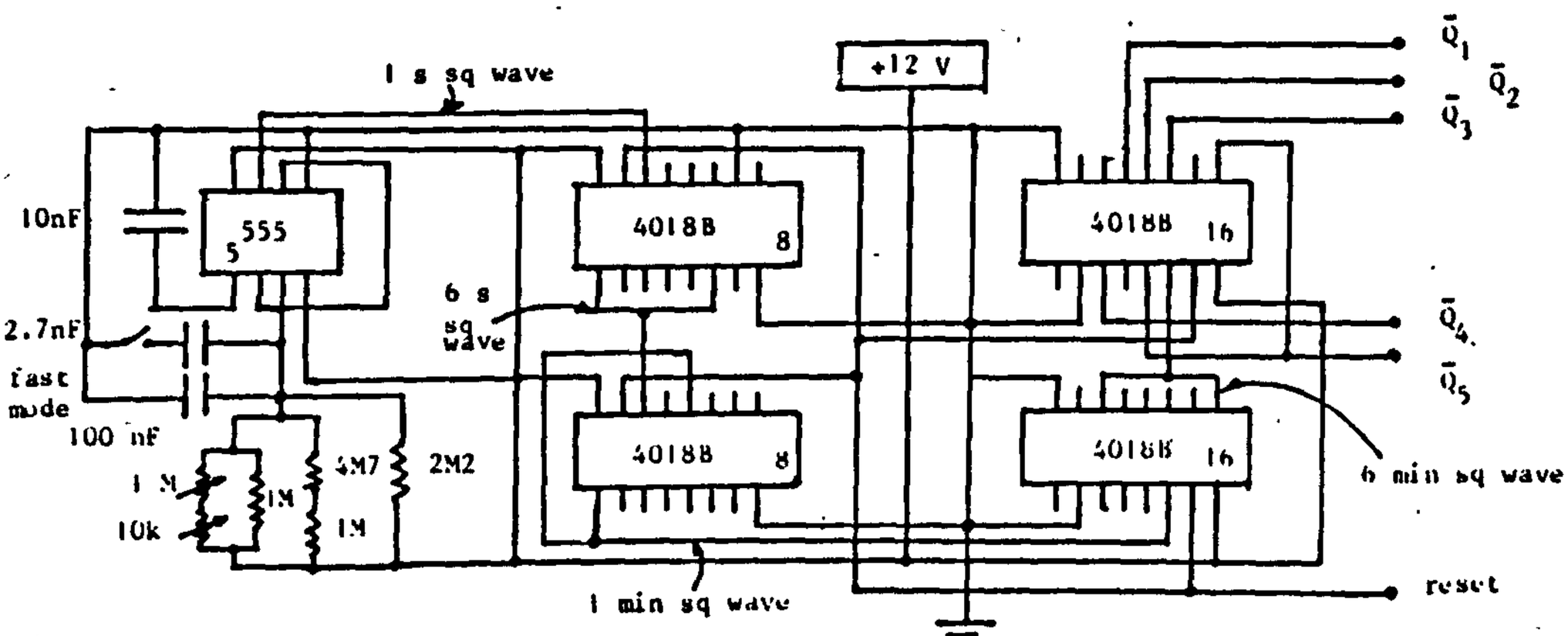

Fig.(1.11b): Timing circuit for weathering unit

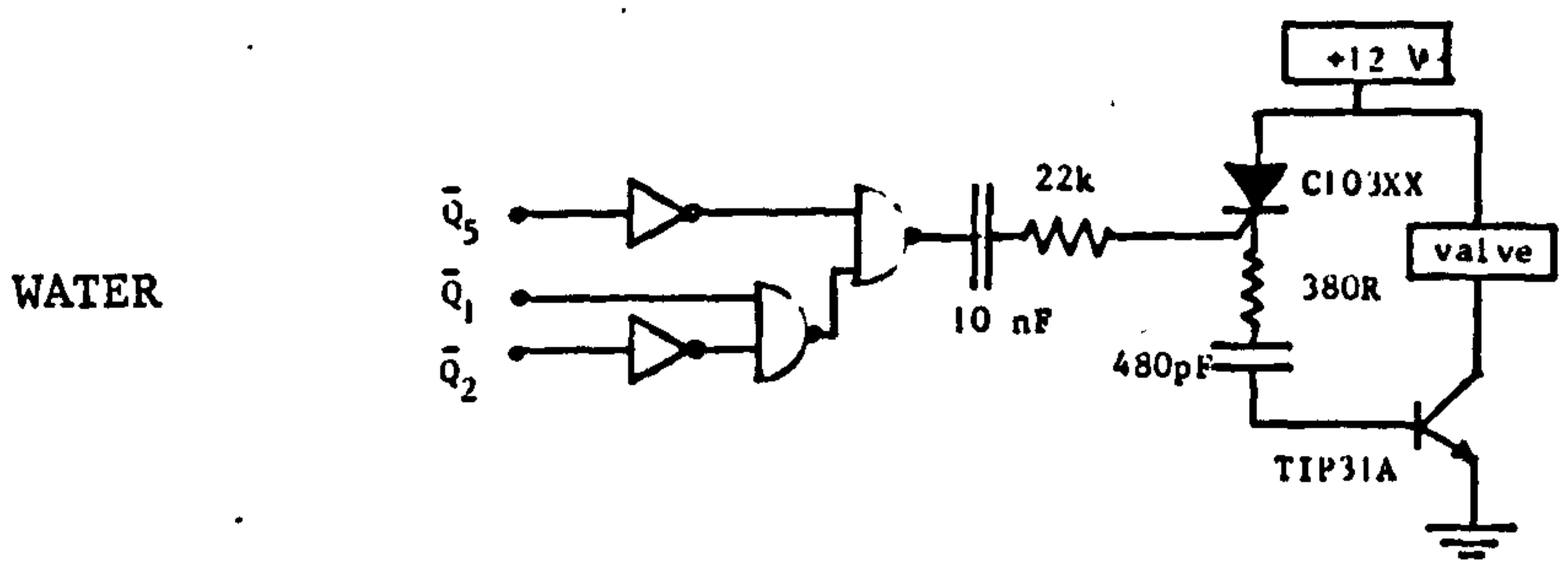

Fig.(1.11c): TTL logic for weathering unit

APPENDIX II

The artificial weathering of glass

The artificial weathering unit described below is shown in Fig.1.10. It was constructed in the laboratory from CMOS logic chips and other easily available components.

The sample of glass (with deposited film upwards) is subjected to a programme of events shown in Fig.1.11a. The cycling is controlled by an astable multivibrator timer (1.24) and TTL circuits shown in Figs 1.11b and 1.11c. The power supply is 12 V DC. The subscripts on the outputs $\bar{Q}_1$ to $\bar{Q}_5$ in Fig. 1.11b indicate the number of periods from the start of the sequence at which the logical values fall from 1 to 0. All outputs remain at zero for 5 periods, and the length of the period is 6 minutes, or 10 s if the 'fast run' button is pressed.

De-ionised water, stored in a plastic container, is squirted downward on to the surface of the glass and evaporates from there in the elevated temperature (about 50°C) produced by the low voltage heater mounted directly beneath. The arrangement gives a very high ratio of glass surface area to volume of leaching solution, which increases the leach rate considerably (1.25). Mechanical stress is applied by bending the sample, using a solenoid activated by another multivibrator of period 0.5 s, powered from the same source.

The unit was developed successfully, and performed to specification, but unfortunately time did not permit its full evaluation. Chaper 8 contains a preliminary set of results.

The unit remains operable for future use.

APPENDIX III

Cascade theory proofs

The full algebraic manipulation required for an understanding of the treatment given in the chapter is provided here.

Proof 1 (of equation 2.12)

Multiplying equation 2.10 throughout by $(2l+1)P_l(\eta)$ and using the recurrence relation for Legendre polynomials

$$(2l+1)\eta P_l(\eta) = (l+1)P_{l+1}(\eta) + lP_{l-1}(\eta) \qquad (a)$$

for the second term on the left hand side, we have the equation

$$(2l+1)\delta(x)(-\eta)\Theta(-\eta)\Theta(E-U/\eta^2)P_l(\eta) - \frac{\partial}{\partial x}\left[H(x,E,\eta)\left\{(l+1)P_{l+1}(\eta) + lP_{l-1}(\eta)\right\}\right]$$
$$= (2l+1)N\int d\sigma\left[H(x,E,\eta)P_l(\eta) - H(x,E';\eta')P_l(\eta) - H(x,E'',\eta'')P_l(\eta)\right] \qquad (b)$$

Expanding the function H in the final two terms in series such as

$$H(x,E,\eta) = \sum_n (2n+1)H_n(x,E)P_n(\eta) \qquad (c)$$

where $$H_n(x,E) = \tfrac{1}{2}\int_{-1}^{+1} P_n(\eta)\, H(x,E,\eta)\, d\eta \qquad 2.11$$

and using the orthonormality relations for Legendre polynomials

$$\int_{-1}^{+1} P_n(\eta)\, P_m(\eta)\, d\eta = \frac{2\delta_{mn}}{2n+1} \qquad (d)$$

when the whole equation is integrated over the full range of η, equation 2.12 results.

Proof 2 (of equation 2.16)

Integration by parts of equation 2.15, subject to the condition $H(E) = 0$ for $E < U_o$, yields:

$$\tfrac{1}{2}(1 - U_o/E) = NCE^{-m}m^{-1}\int_o^E dT\, T^{-m}\left\{H'(E-T) - H'(T)\right\} \qquad (e)$$

where $H'(E) = \frac{dH(E)}{dE}$ and where the subscripts on C and H have been dropped for ease of notation.

Changing the variable in the first integral to E-T,

APPENDIX III

Cascade theory proofs

The full algebraic manipulation required for an understanding of the treatment given in the chapter is provided here.

Proof 1 (of equation 2.12)

Multiplying equation 2.10 throughout by $(21+1)P_1(\eta)$ and using the recurrence relation for Legendre polynomials

$$(21+1)\eta P_1(\eta) = (1+1)P_{1+1}(\eta) + 1P_{1-1}(\eta) \qquad (a)$$

for the second term on the left hand side, we have the equation

$$(21+1)\delta(x)(-\eta)\Theta(-\eta)\Theta(E-U/\eta^2)P_1(\eta) - \frac{\partial}{\partial x}\left[H(x,E,\eta)\left\{(1+1)P_{1+1}(\eta) + 1P_{1-1}(\eta)\right\}\right]$$

$$= (21+1)N\int d\sigma\left[H(x,E,\eta)P_1(\eta) - H(x,E';\eta')P_1(\eta) - H(x,E'',\eta'')P_1(\eta)\right] \qquad (b)$$

Expanding the function H in the final two terms in series such as

$$H(x,E,\eta) = \sum_n (2n+1)H_n(x,E)P_n(\eta) \qquad (c)$$

where $$H_n(x,E) = \tfrac{1}{2}\int_{-1}^{+1} P_n(\eta)\ H(x,E,\eta)\ d\eta \qquad 2.11$$

and using the orthonormality relations for Legendre polynomials

$$\int_{-1}^{+1} P_n(\eta)\ P_m(\eta)\ d\eta = \frac{2\delta_{mn}}{2n+1} \qquad (d)$$

when the whole equation is integrated over the full range of η, equation 2.12 results.

Proof 2 (of equation 2.16)

Integration by parts of equation 2.15, subject to the condition $H(E) = 0$ for $E < U_o$, yields:

$$\tfrac{1}{2}(1 - U_o/E) = NCE^{-m}m^{-1}\int_o^E dT\ T^{-m}\left\{H'(E-T) - H'(T)\right\} \qquad (e)$$

where $H'(E) = \frac{dH(E)}{dE}$ and where the subscripts on C and H have been dropped for ease of notation.

Changing the variable in the first integral to E-T,

$$\tfrac{1}{4}(1 - U_o/E) = NCE^{-m}m^{-1}\int_o^E dT\ H'(T)\left\{ (E-T)^{-m} - T^{-m} \right\} \qquad (f)$$

Making the substitutions $E = U_o e^u$ and $T = U_o e^v$, we have $dT = U_o e^v dv$ and

$$\tfrac{1}{4}(1 - e^{-u})e^{(2m-1)u} = NCm^{-1}U_o^{1-2m}\int_o^u dv\ H'(v)e^{-(u-v)}\cdot$$
$$\left\{(1 - e^{-(u-v)})^{-m} - e^{m(u-v)}\right\} \qquad (g)$$

Taking the Laplace transform of this equation yields, for the left hand side:

$$\tfrac{1}{4}\left\{(s-2m+1)^{-1} - (s-2m+2)^{-1}\right\} = \left[4(s-2m+1)(s-2m+2)\right]^{-1} \qquad (h)$$

and for the right hand side

$$NCm^{-1}U_o^{1-2m}\,\bar{H}'(s)\int du\ e^{-u(s+1)}\left\{ (1-e^{-u})^{-m} - e^{mu}\right\}$$

where $\bar{H}'(s)$ is the Laplace transform of $H'(v)$, and where the convolution theorem of Laplace transforms has been used. The integral becomes, on substituting $t = 1-e^{-u}$

$$\int_o^1 (1-t)^s(t^{-m} - (1-t)^{-m})\ dt = \int_o^1 (1-t)^s t^{-m}dt - \int_o^1 (1-t)^{s-m}dt$$
$$= B(1-m,s+1) - (s-m+1)^{-1}$$

by the definition of the Beta function $B(p,q) = \int_o^1 t^{p-1}(1-t)^{q-1}dt$. Exploiting the relationship between the B and the Γ functions, and the recursive property of the Γ function, this becomes

$$= \frac{\Gamma(1-m)\Gamma(s+1)}{\Gamma(s-m+2)} - \frac{1}{s-m+1}$$

$$= \frac{1}{s-m+1}\left\{\frac{\Gamma(1-m)\Gamma(s+1)}{\Gamma(s-m+1)} - 1\right\}$$

so that the full equation reads

$$\left[4(s-2m+1)(s-2m+2)\right]^{-1} = \frac{NCU_o^{1-2m}\,\bar{H}'(s)}{m(s-m+1)}\left\{\frac{\Gamma(1-m)\Gamma(s+1)}{\Gamma(s-m+1)} - 1\right\} \qquad (j)$$

and $\bar{H}'(s)$ may be found explicitly. Unfortunately, there is no analytic form for the inverse transform of this type of function, so an asymptotic approximation is made at this point.

Accordingly, we write

$$H'(E) = \sum_{\alpha} A_\alpha (E/U_o)^\alpha = \sum_{\alpha} A_\alpha e^{-u\alpha} \qquad (k)$$

so that $\bar{H}'(s) = \sum_{\alpha} \frac{A_\alpha}{s-\alpha}$, by standard transform.

This identifies the exponents α in equation k as the poles of the function $\bar{H}'(s)$. Inspecting equation j reveals poles at

$$s = 2m - 2$$

and at $s = 2m - 1$

which tend to -2 and -1 respectively at m = 0. Another, more significant pole is found if the term in curly brackets is transformed by expanding the Γ functions as Taylor series, thus:

$$\frac{\Gamma(1-m)\Gamma(s+1)}{\Gamma(s-m+1)} - 1 \simeq \frac{\Gamma(1-m)\left\{1 + s\left.\frac{d\Gamma(s+1)}{ds}\right|_{s=o}\right\}}{\Gamma(1-m) + s\left.\frac{d\,\Gamma(s-m+1)}{ds}\right|_{s=o}} - 1$$

Using $\Gamma(1) = 1$,

$$\simeq \frac{1 + s\left\{\frac{d\Gamma(s+1)}{ds} / \Gamma(s+1)\right\}_{s=o}}{1 + s\left\{\frac{d\Gamma(s-m+1)}{ds} / \Gamma(1-m)\right\}_{s=o}} - 1$$

Defining the digamma function (2.5) by the equation:

$$\psi(x) = \frac{d}{dx} \ln \Gamma(x) = \frac{d\Gamma(x)}{dx} / \Gamma(x)$$

we can write the term as

$$\frac{1 + s\psi(1)}{1+s\psi(1-m)} - 1 = \frac{s\{\psi(1) - \psi(1-m)\}}{1 + s\psi(1-m)}$$

which clearly shows that there is a pole at s=0. This is the dominant term in the asymptotic series of equation k. We can therefore write equation j for s approaching zero in the form:

$$\bar{H}'(s) = \frac{m(1-m)}{8NCU^{1-2m}(1-m)(1-2m)} \cdot \frac{1}{\psi(1) - \psi(1-m)} \cdot \frac{1}{s} \qquad (m)$$

which can be inverse transformed and integrated with respect to E to yield equation 2.16.

Proof 3 (of equation 2.17)

The second factor in equation 2.16 becomes $\frac{E}{8NC_o U_o}$ when m approaches zero, and using 1'Hopital's theorem in the same limit for the first factor, we have

$$\left[\frac{m}{\psi\ (1) - \psi\ (1-m)}\right]_{m=o} = \frac{1}{\psi'(1)}\ , \text{ where } \psi'(x) = \frac{d\psi(x)}{dx}$$

By reference 2.5, the function $\psi'(x)$, the trigamma function, is expressable as

$$\psi'(x) = \int_o^\infty \frac{te^{-xt}}{1 - e^{-t}}\ dt$$

so that

$$\psi'(1) = \int_o^\infty \frac{te^{-t}}{1 - e^{-t}}\ dt$$

Substituting x for e^{-t},

$$\psi'(1) = -\int_o^1 \frac{\ln x}{1 + x}\ dx = \frac{\pi^2}{6}$$

by standard tables (2.9).

APPENDIX IV

Development of altered surface layer

The treatment is based upon that of Liau et al (3.9).

The concentration change caused by sputtering a binary compound for a time t is written

$$\int_0^\infty \left[N_2(z,t) - N_1(z,t)\right] dz \equiv \int_0^\infty \Delta N(z,t)\, dz$$

and may be equated to the difference between the sputtered flux from each component

$$\Phi \int_0^t \left[S_1(t') - S_2(t')\right]\ dt'$$

where $\Phi/m^{-2}s^{-1}$ is the incident ion flux.

If we assume that $\Delta N(z,t)$ has a linear decay with depth z, such that $\Delta N(W,t) = 0$ we may write the change after a time t as

$$\tfrac{1}{2}W\ \Delta N(0,t)$$

and the full equation in the form

$$\tfrac{1}{2}W \frac{d}{dt} \Delta N(0) = \Phi \left\{S_1(t) - S_2(t)\right\} \qquad (a)$$

If also the ejection probabilities of the components 1 and 2 are in the ratio r : 1 respectively, we have

$$\frac{S_1(t)}{S_2(t)} = r\ \frac{N_1(0,t)}{N_2(0,t)} \qquad (b)$$

Now, defing the surface concentration ratio at a time t by

$$n(t) \equiv \frac{N_2(0,t)}{N_1(0,t)} \qquad 3.6a$$

the total sputter yield S by

$$S = S_1(t) + S_2(t) \qquad (c)$$

which is a constant, and the total atomic concentration N by

$$N = N_1(z,t) + N_2(z,t) \qquad (d)$$

we obtain immediately the relations

$$S_1(t) = \frac{r}{r+n} S \qquad (e)$$

$$S_2(t) = \frac{n}{r+n} S \qquad (f)$$

$$N_1(t,0) = \frac{N}{1+n} \qquad (g)$$

$$N_2(t,0) = \frac{n}{1+n} N \qquad (h)$$

Thus, equation (a) takes the form

$$\tfrac{1}{2} WN \frac{d}{dt}\left(\frac{n-1}{1+n}\right) = \frac{r-n}{r+n} \Phi S \qquad (a)'$$

leading to

$$\tfrac{1}{2} W N \left\{\frac{(1+n) - (n-1)}{(1+n)^2}\right\} dn = \frac{r-n}{r+n} \Phi S \, dt \qquad (j)$$

$$\left\{\frac{r+n}{(r-n)(1+n)^2}\right\} dn = \frac{\Phi S}{NW} dt \qquad (k)$$

and finally

$$\int_{n(0)}^{n(t)} \frac{r+n'}{(r-n')(1+n')^2} \, dn' = \frac{\Phi S t}{NW} \qquad 3.6$$

which is evaluated numerically by iteration.

APPENDIX V

Ionic energy on entering sheath

If the ions have a density n_o and an average speed v_o in the discharge region, the ionic flux at the sheath boundary is vn_o. At a plane in the sheath where the potential (relative to the plasma) is V, the flux must also be equal to $v'n_i$, where v' and n_i are the new ionic velocity and density respectively.

Thus, $$v'n_i = v_o n_o \qquad (a)$$

and $$(V_o - V)^{\frac{1}{2}} n_i = V_o^{\frac{1}{2}} n_o \qquad (b)$$

where the arriving ions have an initial energy eV_o.

Now if the distribution of electronic velocity components normal to the sheath is Maxwellian, we may write for the density of electrons in this plane

$$n_e = n_o \exp(-qV/kT_1) \qquad (c)$$

where their density in the plasma is equated to that of the ions, $q = -e$ is their charge and T_1 is their temperature.

Considering a plane close to the sheath boundary (that is, for small V) we can expand equations (b) and (c) in Taylor's series to yield

$$n_i = n_o \left[1 + \tfrac{1}{2} \frac{V}{V_o} - \ldots\ldots \right] \qquad (d)$$

$$n_e = n_o \left[1 + eV/kT_1 + \ldots\ldots \right] \qquad (e)$$

Since $n_i = n_e$ at the boundary itself, we obtain directly

$$\tfrac{1}{2} \frac{V}{V_o} = \frac{eV}{kT_1} \rightarrow eV_o = \tfrac{1}{2} kT_1 \qquad (f)$$

and the ions are predicted to be accelerated to the electron temperature on entering the sheath. Equation (f) is verified by experiment (see ref.13 of 4.36) to within a factor of 2.

APPENDIX VI

Dependence of heat flow in coils upon wire gauge

The thermal conductivities, κ, of the three relevant materials are in the ratio $\kappa_{copper}:\kappa_{insulation}:\kappa_{air} = 40000:15:2.7$ which shows that the diffusion of heat throughout the coil is limited by the insulation layer between the turns.

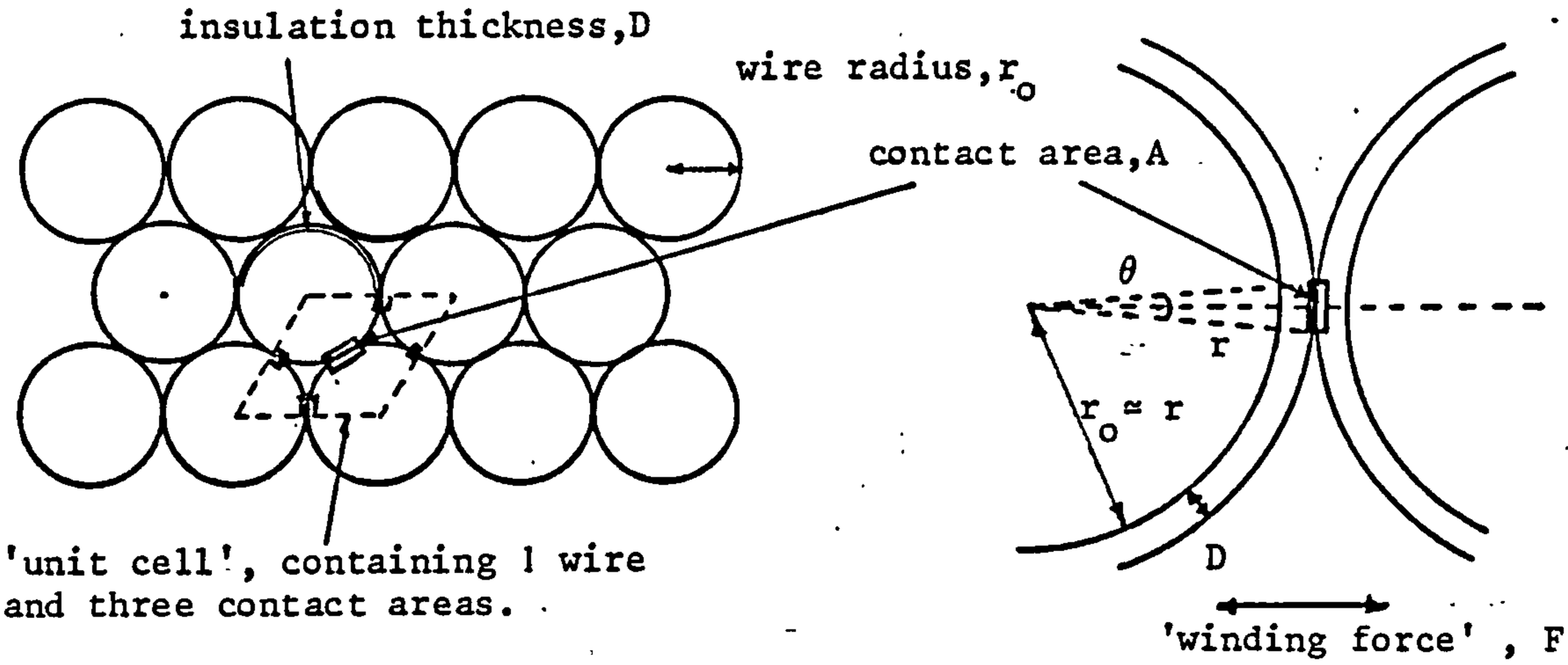

From the diagrams above, it is seen that each wire possesses an area of contact A with the others given by

$$A = 3r\theta$$

so that

$$dA = 3rd\theta + 3\theta dr \qquad (a)$$

Also, we see that

$$\cos(\tfrac{1}{2}\theta) = \frac{r}{r_o}$$

giving

$$d\theta = -2\,\frac{dr}{r_o \sin(\tfrac{1}{2}\theta)}$$

which, at small θ, becomes

$$d\theta = \frac{-4\ dr}{r_o\,\theta} \qquad (b)$$

and substituting this in equation (a) we obtain

$$dA = \left[-\frac{12}{\theta}\left(\frac{r}{r_o}\right) + 3\theta\right] dr$$

showing that at small θ the first term is much the larger. Thus, equation (a) may be approximated by:

PAGE NUMBERING AS ORIGINAL

APPENDIX VII

Steady state radio-frequency analysis

Proof 1 (of equation 5.13)

This proof is based upon that given by E. May in Ref.5.5 Chapter 3.

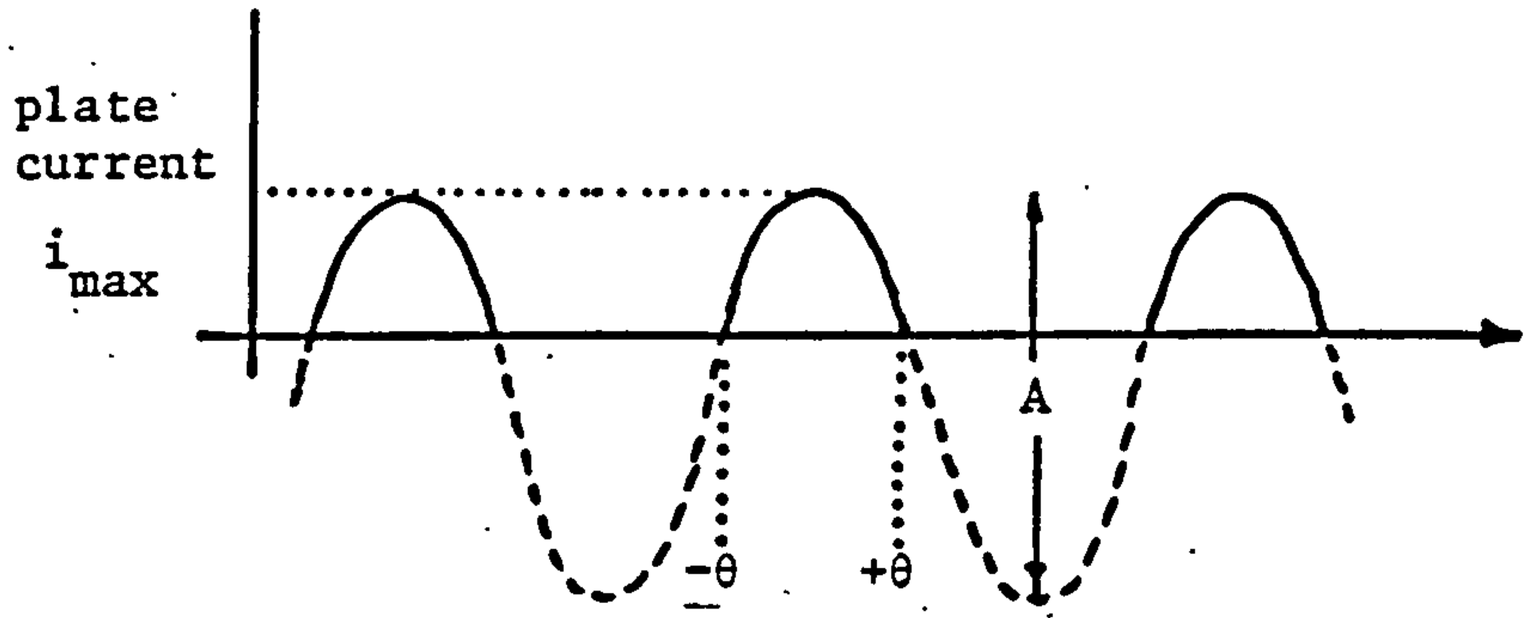

Considering the current pulse of conduction angle 2θ, shown in the figure above, we may write, for the peak current i_{max},

$$i_{max} = A(1-\cos\theta)$$

Hence, at an angle ϕ,

$$i(\phi) = A(\cos\phi - \cos\theta)$$

$$= \frac{i_{max}(\cos\phi - \cos\theta)}{(1 - \cos\theta)} \qquad (a).$$

The average value of the plate current I_{av} is obtained from the integral of $i(\phi)$ over the whole period.

$$I_{av} = \frac{1}{2\pi}\int_0^{2\pi} i(\phi)\, d\phi$$

$$I_{av} = \frac{i_{max}}{\pi(1-\cos\theta)}\left[\int_0^{\theta}\cos\phi\, d\phi - \cos\theta\int_0^{\theta} d\phi\right]$$

$$I_{av} = \frac{i_{max}}{\pi(1-\cos\theta)}\left[\sin\theta - \theta\cos\theta\right] \qquad (b)$$

Writing the current pulse as a series of harmonics:

$$i(\phi) = I_{DC} + a_1\cos\omega t + a_2\cos 2\omega t + a_3\cos 4\omega t + ...$$

the amplitude of the fundamental, a_1, may be obtained from Fourier analysis:

$$dA = 3r_o d\theta, \quad \text{where } r_o \simeq r \tag{c}$$

showing that the deformation of the coating caused by the winding force is primarily such as to increase the area of contact of the wires and not to reduce the thickness of the polyurethane coating.

The definition of the bulk modulus m_B of a sample of material of volume V takes the form

$$m_B = -\frac{dp}{dV} V$$

where p is the pressure. In the case of the coating, of thickness D,

$$V = DA$$

$$dV = D\, dA$$

and we obtain $$dp = -m_B \frac{d\theta}{\theta} \tag{d}$$

However, from the definition of pressure, p=F/A, we have also

$$dp = -\frac{F}{A^2} dA$$

where F is the force between the turns (the 'winding force'), and using equations (a) and (c), this may be written

$$dp = -\frac{F\, d\theta}{3r_o\theta^2} \tag{e}$$

which yields the relation

$$r_o\theta = \frac{F}{3m_B} \tag{f}$$

Now, considering the passage of heat through a medium across which there is a constant temperature difference, the rate of energy flow is proportional to the area of the path divided by its length. That is, the quantity $3r_o\theta/2D$ is a measure of the heat flow, in this case. Equation (f) indicates that for a particular winding force, $r_o\theta$ is constant, to a first approximation. Therefore, the flow of heat through the coil can be considered a weak function of the wire radius, r_o. The thermal conductivity is hence similarly independent of the wire gauge.

$$a_1 = \frac{1}{\pi} \int_0^{2\pi} i(\phi) \cos\phi \, d\phi$$

and using equation (a) we obtain

$$a_1 = \frac{i_{max}}{\pi(1-\cos\theta)} \left[\theta - \sin\theta \cos\theta\right] \qquad (c)$$

Using equation (b), the relation

$$a_1(\theta) = \frac{\theta - \sin\theta \cos\theta}{\sin\theta - \theta\cos\theta} I_{av} \qquad 5.13$$

follows.

Proof 2 (of equation 5.19)

The impedance of the circuit shown below may be written as follows:

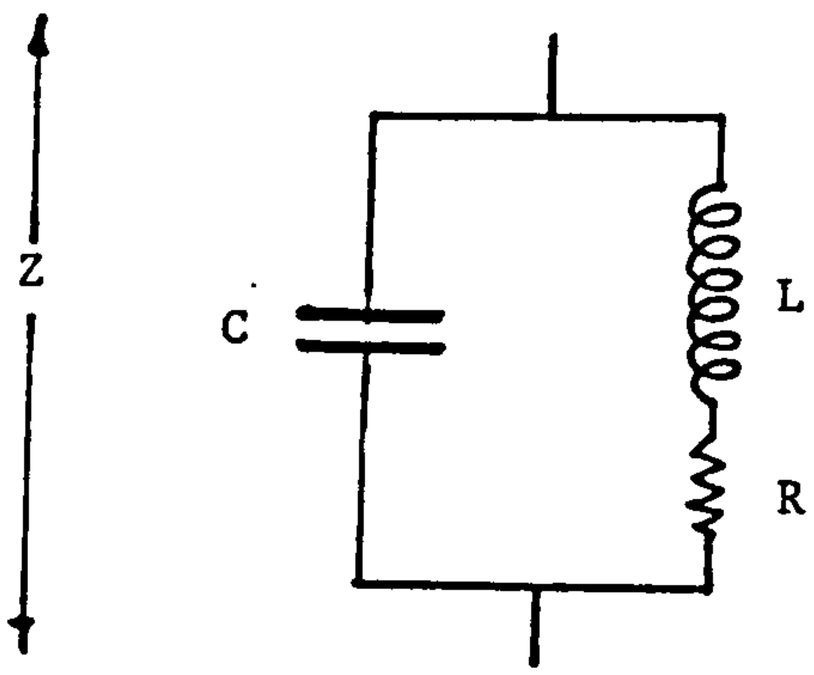

A parallel resonant network

$$\frac{1}{Z} = i\omega C + \frac{1}{i\omega L + R}$$

$$= \frac{-\omega^2 CL + 1 + i\omega CR}{i\omega L + R}$$

If $\omega = \omega_o$, the resonant frequency, the equation

$$\omega_o^2 CL = 1$$

holds and we may write, for $R \ll \omega L$,

$$Z = R_o = \frac{i\omega_o L + R}{i\omega_o CR} \sim \frac{L}{CR} \qquad (a)$$

The pure resistance R_o is known as the 'dynamic impedance'of the circuit.

The definition of the Q-factor of a circuit is commonly written in the form (5.13):

$$Q = \omega \frac{\text{maximum stored energy}}{\text{energy dissipated per sec}}$$

For the parallel LCR circuit above, the maximum instaneous stored energy is CV_o^2, where V_o is the rms voltage across the tank (5.13,p56) and the power dissipated is V_o^2/R_o, at resonance. Thus,

$$Q = \frac{\omega_o CV_o^2}{V_o^2/R_o} = \omega_o CR_o = \frac{\omega_o L}{R} \qquad 5.18$$

having used equation (a).

/

The principal of duality (5.13,p202) allows the equations for the parallel network to be obtained directly from those of the series network, which is easier to analyse. Following this principle, the quantities I,C and L are exchanged for V,L and C respectively, impedance replaces admittance, and resistance replaces conductance.

Hence, the Q-factor of the series LCR network is also given by equation 5.18.

Proof 3 (of equations 5.22)

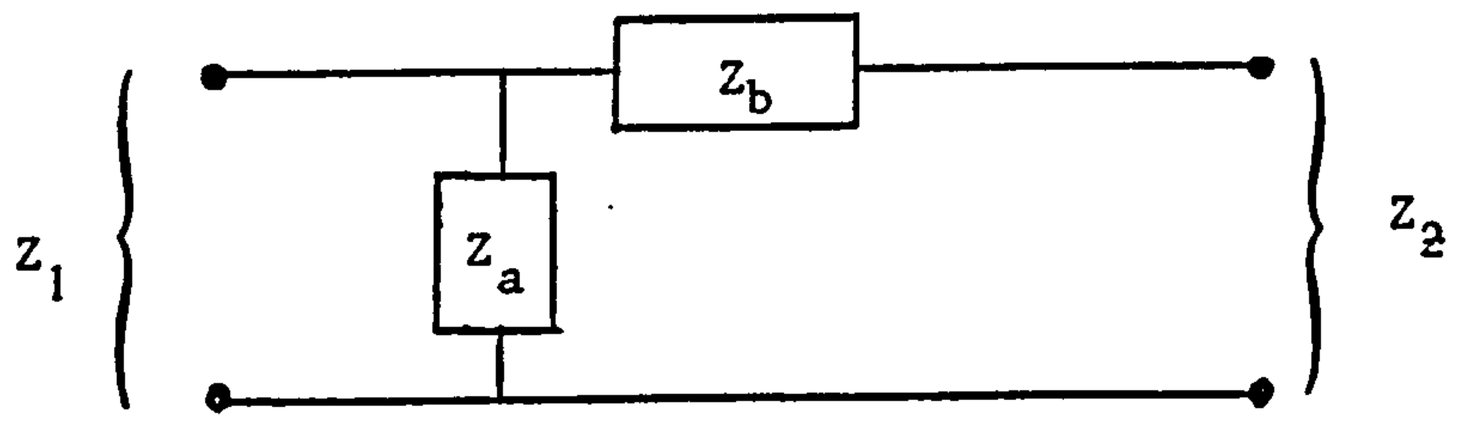

The impedance presented at the left hand pair of contacts of the network shown above is given by

$$Z_{1(o)} = Z_a \quad \text{at open circuit } (Z_2 = \infty)$$

$$\text{and} \qquad Z_{2(s)} = Z_a Z_b/(Z_a+Z_b) \quad \text{at short circuit } (Z_2=0)$$

Similarly, at the right hand end,

$$Z_{2(o)} = Z_a + Z_b$$

$$\text{and} \qquad Z_{2(s)} = Z_b$$

From many standard texts on networks and transmission lines (5.2), the

impedances that must be connected to each end of the network, for zero power reflection, are the 'image' impedances

$$Z_1^I = \left[Z_{1(o)}Z_{1(s)}\right]^{\frac{1}{2}} = Z_a\left[\frac{Z_b}{Z_a + Z_b}\right]^{\frac{1}{2}} \qquad (a)$$

and $$Z_2^I = \left[Z_{2(o)}Z_{2(s)}\right]^{\frac{1}{2}} = \left[(Z_a+Z_b)Z_b\right]^{\frac{1}{2}} \qquad (b)$$

Now, $$1 - Z_1^I/Z_2^I = 1 - \frac{Z_a}{Z_a+Z_b} = \frac{Z_b}{Z_a+Z_b}$$

and we may write, from equation (a),

$$Z_a = Z_1^I\left[1 - \frac{Z_1^I}{Z_2^I}\right]^{-\frac{1}{2}} \qquad (c)$$

and from equation (b),

$$Z_b = Z_2^I\left[1 - \frac{Z_1^I}{Z_2^I}\right]^{\frac{1}{2}} \qquad (d)$$

For the purposes of this application,we note the inequality $Z_1^I > Z_2^I$, and write equations (c) and (d) in the form

$$Z_a = -i\,Z_1^I\left[\frac{Z_1^I}{Z_2^I} - 1\right]^{\frac{1}{2}}$$

$$Z_b = \quad i\,Z_2^I\left[\frac{Z_1^I}{Z_2^I} - 1\right]^{-\frac{1}{2}}$$

When the substitutions $Z_2^I = Z_g$ (the glow impedance) and $Z_1^I = Z_i$ (the required input impedance) are made, equations 5.22 are obtained.

Proof 4 (of equations 5.25)

If the quantities f,g,x,and y are related through the equation

$$\frac{1}{f + ig} = x + iy \qquad (a)$$

then $$f = \frac{x}{x^2 + y^2} \quad \text{and} \quad g = \frac{-y}{x^2 + y^2}$$

Taking the total differentials,

$$\Delta f = (x^2+y^2)^{-2}\left\{(y^2-x^2)\,\Delta x + 2xy\Delta y\right\}$$

and $$\Delta g = (x^2+y^2)^{-2}\left\{2xy\Delta x + (y^2-x^2)\Delta y\right\}$$

Let : $x << y$ (b)

then $\Delta f = \frac{1}{y^2}\left\{\Delta x + \frac{2x\Delta y}{y}\right\}$ (c))

$\Delta g = \frac{1}{y^3}\left\{2x^2\left(\frac{\Delta x}{x}\right) + y^2\left(\frac{\Delta y}{y}\right)\right\}$ (d)

The complex load impedance Z_g is related to the load admittance Y_g through

$$\frac{1}{Z_g} = Y_g$$

yielding the equation

$$\frac{1}{R_g + iX_g} = G_g + iX_p \quad \text{(e)}$$

where R_g and X_g are the real and imaginary series impedance components and G_g and X_p are the equivalent parallel components. The quantities in equations (a) and (e) may be seen to be related through

$$(f,g,x,y) \equiv (R_g, X_g, G_g, X_p)$$

and since $G_g << X_p$, equations (c) and (d) hold, and

$$\Delta R_g = X_p^{-2}\left(\Delta G_g + 2G_g \frac{\Delta X_p}{X_p}\right) \quad \text{5.25a}$$

If the fractional errors $\Delta x/x$ and $\Delta y/y$ are considered roughly equal, we may write, using inequality (b)

$$\Delta X_g = \frac{\Delta X_p}{X_p^2} \quad \text{5.25b}$$

APPENDIX IX

Electric field as a function of depth in the analyte

The electric field F at a point outside a sheet of charge density ρ is found simply from

$$\nabla . F = \rho/\varepsilon$$

by applying Gauss' theorem. Thus,

$$\int_S \underline{F}.\underline{dS} = \frac{1}{\varepsilon} \int_V \rho \, dV$$

and considering a cylinder of unit cross-sectional area as the Gaussian surface (as shown below) we obtain

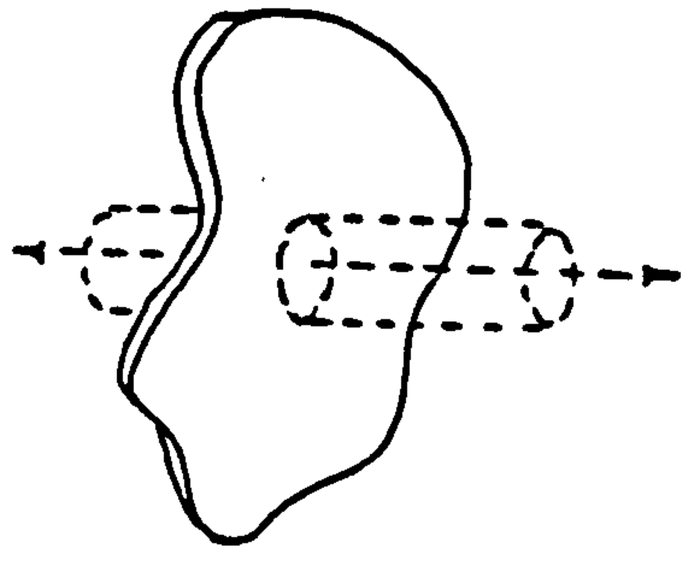

$$\varepsilon F = Q/2$$

where Q is the total charge per unit area.

Hence, at a point outside the glass, the field is given by

$$F(y<0) = Q/2, \quad \text{where} \quad Q = \int_0^\infty q(y)\, dy$$

Making the linear approximation shown in Fig 8.16b, where the peak of the charge distribution occurs at the point (y_p, q_{max}), we may write immediately

$$q(y) = \frac{q_{max}}{1-y_p} (y+1-2y_p) \qquad (a)$$

and

$$Q = \frac{q_{max}}{2(1-y_p)} (1-2y_p^2) \qquad 8.15a$$

where both equations are subject to the constraint

$$0 < y < y_p < \tfrac{1}{2}.$$

Now, subtracting that charge distributed in the region between y and the surface, we write

$$\varepsilon F(y) = \frac{Q}{2} - \int_0^y q(y)dy$$

which, using equations (a) and 8.15a, becomes

$$\varepsilon F(y) = \frac{Q}{2} - \frac{2Q}{1-2y_p^2} \int_0^y (y+1-2y_p)\, dy$$

and

$$F(y) = \frac{Q}{2\varepsilon} \left[1 - D(y,y_p)\right] \qquad 8.15$$

where $D(y,y_p)$ is defined by equation 8.15b

Oxide(i)	$a_{\alpha i}$	Durable ternary _ mol% (wt%)	Durable four-component	Durable multi-component
SiO_2	2.8	72.0(72.3)	72.2(73.5)	71.15(68.7)
Al_2O_3	2.4			0.96(1.57)
Na_2O	38.4	15.0(15.5)	15.2(16.0)	16.8(16.8)
K_2O	28.3			1.1(1.67)
P_2O_5	15.0			0.53(0.88)
CaO	13.6	13.0(12.2)	7.0(6.7)	8.04(7.24)
BaO	10.0			
MgO	0.3		5.6(3.8)	1.25(o.81)
PbO	10.0			0.18(0.63)
'SiO_2'		72.0	72.2	73.6
'R_2O'		15.0	15.2	17.0
'RO'		13.0	12.6	9.4
Exp. coeff. α /10^{-6} $°C^{-1}$		9.64	9.12	10.05

TABLE I: DURABLE GLASSES AND COEFFICIENTS

Oxide	Glass 1	Glass 2
	Wt%	Wt%
SiO_2	46.08	54.9
Al_2O_3	1.57	1.32
Na_2O	3.0	1.95
K_2O	13.92	17.65
P_2O_5	7.0	5.08
CaO	18.84	11.7
MgO	7.44	5.91
PbO	0.01	0.04
MnO	1.73	1.16
Fe_2O_3	0.35	0.24
CuO	0.01	0.01
ZnO	0.05	0.05

TABLE II: NON-DURABLE GLASSES MELTED BY PILKINGTON

Principal quantum number n	Orbital angular momentum l	z-component of angular momentum m_l	Total angular momentum $j=l\pm\frac{1}{2}$	Orbital	X-ray notation	Orbital occupancy	Shell occupancy
1	0	0	$+\frac{1}{2},-\frac{1}{2}$	1s	K	2	2
2	0	0	$+\frac{1}{2},-\frac{1}{2}$	2s	L_1	2	
	1	−1, 0, +1	$\frac{1}{2}$	$2p_{\frac{1}{2}}$	L_2	6	8
			$\frac{3}{2}$	$2p_{\frac{3}{2}}$	L_3		
3	0	0	$+\frac{1}{2},-\frac{1}{2}$	3s	M_1	2	
	1	−1, 0, +1	$\frac{1}{2},\frac{3}{2}$	$3p_{\frac{1}{2}},3p_{\frac{3}{2}}$	M_2,M_3	6	
	2	−2 to +2	$\frac{3}{2}$	$3d_{\frac{3}{2}}$	M_4	10	18
			$\frac{5}{2}$	$3d_{\frac{5}{2}}$	M_5		
4	0	0	$+\frac{1}{2},-\frac{1}{2}$	4s	N_1	2	
	1	−1, 0, +1	$\frac{1}{2},\frac{3}{2}$	$4p_{\frac{1}{2}},4p_{\frac{3}{2}}$	N_2,N_3	6	
	2	−2 to +2	$\frac{3}{2},\frac{5}{2}$	$4d_{\frac{3}{2}},4d_{\frac{5}{2}}$	N_4,N_5	10	32
	3	−3 to +3	$\frac{5}{2}$	$4f_{\frac{5}{2}}$	N_6	14	
			$\frac{7}{2}$	$4f_{\frac{7}{2}}$	N_7		

TABLE III: Spectroscopic notation of atomic energy levels

Reference	8.33	8.35	8.33	8.36	A13	A14
Technique	ELS	ELS	ELS	UV refl	ELS	ELS
		3.5			3.5	
	3.9					3.9
			4.0		4.0	
			5.0			5.0
		5.1			5.2	
	5.3					
						6.0
				6.3		
					6.4	
				6.8		
			7.0			
	7.2			7.2		7.2
		7.3				
					7.7	
						8.4
				9.0	9.0	

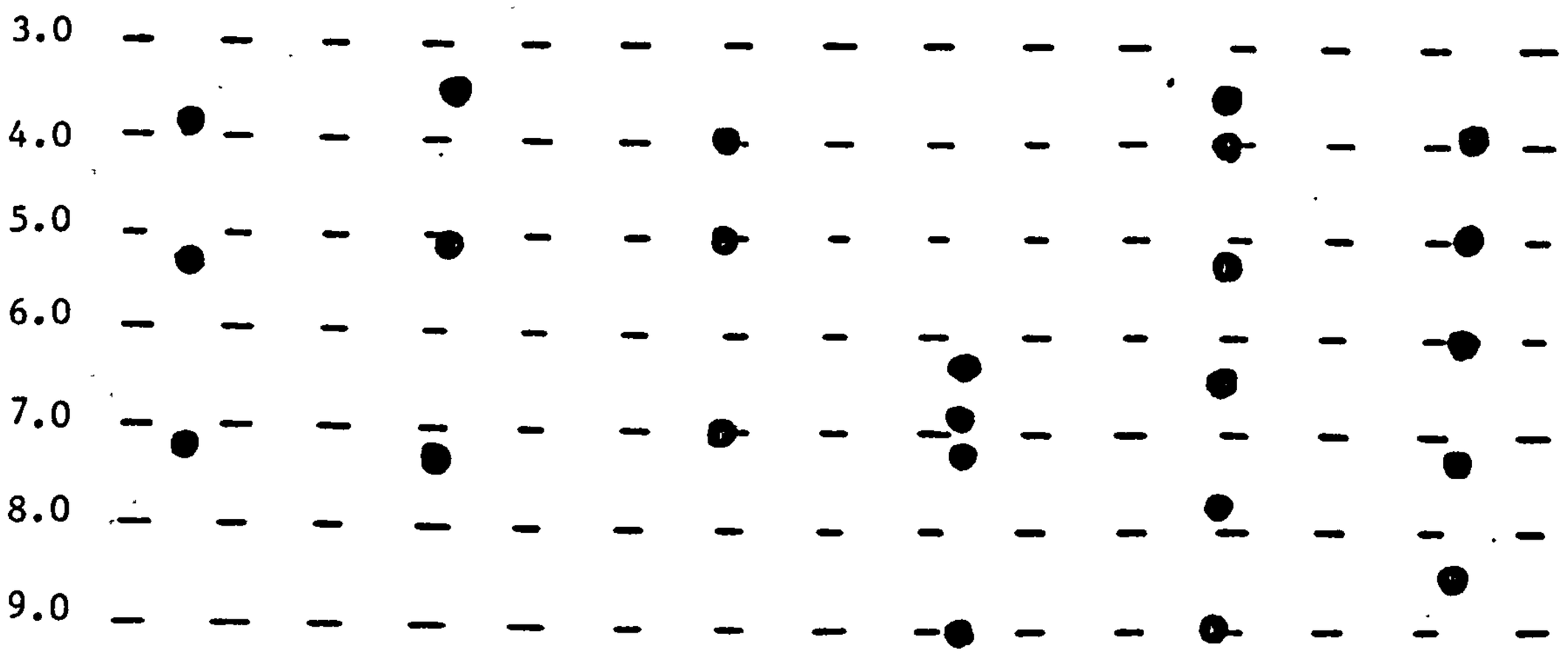

TABLE IV: SiO_x energy losses un silica, glass and glass films.
Energies in eV.

REFERENCES

1.1 B.E. Warren J Appl Phys 13 p602 1943

1.2 D.G. Holloway 'The physical properties of glass' Wykeham Pubs London and Winchester 1973

1.3 W.H. Zachariasen J Amer Ceram Soc 54 p3841 1932

1.4 P.W. McMillan Phys Ed 14 p441 1979

1.5 E.F. Kaeble Ed:'Handbook of X-rays' McGraw-Hill Nes York 1967

1.6 R.W. Douglas, J.O. Isard J Soc Glass Tech p289 1949

1.7 F.M. Ernsberger Phys Chem Glasses 21 (4) p146 1980

1.8 T.M.M. El-Shamy, J. Lewis, R.W. Douglas Glass Tech 13 p81 1973

1.9 R.W. Douglas, T.M.M. El-Shamy J Amer Ceram Soc 50 (1) p1 1967

1.10 R.J. Charles J Appl Phys 29 (11) p1549 1958

1.11 K. Hlavac Silikaty 1 p361 1963

1.12 H. Scholzen, D. Helmreich, I. Bakardjiev Glastech Bei Zeits f Glast 12 p59 1975

1.13 M.A. Rana, A.W.D. Douglas Phys Chem Glasses 2 (6) p179 1961

1.14 I.P. Beattie Trans Faraday Soc 49 p1059 1953

1.15 G.A. Cox, A.M. Pollard, A.G. Newton, O.S. Heavens Physics Department University of York

1.16 A.M. Pollard, D Phil Thesis University of York 1979 Chapter 2

1.17 G.A. Cox, O.S. Heavens, R.G. Newton, A.M. Pollard J Glass studies 21 p54 1979

1.18 G.A. Cox, A.M. Pollard Arcaeometry 19 p45 1977

1.19 E.P. Bertin 'Principles and practice of X-ray spectrometric analysis' Plenum London 1970

1.20 C.J. Iliffe, R.G. Newton Verres Refract 30 (1) p30 1976

1.21 T.M.M. El-Shamy Phys Chem Glasses 14 p1 1973

1.22 C.L. Babcock 'Silicate glass technology methods' Wiley 1977 p275

1.23 G.M. Morey 'The properties of glass' American Chemical Soc Monograph series 1954 p272

1.24 M.M. Cirovic 'Basic Electronics: Devices, circuits and systems' 2nd Ed. Reston Virginia

1.25 E.C. Ethridge, D.E. Clark, L.L. Hench Phys Chem Glasses 20 p35 1979

2.1 P. Sigmund Phys Rev 184 p383 1969

2.2 P. Sigmund 'Sputtering by ion bombardment: Theoretical concepts' to be published in 'Sputtering by ion bombardment' Ed: R. Behrisch Topics in Applied physics 1980

2.3 P. Sigmund Rev Roum Phys 17 pp823,909,1079 1972

2.4 K.B. Winterbon, P.Sigmund, J.B. Sanders Dan Vid Selsk Matt Phys Medd 37 (14) 1970

2.5 M Abramovitz, I.E. Stegun 'Handbook of mathematical functions' Dover 1965 p259

2.6 H. Cramer 'Mathematical methods in statistics' Princeton New Jersey 1945

2.7 P. Sigmund, J.B. Sanders in 'Proceedings of the International Conference on applications of ion beams to semiconductor technology' Ed: P. Glotin Paris 1967 p215

2.8 J. Lindhard, V. Nielsen, M. Scharff, P.V. Thomsen Dan Vid Selsk Matt Phys Medd 33 (10) 1969

2.9 'Handbook of Chemistry and Physics' Ed: Weast. Chemical Rubber Co

2.10 Private communication, from P. Sigmund, March 1980 Physics Institute, University of Odense,DK 5230, Odense M, Denmark

2.11 G. Dupp, A. Scharmann Z Physik 194 p448 1966

2.12 P. Sigmund, A. Gras-Marti Nuc Inst Meth 168 p389 1980

2.13 R. Weissmann. P. Sigmund Rad Eff 19 p7 1973

2.14 P. Sigmund Can J Phys 46 p731 1968

2.15 P. Sigmund App Phys Lett 25 (3) p169 1974

2.16 R. Kelly Rad Eff 32 p91 1977

2.17 R.S. Nelson Phil Mag 11 p291 1962

2.18 O. Olmen, G. Bruce Nucl Inst Meth 11 p37,p257 1961

2.19 K. R. Pollitt, J.C. Robb, D.W. Thomas Nature 272 p437 1978

2.20 J. Lindhard, V. Nielsen, M. Scharff Mat Phys Medd 36 (10) 1968

2.21 M.W. Thomson: Lectures at the summer school on the physics of ionised gases. Herlag-Novi Yugoslavia 1970 p211

3.1 G. Betz Surf Sci 92 p283 1980

3.2 P. Sigmund: 'Sputtering of multi-component materials' presented at the 26th National symposium of the American Vacuum society New York Oct 1979

3.3 J.J. Jimenez-Rodriguez, M. Rodriguez-Vidal, J.A. Valles-Abarca Rad Eff 41 p165 1979

3.4 Z.L. Liau, J.W. Mayer, W.L. Brown, J.M. Poate J Appl Phys 49 (10) p5295 1978

3.5 W.K. Chu, J.W.Mayer, M.A. Nicolet, T.M. Buck, G. Amsel, F. Eisen Thin Solid Films 17 p1 1973

3.6 P.S. Ho Surf Sci 72 p253 1978

3.7 B. Rauschenbach, M. Hinz Phys Stat Sol (a) 47 p79 1978

3.8 R. Underhill D. Phil Thesis University of York Physics Dep. 1980

3.9 G. Staudenmaier Rad Eff 13 p87 1972

3.10 W. Gerhard, H. Ochsner Z Phys B22 p91 1975

3.11 G.P. Konnen, A. Tip, A.E. deVries Rad Eff 26 p23 1975

4.1 P.D. Davidse, L.I. Maissel J Appl Phys 37 (2) p257 1966

4.2 J.L. Vossen, J.J. O'Neill RCA Rev 29 p149 1968

4.3 G.N. Jackson Thin solid films 5 p209 1970

4.4 L. Holland, W. Steckelmacher, J. Yarwood: in 'Vacuum Manual' Eds: E. & F. Spon London 1974 p384

4.5 F. Kirshner Ann. Physik 77 p287 1925

4.6 E.W.B. Gill, A. von Engel Proc Roy Soc A192 p446 1947

4.7 A.J. Hatch, H.B. Williams J Appl Phys 25 (4) p417 1954

4.8 S.C. Brown 'Basic data for plasma physics' MIT press 1954 p209

4.9 H.S. Butler, G.S. Kino Phys Fluids 6 p1346 1963

4.10 L.I. Maissel: in 'Handbook of thin film technology' Eds. L.I.Maissel & H. Glang McGraw New York 1970 p3-10

4.11 J. Cobine 'Gaseous Conductors' Dover Pubs. ISBN:486 60442 p123

4.12 A. von Ardenne: in 'Tabellen zur angeworten Physik' (1) V.E.B. Verlag der Wissenschaften, Berlin 1962 p616

4.13 R.T.C. Tsui Phys Rev 168 (1) p107 1968

4.14 J.H. Keller, W.B. Pennebaker IBM J Res Dev 23 (1) p3 1979

4.15 J.R. Acton, J.D. Swift 'Cold cathode discharge tubes' Academic press 1963 p236

4.16 S.C. Brown 'Basic data for plasma physics' MIT press 1954 p55

4.17 S. Vacquie, J. Bacri, G. Serrot Compt Rendu 266 p387 1968

4.18 R.E. Jones, C.L. Standley, L.I. Maissel J Appl Phys 38 (12) p4656 1967

4.19 B.A. Probyn Vacuum 18 (5) p253 1967

4.20 J.L. Vossen J Vac Sci Tech 8 (5) pS12 1971

4.21 L. Holland, T. Putner, G.N. Jackson J Phys E Series 2 (1) p32 1968

4.22 G.N. Jackson Elec Equip News 16 (3) p71 1974

4.23 P. Lorrain, D.R. Corson 'EM fields and waves' W.H. Freeman San Fransisco 1970 p127

4.24 F.L. Paradis J Vac Sci Tech 11 (6) p1170 1974

4.25 W.D. Westwood, R. Boynton J Appl Phys 43 (6) p2691 1972

4.26 F.W. Aston Proc Roy Soc A79 p80 1907

4.27 I. Brodie, L.T. Lamont, D.O. Myers J Vac Sci Tech 6 p124 1968

4.28 J.D. Cockroft Proc Com Phil Soc 22 p759 1925

4.29 T.J. Higgins Trans Amer Soc Mech Eng 66 p665 1944

4.30 H.S. Carslaw, J.C. Jeager 'Conduction of heat in solids' Clarenden Press 1954 p224

4.31 M.A. Abramovitz,I.A. Stegun 'Handbook of mathematical functions' Dover Pubs New York 1965 p378

4.32 BICC publication number 659 'Enamelled round wire winding data'

4.33 'Glass at a glance' J.A. Jobling & Co Ltd Sunderland 1964 p8

4.34 L. Holland Vacuum 28 (10/11) p439 1978

4.35 J.L. Vossen, J.J. O'Neill J Vac Sci Tech 12 (5) p1052 1975

4.36 D.M. Usher, G.A. Cox Vacuum 31 p23 1981

5.1 F.E. Terman 'Radio Engineer's Handbook' McGraw-Hill 1943

5.2 W.C. Johnson 'Transmission lines and networks' New York McGraw-Hill 1950

5.3 E.N. Lurch 'Fundamentals of electronics' New York Wiley 1960

5.4 M.M. Cirovic 'Basic electronics' 2nd Ed. Reston Publ. 1979 p246

5.5 E. May 'Industrial high frequency electric power' Wiley 1950

5.6 Type TX5 transmitting capacitors, Jackson Brothers (London).

5.7 P. Lorrain, D.R. Corson 'EM fields and waves' W.H. Freeman and Co 1962 p347

5.8 Ref 5.1 p55

5.9 H. Norstrom Vacuum 29 (10) p341 1979

5.10 W.T. Scott 'The physics of electricity and magnetism' 2nd Ed Wiley p330 1966

5.11 Ref 5.1 p71

5.12 F. Grover, H. Dwight Elect Eng 56 p347 1937

5.13 R.G. Meadows 'Electric network analysis' Penguin 1972 p178

5.14 R. Bruce McDowell Solid Stat Tech Feb p23 1969

5.15 Ref 5.13 p303

5.16 G.C. Southworth Microwave J Jan p25, Feb p24 1954

5.17 J.S. Logan, N.M. Mazza, P.D. Davidse J Vac Sci Tech 6 (1) p120 1969

5.18 G.N. Jackson Vacuum 21 p533 1971

5.19 Ref 5.13 p370

5.20 'Thruline' RF Wattmeter 'Bird' Model 4527 Aspen Electronics Ruislip

5.21 G.D. Monteath Proc. Inst Elect Eng 102 B p383 1955

5.22 H.C. Early Proc IRE Nov p883 1946

5.23 R.L. Conhaim Electronics World Oct p53 1963

5.24 A.Y. Rumfelt, L.B. Elwell Proc IEEE 55 (6) p837 1967

5.25 American Radio Relay League HQ staff 'The Radio Amateurs' Handbook' 1967 p365

5.26 J.J. Brophy 'Basic electronics for scientists' McGraw-Hill 1966 p48

6.1 Optical pyrometer: Leeds and Northup Co Serial No 1678032 Cat No 8632-C

6.2 Spot Photometer: Infra-red Industries Inc Model No. TD-7B Serial No 1354

6.3 A. Rothen Rev Sci Inst 28 (4) p283 1957

6.4 O.S. Heavens Rep Prog Phys 23 p1 1960

6.5 Rank Taylor Hobson Talystep Machine Model 283-7

6.6 T. Putner Thin Solid Films 1 p165 1967

6.7 Thin Film Deposition Controllers Leybold-Herhaus GMBH Bonner Strasse 504 POB510760 D-500 Koln 51

7.1 L. Holland, W. Steckelmacher, J. Yarwood 'Vacuum manual' Ed: E. & F.N. Spon 1974

7.2 M. Prutten 'Surface physics' Clarendon 1975 p5

7.3 P. Auger J Phys Rad 6 p205 1925

7.4 K. Siegbahn 'Atomic, molecular and solid state structure studied by means of electron spectroscopy, ESCA' Almqvist and Wiksell, Uppsala 1967

7.5 T.E. Gallon, J.A.D. Matthew Rev of Phys in Technology 3 (1) p31 1972

7.6 T.E. Gallon 'Current problems in AES' in 'Electron spectroscopy of solids' Eds: L. Fiermans, J. Vernik, W. Dekeyser Plenum Press New York 1978 p230

7.7 C.C. Chang 'Analytical Auger spectroscopy' Chap 20 'Characteristics of solid surfaces' Eds: P.F. Kane G.B. Larrabee Plenum New York 1974

7.8 H. Ibach 'Electron spectroscopy for surface analysis'

7.9 E.U. Condon, G.U. Shortley 'The theory of atomic spectra' C.U.P. London 1970

7.10 N.F. Mott Rev Mod Phys 50 (2) p203 1978

7.11 N.F. Mott Contemp Phys 18 (3) p225 1977

7.12 G. Pfister, H. Scher Proc 7th Conf on Amorphous and liquid semiconductors 1977 p197 Ed: W.E. Spear

7.13 J.A. Bearden, A.F. Burr Rev Mod Phys 39 p125 1967

7.14 J.A.D. Matthew J Phys B 10 p783 1977

7.15 C.A. Nicolaides, D.R. Beck Chem Phys Lett 27 p269 1974

7.16 S.M. Barlow D Phil Thesis Physics Department University of York 1979 Chapter 2

7.17 P.W. Palmberg, G.E. Riach, R.E. Weber, N.C. MacDonald 'Handbook of Auger electron spectroscopy' Minnesota 55435

7.18 E.S.H. Burhop 'The Auger effect and other radiationless transitions' C.U.P. 1952 para 3.7

7.19 H.E. Bishop, J.C. Riviere J Apple Phys 40 (4) p1740 1969

7.20 E.H.S. Burhop J Phys Rad 16 p625 1955

7.21 K.D. Sevier 'Low energy electron spectrometry' Wiley New York 1972 p157

7.22 C.R. Worthington, G.G. Tomlin Proc Phys Soc A69 p401 1950

7.23 M. Gryzinski Phys Rev 138 A305 1965

7.24 R.F. Weber Res Rev 10 p22 1972

7.25 T.E. Gallon, M. Prutton, L. Wray J Vac Sci Tech 9 (2) p911 1972

7.26 K. Kanaya, S. Okayama J Phys D 5 p43 1972

7.27 J. Lindhard, M. Scharff, H.E. Schiott Kgl Danske Vid Selsk Matt Phys Medd 33 (14) 1963

7.28 W.E. Spear Proc Roy Soc B68 p991 1955

7.29 J. Lineweaver J Appl Phys 34 (6) p1786 1963

7.30 C.R. Brundle Surf Sci 48 p49 1975

7.31 C.C. Chang Surf Sci 48 p9 1975

7.32 M.P. Seah, W.A. Dench Surface and Interface Anal 1 p2 1979

7.33 P.H. Holloway J Elec Spec 7 p215 1975

7.34 A.M. Pollard D Phil Thesis Physics Department University of York 1979 Chapter 4

7.35 H.E. Bishop, J.P. Coad, J.C. Riviere J Elec Spec p389 1 1972

7.36 R.W. Roberts, T.A. Vanderslice 'Ultra-high vacuum and its implications' Prentice Hall New Jersey 1963

7.37 E. Bauer Vacuum 22 (11) p539 1972

7.38 V.V. Zashkvara, M.I. Korsunskii, O.S. Kosmachov Soviet Phys Tech Phys 11 (1) p96 1966

7.39 H.Z. Sar-El Rev Sci Inst 38 p1210 1967

7.40 H. Hafner, J.A. Simpson, C.E. Kuyatt Rev Sci Inst 39 p33 1968

7.41 J.S. Risley Rev Sci Inst 43 (1) p95 1972

7.42 H. Froitzheim 'Electron energy loss spectroscopy' in 'Electron spectroscopy for surface analysis' Ed: H. Ibach Springer-Verlag Heidlberg New York 1977

7.43 J.M. Hill, D.G. Royce, C.S. Fadley, W.F. Wagner Chem Phys Lett 44 (2) p225 1976

7.44 F.C. Brown 'UV spectroscopy of solids' Solid state Phys 29 p29 1974

7.45 R. de L. Kronig J Opt Soc Amer 12 p549 1926

7.46 F. Stern Solid state Phys 15 p341 1963

7.47 C. Kittel 'Introduction to solid state physics' Wiley New York 1971

8.1 F. Ohuchi, M. Ogino, P.H. Holloway, C.G. Pantano Jr abstract J Vac Sci Tech 16 (2) p257 1979

8.2 C.A. Friskney, C.W. Haworth J App Phys 38 p3796 1967

8.3 B.G. Baker, B.A. Sexton Surf Sci 52 .353 1975

8.4 L.G. Pittaway Brit J Appl Phys 15 p967 1964

8.5 C.L. Babcock 'Silicate glass technology methods' Wiley 1977 p271

8.6 R.W. Douglas, J.O. Isard J Soc Glass Tech 33 p289 1949

8.7 L.W. Barr, J.N. Mundy, A.H. Rowe in 'Amorphous materials' Eds: R.W. Douglas, B. Ellis Wiley Interscience 1972 p293

8.8 P.T. Dawson, O.S. Heavens, A.M. Pollard J Phys C 11 p2183 1978

8.9 C.G. Pantano, D.B. Dove, G.Y. Onada J Non-Cryst Solids 19 p41 1975

8.10 C.G. Pantano, D.B. Dove, G.Y. Onada J Vac Sci Tech 13 (1) p414 1976

8.11 L. Vaskova, V. Hulinskij, E. Drncova Silikaty 20 (4) p289 1976

8.12 S. Thomas J Appl Phys 45 (1) p161 1974

8.13 D. L. Lacharme, P. Champion Comptes Rendues Hebd Seances Acad Sci 287c p139 1978

8.14 O.S. Heavens, D.M. Usher "Problems avec l'examen du verre par spectroscopie Auger" given at the 'Union scientific continentale du verre' meeting at Avon, France Oct 1980 entitled "La surface du verre: ses proprietes et les moyens de les ameliorers"

8.15 D.M. Usher Paper accepted for publication by J Phys C,1981

8.16 'Handbook of physics' Condon & Odishaw McGraw-Hill 1967 p4-123

8.17 R.D. Townsend, J.C. Kelly 'Colour centres and imperfections in insulators and semiconductors' Chatto & Windus 1973

8.18 A. Bishay J Non-Crys Solids 3 p54 1970

8.19 E. Lell, N.J. Kreidl, J.R. Hensler Prog Ceram Sci 4 p11 1966

8.20 R.A. Weeks Phys Rev 130 (2) p570 1963

8.21 G.T. Petrovskii, D.M. Yudin Sov Phys Dokl 23 (5) p335 1966

8.22 A. Doi Jap J Appl Phys 17 (2) p279 1978

8.23 N. Mott Contemp Phys 18 (3) p225 1977

8.24 N.C. MacDonald, T.E. Everhart J Appl Phys 39 (5) p2433 1977

8.25 R.S. Barker, P.A. Richardson, E.A. McConkey, R. Rimmer Nature 187 p135 1960

8.26 B. Gross Phys Rev 107 (2) p368 1957

8.27 A.P. Balashov, Yu.B. Govyadovskii, V.F. Kosmach Sov Atomic Energy 44 p530 1978

8.28 A. Smakula Z Physik 59 p603 1930

8.29 D.L. Dexter Phys Rev 107 (1) p48 1955

8.30 N.F. Mott Rev Mod Phys 50 (2) p203 1978

8.31 D.A. Stephenson, N.J. Binkowski J Non-Cryst Sol 22 p399 1976

8.32 E. Ellis, D.W. Johnson, A. Breeze, P.M. Magee, P.G. Perkins Phil Mag B 40 (2) p105 1979

8.33 A. M. Pollard D Phil Thesis Physics Department University of York 1979 Chapter 5

8.34 J.A.D. Matthew, A.M. Pollard, O.S. Heavens Conference of Soc Glass Tech, Nottingham 1980

8.35 J.E. Rowe Appl Phys Letts 25 p576 1974

8.36 B. Bagley J Non-Cryst Solids 22 p107 1975

8.37 H. Ibach, J.E. Rowe Phys Rev B 10 (2) p710 1974

8.38 A. Koma, R. Ludeka Phys Rev Lett 35 p107 1975

8.39 C.E. Moore 'Atomic energy levels Vol 1' Circ of NBS p467 1949

8.40 D.L. Malm, M.J. Vasile, F.J. Padden, D.B. Dove, C.G. Pantano J Vac Sci Tech 15 (1) p35 1978

8.41 L.L. Hench, D.E. Clark J Non-Cryst Solids 28 p83 1978

9.1 C.V. Raman, Nobel Prize 1928

9.2 D.A. Long 'Raman spectroscopy' McGraw-Hill 1977

9.3 N. B. Colthup. L.H. Daly, S.E. Wiberley 'Introduction to infra-red and Raman sepctroscopy' Academic Press 1964

9.4 G.W. Chantry 'The Raman effect, Vol 1, Principles' Chapter 2. Ed: A. Anderson Marcel Dekker New York 1971

9.5 Cat, No. 1403, serial no.6033 Metuchen New Jersey

9.6 I. Simon 'Modern aspects of the vitreous state' Ed: J.D. MacKensie Butterworths 1960 1 p120

9.7 M. Hass J Phys Chem Solids 31 p415 1970

9.8 W.L. Konijnendijk, J.M. Stevels J Non-CrystSolids 21 p447 1976

9.9 J. Wong, C.A. Angell 'Glass structure by spectroscopy' Marcel Dekker New York Chapter 7

9.10 J.R. Ferraro, M.H. Manghnani J Appl Phys 43 p4595 1972

9.11 I. Bock, Su Gouq-Jen Amer Cer Soc 53 p69 1970

9.12 W.A. Pliskin, P.D. Davidse, H.S. Lejman, L.J. Maissel IBM Journal p461 1967

9.13 J.F. Rabolt, R. Santo, J.D. Swalen App Spect 33 (6) p549 1979

10.1 Ion plating and allied techniques Conference Edinburgh June 1977

10.2 D.M. Mattox J Appl Phys 34 p3493 1963

10.3 D.M. Mattox Proc VI Int Vacuum Congress Kyoto 1974 Jap J Appl Phys 1974 Suppl II

10.4 K.C. Park, E.J. Weitzmann J Vac Sci Tech 14 (6) 1977 p1313

10.5 E.Kny, G Nauer Glass Tech 22 (1) p $_{38}$ 1981

10.6 The assistance of Dr T. Robards of the biology department, University of York, is gratefully acknowledged

10.7 W. Fedrowitz, W.A. Pliskin Thin Solid Films 72 (3) p485 1980

10.8 D.E. Niesz, H.A. Beale Thin Solid Films 72 (3) p495 1980